Functional Polysaccharide Nanomaterials (PS-NMs) for the reduction of elevated serum cholesterol & progressive diet-induced obesity (DIO):

A 'novel' application of PS-NMs

by

Muhammad Shahidul Islam

A thesis
presented to the University of Waterloo
in fulfillment of the
thesis requirement for the degree of
Doctor of Philosophy
in
Chemical Engineering (Nanotechnology)

Waterloo, Ontario, Canada, 2022

© Muhammad Shahidul Islam 2022

Examining Committee Members

Kam C. (Michael) Tam:	Supervisor/Principal Investigator
Evelyn K.F. Yim:	Committee member (Internal)
Perry Chou:	Committee member (Internal)
Michael Beazely:	Committee member (Internal–External)
Jin Zhang:	Committee member (External)

Author's Declaration

I hereby declare that I am the sole author of this thesis. This is a true copy of the thesis, including any required final revisions, as accepted by my examiners.

I understand that my thesis may be made electronically available to the public.

Abstract

High plasma cholesterol (hypercholesterolemia) is a potential consequence of obesity that is becoming a major public health challenge. Excess caloric intake without a corresponding increase in energy expenditure is believed to be the major contributing factor to weight gain among Canadians leading to hypercholesterolemia. This ‘silent killer’, hypercholesterolemia is characterized by increased low-density lipoprotein cholesterol (LDL–C) that increases the risk of cardiovascular diseases which are still the leading cause of death and disability worldwide. Bile acid sequestrants (BAS), such as cholestyramine are positively charged indigestible resins that have been widely used for the treatment of hypercholesterolemia. However, it has many side effects, such as increasing the triglycerides level, constipation, flatulence, and abdominal pain all of which are due to its hydrophobic nature and large dose required for treatment.

Biopolymers are naturally occurring polymers and the polysaccharides (PS) is one of the subclasses, including cellulose, hemicellulose, starch, lignin, and chitin chitosan, gums etc. Among the PSs, cellulose is the most abundant and chitin the second. The amorphous regions of cellulose and chitin can be dissociated by acid hydrolysis, yielding high aspect-ratio rigid rod-like nanocrystals called cellulose nanocrystals (CNC) and chitin nanowhiskers (Cht.NWs). Moreover, chitosan (CS), which has a myriad of biomedical applications reported over the past centuries, can also be derived from chitin. All these nanoparticles (NPs) are proven to be excellent candidates for various applications as they possess S.M.A.R.T.© characteristics, which are sustainable, modifiable (due to the abundant surface primary hydroxyl groups), active (highly dispersible in water and shows physicochemical activity) renewable (easy surface modification making them renewable), and non-toxic (being natural, they are biocompatible). Thus, there is a significant motivation to modify these NPs with different cationic functional groups or polymers providing a platform to develop more efficacious natural polysaccharide nanomaterial (PS-NM) as BASs.

In this Ph.D. study, PS-NMs based biocompatible BASs were synthesized via the grafting of compounds with different quaternary ammonium groups (QAGs) (e.g. glycidyl trimethylammonium chloride *i.e.* GTMAC) or amino polymers (e.g. poly[2-(dimethylamino) ethyl methacrylate] *i.e.* PDMAEMA) onto CNCs, Cht.NWs and/or CS yielding quaternized/cationic NPs (Q-NP/C-NPs) with varying degrees of surface charge densities. The syntheses suggested that the (CNC/Cht.NW):(QAG containing compounds) of 1:10 yielded the largest surface charges. After purification, these Q-NPs were then characterized and evaluated using FTIR, dynamic and static light scattering (for structure confirmation, size, and zeta potential), potentiometric titration (for QAG or tertiary amino groups content, binding capacity), transmission electron microscopy (for the morphology of NPs), and UV-Vis spectroscopy. Most of the synthesized NPs possessed good aqueous dispersibility with diameters (D_H) within the nano range (< 1µm), and the zetapotential (ZP) to be within the colloidally stable range (≥ ± 25 mV). The quaternary ammonium groups (QAGs) validated their high ZP values and the QAGs were from 0.8 mmol/g to 2.9 mmol/g.

The PS based NMs were strongly cationic, and they could be used to sequester negatively charged ligands (eg., anionic dyes or impurities, the bile salts from human GI systems, etc.) from aqueous samples in effluent treatment or reduced the LDL–C levels. Initially, the batch adsorption tests (BATs) with all these NMs were conducted using methyl orange (MO), a negatively charged dye as a model compound due to the lack of available techniques to quantify bile salts. The Q_{max} determined from the Langmuir Isotherm fitting model (~ 200 mg/g) strongly suggested that the nano-systems were excellent sequestrants for anionic compounds. Their scavenging performance for bile salt were evaluated using sodium cholate (SC or Na-Ch), one of the bile salts/acids (BS/BA) in the human body. The Q_{max} values were higher (Q_{max} for most of the NMs were > 300 mg/g) than MO, suggesting that the scavenging effects for SC were higher due to the combination of all three binding mechanisms, namely electrostatic, hydrophobic, and hydrogen bonding.

An electrochemical based sensor for detecting SC was developed to quantify free or unbound BA/BSs in aqueous solutions. The Q_{max} data obtained from the BAT using this sensor

showed promising binding of NMs with SC that further reinforced that all the NMs developed in this study were active bile acid sequestrants. In addition, from the carbon dioxide evolution analysis using Baker's yeast, the PS-NM developed in this doctoral research displayed toxicity below that of cholestyramine, the widely used BAS in the market. Binding kinetics experiments showed the adsorption of SC onto these NPs was faster than cholestyramine, which suggested that the PS-NMs could be the BASs of choice and *in vivo* studies animal should be pursued.

Acknowledgements

First and foremost, I would like to convey my profound gratitude and earnest appreciation to Dr. Michael K.C. Tam, Professor of Chemical Engineering, Faculty of Engineering; University of Waterloo for his expert supervision, constant inspiration, invaluable counselling, constructive instructions, and concrete suggestions throughout the research work. His guidance helped me to overcome impediments encountered during my graduate studies. I would not be here without his expertise and innovative input that spurred my inquisitiveness and helped me to be an aspiring researcher. It has been an amazing experience for personal and professional growth, and an absolute honor to have a supervisor/mentor that I can rely on for advice and support now and, in future.

I would like to thank my committee members: Dr. Evelyn K.F. Yim (internal), Dr. Valerie Ward (internal), and Dr. Michael Beazely (internal/external) for all their encouragement and instructions on my research. Many thanks to Dr. Juewen Liu for providing me the opportunity to use many of his instruments, and to Dr. Leonardo Simon (especially, Sophie Campbell from his lab) for allowing me to use his FTIR machine.

I had the opportunity to work with many of my coworkers in Dr. Tam's group. I would like to thank **ALL** the members for all their support. A special thanks go to Dr. Reynard Tang, Dr. Grishkewich, Dr. Nasseri, and Dr. Ram for their professional help, and extraordinary guidance to conduct experiments throughout this program. A few more distinct mentions include Lian (all TEM images), Iflah (python installation and introduction), and Yebin (yeast experiments).

I am grateful for the continuing support, inspiration, and tremendous patience from my loving wife for all the good/tough times and my presence in the lab for unusually extended periods. My Ph.D. journey would not be possible without her support and sacrifices. So, "Thank you"!! I had the opportunity to be the proud dad to three fantastic children (the younger two during my Ph.D. study) and my presence in the lab was mostly possible as she took full responsibilities of all three children during my study! Although being from Social Science

(MSS; Economics) background, she patiently read the introduction and 1st chapter of my thesis and provided some insights that improved the clarity of the thesis.

Lastly, I would like to express my heartfelt thanks to all the students and volunteers for their priceless help, namely Lian, Carlos, Logan, Amber (Yifan), Jassie (Yuxin), Ashley, Sheng, Nathania, Anjiya, Jing, Aryan, Sarah, Julie, Manal, and Romey. It was a pleasure and fun working with you all.

Dedication

TO MY PARENTS

for raising me to believe that anything was possible

TO MY BELOVED WIFE, FARZANA

for making everything possible

"Testimonies are wonderful. But so often our lives don't fit our testimonies"

– Leonard Ravenhill (1907–1994)

Disclaimer

The following thesis work is designed with the aim of indirectly reducing the plasma cholesterol (LDL–C) level in hypocholesterolemic patients. This is achieved through the direct removal of irreversible complex formation between the developed NPs and bile salts, representing one of the mechanisms for lowering the elevated cholesterol level. Bile salts/acids are secreted from the gall bladder to the duodenum due to regular hepatobiliary function in response to the presence of fatty food chyme in the duodenum. The complexes formed in the small intestine are eventually excreted through stool. However, the NMs would not work in reducing the LDL–C **IF** there is a disruption in the regular hepatobiliary function leading to no secretion of bile @ duodenum in response to appropriate trigger(s) in the GIT.

In such conditions, these NPs may still work for the cessation of 'progressive' obesity due to ingestion of the fatty meal or any of the meals with heavy cream or fat portion (diet induced obesity, DIO).

~~Muhammad~~ Shahid~~ul~~ Islam,
Author; 2022

Table of Contents

Examining Committee Members ii

Author's Declaration iii

Abstract iv

Acknowledgements vii

Dedication ix

Disclaimer x

List of Figures xvii

List of Tables xxxviii

List of Abbreviations xl

Chapter 1 : Motivation, scope, and novelty of work 1

1.1 Introduction 1

1.2 Problem Statement & Motivation 2

1.3 Background 8

1.4 Objective and Scope 11

1.5 Hypothesis 12

1.6 Motivations 13

1.7 Novelty of the project 14

1.8 Thesis outline 16

Chapter 2 : Literature Review 19

2.1 Introduction: Chemistry, and Properties of Bile Acids/Salts (BAs/BSs)' 19

2.2 BA synthesis, metabolism, & enterohepatic circulation (EHC)/bile pool 22

2.3 Polymeric BASs in the market and their limitations 24

2.4 Concurrent polymeric BA sequestrants (BAS) from literature 26
2.5 Biopolymer-based BA sequestrants (BAS) 27
2.6 Cellulose and derivatives as the BASs 29
2.7 Other bio-PS based BAS: 37
2.7.1 Functionalized Paramylon 37
2.7.2 Functionalized Ulvans 41
2.7.3 Polysaccharides from sea cucumber, *Apostichopus japonicus* (AJP) 44
2.7.4 Amino-bio-PS based BASs: Chitosan and Chitin/derivatives 45
Chapter 3 : Cellulose nanocrystals (CNCs) based BAS 47
3.1 Introduction 47
3.2 CNC Extraction and notable properties 48
3.3 Development of cationic CNC 50
3.4 Materials and Methods 50
3.4.1 Materials 50
3.4.2 Desulfation of NCC™ 51
3.4.3 Grafting of GTMAC onto CNCs 55
3.4.4 FTIR Characterization of DS–CNCs and Q–CNCs 59
3.4.5 Elemental Analysis of DS–CNCs 60
3.4.6 Potentiometric/Conductometric titration of DS–CNCs 60
3.4.7 Potentiometric/Conductometric titration of Q–CNCs 62
3.4.8 Aggregates sizes (D_H) and zeta potentials (ZP) of NPs 63
3.4.9 Transmission electron microscope (TEM) images of NPs 64
3.4.10 Batch Adsorption Tests (BATs) for binding efficiencies of NPs 64
3.5 Results and Discussion 71

3.5.1 Percentage yield and Desulfation of NCC™ 71
3.5.2 FTIR characterization of DS–CNC and Q–CNCs 75
3.5.3 Grafting efficiencies and QAG contents of the Q–CNCs 77
3.5.4 Sizes and Zeta potentials of DS–CNCs and Q–CNCs 82
3.5.5 Sizes and Zeta potentials of the chosen Q–CNC @ different pH ranges 85
3.5.6 TEM images of DS–CNCs and Q–CNC 87
3.5.7 Batch Adsorption Tests (BAT) for chosen/selected NPs 88
3.5.7.1 BAT with Methyl Orange (MO) via UV-Vis method 89
3.5.7.2 BAT with Sodium Cholate (SC) via Conductance and UV–Vis method 95
3.6 Conclusions 99
Chapter 4 : Hydrophobically modified PS based NMs as BAS 101
4.1 Introduction 101
4.2 Materials and Methods 103
4.2.1 Materials: 103
4.2.2 Synthesis of DDEAC surfactant & Q–C_{12}–CNC_a NPs 104
4.2.3 Synthesis of quaternized chitosan (Q–CS) 108
4.2.3.1 Synthesis of the quaternized chitosan (Q–CS), the HTCC 108
4.2.3.2 Synthesis of the oxidized CNCs (CNC_{OX}): TEMPO mediated oxidation 110
4.2.3.3 Grafting of QCS on the CNC_{OX} NPs using EDC crosslinker 112
4.2.4 Synthesis of pQDMAEMA–g–CNC NPs by Free Radical Polymerization[116] 112
4.2.4.1 Synthesis of pDMAEMA–g–CNC by ATRP 112
4.2.4.2 Quaternization of the synthesis of pDMAEMA–g–CNC by MeI[192,193] 114
4.2.5 Method: ^{1}H NMR characterization 116
4.2.6 Surface Tensiometry (ST) 116

4.3 Results and Discussion 117
4.3.1 CMC determination of DDEAC 117
4.3.2 Yield and QAG contents 118
4.3.3 FTIR Characterization 120
4.3.4 Aggregate sizes (D_H) and zeta potentials (ZP) 122
4.3.5 TEM Images of the NMs 124
4.3.6 BATs for the NMs with MO and SC 125
4.4 Conclusions 129
4.5 Future Directions 130
Chapter 5 : Amino–PS, Chitin based NMs as BAS 131
5.1 Introduction 131
5.2 Materials and Methods 135
5.2.1 Materials 135
5.2.2 Alkali mediated deacetylation of α–Chitin followed by Cht.NF extraction 135
5.2.3 Cht.NFs (nanochitin) extraction via mechanical treatment 138
5.2.4 HCl mediated deacetylation of α–Chitin (Cht.NW/NC extraction) 141
5.2.5 Quaternization of the extracted Cht.NW_a/NC_a 143
5.2.6 Other methods 145
5.2.7 Batch Adsorption Tests (BATs) of the NPs with MO 145
5.3 Results and discussion 147
5.3.1 Yield % of the developed NMs (chitin based) 147
5.3.2 FT-IR of the developed Chitin–NMs 147
5.3.3 QAGs and cationic groups contents via conductometric titrations 149
5.3.4 Ave D_H and zeta potentials (ZPs) of the developed Chitin–based NMs 151

5.3.5 TEM images of Chitin–based NMs 156
5.3.6 BATs of Chitin–based NMs with MO 157
5.4 Conclusions 163
5.5 Future Directions 163
Chapter 6 : Development of Sodium Cholate detection System 164
6.1 Introduction 164
6.2 Ion-selective electrode (ISE) 166
6.3 Cholate selective membrane electrode (CSE): Components 169
6.4 Working principal of the CSE: Nernstian response 172
6.5 Mechanism of the developed potentials @CSM: Ion transduction 174
6.6 Materials and Methods 177
6.6.1 Materials: 177
6.6.2 Synthesis of ionophore 177
6.6.3 FT–IR of the ionophore 180
6.6.4 Casting of CSM 180
6.6.5 Electrode head fabrication and conditioning 182
6.6.6 Construction of calibration curve of SC with the CSE 185
6.6.7 Calibration curve of SC via Tensiometry & Conductometry 187
6.6.8 BATs of SC for selected NMs and Q_{max} determination by the CSE 189
6.6.9 Binding/Adsorption Kinetic Tests (AKTs) of SC with the NMs 192
6.7 Results and Discussion 194
6.7.1 Yield and FT–IR of BDMCA–Cholate ionophore 194
6.7.2 Calibration curves of SC via EMF technique from the CSE 195
6.7.3 Micellization and CMC determination of SC from EMF *vs* Log(C) plots 197

6.7.4 Calibration curves & CMC of SC from Tensiometry and Conductometry 199
6.7.5 BATs of selected NPs with SC and Q_{max} determination through CSE 202
6.7.6 Adsorption Kinetic Tests (AKT) for the NMs with SC 208
6.8 Conclusions 213
6.9 Future directions 214
Chapter 7 : Biosafety of the developed NMs 215
7.1 Introduction 215
7.2 Yeast cell: Anatomy and fermentation of glucose 216
7.3 Reported effects of polymers on yeast cells & mechanism of inhibition 218
7.4 Materials and methods 222
7.4.1 Materials 222
7.4.2 Methods 222
7.5 Results and discussion 224
Chapter 8 229
8.1 Conclusions and Future directions 229
8.1.1 Conclusions 229
8.1.2 Future directions 232
References 235
Appendix A 265

List of Figures

Figure 1.1: Schematic illustration of the impact of hypercholesterolemia (HL) on HDL remodeling. The 'silent killer' HL induces HDL lipidomic changes, losing phosphatidylcholine-lipid species and gaining cholesteryl esters, with losses in cardioprotective proteins. Such remodeling of HDL particles shifted them towards a dysfunctional state. Modified from[17]. 3

Figure 1.2: Chemical structures of BASs or resins available in the Canadian market for the treatment of hypercholesterolemia, A) Cholestyramine (1st generation BAS), B) Colestipol (1st generation BAS), and C) Colesevelam (2nd generation BAS; colestimide is also 2nd generation, the structure of which is not shown here and is not available in Canada). 6

Figure 1.3: Scheme representing the simplest classification of bio-polysaccharides (bio-PSs) based on their sources of origin. This illustration is just an example and is not a comprehensive list of all the reported bio-PSs. Many of the enlisted bio-PSs possess S.M.A.R.T.© properties and have biomedical applications. (S.M.A.R.T. © coined by the author of the thesis for the 1st time and is derived as the abbreviation of sustainable, modifiable, active, renewable, and natural & non-toxic). 9

Figure 1.4: A) Flow diagram of enterohepatic circulation (EHC) of bile showing the reabsorption (95% of the secreted bile) of freed up BA/BS for storage at gall bladder. B) Schematic illustration of the mechanism of action of a typical BAS. 14

Figure 1.5: A) Number of publications in the area of nanocellulose. Data analysis was performed on SciFinder using terms nanocellulose, cellulose nanocrystals, microfibrillated cellulose, nanofibrillated cellulose. Reused from[54]. B) Elaboration of S.M.A.R.T.© nanomaterials (NMs) and an example of such NMs presented in the insert. 15

Figure 1.6: Overall illustration on the thesis and chapters. 16

Figure 2.1: Chemical structures of different BAs available in humans. A) 1^0 & 2^0 BAs in the body. B) Conjugated BA derivatives, commonly known as bile salts (BSs). 21

Figure 2.2: Two different pathways for the synthesis of BAs: Classical (neutral) pathway that occurs in the liver (hepatocyte) and the alternate (or acidic) pathway found in peripheral tissues and the liver, showing the primary and secondary BAs. In the classic pathway, the primary bile acid cholic acid (CA) is formed after subsequent conversions from sterol 12α-hydroxylase (CYP8B1) and chenodeoxycholic acid from sterol 27-hydroxylase (CYP27A1). In the alternative or acidic pathway, mitochondrial CYP27A1 in peripheral tissues convert cholesterol into 27-hydroxycholesterol. Oxysterol 7α-hydroxylase (CYP7B1) is an additional assisting enzyme in this pathway and the resulting products feed back into the liver, indicated by the red arrow feeding into the classical pathway under CYP27A1. The 1^0 & 2^0 BAs specific to rodents are listed in purple at the bottom right inset of the image. Bile acids can become conjugated with glycine or taurine after interactions with gut flora. Modified and reused from[66,67]. 23

Figure 2.3: Some examples of natural polysaccharides commonly used in biomedical applications. Reused from[73]. 28

Figure 2.4: Schematic of extraction of CNCs from a cellulose source (here, it is hardwood). CNCs can be extracted through mechanical, chemical or combination of mechanical, chemical and/or enzymatic (endoglucanase) treatments. Sulphuric acid (H_2SO_4) mediated hydrolysis is the most common and widely used technique for CNC production. The table drawn from[39–41]. 30

Figure 2.5: Schematic of hPEI-CE preparation and the sorption of sodium cholate (SC). Reused from[55]. 32

Figure 2.6: A) Schematic illustration of the efficacy of NCs/CNFs on modulation of fat digestion leading to the reduction of raised LDL-C from the outcome of scavenging BSs and interruption in the increasing trends of the DIO. Graphical representations of the effect of cellulose and other fibres on in vitro triglyceride digestion: (B) Total NaOH (0.25 M) titrant used during small intestinal digestion of heavy cream. (C) Total percentage of FFA released during small intestinal digestion of heavy cream. Reused and adapted from[53]. 36

Figure 2.7: Illustration showing the chemical structure of Paramylon. Here, if the R group is H, then it is paramylon. And if the R is H and/or glycidyl trimethylammonium chloride / (2,3-Epoxy-propyl) trimethylammonium chloride GTMAC/EPTMAC, then it is 2-hydroxy-3-(trimethylammonio) propyl paramylons (HTAPs). 38

Figure 2.8 Nomenclature and structure of the major repeating disaccharide units that comprise ulvan. Ulvanobiuronic acid A_{3s} contains glucuronic acid (blue) attached to rhamnose 3-sulphate (red), while the similar B_{3s} also contains rhamnose 3-sulphate but has iduronic acid (green) in the place of glucuronic acid. Ulvanobioses are comprised of rhamnose 3-sulphate attached to xylose (orange). Xylose can contain a sulphate group, as seen in $U_{2's,3s}$. Reused and adapted from[91,96]. 42

Figure 3.1: A) Illustration of cellulose showing the intra and inter-chain H-Bonding for the individual microfibril and the molecular representation of β1,4 glycosidic linkages between the AGU units. B) Hierarchical structure of cell walls from which the elementary fibrils and the CNC can be obtained. Drawn from[111]. 48

Figure 3.2: A) NCC^{TM} supplied from CelluForce, Canada, and the desulfation reaction scheme. After the surface desulfation, the primary alcoholic (1^0) groups may get converted to alkoxy-sodium form after alkali-mediated desulfation (if HCl is not used for NaOH neutralization). B) Schematic representation showing the reaction set up for the desulfation of NCC^{TM} or extraction of CNC (the CNCmcc or CNC_{MCC}) from MCC. C) Schematic of the desulfation reaction setup. After the reaction, the colour changed, and bigger lumps of precipitates were observed. D) Extractions steps of CNC from MCC (20 μ powder) during which a more pronounced colour change was observed. During dialysis, the extracted CNC_{MCC} was found a bit unstable in aqueous dispersion and settle at the bottom within a few hours. 53

Figure 3.3: A) Schematic showing the quaternization reaction for the CNC systems with GTMAC, added dropwise. Such reactions are S_N2 etherification reactions and if not done in organic media, then the degree of quaternization, DQ and the yield % get drastically low due to the occurrence of undesired side reactions. And the obtained Q–CNCs from the NCC^{TM}, DS–CNCs or CNC_{MCC} were structurally considered as

Zwitterionic of different degrees, where NCC™ leading Q–CNC was the most Zwitterionic and the CNC_{MCC} leading Q–CNC was the least Zwitterionic. B) Schematic of the quaternization reaction setup. After the reaction was completed, the colour of the mixture was found to be a bit darker yellowish in DMSO media. 57

Figure 3.4: Ion exchange steps for the conversion of Na–form of sulfate half ester, SHE (—OSO_3Na) groups to acidic forms of the SHE (—OSO_3H) groups done by the cation–exchange resin, Dowex® Marathon™ C, hydrogen form (DM–C). Literature suggested conducting multiple cycles of ion–exchange can ensure complete exchange of the targeted ion onto the surfaces of the nanoparticles (NPs). During the exchange process, the known starting concentration (conc.) of the dispersion get diluted due to rinsing the beads with MQ water each cycle, and the final conc. can be determined through gravimetric analysis (GA). 61

Figure 3.5: Schematic of the experimental setup for the BAT of NPs A) with Methyl Orange (MO), an anionic dye, and B) with Sodium cholate (SC), one of the primary bile acids in the human body. Here, the 1 and 2 represent the vials of two trials for the same conc. of ligands (and the NPs) to minimize the manual/experimental error, and the B vial stands for blank for each set of conc. For simplicity, the set of two vials for only one conc. of the ligands are shown here. For Langmuir adsorption isotherm nonlinear fitting model, a min of five (5) conc. of the ligands were chosen to conduct the BAT with constant conc. of the NPs/adsorbents. C) and D) represent the chemical structures of MO and SC, respectively in aq. solutions. 68

Figure 3.6: A) Reaction scheme between furfural and sodium cholate[157]. B) Color produced after 13 mins of reaction. C) Color produced after the addition of acetic acid as the final step. 69

Figure 3.7: Yield % obtained for the A) DS–CNCs and B) the corresponding Q–CNCs (except the Q–NCC™ and $Q–CNC_{MCC}$, which were not synthesized from any DS–CNC) C) Column chart representing the sulfate half ester groups (—OSO_3^-) contents for different DS–CNCs determined via conductometric titration and EA. D) Average % reduction of surface —OSO_3^- contents based on the two methods. 72

Figure 3.8: Post dialysis suspension (concentrated) of quaternized CNCs, Q–CNCs where the leftmost indicates the Q–CNC_6 and the next to the right refers to the Q–CNC_a. The rightmost image is the schematic representations of the synthesized Q–CNCs which are also the Zwitterionic NPs. All the Q–CNCs developed thus far for this chapter, being more hydrophilic, were found very easily dispersible in water. In aq. suspensions, both the counterions, the Cl^- for the grafted QAG groups and the Na^+ for the leftover/trace SHE groups (—OSO_3^-) are ionized making them Zwitterionic but overall cationic. These phenomena of Zwitterions also shed light on why and how the Q–CNCs exhibit some degrees of aggregations in colloidal suspensions. 74

Figure 3.9: A) FTIR spectra of (i) raw material (corn stalk); (ii) the extracted cellulose; and (iii) the CNCs. Reused from. B) FTIR spectra of (a) unmodified sulfuric-acid-hydrolyzed CNCs and (b) GTMAC-CNCs. Reused from. C) FTIR spectra of NCC™ and the corresponding DS–CNCs showing the reduction of the peak heights @ 1033 cm^{-1} which is reported to be for the —OSO_3^- groups (very subtle, and discernible easily if zoomed in). D) FTIR spectra of all the corresponding Q–CNCs based on the gradient DS–CNCs. Literature reported the peaks would be more intense than its precursors and we had such agreement for the synthesized Q–CNCs. Individual plots (not presented here) of DS–CNC_x and respective Q–CNC_x showed the distinct difference of peaks' intensities although no new peaks were discernible. 76

Figure 3.10: A) An acid–base conductometric titration curve & the equation utilized for determining the sulfate half ester (SHE) contents (mmoles/Kg of the CNC). Usually, three distinct zones are observed in such forms of conductometric titration plots, and in this case the volume (mL) required to neutralize the acidic forms of the SHE groups in zone–2 is the number considered for calculation. B) $AgNO_3$ mediated conductometric titration plots for determining the QAG contents and the equations used to determine various parameters. 78

Figure 3.11: A) The QAG contents of all the synthesized Q–CNCs which were determined from the equivalence (end) points obtained in the conductometric titrations of the 10 mM $AgNO_3$ with individual NPs. B) Comparison of the degrees of substitution of QAG

onto the NPs' surfaces with the QAG contents. Essentially, a higher achieved DS from a higher reaction efficiency (RE%) usually ensures a greater amount of grafting of the QAG, which was one of the expected outcomes for the target-specific application. C) Comparison of SHE and QAG contents of the modified CNCs (M–CNCs). The QAG contents exhibited a pattern of gradient increase over the Q–CNCs especially for those that were synthesized from the gradient desulfated CNCs (DS–CNCs) with decreasing contents of surface —OSO_3^- groups. D) The DS and CRE% of all the Q–CNCs made from DS–CNCs. 80

Figure 3.12: A) Summary of the average sizes (D_H) and ZP of all the DS–CNCs and the CNC_{MCC}. Here the gradient reduction of the surface negative charges of these NPs also establishes the fact of gradient removal (desulfation) of surface SHE groups (—OSO_3^-). Due to such phenomena, interparticle repulsions got reduced and aggregations of the NPs were seen from the D_H data. B) Gradient increasing trend of surface cationic charges of the Q–CNCs obtained from the corresponding DS–CNCs. In this case, being the Q–CNCs Zwitterionic, inconclusive trends of aggregation of the NPs were seen from the D_H data. C) Effect of organic solvents as the media of cationization reaction, giving the highest cationization for the DS–CNC_a in THF solvent (an ether). D) Summary of D_H and ZP of the Q–CNCs obtained from different cationization reactions done in DMSO, IPA, & THF solvents. 84

Figure 3.13: Summary of the average aggregate sizes (D_H) in A) and the average ZPs in B) of the three chosen Q–CNCs for which the ZPs were found highest discussed earlier. 85

Figure 3.14: TEM images of pristine CNCs (NCC^{TM}), the DS–CNCs and the CNC_{MCC} shown on the top row. Although the aqueous suspensions of the samples were made in diluted concentrations and sonicated prior to pipette onto the CFC grids, they showed interparticle aggregation due to drying. The bottom row shows the TEM images of representative Q–CNCs samples made and dried similarly to the other NPs as mentioned above. 87

Figure 3.15: Schematic representations of all probable interactions of MO with NP systems. The figure explains a fraction of the overall adsorption @ the surfaces is still possible

even though the NP is negatively charged, and this is feasible due to the existence of other non-electrostatic binding forces (hydrophobic interactions, H-bondings etc.). A strong complex of NP–MO is possible for the cationic NPs even though the NPs are happened to be Zwitterionic. 89

Figure 3.16: A) The calibration curves of filtered and unfiltered MO reference stock solutions. B) Average of the two calibration curves obtained for the filtered and unfiltered ref. solutions of MO. C) Average D_H and the calculated Q_{max} from the BAT with MO for the chosen NPs. The BATs were done in RT, in inherent (neutral) pH, and the amount/mass of the individual NPs added into the BAT vials was the same for all conc. of the MO. and for the D_H measurements, the conc. of the individual NP was at 0.05% (w/v) aq. suspension. D) Average ZP and the calculated Q_{max} from the BAT with MO for the chosen NPs. 91

Figure 3.17: A) The outlook of sonicated aq. DS–CNC_a at two different conc. (0.05 & 0.1 %, w/v) in 50 mM and 100 mM NaCl solutions. All the suspensions became cloudier after the dispersions were made in the NaCl solutions due to the significant extent of aggregation as a result of the charge shielding. Such aggregations are evident from the D_H and the ZP data presented in plot–B). Both controls (NCC^{TM} and DS–CNC_a) at a conc. of 1 mg/mL (0.1%, w/v) were considered for conducting the BATs in charge shielded state with the MO. C) Plot comparing/summarizing the ZP, and the Q_{max} values obtained from the BATs with MO through the LMAI linear fitting model. D) Plot summarizing the D_H and Q_{max} values of the charge-shielded controls. 94

Figure 3.18: A) The possible mechanisms of physicochemical adsorption of SC onto the surface of a Q–CNC system. During the BATs, most of the Q–CNCs showed distinct and visible aggregates and the commencement of such lumps started appearing slowly the moment after adding the NPs into the vessel containing the aq. solutions of SC. Although the mixture got a bit cloudy for NCC^{TM}, cloudier for DS–CNCs or CNC_{MCC}, no distinct aggregates were visible for such NP systems. B) & C) Calibration curves of aq. reference solutions of SC constructed through conductance and UV–Vis measurements, respectively. 96

Figure 3.19: The Q_{max} values obtained for SC through the LMAI linear fitting from the BATs via A) Conductance measurements, and B) UV–Vis measurements. The plots C) and D) summarized those Q_{max} values with the ZP and the D_H respectively. 98

Figure 4.1: A) Molecular structure of commercially available CS (DD = 85%) showing the groups/positions that can be functionalized: chemical modifications are feasible on the C–6 @ the primary alcoholic groups and on the —NH_2 groups @ C–2. Due to a very strong steric hindrance, no chemical modification is possible on the —OH groups @ C–3. The available free —NH_2 groups @ C–2 are the primary amines which always gets protonated at any pH below ~8 (thus pH responsive) to provide cationic functionalities of the molecule. B) A basic representative of cationic CS where many of the —OH groups (depending on reaction efficiencies) @ C–6 have been functionalized with GTMAC making the CS permanently cationic (the Q–CS), regardless of the pH. 103

Figure 4.2: A) Reaction mechanism of synthesis of DDEAC surfactant containing epoxide ring within the structure. B) DDEAC synthesis setup and outlook of the final product as in solution in IPA. Stored in RT after recording the conc. via the GA while the yield was also recorded. 105

Figure 4.3: Schematic representation of the quaternization (a de novo synthesis) of DS–CNC_6 with the synthesized DDEAC. A) Reaction steps showing the S_N2 reaction and the final Q–NP, structurally which is a Zwitterion having a C–12 hydrophobe (dodecyl alkyl chain) onto the grafted QAG. B) Schematic of the reaction setup at the laboratory scale, the insert represents the purified Q–C_{12}–CNC_6 Zwitterions which was then stored under refrigeration as the never dried suspension for further usage. 107

Figure 4.4: A) Schematic representation of the reaction scheme for the synthesis of Q–CS (HTCC). B) The overall reaction setup and purification of HTCC. The purified HTCC was found completely water soluble and was seen as slightly yellow/brown in aq. solution. The solution was stored at RT recording the conc. (obtained via GA) and was ready to use. 109

Figure 4.5: A) Reaction scheme and laboratory setup for the synthesis of A) TEMPO oxidized CNC from a selected DS–CNC or NCC^{TM}, and B) the QCS–g–CNC_{OX} from

the oxidized CNC NPs, which are structurally considered as a block type (M–N–M type) NPs and are Zwitterions having traces of both of the SHE groups (—OSO_3^-) and —COO^- groups along with the grafted Q–CS fibers. This overall cationic NPs were stored in the fridge for longer storage as the never dried suspensions, recording the conc. and yield%. In both cases of the syntheses, the NPs obtained was found less stable, especially the DS–CNC_{OX} which readily settled down at the bottom form the dispersions. The QCS–g–CNC_{OX} NPs were found a bit more stable than those of the CNC_{OX} NPs. 111

Figure 4.6: A) Synthesis set up and steps of pQDMAEMA with the monomer DMAEMA. B) Corresponding polymerization reaction scheme of the synthesis from DS–CNC_x via ATRP. 113

Figure 4.7: Quaternization of the pDMAEMA–g–CNC using MeI at the RT[192,193]. The pQDMAEMA–g–CNC is structurally a Zwitterion, and a significant extent of aggregation was seen in the post dialyzed suspension, which was stored at 4–8^0C. 115

Figure 4.8: Schematic structural representations of Zwitterionic NPs to be discussed in this chapter, A) the Q–C12–CNC_6, B) the QCS–g–CNC_x, and C) the pQDMAEMA–g–CNC_x NPs which resemble like the bottle-brush. The associated counter ions for the QAGs are chloride (Cl^-) for A) and B), and for the C) it is iodide (I^-) 115

Figure 4.9: A) SFT plot of DDEAC obtained from the Tensiometer. B) DDEAC molecule's chemical structure and schematic representation of the micelles. C) Fate of the DDEAC molecules at the water–air interface as the conc./no. of the molecules increases due to addition. 117

Figure 4.10: A) Percentage yield of the selected NPs synthesized. Here, except for the Q–CS, all the NPs are structurally considered as Zwitterions where, the QCS–g–MCC_a (or in another written format QCS–g–CNC_{MCC}) was the least or non-Zwitterions. B) The quaternary ammonium groups (QAG) contents determined from the $AgNO_3$ mediated conductometric titrations. C) The N,N-dimethyl-N-dodecyl amine monomer showing point of polymerization and the formation of tertiary (3^0) amino groups (due to

protonation) that can be quantifiable by HCl—NaOH mediated conductometric titration. 119

Figure 4.11: FT–IR spectra of A) CNC, Q–C_{12}–CNC, and the pQDMAEMA–g–CNC showing some characteristic peaks, and B) the CNC_{OX}, Q–CS, and the QCS–g–CNCs with notable characteristic peaks. 120

Figure 4.12: A) Average aggregate sizes (D_H) and the ZP of selected NPs. B) Experimental pH of the aq. suspensions of the NPs. C) The ave. D_H – pH profile of the three selected NPs (Zwitterions), and D) The ZP – pH profile of the three selected NPs. 123

Figure 4.13: Best possible obtained TEM images of the cationic (Zwitterionic) NMs systems; the Q–C12–CNC6, Q–CS, QCS–g–CNC_a, QCS–g–CNC_{MCC}, and the pQDMAEMA–CNCs. 125

Figure 4.14: A) The sodium cholate molecule and its two different faces in flat stereochemical conformation (schematic). B) Schematic illustration of the Q–C12–CNC6 and the complex formed with SC due to the physicochemical adsorption via ionic interactions (attractive long-range force, predominant, H–bonding as well as the hydrophobic interactions. Once the NP gets fully saturated as the monolayer formed, it is least likely to form another layer of adsorbates (the SC in this case) over the already formed monolayered complex. The dispersibilities of the NPs were seen drastically and significantly decreased right after the complexes were formed. 126

Figure 4.15: Comparison of the Q_{max} values for the Q–C_{12}–CNC_6, brush–CNC, and the Q–CS with A) average ZP and, B) average D_H. C) The Q_{max} values of the three NPs obtained from the BATs where the quantifications were done via conductance measurements. For A), B), and C) the QCS–g–CNCs were under synthesis. D) Q_{max} values for all the NPs via UV-Vis method. 127

Figure 5.1: A) Sources of chitin from sustainable sources and how chitin exists inside the exoskeletons. Here, I: Plywood structure of chitin, II: Ch-MFs in the matrix, and III: Mechanically extracted individual chitin NFs from the demineralized and deproteinized pure α–Chitin (powder). The insert to the right shows the crystalline (ordered, resistant to acid hydrolysis) and amorphous (disoriented/disordered, easily accessible for and

prone to acidic hydrolysis) region of individual bundle of chitin fibers. B) Parallel anti-parallel and mixed alignment polymorphs of chitin showing their different orientations of chains. The arrow indicates the reducing terminus/end. C) Basic chemical structure of the α–Chitin skeleton showing the glucosamine (GA) and N-Acetyl glucosamine (NAGA) attaching through the β-(1→4) linkages. Here the position 2 (C–2, for the acetamido groups) and position 6 (C–6, for the 1^0 alcoholic groups, CH_2OH) of the glucopyranose unit are the positions where most of the chemical functionalization occurs. A) & B) Adapted from[194,196,198,199]. 132

Figure 5.2: Microscopic images of A) Chitin nanofibers or nanochitin (Cht.NFs), and B) chitin nanowhiskers or nanocrystals (Cht.NWs or Cht.NCs). Adapted form[198,211–214]. 134

Figure 5.3: A) Overall roadmap for the defibrillation of the chitin to produce Cht.NFs from the deacetylation of α-Chitin powder. Adapted from[215]. B) Deacetylation reaction steps at molecular level showing the partial deacetylation giving rise to the 1^0 amino groups onto the surfaces. Drawn and adapted from[224]. C) Processing of deacetylation at laboratory scale from reaction to purification steps. The De–$Cht._B$ was found very unstable and within few hours, they form loosely settled sediments at the base of the contained bottle or glassware. Several pilot batches of De–$Cht._B$ were made and instantly non–using products were kept in the fridge (2–8^0C) for longer storage. 137

Figure 5.4: A) The processing of the De–$Cht._B$ dispersions for mechanical pre–treatment prior to run through the microfluidizer (μFD): from pH adjustment to multiple cycles of homogenization/sonication. The snapshot of table enlists a few specific parameters for the sonication steps. B) Schematic illustration for the impact of the mechanical pre–treatment steps on the bundled De–$Cht._B$ fibers which get slightly loosened up as such. Drawn from[206]. C) Schematic of the operational principal of the μFD. D) The steps showing how the multiple cycles of runs passed though the in–house μFD to obtain/collect the $Cht.NFs_P_{1\text{-}5}$. For the pass–2 and above, the channels/pathway of the μFD was flushed, let bleed, and collected in the same vessel with only a few mL of MQ water (~5 mL) before the collected content was dumped into the feeding (inlet

reservoir). Thus, gradually increased dilution effects (for conc.) were seen as expected for the Cht.NFs samples which are > pass–1. 139

Figure 5.5: The Cht.NF_$P_{1–5}$ solutions after the collections from the microfluidizer, μFD (the top row; before dialysis) and the purified solution after the dialysis. The relative viscosity was found increasing towards the Cht.NF_P_5 solution just through the visual inspection (glass rod assisted) by the experimenter. 140

Figure 5.6: Schematic representation of the acidolysis of chitin's bundled microfibrils[206], and the particle structure of the Cht.NWs (to the right). The bottom row shows the extraction and the purification steps of the of the Cht.NWs from the commercially available –chitin powder. Several pilot batches of Cht.NWs were extracted, stored at the fridge, and utilized as required. 142

Figure 5.7: A) The etherification S_N2 reaction for the grafting of GTMAC onto the surface 1^0 alcoholic groups (—CH_2OH) producing the Q–Cht.NW_a. B) The overall process of the synthesis and purification of the cationic chitin NWs (the Q–Cht.NW_a). The purified NWs were found to retain their stability up to ~24 hrs, as after that loosely formed and easily redispersible sediment was seen to form at the bottom of the container. 144

Figure 5.8: A) The modified BATs done with Cht.NFs and Cht.NWs for MO of 10 different concentrations (50–500 ppm) at RT on a shaker. The data obtained from the UV-Vis measurement @ λ_{max} (after appropriate dilutions as required) was then fitted through the linearized Langmuir Monolayer Adsorption Isotherm (LMAI). B) Molecular structure of MO and schematic representations of monolayer adsorption of the MO molecules onto the nanocrystals (NCs) of sustainable nanomaterials (e.g., Q–CNCs or Q–Cht.NWs). 146

Figure 5.9: A) The percentage yields of the chitin derivatives including NFs and NWs. B) The schematic representation of the quaternized Cht.NW_a, of which in aq. suspensions, the available surface (—NH_2) groups got protonated making them more cationic over the grafted QAGs at the protruded 1^0 alcoholic groups (—CH_2OH). 147

Figure 5.10: A) Freeze–dried samples of the α–chitin derivatives. B) Notable peaks of Chitin and chitin–NWs from literature. C) & D) FT–IR spectra of the α–chitin and all chitin derivatives, including the NFs, NWs, and the Q–Cht.NWs. 148

Figure 5.11: A) The QAG contents and the protonated —NH_2 groups' contents of chitin based NMs determined through conductometric titrations using 0.01 M $AgNO_3$ and 0.1 M NaOH respectively as the titrant. B) A representative plot where two modes of conductometric titrations were plotted in the same graph. 150

Figure 5.12: The prepared dispersions of α–chitin and its derivatives. The commercial α–chitin is insoluble/non–dispersible in MQ water and thus a lower conc. (0.05%, w/v) of the suspensions was prepared and adjusted the pH. For the chitin NFs prepared (0.1%, w/v) derived from the 5 different passes @ μFD, more thick suspensions were seen for the vials having the adjusted pH of ~7 and ~10. The $Cht.NW_a$ and the further deacetylated NWs ($Cht.NW_{ab}$) were found stable at any pH without any precipitation or sediment/cake formation, but the later were seen cloudier at the same conc. The ZP/D_H of any GTMAC grafted NPs were seen not so variant over pH changes in the previous chapters. The inherent pH of the post–dialyzed $Q–Cht.NW_a$ were found > ~5.6, thus only the three different pH adjusted suspensions were prepared in this case. 152

Figure 5.13: A) Average aggregates' sizes (D_H) and the ZPs of commercial α-chitin and its derivatives: deacetylated chitin (alkaline; $De–Cht._B$), chitin nanowhiskers ($Cht.NW_a$), deacetylated chitin nanowhiskers ($Cht.NW_{ab}$), and quaternized chitin nanowhiskers ($Q–Cht.NW_a$). B) Comparison of D_H and ZPs of $Q–Cht.NW_a$ and the $Cht.NF_P_x$ NMs along with the quaternized chitosan (Q–CS). C) and D) Effect of different pH on the D_H and the ZPs respectively for the chitin derivatives. The ZPs of the $De–Cht._B$, $Cht.NW_a$ and the $Cht.NW_{ab}$ were found negative at alkaline pH (pH ~10) most probably due to the deprotonation of the primary alcoholic groups at C–6 producing the anionic alkoxy (—CH_2O^-) ions. At that strongly alkaline pH (~10), all the protonated amino groups (—N^+H_3) would be deprotonated and would thus revert back to the uncharged primary amino groups, PAGs (—NH_2). 154

Figure 5.14: Effect of various pH of the dispersion medium on the A) D_H of the De–Cht.$_B$ (Cht.MF_P_0) and the Cht.NF_$P_{1–5}$, and B) ZPs of the same NPs. 156

Figure 5.15: The TEM images of the extracted Chitin derivatives: the Cht.NFs and the Q–Cht.NWs. 157

Figure 5.16: A) The determined Q_{max} values obtained from the linearized Langmuir Monolayer Adsorption Isotherm (LMAI) of the chitin derivatives and comparisons of the Q_{max} values of some selected NPs with the chitin derivatives against the ZP values. B) Same data against the aggregates' sizes (D_H) explaining the possible relationship between the surface charges and the adsorption. The Q_{max} values of the five different Cht.NFs from 5 different passes are plotted against the C) ZP values and D) the aggregate sizes (D_H). Here, the P-0 is the De–Cht.$_B$. 159

Figure 5.17: The schematic representation of all the probable in-effect forces that are responsible for binding/adsorption between the cationic NPs and the anionic MO molecules. The top image is for the Q–CNC NPs and the bottom is for the Q–Cht.NW_a. The Q–Cht.NW_a possess surface PAGs (—NH_2) that got protonated @ the pH of ~7 and thus are able to establish the additional ionic attractive forces between the —N^+H_3 groups and the sulfonate groups (—SO_3^-) of the MO molecule during the BATs. Such phenomena explain the most likely reason of greater extent of MO adsorption by the Q–Cht.NW_a over the Q–CNCs. 160

Figure 6.1: Common techniques utilized for detection of BS, their advantages and disadvantages. Except the enzyme kit, all the methods are used at industrial scale of detection. Table drawn and adapted from[143]. 165

Figure 6.2: A) UV–Vis spectra of aqueous solution of sodium cholate (SC). The peak appeared was for cyclohexane ring, and doesn't show any hypsochromic/bathochromic (blue/red) or hypo–/hyperchromic shift based on the changes in conc. The chemical structure of the SC is shown just below the spectrogram. B) A basic schematic of an electrochemical cell consisting of the ISE (half–cell) and the RE (a Ag/AgCl electrode, another half–cell) connected to a voltameter or a benchtop pH meter. For the RE, the

inner solution used was the aq. 3M KCl saturated with AgCl for which the known half-cell potential is +0.2225 V (with respect to the standard H–electrode). 167

Figure 6.3: A) The schematic illustration of the components of CSE showing all the 4 parts of that half–cell. **B)** The success in preparing the unprecedented CSM for the 1st time after several trials and errors. The during the working mechanism of the electrode system, this CSM is considered as the salt bridge. **C)** The Ag/AgCl reference electrode, RE (a half cell) to be used to construct a full electrochemical cell (E–Cell). 170

Figure 6.4: The cell diagram (shorthand notation) of the E–cell to be used in this chapter's work which is the quantification of SC from unknown conc. of the samples obtained from the BATs conducted between SC and the selected developed NMs. 171

Figure 6.5: The two possible mechanisms of electromotive potential (EMF) development at different phase boundaries: the bulk/CSM, the CSM/inner filling solution, & the inner solution/Ag–electrode. These two mechanisms of EMF development across the CSM (shown in the bottom part of the image) are the most described in literature. Image not drawn to scale and proportions; the numbers of various arrows are NOT indicative of corresponding numbers of ions shown, wherever applicable. 176

Figure 6.6: A) A retrograde flowchart indicating the stepwise construction of a CSE starting from the synthesis of the ionophore. B) Molecular reactants for the synthesis of the ionophore called benzyldimethylcetylammonium–cholate (BDMCA–Cholate). C) Casting of CSM prepared from PVC, ionophore and plasticizer. The zoomed insert shows the outlook of the casted and dried flexible CSM where the ionophore molecules are embedded and distributed. 178

Figure 6.7: Synthesis and purification of BDMCA–Cholate ionophore (lipophilic in nature). 179

Figure 6.8: The overall procedure of CSM casting. The CSM have three components: PVC (HMW) as the base material, DOS as the most used plasticizer with PVC, and the BDMCA.Ch ionophore which had been synthesized in house. A ration of PVC : DOS : Ionophore = 32 : 63 : 5 (wt.) was followed per CSM. The ionophore solution (THF is

the solvent) starts precipitating out gradually when solution temperature decreases below 55^0C (say, ~50^0C). 181

Figure 6.9: Stepwise fabrication of the electrode heads with the cholate selective membrane (CSM) and curing of the glued CSMs, followed by conditioning. After analyses of several results, this conditioning step was discarded as it failed to revert the desensitized CSM/tips back to their pristine conditions. Additionally, usage of ionophore was meant to eliminate the conditioning steps for any ion selective electrodes (ISEs). 184

Figure 6.10: A basic representation of the process of constructing EMF (mV) vs Log (C_M) calibration curves through continuous addition modes, conducted with the E–cell composed of CSE & a RE. The 10 mM NaCl (ISA) is used the blank. The inner filling solution for the CSE was 10 mM SC prepared in ISA, and the for the RE, it was the 3 M KCl solution saturated with AgCl. The calibration curves were conducted at RT and the EMF reading for each data points were taken at least in triplicate manner to report the average. 186

Figure 6.11: Schematic illustration of the methods of producing calibration curve by Tensiometry and Conductometry. For the latter case, the whole experiment was conducted in MQ water including the preparations of the four concentrated reference solutions of SC. The 60 data points (SFT or the sp. conductance) obtained in triplicate manner in both cases were baseline corrected and then plotted against Log (C_M) (for Tensiometry) or against the C (for Conductometry). 188

Figure 6.12: Steps showing the overall BAT of a selected NM with SC followed by the detection of unbound/free SC left in the post–adsorption liquid. The BATs for all the selected NMs were done in the same way and for each individual Falcon tube in each test, the new/unused tip as well as fresh inner solutions for both electrodes were used to maintain consistency of results. Except for the anionic or neutral NMs, all the other NMs' BATs' tubes got cloudy during and after the adsorption tests, and visible aggregates/lumps were seen for all the tubes of ascending conc. of the SC. The quantification of the free SC from each tube was tedious & time consuming, and thus at times that portion was divided in two days, where applicable. 191

Figure 6.13: Adsorption kinetic tests (AKTs) of NMs followed by quantification of the free SC in the collected samples at different time intervals. 193

Figure 6.14: A) The FT–IR spectra of SC, 16–BAC (the cationic detergent, BDMCA–Chloride), and the synthesized ionophore, BDMCA–Cholate. B) Chemical structure of the ionophore showing the newly formed bond —N- - -O— between the 16–BAC and the SC. 194

Figure 6.15: A) Effect of the strength of inner filling solutions for the CSE on the EMF responses over a range of conc.: 50 µM–25 mM SC prepared in ISA. The CMCs, enlisted below the plot, were determined form the visibly distinct breakpoints of the calibration plots which are not easily discernible from this combined plot of the average data. B) The average (from T–1 & T–2) of cal. curves obtained from two of the representative tips from that respective batch of the casted CSM. Inconsistent results were seen for the CSMs from the batch #3 and 6, probably due to the lack of homogenous distribution of the embedded ionophore. The CSMs from those two batches were seen a bit cloudier than the rest of the batches, and the most likely reason for this could be the partial precipitation (insolubilities) of the ionophore prior to proper drying. The determined CMCs from this data were also enlisted in the table presented just below the plot. 196

Figure 6.16: A) Chemical structure of SC monomer molecule and its two faces: the hydrophobic and hydrophilic faces. Schematic of the 1^0 & the 2^0 micelles are also presented. B) Different micelle formation reported in literature and their corresponding sizes (diameter) investigated by small-angle neutron scattering (SANS). Reused from[270]. 197

Figure 6.17: A) One of the calibration plots within a range of 0.05–25 mM from the average (T–1 & T–2) data obtained by the CSE using 200 mM SC in ISA as the inner solution. B) The same plot of A) showing the 3 distinct breakpoints (point of intersections, POI) and the trendlines showing the major linear zones in the plot. Here, it is obvious that the POI–1, POI–2, and the POI–3 indicates the pre–micellar aggregations and the 1^0 & 2^0 CMCs respectively. 199

Figure 6.18: A) Calibration curve of SC within the conc. range of 0.05–25 mM, constructed via Tensiometer @ RT in 10 mM NaCl media as the ISA. The premicellar aggregation point, the 1^0 & 2^0 CMC points: all of them are distinctly noticeable form this SFT vs Log(C) plot. B) Calibration curve of SC in the same conc. range (0.05–25 mM), constructed via conductance measurement @ RT in MQ water plotting the baseline corrected specific conductance vs mM concentrations. In this case only one breakpoint was distinguishable which represents the 2^0 CMC, depending on the position/location of the breakpoint. C) The average plot for the calibration curve obtained from the CSE via EMF measurement @ RT using the 10 mM SC in ISA as the inner filling solution. D) The enlisted values of the 1^0 and 2^0 CMCs of SC at RT obtained through different tools. 200

Figure 6.19: Interaction mechanisms of a representative NM with SC for its physicochemical adsorption onto the surfaces of the NM. The resultant complexes (NM–SC) were easily visible withing the Falcon tubes after the BATs were done for 2.5 hrs, regardless of the tubes be @ 38^0C or @ RT. The labels of the tubes indicate the initial conc. of the SC taken, NOT the conc. after adding the NMs' dispersions. 202

Figure 6.20: The post–BATs tubes for most of the selected NMs on which the BATs were conducted with SC. The negative controls or the tubes for anionic NPs are not shown here. 204

Figure 6.21: Comparison of Qmax values of the selected NMs for SC with A) ZPs of the NMs, B) Aggregate sizes (D_H) of the NMs. C) The D_H and the ZP of the chosen NMs. D) The Q_{max} values of the cationic NMs among all the selected NMs (i.e., without the negative controls). 205

Figure 6.22: A) Schematic representation of the possible simultaneous existences of all the binding forces between the Q–Cht.NW_a (amino–PS based NMs, other examples include Q–CS, QCS–g–CNCs, Cht.NW_a and the Cht.NFs) and the SC molecules. B) Cholestyramine resin's dispersions @ 0.5 % w/v (aqueous, top-left; and in ISA, top right) which were found almost insoluble and non–dispersible. In the bottom row, the Falcon tubes of the BATs are shown which are labeled as the initial conc. of the SC

taken. And to the right-side column, the sachet of the cholestyramine commercially available in the US market, and the chemical structure of the resin is given just below the sachet. 207

Figure 6.23: The adsorption kinetic test (AKT) of a representative NMs with SC and the withdrawn 5 mL samples in the scintillation vials at different time intervals. The SC–NP complexes were found sedimented at the bottom of the vials while the set–up of the E–cell was carried out. 209

Figure 6.24: A) Adsorption/binding/association kinetic tests (AKTs/BKTs) conducted for one of the developed NMs (here, the Q–CNC_a NPs was chosen) and for Questran™ (cholestyramine) as the BASs. The rate and extent of the sorption of the SC onto the Q–CNC_a was found higher than that of the cholestyramine manifesting the Q–CNC_a to be more efficacious BASs. B) The adsorption kinetics of a novel BAS named SK&F 97426–A and cholestyramine with the radiolabeled (^{14}C) – glycocholate (GC), taurocholate (TC), and taurochenodeoxy cholate (TCDC). Here the size of the cholestyramine used was mostly within the range 38–212 μm (measured by dry sieving) and the 0.4% (w/v) BASs' slurry prepared in glucose-free Krebs-Henseleit buffer was used for the 5 mM of the radiolabeled BAs for the AKT. The radioactivity was measured by liquid scintillation counting. Adapted from[275]. 211

Figure 6.25: Chemical structures of cholestyramine (top left), the novel compound SK&F 97426-A (top right), sodium cholate (bottom right), and the schematic representation of the Zwitterionic NPs Q–CNC_a (bottom left). 212

Figure 6.26: A) The max. adsorption capacities (Q_{max}) of some of the NPs which lies in common over the three methods of detection for the free/unbound SC. B) The averaged plot based on the three detection methods. 214

Figure 7.1: A) The main features of the baker's yeast cell, Saccharomyces cerevisiae. The cellular division usually leaves bud scars on the mother cells which are composed mainly of chitin. Reproduced from[285]. B) An example of the commercially available bakers' yeast, Lallemand Instaferm® Instant dry yeast. The insert represents the schematic of the cellular structure of the yeast. C) The overall intracellular anaerobic

fermentation process of a glucose molecule to its products: ethanol (C_2H_5OH) and carbon dioxide (CO_2). The groups of enzymes, zymase usually catalyze the fermentation reaction through the Embden–Meyerhof–Parnas (EMP) pathway. Under anaerobic conditions, the yeasts convert pyruvate to ethanol and CO_2. 217

Figure 7.2: A) The schematic representation of the mechanism of inhibition of the yeast cells by the physicochemical adsorption of the cationic nanofibers (Q–NFs) of carbohydrate polymers, like the chitosan or DDEA–Cellulose. The yeast cell wall is negatively charged, and thus the NFs are ionically attracted thus bound onto the surface causing the gradual cessation of glucose influx to complete blockage of the intake. Consequently, no further fermentation takes place as well because the NF–bound yeast cells got flocculated and precipitated out. The schematic of the adsorption of cationic NFs onto the yeast cells was drawn based on the discussion from. B) Effect of buffer and chitosan on the fermentation rate of glucose and CO_2 output. Both A) and B): Drawn from the discussions of [291]. 221

Figure 7.3: A) Set–up for yeast fermentation experiments which apparently is similar to the mimicked & modified version of the Warburg flask. An arbitrary conc. of MO solution was used as the colored liquid for the ease of measuring the liquid level inside the burette. B) The 10 mL volumetric flasks in which the yeast's fermentation experiments were conducted. The two flasks are @ t= 0 mins (when the temperature was 43^0C, the yeast got dissolved) and t= 30 mins, where @ t= 30 mins, most of the yeasts were found precipitated at the bottom (not clearly visible from the image). 223

Figure 7.4: The released CO_2 vs time (mins) plots for the control, positive & negative controls, and the experimental NMs obtained from the yeast mediated fermentation of glucose. Wherever applicable, the concentration of the NMs was considered to be 100 ppm in the flasks. 225

Figure 7.5: A) Rate of release of CO_2 —, and B) Volume fractions of released CO_2 — due to the yeast mediated fermentation of glucose by the control, positive (Questran^{TM}) and negative controls (NCC^{TM}), and the Q–NPs. C) Relative % inhibition of yeast cells'

activities leading to reduced fermentation rate, and D) Schematic of yeast cell's inhibition by the Q–NPs. 227

Figure 8.1: Gradient desulfation of NCC^{TM}, the nanocellulose (NCC^{TM}) used as the base materials for the work done in chapter 3, and the ion exchange procedure for to convert the Na–form of the surface sulphate half ester groups, SHE (—$OSO_3^-Na^+$) to acid (protonated, H) forms of the SHE groups(—$OSO_3^-H^+$). 265

Figure 8.2: Degree of substitutions (DS) and cationization reaction efficiencies (CRE%) of selected Q–NPs that are modified with hydrophilic/hydrophobic moieties or polymerized. 266

Figure 8.3: Effect of $CaCl_2$ on the sizes (A, C) and ZP (B, D) of Q–NPs based on CNCs. 266

Figure 8.4: A) Effect of conditioning the desensitized cholate selective membrane, CSM/tip on sensing/detecting the target analyte (sodium cholate, SC). The conditioning of the used CSM/tip (that lost sensitivity) were carried out into highly concentrated (400 mM) sodium cholate (SC) solution in ISA (10 mM NaCl) and in ISA only. The results proved that the conditioning of used CSM does not revert the CSMs to their pristine condition. B) Effect of used and fresh inner solutions in reference electrode (RE) for the detection of SC from aqueous samples. 267

Figure 8.5: A) Example showing the occurrence of loss of sensitivity of the CSM over time after more than 150 readings. B) Rinsing the desensitized CSM/tip with MQ water does not help to establish the sensitivity for continuous usage of the same tip. 267

Figure 8.6: The results of the A) unblind test (UBT) and B) single blind test (SBT) conducted for the CSE developed in the lab. 268

List of Tables

Table 1.1: Lipid-Lowering Agents—Effect on Lipoproteins[23] 7

Table 2.1: Comparisons of maximum adsorption capacities (Q_{max}) of novel hPEI–CE with both controls at an equal weight (700 mg/mL, 37^0C, 120 rpm). Reused from[55] 31

Table 2.2: Comparison of adsorption percent relative to cholestyramine of hPEI-CE with other adsorbents for bile acid. Adapted from[55]. 33

Table 2.3: Maximum cholic acid sorption capacity at pH of 4 – 6. Reproduced from[81]. 34

Table 2.4: Comparison in % of BSs bound to the adsorbent. BAT was conducted in PBS (pH 6.8) and an enzyme kit/UV-Vis was used to quantify the free BSs. Reproduced from[84]. 39

Table 2.5: Bodyweight change of high-fat diet-treated C57BL/6 J mice after a 5-week treatment. Adapted from[84]. 39

Table 2.6: Effects of U, HU, and inositol nicotinate (commercially available standard antihyperlipidemic drug) on serum lipid profiles (HDL-C is not shown here) in mice supplemented with a cholesterol-rich diet (composition: 2.0% cholesterol, 8.0% lard, 0.3% sodium cholate and 89.7% commercial chow). Adapted form[97]. 43

Table 3.1: Reaction parameters for the desulfation of NCC™, extracting CNC from MCC and quaternization of CNCs with GTMAC to prepare Q–CNCs. 59

Table 3.2: The quaternary ammonium groups (QAG) contents, degree of substitution (DS), and the cationizing reaction efficiencies (CRE%) of the cationic CNC NPs ($Q–CNC_X$).. 77

Table 3.3: The average sizes (D_H) and zeta–potentials (ZPs) of the 0.05% (w/v) aqueous suspensions of DS–CNCs and their corresponding Q–CNC, determined from the zetasizer. 82

Table 3.4: Summary of the Q_{max} values obtained from the BATs with MO with the control and non-control NPs, and their corresponding aggregate sizes, D_H and ZPs. The sodium salt of the MO of MW of 427.33 g/mole was used for the BATs in this section. 90

Table 4.1: Average aggregate sizes (D_H) and ZP of the selected NPs 122

Table 5.1: The determined Q_{max} values of some selected NPs (including the chitin-based NPs), from the batch adsorption tests (BATs) with methyl orange (MO), and the corresponding zeta potentials (ZP) and sizes (D_H) of the NPs. 158
Table 5.2: The determined Q_{max} values of the chitin nanofibers (Cht.NFs) from the batch adsorption tests (BATs) with methyl orange (MO), and the corresponding zeta potentials (ZP) and sizes (D_H). 161
Table 6.1: Rationale for the selected NPs for batch adsorption tests (BATs) with sodium cholate (SC) followed by quantification of free SC with the cholate selective electrode (CSE). 190
Table 7.1: The determined experimental parameters obtained from the recorded V_{CO2} till 30 mins intervals during the fermentation experiments. For the volume fraction and % inhibition calculations, the control was considered as 1 and 0 respectively, and the same parameters for the other NPs were calculated based on the corresponding data of the control. 226

List of Abbreviations

AcOH / HAc	Acetic Acid (CH_3COOH)
AD	Atherogenic Dyslipidemia
AK/AKT	Adsorption Kinetics / Adsorption Kinetics Test
APS	Ammonium persulfate
BAs	Bile Acids
BAS	Bile Acid Sequestrants
BATs	Batch Adsorption Tests
BDMCA.Cl	Benzyl-dimethyl-cetyl-ammonium chloride, or benzyl-dimethyl-hexadecyl-ammonium chloride [16-BAC (benzalkonium chloride), or Cetalkonium chloride]
BDMCA.Ch.	Benzyl-dimethyl-cetyl-ammonium **Cholate**, or benzyl-dimethyl-hexadecyl-ammonium **Cholate** [or Benzalkonium **cholate**, or Cetalkonium **cholate**]
BK/BKT	Binding Kinetics / Binding Kinetics Test
BSs	Bile Salts
C	Concentration (mM)
Conc.	Concentration
C_M	Concentration in Molar units
Cht.NWs	Chitin Nanowhiskers
Cht.NFs	Chitin Nanofibers
Cht.MF_P_0	Chitin Microfiber pass '0' meaning these fibers were not passed through the microfluidizer. [They are basically deacetylated chitin, the De–Cht.]
Cht.NF_P_X	Chitin Nanofibers, with pass number. Pass number indicates how many times (cycles) the fibers were run/passed through the microfluidizer.
$Cht.NW_{ab}$	Chitin nanowhiskers further deacetylated by alkali (NaOH) mediated deacetylation reaction

CMC	Critical Micelle Concentration
CNC	Cellulose Nano Crystals
CNC_{OX}	Oxidized CNC or Carboxylated CNC
CNF	Cellulose Nanofibers
CRE%	Percentage Cationization Reaction Efficiency
CS	Chitosan
CSE	Cholate Selective Electrode
CSM	Cholate Selective Membrane
DD%	Percentage Degrees of Desulfation **or** Deacetylation
DDEAC	N-dodecyl-N, N-dimethyl-(2,3-epoxy propyl) ammonium chloride
De–Chitin/ De–$Cht._B$	Deacetylated Chitin done through alkaline (NaOH) deacetylation reaction
D_H	Hydrodynamic diameter
DIO	Diet Induced Obesity
DM–C	DOWEX Marathon C Ion Exchange Resin Beads
DLS	Dynamic Light Scattering
DOS / DEHS	Bis(2-ethylhexyl) sebacate or Dioctyl sebacate / Di(2-ethylhexyl) sebacate
DS–CNC	Desulfated CNCs
$DS–CNC_{3—6}$	Desulfated CNC obtained from alkaline desulfation using 3 M, 4 M, 5 M, and 6 M Sodium Hydroxide (NaOH)
$DS–CNC_{\mathbf{a}}$	Desulfated CNC obtained from acidic desulfation using a 6 M Hydrochloric Acid (HCl)
E–Cell	Electrochemical cell
EDC	1-ethyl-3-(3-dimethylaminopropyl) carbodiimide
EMF	Electromotive Force
et. al.	And others
EtOH	Ethanol (C_2H_5OH)
FTIR	Fourier Transform Infrared Spectroscopy

F–PS–NMs	Functionalized Polysaccharide Nanomaterials
—g—	Grafted or graft
GA	Gravimetric Analysis
GIT	Gastrointestinal Tract
GPa	Giga Pascal
GTMAC	Glycidyl Trimethyl Ammonium Chloride
HDL–C	High Density Lipoprotein Cholesterol
HL	Hypercholesterolemia
hPEI	Hyperbranched Polyethylene Amine
HTCC	N-(2-hydroxyl) propyl-3-trimethyl ammonium chitosan chloride / Cationic Chitosan or GTMAC–Chitosan
IPA	Isopropyl Alcohol (an alcohol)
ISA	Ionic Strength Adjustor
ISE	Ion Selective Electrode
ISM	Ion Selective Membrane
kDa	Kilo Dalton
LDL–C	Low Density Lipo–protein Cholesterol
LDL–R	Low Density Lipopeotein Receptor
LMAI	Langmuir Monolayer Adsorption Isotherm
Max.	Maximum
MCC	Microcrystalline Cellulose
MCC_{OX}	Oxidized CNC/Carboxylated CNC, where the CNC is extracted from MCC
MES	2-(N-Morpholino) ethanesulfonic acid buffer
MQ	Milli Q
MO	Methyl Orange
μFD	Microfluidizer
mV	Milli Volts
MWCO	Molecular Weight Cut Off

NAG/NAGA	N-Acetyl Glucosamine
NC	Nanocellulose
NCC^{TM}	Nanocrystalline Cellulose, the pristine/sulfated CNC supplied by CelluForce
NHS	N-Hydroxysuccinimide
NMs	Nanomaterials
NPs	Nanoparticles
PAG	Primary Amino Groups
PDMAEMA	Poly[2-(Dimethylamino) Ethyl Methacrylate
pQDMAEMA	Poly–Quaternized–[2-(Dimethylamino) Ethyl Methacrylate
PS	Polysaccharide
PS–NMs	Polysaccharide Nanomaterials
PVC	Poly Vinyl Chloride
PVDF	Polyvinylidene Difluoride
QAG	Quaternary Ammonium Groups
Q–CNC$_{3—6}$	Quaternized/Cationic CNCs produced from the desulfated CNC obtained from alkaline desulfation using 3 M, 4 M, 5 M, and 6 M Sodium Hydroxide
Q–CNC$_{\mathbf{a}}$	Quaternized/Cationic CNCs produced from the desulfated CNC obtained from acidic desulfation using a 6 M Hydrochloric Acid
Q–CNC$_{6\mathbf{a}}$	Quaternized CNC obtained from DS–CNC$_6$ using alcohol media (isopropyl alcohol) during cationization reaction/GTMAC grafting
Q–CNC$_{6\mathbf{e}}$	Quaternized CNC obtained from DS–CNC$_6$ using ether media (tetrahydrofuran) during cationization reaction/GTMAC grafting
Q–CNC$_{MCC}$	Quaternized/Cationic CNCs produced from the CNC extracted from acidic desulfation using a 6 M Hydrochloric Acid
Q–NPs	Quaternized Nanoparticles
Q–CS	Quaternized Chitosan (or HTCC)

Q_{max}	Maximum Adsorption Capacity of an adsorbate for an adsorbent at equilibrium, usually express in mg of adsorbate/g of adsorbent
RBF	Round Bottom Flasks
RE	Reference Electrode
RE%	Percentage Reaction Efficiency
RT	Room Temperature
SA	Surface Area
SC	Sodium Cholate
SFT	Surface Tension
SHE	Sulfate Half Ester (—OSO_3^-)
S.M.A.R.T.	Abbreviation of Sustainable, Modifiable, Active, Renewable, and natural/non-Toxic. **Coined for the 1st time** by the author of this thesis.
TBAH	Tetrabutylammonium hydroxide
TEM	Transmission Electron Microscope
TEMPO	2,2,6,6-tetramethyl-1-(pyperidinyloxy) radical
THF	Tetrahydrofuran (a cyclic ether)
TG	Triglycerides
V	Volts
WHO	World Health Organization
w.r.t.	With Respect To
ZP	Zeta Potentials

Chapter 1: Motivation, scope, and novelty of work

1.1 Introduction

With a growing interest in nanoscience and nanotechnology, the synthesis and modification of nanomaterials with well-defined structures and specific functionalities have become one of the most promising and versatile fields for potential development in the 21st century[1–3]. Recent advances in nanomaterials have streamlined the development of functionalized nanoparticles, which hold promise to revolutionize applications in the fields of medicine, electronics, biomaterials, and energy production[4–9]. However, many of the chemicals used to synthesize such nanomaterials are derived from petroleum-based resources and the processes involve the use of toxic reagents that are harmful to the environment[10]. As research advances in the last decade, the demand for non-petroleum-based, carbon-neutral biodegradable products from sustainable resources having low environmental, animal/human health and safety risks are increasing in the field of nanotechnology[11]. The environmental safety issues, global warming, and the emphasis on "green synthesis (solvent-free)" from industries and government have generated significant interest to replace conventional resources with nanomaterials based on renewable and sustainable natural resources. In this regard, this Ph.D. research includes the systematic development of several nanomaterials (NMs) based on the naturally occurring biopolymers through the green synthesis for biomedical application, namely the reduction of raised cholesterol and the regulation of diet-induced obesity (DIO). As this Ph.D. study mostly involves the development and evaluation of various biopolymer-based NMs for human application, the biosafety of these NMs was also evaluated using a protocol developed in our laboratory.

1.2 Problem Statement & Motivation

The incorporation of cholesterol in diets is an important part of leading a healthy life, as it is an essential component of the cell membrane; however, consuming excessive amounts of cholesterol can be harmful. In the human body, cholesterol exists in 2 forms, low-density lipoprotein (LDL-C) and high-density lipoprotein (HDL-C)[12,13]. LDL is considered the "bad" cholesterol as it can build up on the inner lumen of blood vessels to form plaques via atherosclerosis. This can cause the vessels to narrow and restrict blood flow to and from the heart and other organs resulting in conditions, such as angina, stroke, or heart attack. HDL is considered the "good" cholesterol as it absorbs LDL and transports it to the liver, lowering blood LDL levels. Maintaining high levels of HDL is essential as it ensures that LDL levels are low, thus reducing the risk of fatal vascular conditions[12–14].

Atherogenic dyslipidemia (AD) is a condition resulting in a lower plasma level of high-density cholesterol (low HDL-C) associated with a higher level of serum triglycerides (TG)[15]. The elevated levels of small, dense LDL-C particles – in conjunction with the former components are called 'lipid triad', factors responsible for hypercholesterolemia (high plasma total cholesterol level). In clinical practice, testing of small dense LDL-C is rarely performed due to cost considerations. Therefore, the combination of high TG (>200 mg/dL), low HDL-C (<35 mg/dL), and a total plasma cholesterol/HDL-C ratio >5 is often used. On the other hand, several guidelines stipulate different cut-off values for HDL-C, mainly <40 mg/mL for men and <50 mg/mL for women[15,16]. If such a condition is not treated resulting in chronic

hypercholesterolemia, the LDL causes morphological remodeling of the HDL (illustrated in Figure–1.1) as reported in a recent study[17].

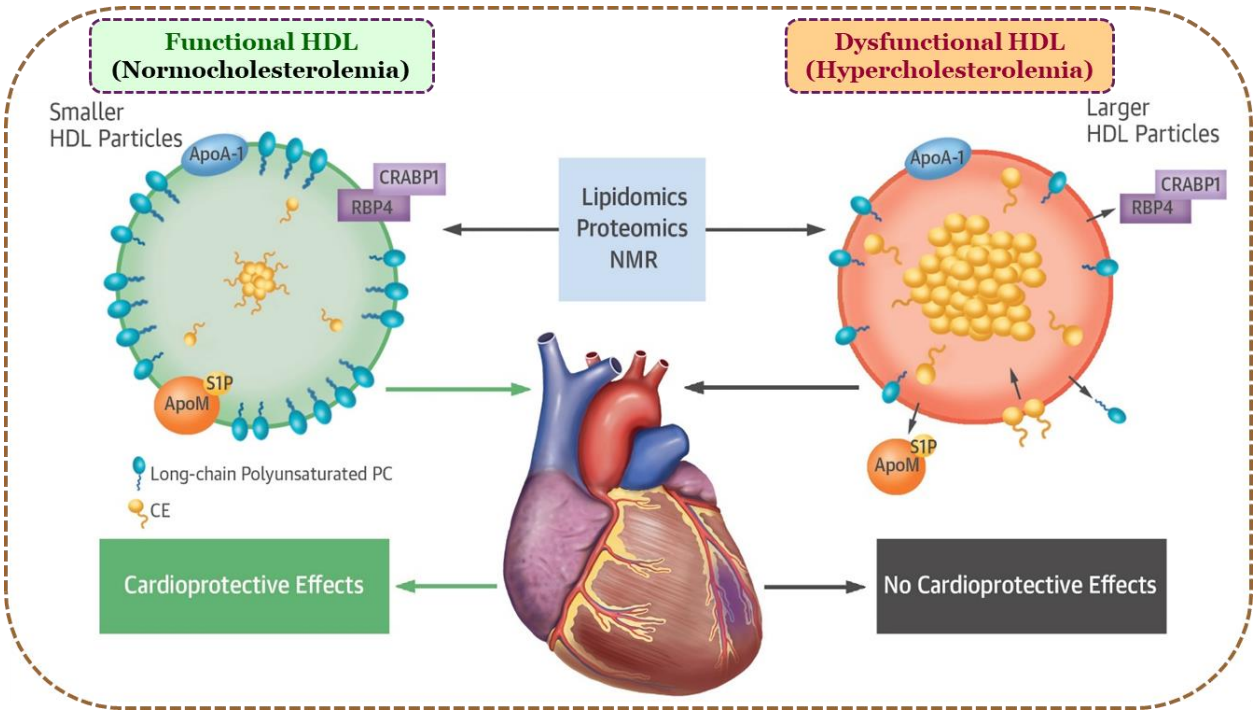


Figure 1.1: *Schematic illustration of the impact of hypercholesterolemia (HL) on HDL remodelling. The 'silent killer' HL induces HDL lipidomic changes, losing phosphatidylcholine-lipid species and gaining cholesteryl esters, with losses in cardioprotective proteins. Such remodelling of HDL particles shifted them towards a dysfunctional state. Modified from*[17].

Legends in the schematic: *apo M = apolipoprotein M; CE = cholesteryl ester; CRABP1 = cellular retinoic acid binding protein 1; HDL = high-density lipoprotein; HL = hypercholesterolemia; LDL-C = low-density lipoprotein cholesterol; NMR: nuclear magnetic resonance; PC = phosphatidylcholine; RBP4 = retinol binding protein 4; S1P = sphingosine 1-phosphate.*

It is possible that hypercholesterolemia can usually be a direct consequence of chronic uncontrolled obesity and is becoming a major public health concern. According to World

Health Organization (WHO), the global prevalence of obesity and overweight in 2016 are 13% and 39% of the world's adult population respectively (WHO 2018). This usually leads to the increased likelihood of developing non-alcoholic fatty liver disease characterized by excess lipid accumulation in hepatocytes resulting in the disruption of lipid metabolism[18].

Additionally, the Canadian Community Health Survey (CCHS) data (2005) indicates that 18% of Canadian adults are obese (at least 20% over the ideal body weight) and an additional 34% are overweight[19] and thus are at risk of developing high plasma cholesterol. In general, the excess caloric intake without a corresponding increase in energy expenditure is believed to be the major contributing factor to weight gain among Canadians leading to hypercholesterolemia. This "silent killer" hypercholesterolemia, is characterized by increased LDL–C and increases the risk of cardiovascular diseases which are the leading cause of death and disability worldwide[20].

High blood cholesterol levels can also be genetically linked, resulting in familial hypercholesterolemia (FH), as individuals can inherit an altered gene from a parent in an autosomal dominant manner. FH is caused by problems in the hepatic uptake and degradation of LDL, which occurs through the LDL-receptor pathway, which is caused by a defective LDL-receptor gene (LDLR) or by a mutation in a gene that is responsible for creating apolipoprotein B (APOB)[21,22]. Because of this, ingested cholesterol, specifically LDL, cannot be degraded; thus, it accumulates in the bloodstream. One in 500 people inherits this disorder which can cause dangerously high cholesterol levels above 300 mg/dL (where average levels should be less than 100 mg/dL[12]) resulted in the formation of plaques in blood vessels.

For the patients suffering from such forms of lipid abnormalities, lipid-lowering therapy is a treatment that requires patients' active engagement and participation. Where, the patients' diet (e.g DASH diet, DASH= dietary approaches to stop hypertension) aimed at reducing blood lipid levels and weight (if needed) should always be part of the pharmacological treatment, other lifestyle changes (such as weight loss and reduction of abdominal obesity, 30–60 min/day moderate to vigorous-intensity physical activity, smoking cessation, sufficient duration like 6–8 h per night of sleep, stress management) are important to further modify the lipoprotein profile[23].

In terms of pharmacological treatments, the available lipid-modifying drugs used in the management of dyslipidemia include 3-hydroxy-3-methyl-glutaryl-CoA reductase (HMG-CoA-reductase) inhibitors (statins), the cholesterol absorption inhibitor (e.g. ezetimibe), fibric acid derivatives (the fibrates), bile acid sequestrants, BASs (Figure–1.2), and the proprotein convertase subtilisin/kexin type-9 (PCSK9) inhibitors. These monoclonal antibodies, alirocumab and evolocumab in the PCSK9 inhibitors class are administered subcutaneously either every 2 weeks or once monthly as part of the treatment[23–28].

The bile acid sequestrants, BASs, also called resins, are non-absorbable and indigestible polymeric molecules[23–28]. Being cationic, they can electrostatically bind to negatively charged bile acids (BAs) and are excreted through the feces. The entire process interrupts the enterohepatic recycling of BAs as well as triggers the breakdown of plasma LDLc to produce more BAs in the liver to regulate bile salts in the digestive system.

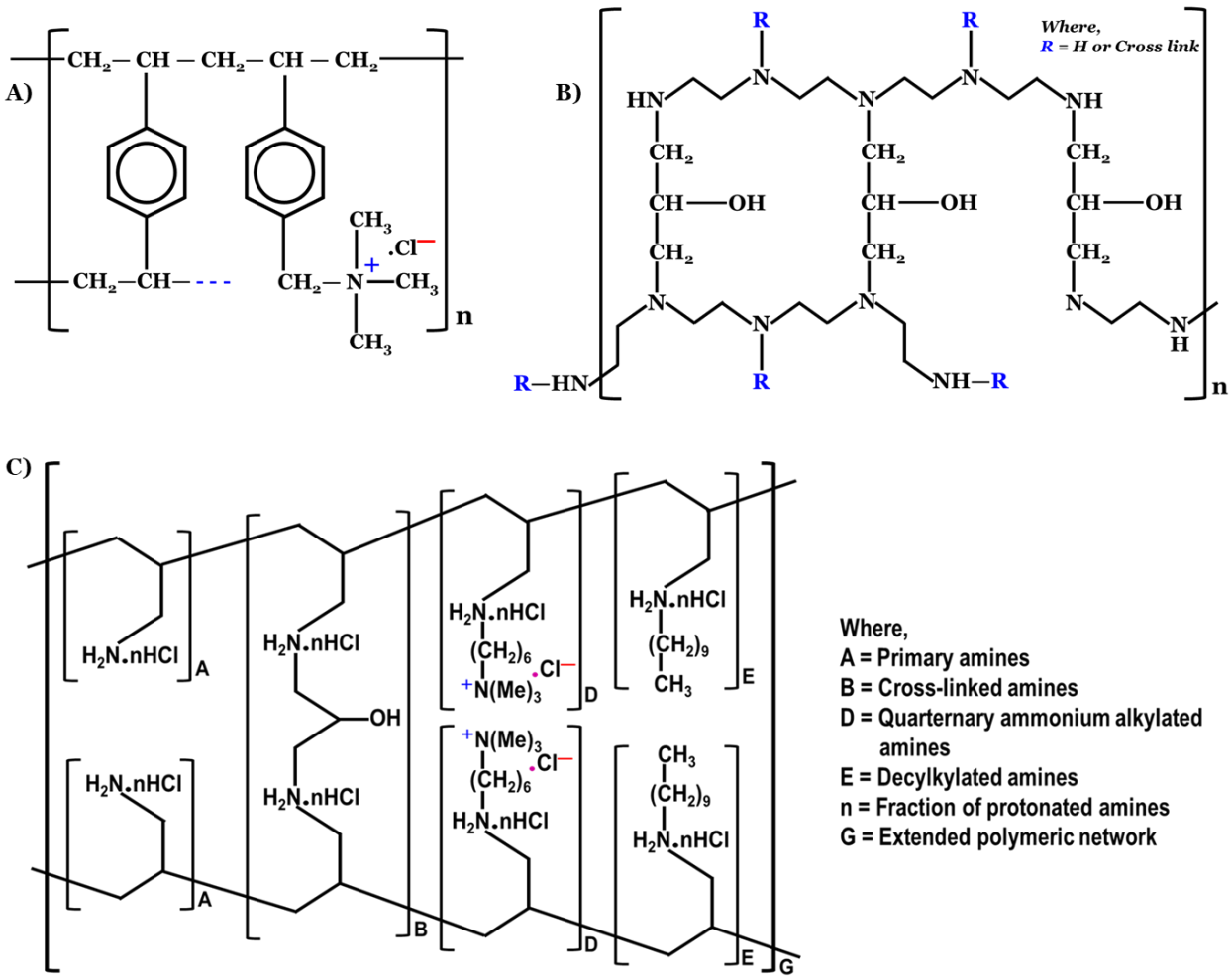


Figure 1.2: *Chemical structures of BASs or resins available in the Canadian market for the treatment of hypercholesterolemia,* ***A)*** *Cholestyramine (1st generation BAS),* ***B)*** *Colestipol (1st generation BAS), and* ***C)*** *Colesevelam (2nd generation BAS; colestimide is also 2nd generation, the structure of which is not shown here and is not available in Canada).*

Cholestyramine, a widely used BAS, has side effects, such as increasing the TG level, constipation, flatulence, and abdominal pain due to its hydrophobic nature and a large dose required for treatment[29] (Table 1.1)[23]. These BASs are effective in reducing cardiovascular (CV) risk both as a monotherapy and in combination with other marketed drugs for

hypercholesterolemia treatment (niacin, fibric acid derivatives, and statins). Several clinical studies have discussed the use of BASs to control glucose homeostasis and regulation of energy balance[30,31].

Table 1.1: Lipid-Lowering Agents—Effect on Lipoproteins[23]

Cholesterol Lowering Agents	LDL-C	HDL-C	Triglyceride (TG)
Resins	**↓ 10–30%**	↑ 3–10%	**↑ 10–25%**
HMG-CoA Reductase Inhibitors	↓ 20–60%	↑ 5–15%	↓ 7–30%
Niacin	↓ 5–25%	↑ 15–35%	↓ 20–50%
Fibrates	↓ 5–20%	↑ 10–35%	↓ 20–50%
Ezetimibe	↓ 14–25%	↑ 1%	↓ 7–9%
PCSK9 Inhibitors	↓ 50–70%	↑ 5–10%	↓ 15%

To date, quaternized/cationically modified hydrogels, functionalized polymers, and polysaccharides to reduce cholesterol levels have been reported. Many of these studies lack biological evaluation, however, a few animal studies highlighted the lack of efficacy data over the commercialized drugs. None of these were conducted in Canada and very few studies that use sustainable nanomaterials have been reported. Thus, there is a compelling motivation to develop alternative materials that are natural, biocompatible, effective, and possess minimal side effects.

1.3 Background

Biopolymers are polymers produced from natural/renewable sources either chemically synthesized from a biological material or entirely biosynthesized by living organisms that could be degraded in the environment[32,33]. These biopolymers can be classified differently based on different criteria, such as the source of origin, where three types of biopolymers are traditionally distinguished into natural, synthetic, and microbial biopolymers. Due to their S.M.A.R.T.© physicochemical characteristics, i.e., their sustainable, modifiable (due to the abundant surface primary hydroxyl groups), active (highly dispersible in water and shows physicochemical activity) renewable (easy surface modification making them renewable), and non-toxic (being natural, they are biocompatible) nature, these biopolymers have a myriad of applications in many industrial sectors. Cellulose and its derivatives, lignin, starch, chitin, chitosan, dextran, glucan, etc. are the most promising and widely utilized polysaccharides (PS) in the biodegradable class of biopolymers with many applications in the biomedical, pharmaceutical, environmental field and food industries[32–37]. The scheme represented in Figure–1.3 illustrates the simplest classification of biopolymers[38].

From the current perspective, cellulose is the most common organic biopolymer obtained from nature. It represents about $1.5x10^{12}$ tons of total annual biomass production and is considered an inexhaustible source of raw material supply to meet the increasing demand for environmentally friendly and biocompatible products[39–44]. Cellulose nanocrystal (CNC), derived from acid hydrolysis of cellulosic sources, has mostly been used to reinforce composites and polymers due to its remarkable strength that rivals carbon nanotubes[39–41]. They are proven to be excellent candidates for many applications since they possess promising

S.M.A.R.T.© properties[39–41]. Thus, functionalizing CNC with alterative functional groups, for example grafting quaternary ammonium groups (QAGs) or surface polymerization with methacrylate monomers having the amino groups (—NH_2), provides a platform to produce newer advanced functional NMs for use as BAS.

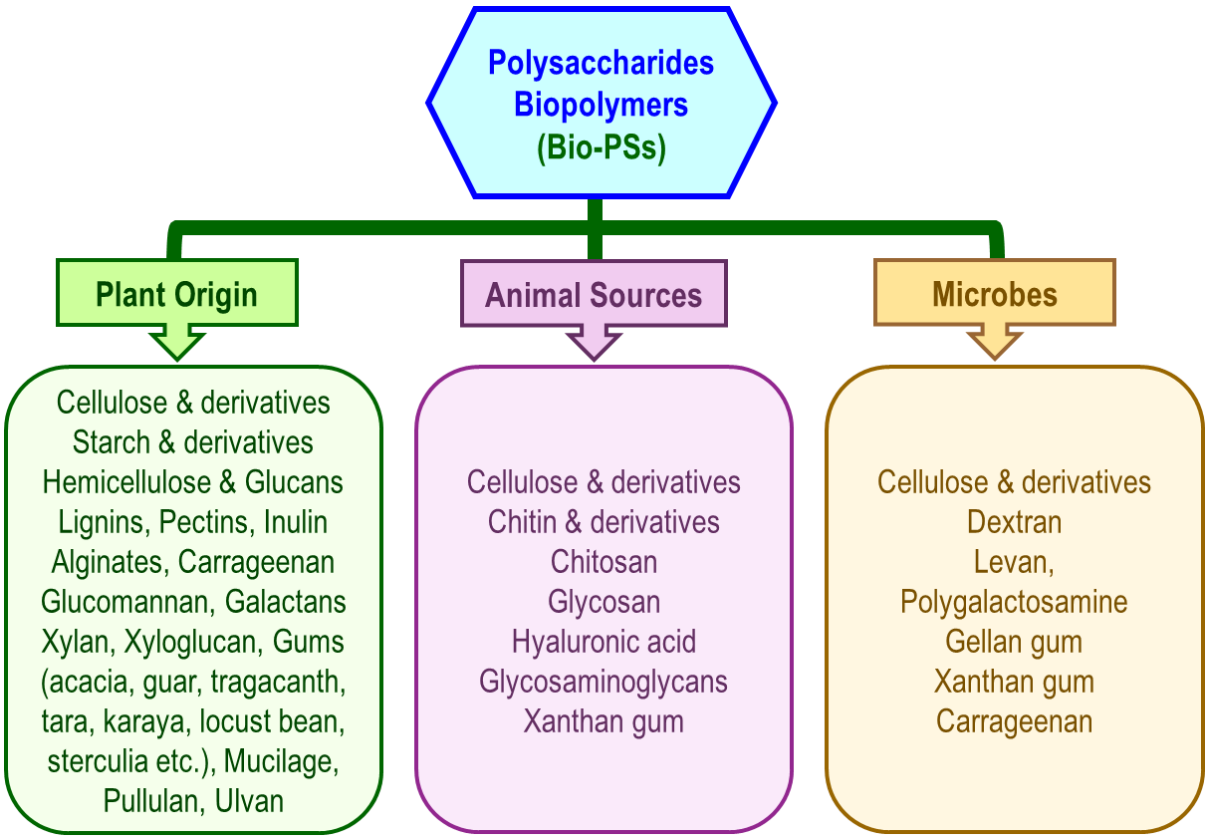


Figure 1.3: *Scheme representing the simplest classification of bio-polysaccharides (bio-PSs) based on their sources of origin. This illustration is just an example and is not a comprehensive list of all the reported bio-PSs. Many of the enlisted bio-PSs possess S.M.A.R.T.© properties and have biomedical applications. (S.M.A.R.T.© coined by the author of the thesis for the 1st time and is derived as the abbreviation of* ***s****ustainable,* ***m****odifiable,* ***a****ctive,* ***r****enewable, and na****t****ural & non-****t****oxic).*

α–chitin is the second most abundant PS in nature and chitosan (CS) can be derived from the α–chitin through partial deacetylation[45,46]. Two marine crustaceans (shrimp and crabs) are the main sources of chitin. Both chitin and CS are polyamine polysaccharides with positive charge groups in acidic media arising from the protonation of the amino groups (—NH_2) on their polymer backbone[45,47,48]. Like celluloses, chitin/CS also possess the S.M.A.R.T.© properties and the positive charges which interact with anionic drugs or polymeric systems[46–49]. Additionally, both amino-polysaccharides (amino-PS) can also be functionalized by grafting with QAGs making them more cationic and more hydrophilic (leading to better dispersibility) that are pH-independent i.e., the surface charges remain unaffected at the physiological pH. Consequently, these amino-PS-based NM systems have a great potential for drug delivery vehicles or as a prodrug. Furthermore, the CS is known for its bioadhesive/mucoadhesive properties[50–52], thus it is expected that the CS-based NM systems are capable to induce physicochemical adsorption of BS from the gastrointestinal tract (GIT).

Throughout this Ph.D. study, I had modified and functionalized the NMs based on cellulose derivatives (cellulose nanocrystals, CNCs), chitin and CS with QAG containing compounds and evaluated their binding efficiencies with negatively charged molecules, such as MO and the SC. Developing a block type or hybrid nanocomposites of CS and CNC, and then quaternizing these NPs was another variety of NMs developed in the Ph.D. research. Furthermore, the development of chitin nanofibers (Cht.NFs) and chitin nanowhiskers/nanocrystals (Cht.NWs) further broadened the range of novel BAS being explored in this study. Lastly, a membrane electrode (sensor) capable of detecting the BAs in an aqueous solution was considered. Using this electrode, the unbound or non-adsorbed BAs

from the post-adsorption experiment samples were quantified and the maximum adsorption capacities were determined.

1.4 Objective and Scope

Based on the description outlined above, the overall objective of this Ph.D. study is to exploit potential applications, particularly the BAS by modifying renewable PS nanomaterial (CNC, Chitin and CS) with various functionalities and taking advantage of their unique properties, especially size effect, cationic charge densities, presence of hydrophobic/H-Bond forming groups, and viscosity of the aqueous dispersions. Thus, in the present study, the main goal is to develop novel, biocompatible, and nontoxic "Nano" systems that can be used as BAS. It is anticipated that chemically modified PSs will exhibit a more desirable BS binding capability compared to unmodified counterparts. Keeping this in mind, the detailed objectives for the doctoral study are identified and proposed as follows:

- Modification of CNC, CS and Cht.NWs with GTMAC (commercially available) as BAS (particle size & charge density effect). Here the NCC^{TM} and/or the CNC extracted from the MCC were used (denoted as CNC_{MCC}).
- Modification of CNC with a newly synthesized monomer [N-dodecyl-N, N-dimethyl-(2,3-epoxy propyl) ammonium chloride (DDEAC), which is commercially unavailable] like the GTMAC, but with a C–12 chain as BAS (particle size, charge density, and hydrophobic effect)

- Modification of CNC with quaternized CS as BAS (charge density, and effect of this block type nanoparticles, like CS-CNC-CS)
- Modification of CNC with poly[2-(dimethylamino) ethyl methacrylate] as BAS (charge density, morphology, pendant hydrophobic effect)
- Development of Cht.NFs and Cht.NWs; functionalization of the Cht.NW with GTMAC (charge density, and effect of pH responsiveness for scavenging effects)

1.5 Hypothesis

It is hypothesized that surface-functionalized PS NMs with various (quality and quantity) quaternary ammonium groups will yield nanoparticulate systems with the desirable morphology that could be utilized for the reduction of high plasma cholesterol levels through the direct sequestration of BS (Figure-1.4).

Several sub-hypotheses are listed below:

- The surface permanent cationic charge of functionalized PSs nanomaterials (F–PS-NMs) can effectively bind to negatively charged BA in the small intestine through strong electrostatic interactions.
- The alcoholic groups present on the surface of F-PS-NMs can interact with the negatively charged BS via hydrogen bonding. Additionally, hydrophobic interactions are also feasible at the nanoparticulate level regardless of the morphology of the NPs as BAS.

- The large surface areas (SAs) offered by the NPs can provide an effective platform for all the possible binding interactions (several folds higher in magnitude due to SA) of the NPs with the BAs, and thus can sequester the BA via the elimination from the body through feces resulting in the reduction of high plasma cholesterol as an indirect effect of BA sequestration.
- By altering the absorption process from the gut wall, these nondigestible F-PS-NMs can effectively reduce progressing 'diet-induced obesity' of the human subject (which has been proven for CNC & cellulose nanofibers, CNF[53], 2018).
- Having surface quaternary ammonium group for the cationic component of the NPs, these F-PS-NMs possess antimicrobial activity as an additional benefit.

1.6 Motivations

As mentioned above, the recent report[53] on the efficacy of the nanocellulose for reduction of fat absorption and reduction of obesity propelled us to work on this doctoral research. We aimed to focus on the sustainable bio–polysaccharide (bio–PS) based functional NMs and were interested to evaluate such NMs' efficiencies for bile salts/acids (BSs/BAs) removal as one of the treatment approaches for elevated cholesterol. Recent work on finding an alternative to commercially available artificial BAS (Cholestyramine) by multiple research groups was our motivation to work on the bio–PS-based NMs (as mentioned in the 'Objectives') for finding newer and naturally derived alternatives to Cholestyramine.

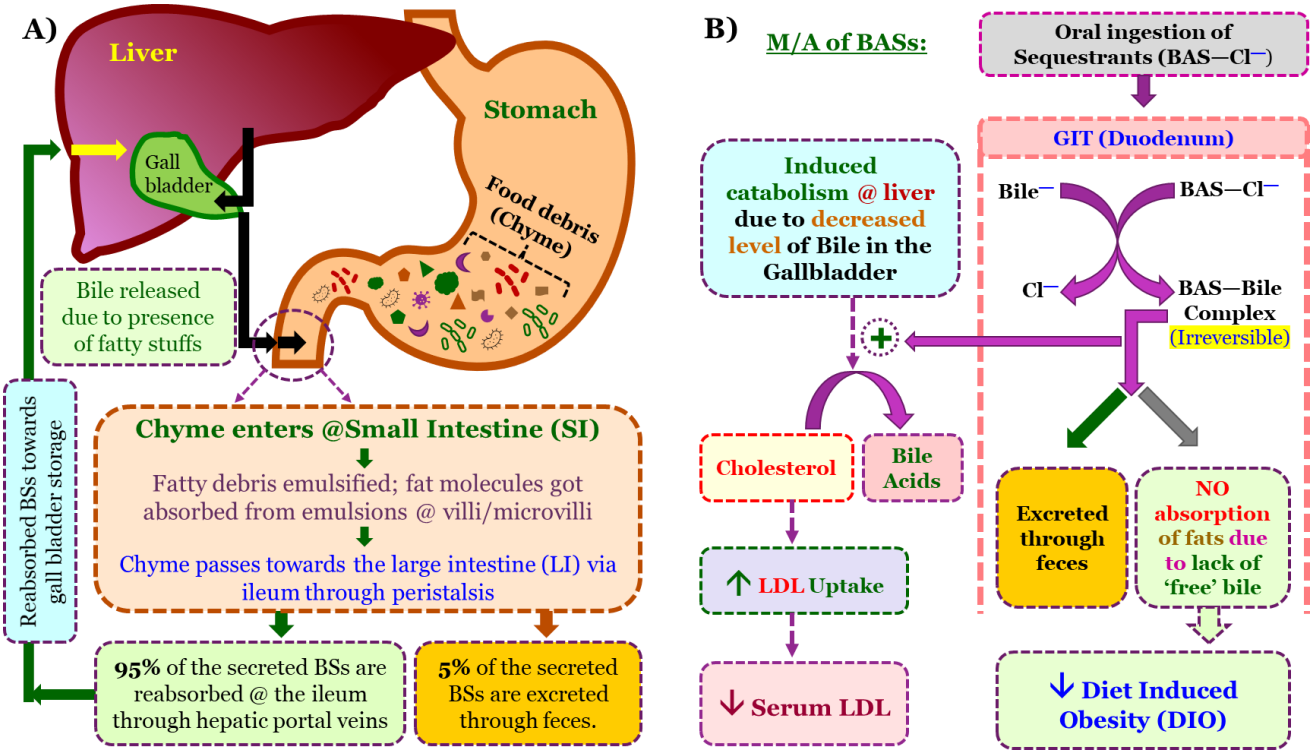


Figure 1.4: A) *Flow diagram of enterohepatic circulation (EHC) of bile showing the reabsorption (95% of the secreted bile) of freed up BA/BS for storage at the gall bladder.* ***B)*** *Schematic illustration of the mechanism of action of a typical BAS.*

1.7 Novelty of the project

Recently, PS–NMs have gained increasing attention by many research communities, and this is evident from the increasing number of scientific publications over the past two decades,[42,54] especially for CNCs (2001–2021) (Figure-1.5). From our analysis of published literature to date, no attempts have been made in exploiting the advantages of modifying the surface of the NCC^{TM} or Cht. NWs alone or combinedly NCC^{TM}/CS hybrids, and their derivatives can be used for BA sequestration to reduce the high plasma cholesterol in humans.

Moreover, no studies have reported on the effect of mucoadhesion on BS binding of such systems, although this topic will not be considered in this Ph.D. study. A significant amount of research (based on a wide array of polymers/copolymers, oligosaccharides, resins, acrylates etc.) has been (and is being) conducted on 'non-nanostructure' systems to address problems associated with the available BAS in the market.

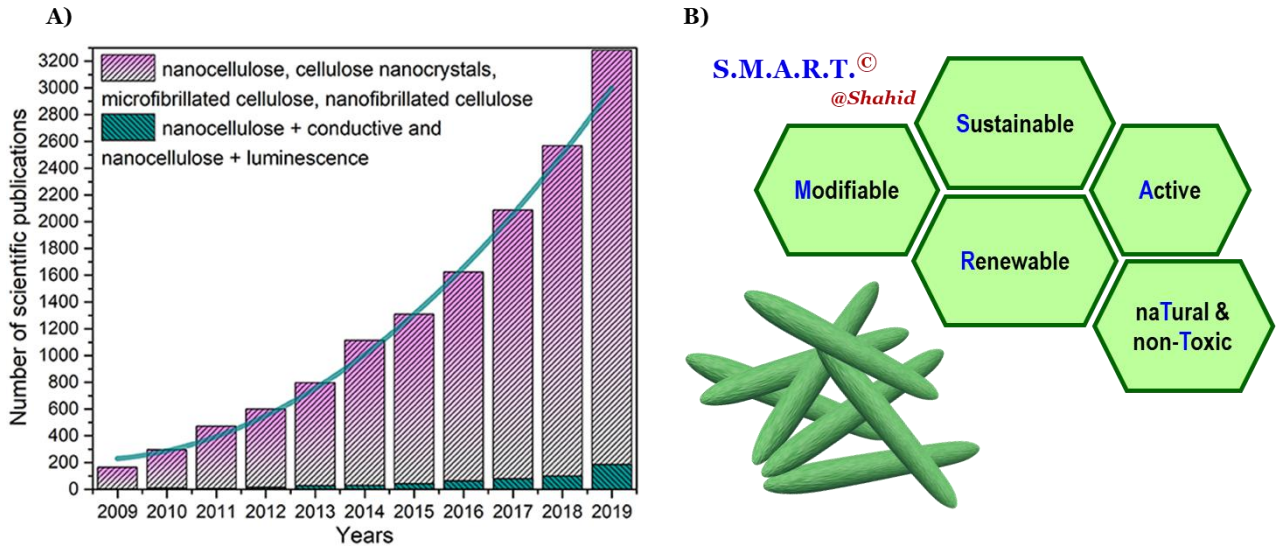


***Figure 1.5**: **A)** Number of publications in the area of nanocellulose. Data analysis was performed on SciFinder using the terms nanocellulose, cellulose nanocrystals, microfibrillated cellulose, nanofibrillated cellulose. Reused from.*[54] ***B)** Elaboration of S.M.A.R.T.© nanomaterials (NMs) and an example of such NMs presented in the insert.*

Most recently (2018) it was reported[53] that nano-sized cellulose fibres added to food could reduce fat absorption by up to half in laboratory and animal experiments, no studies on BA sequestration were reported. Additionally, there was one study in 2021 on functionalized cellulose fibres for scavenging BAs/BSs, however, they were not the nanosized systems.[55]

Furthermore, chitosan and chitin-based 'nano'-systems have never been exploited for application in BAs/BSs sequestration. Thus my Ph.D. goal in developing the S.M.A.R.T.© bile acid sequestrant (BAS) NPs based on CNC is novel. Lastly, although the idea of membrane electrodes is not new, the development of flexible membrane-based electrodes (sensor) for the 'detection of BA/BS' will be critical to quantifying the performance of the BA sequestrant.

1.8 Thesis outline

This Ph.D. thesis contains six chapters that describe the overall work done. The specific contents of the chapter are described below (also illustrated in Figure 1.6):

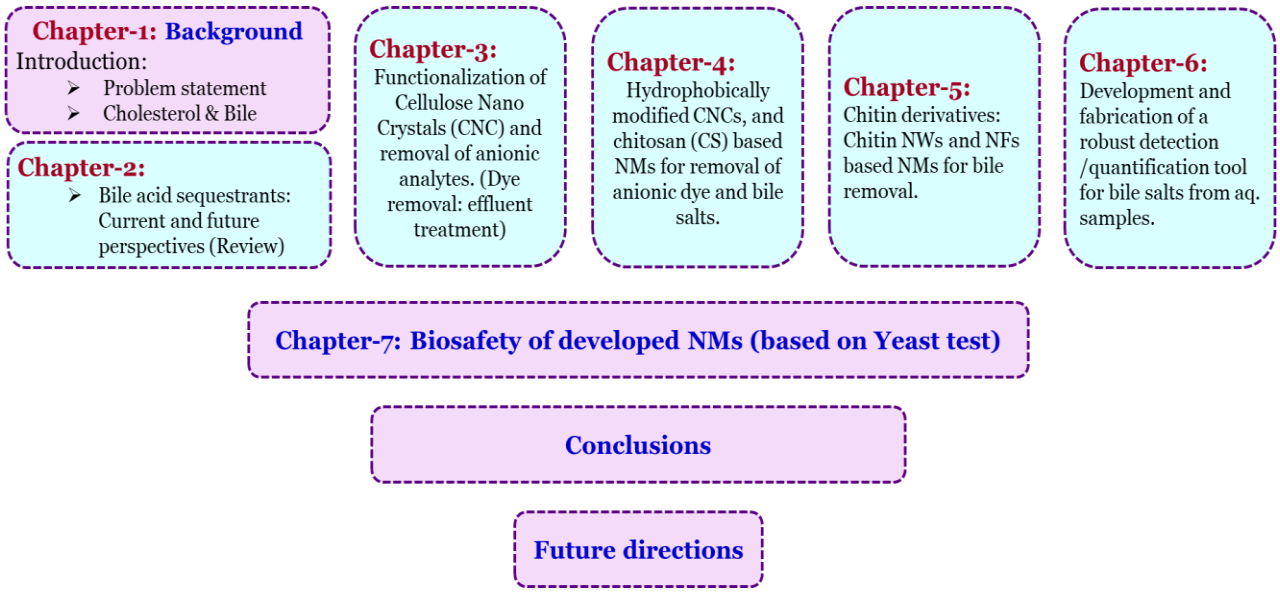


Figure 1.6: *Overall illustration on the thesis and chapters.*

Chapter 1: Contains the introduction, background information, objective, hypothesis, the novelty of the work, and the thesis outline.

Chapter 2: Covers the literature review and introduces bile salts (BS), BS regulation, available bile acid sequestrants (BASs), concurrent research on BASs mostly based on PS based and future perspectives on the S.M.A.R.T. sequestrants for BSs.

Chapter 3: Outlines the development of CNC-based BASs. The base material used in this chapter is NCC^{TM} and CNC extracted from microcrystalline cellulose (MCC) via HCl-mediated hydrolysis. Both types of CNCs were functionalized and their sequestering efficacies for BAs/BSs were evaluated using MO as a surrogate or model drug. Langmuir monolayer adsorption isotherm (LMAI) studies were adopted to evaluate the NMs' efficacies (Q_{max}).

Chapter 4: Includes the fabrication of CNCs and CS with QAGs by grafting onto the surfaces. The effect of a C-12 alkyl chain as the hydrophobic moiety was also evaluated for CNCs. Lastly, the block type hybrid CNC with the quaternary-CS (Q-CS), like CS-CNC-CS nano-system and the polymeric-CNC obtained via the atom transfer radical polymerization (ATRP) of a methacrylate monomer were also developed and evaluated for BA binding efficiencies. In this chapter, the BS sequestration capabilities were evaluated using a model drug MO, as well as SC. The quantifications of unbound SC were determined by converting the free SC to its coloured analogs that were detectable by the UV-Vis. As usual, unless otherwise stated, the Langmuir model was used to determine the NMs' efficacies (Q_{max}) for binding.

Chapter 5: Describes the development of chitin nanofibers (Cht.NFs) and chitin nanowhiskers /nanocrystals (Cht.NWs / ~NCs) from commercially available α–chitin powder. Here, the α–

chitin underwent alkaline deacetylation followed by vigorous successive mechanical treatment (homogenization, sonication and then passing through microfluidizer) to produce a library of different sizes of the Cht.NFs, whose surfaces are comprised of primary amino groups, PAGs (—NH_2) that protonate at pH below 8. If the α–chitin is deacetylated by HCl-mediated hydrolysis, the end–product is Cht.NWs. In this chapter, only the Cht.NWs were cationized with GTMAC molecules and their sequestration abilities to BA/BS were examined.

Chapter 6: Illustrates the development and fabrication of polymeric membrane-based electrode (sensor) for the detection of free BS in aqueous solutions. Such membrane-based electrode works based on the fundamentals of electrochemistry. This elementary model of the electrode has been routinely and repeatedly utilized for the detection of free SC molecules in many of the batch adsorption tests (BATs) conducted for the NMs (following the methods discussed in previous chapters) and SC.

Chapter 7: Mostly covers the biosafety of the developed NMs. Based on various physicochemical characterization data and adsorption efficiency data, several NPs were selected to estimate their toxicity using the CO_2 production by Baker's yeast. The fermentation rate would provide information on the toxicity of NMs to eukaryotic cells.

Chapter 2: Literature Review

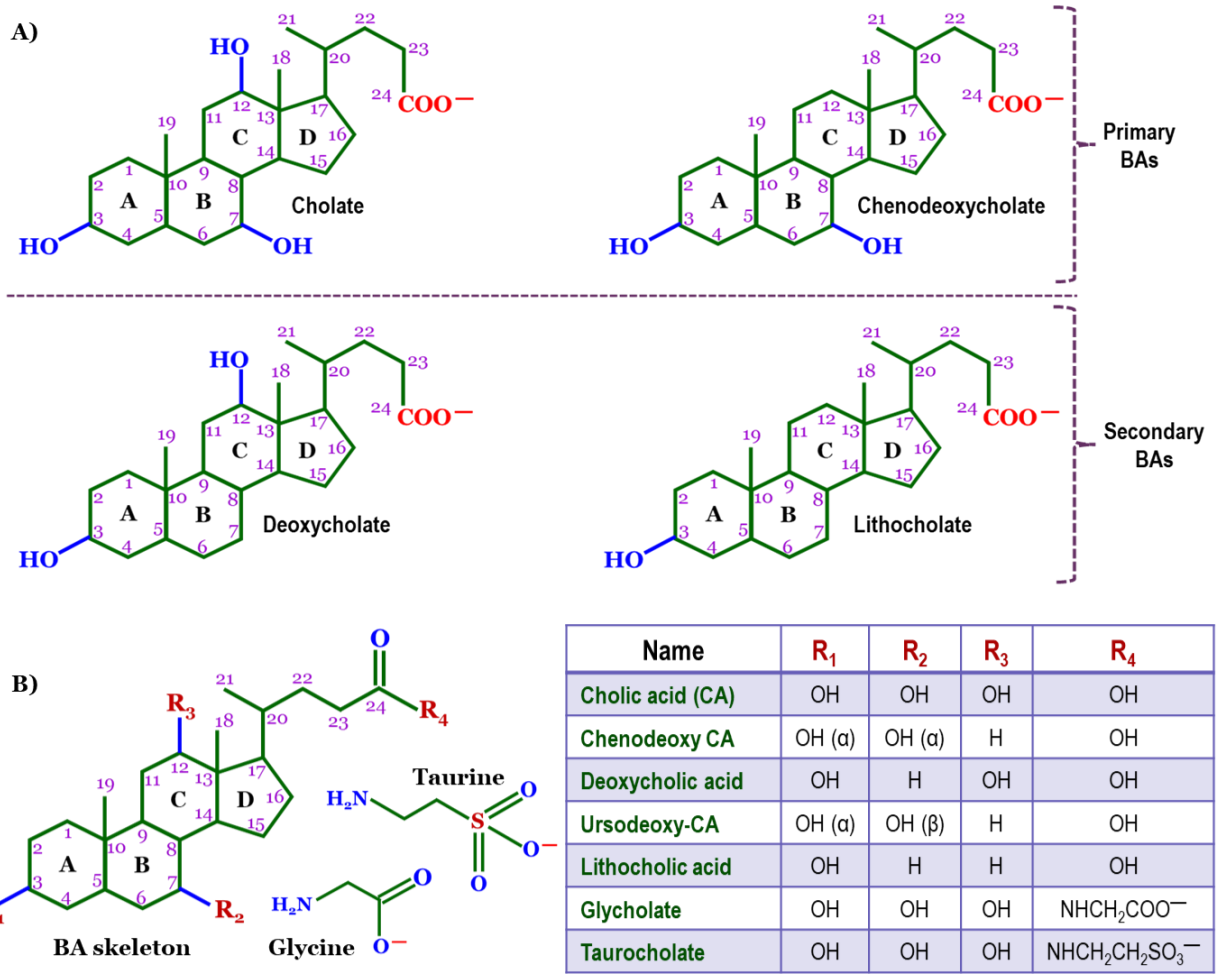
2.1 Introduction: Chemistry, and Properties of Bile Acids/Salts (BAs/BSs)'

Bile acids (BAs), the biological detergents, are the amphipathic/amphiphilic end products of cholesterol metabolism, which is facilitated by hepatocytes in the liver. They are a type of cholanic acid, representing a group of molecules with a similar structure as steroidal acids. The cholane consists of a carboxy group rather than a methyl group at position 24, and they can be further classified into primary BAs and secondary BAs.[56,57] They all have 24 carbon atoms and are commonly abbreviated as C–24 bile acids (Figure 2.1). Primary BAs are those synthesized in the liver by the hepatocytes, while secondary BAs are synthesized by bacteria in the colon. BAs closely resemble cholesterol molecules, as they are produced from the cholesterol precursors through an enzymatic process. BA production utilizes peroxisomal enzymes, which perform the hydroxylation and modification of cholesterol into BAs, making this the primary metabolic pathway for the catabolism of cholesterol in humans.[56–58] In human bile, these C-24 bile acids are almost completely in a conjugated form with either glycine (75%) or taurine (25%) as shown in Figure–2.1. Under physiological conditions, conjugation increases their water-solubility.[58]

Chemically, BAs have a unique molecular structure derived from a saturated tetracyclic hydrocarbon cyclopentanoperhydrophenanthrene (CPPP) system, usually known as the steroid nucleus. The steroid nucleus (Figure 2.1) consists of three six-member rings (A, B and C) and a five-member ring (D), with a curved (beaked) or flat structure (depending on a *cis*- or *trans*-fused configuration between the A and B rings).[59] The mammalian bile acids have a 5β-

configuration at the nucleus (A/B junction in *cis* configuration) with hydroxyl groups at 3α, 7α and 12α.[59] Such presence of chemically "nonequivalent" 3α, 7α and 12α hydroxyl groups and the side chain structure supporting a carboxylic acid group in bile acid molecules confer their unique physicochemical characteristics.[28,58] These physicochemical properties are related to their amphipathic nature due to the existence of hydrophilic (α-face, concave lower side) and hydrophobic sides (β-face, convex upper side, which is rigid and planar).[13,56,58,59]

Commonly, in biomedical literature, the terms "bile acids (BAs)" or "bile salts (BSs)" are used interchangeably as the BSs are relatively similar to BAs. They both are surfactant molecules, but the primary difference between the two molecules is that BSs are BAs conjugated with taurine or glycine residues, thus, making them anionic and more water-soluble. They are conjugated between the carboxyl group of BA and the amino group of glycine or taurine molecules.[60] After conjugation with either glycine or taurine, the pKa of the carboxyl group (glycine) or the sulfonate group (taurine) is reduced, causing the BS to be fully ionized at physiological pH, yielding a negative charge[60] (Figure 2.1). This allows BSs to have enhanced amphipathic function, making them more effective surfactants than BAs.



Name	R_1	R_2	R_3	R_4
Cholic acid (CA)	OH	OH	OH	OH
Chenodeoxy CA	OH (α)	OH (α)	H	OH
Deoxycholic acid	OH	H	OH	OH
Ursodeoxy-CA	OH (α)	OH (β)	H	OH
Lithocholic acid	OH	H	H	OH
Glycholate	OH	OH	OH	$NHCH_2COO^-$
Taurocholate	OH	OH	OH	$NHCH_2CH_2SO_3^-$

Figure 2.1: *Chemical structures of different BAs available in humans.* ***A)*** *1^0 & 2^0 BAs in the body.* ***B)*** *Conjugated BA derivatives, commonly known as bile salts (BSs).*

2.2 BA synthesis, metabolism, & enterohepatic circulation (EHC)/bile pool

In humans, there are two pathways[61] for the synthesis of BA, the classical (neutral) and alternative (acidic) pathways (Figure 2.2), which result in the formation of primary BA, cholic acid (CA, 3α,7α, 12α -trihydroxy-5β-cholanoic acid), and chenodeoxycholic acid (CDCA, 3α,7α-dihydroxy-5β-cholanoic acid).[58] The classical (or neutral) pathway accounts for at least 75% of bile acid production under normal conditions is initiated by 7α-hydroxylation (rate-limiting step) of cholesterol catalyzed by cholesterol 7α-hydroxylase.[62] Here, the size of the bile acid pool is tightly regulated within the liver and intestine to prevent cytotoxic accumulation of bile acids.[30] BA synthesis is regulated by a negative feedback mechanism. The coordinated regulation of the different steps of BA enterohepatic circulation (synthesis, transport, and elimination) is important for the maintenance of BAs and cholesterol homeostasis. BAs returning to the liver via enterohepatic circulation may directly or indirectly inhibit BAs synthesis by inhibiting the 7α– and 12α– cholesterol hydroxylase enzymes.[63]

The quantity of bile acid that the liver normally produces and secretes in a day varies with the number of meals and the fat content of these meals, but it typically ranges anywhere between 400 to 800 mL of bile per day, of which roughly 0.2—0.6 g are BAs/BSs.[61,64,65] The liver's basal rate in the synthesis of bile acids from cholesterol is only ~600 mg/day in healthy humans, sufficient to replace the equivalent losses of BA in the feces (~ 200 mg—600 mg/day). Obviously, the gastrointestinal tract must have an extremely efficient mechanism to recycle BAs secreted by the liver. This process of recycling and circulating bile is maintained by two mechanisms, enterohepatic circulation, EHC and the *de novo* synthesis of BAs from cholesterol molecules.[65]

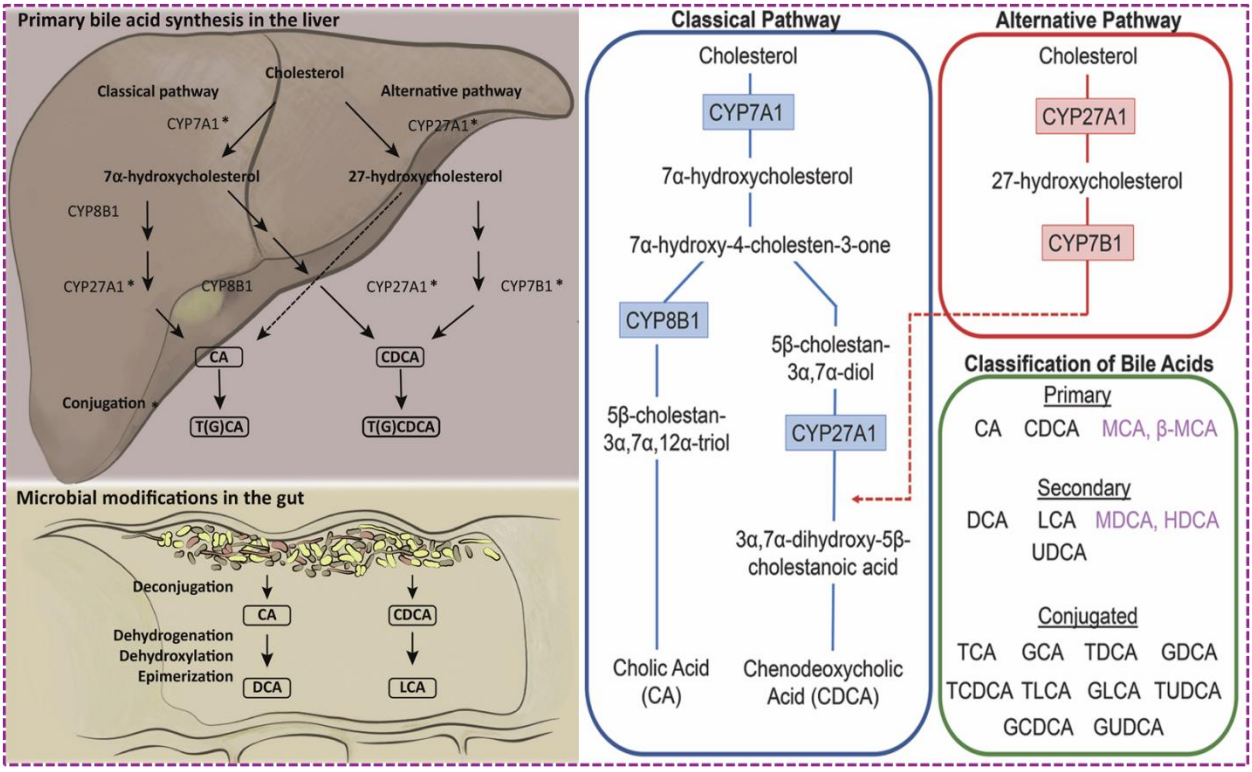


Figure 2.2: *Two different pathways for the synthesis of BAs: the Classical (neutral) pathway that occurs in the liver (hepatocyte) and the alternate (or acidic) pathway found in peripheral tissues and the liver, showing the primary and secondary BAs. In the classic pathway, the primary bile acid cholic acid (CA) is formed after subsequent conversions from sterol 12α-hydroxylase (CYP8B1) and chenodeoxycholic acid from sterol 27-hydroxylase (CYP27A1). In the alternative or acidic pathway, mitochondrial CYP27A1 in peripheral tissues convert cholesterol into 27-hydroxycholesterol. Oxysterol 7α-hydroxylase (CYP7B1) is an additional assisting enzyme in this pathway and the resulting products feed back into the liver,* ***indicated by the red arrow*** *feeding into the classical pathway under CYP27A1. The 1^0 & 2^0 BAs specific to rodents are listed* ***in purple*** *at the bottom right inset of the image. Bile acids can become conjugated with glycine or taurine after interactions with gut flora. Modified and reused from.*[66,67]

Legends in the image: *MCA = Muricholic acid, TCA = Taurocholic acid, GCA = Glycocholic acid, UDCA = Ursodeoxycholic acid, DAC = Deoxycholic acid, LCA = Lithocholic acid, TCDCA = Taurochenodeoxycholic acid, GCDCA = Glycochenodeoxycholic acid, MDCA = Murideoxycholic acid, etc.*

This recycling, known as the enterohepatic circulation (EHC), occurs as the terminal ileum and colon reabsorb bile acids and return them to the liver in the portal blood. The total pool of bile acids in the gastrointestinal tract is ~3 g which recirculates ~4 to 12 times per day or as many as 5 or more times for a single fat-rich meal[64,65,68]. If reabsorption of bile acids is defective, as can happen after resection of the ileum (Bariatric surgery), *de novo* synthesis of bile acids by the liver can be as high as 4 to 6 g/day.[64,65,68]

2.3 Polymeric BASs in the market and their limitations

For patients who are indicated for lipid-lowering drug therapy, statins are usually the drugs of choice. However, in hypercholesterolemic subjects with statin intolerance or those resistant to statin treatment, usually other lipid-lowering drugs, especially the BASs are considered. The principal non-statin lipid-lowering drugs and their efficacies in cholesterol regulation are summarized in Table–1.1. Until now, there are two generations of BAS, also known as resins that are available in the market[23,69] and their chemical structures were shown in Figure 1.2.

Both generations of BASs are positively charged, high molecular weight (MW), non-absorbable, indigestible polymeric molecules that bind negatively charged bile acids (BAs) in the intestine. Due to these characteristics, they form poor dispersions in the intestinal fluids leaving their many active/functional sites mostly inaccessible, thus the reason for their low efficacies.[70] They are not absorbed or altered by digestive enzymes; hence their primary effects are localized in the intestine. The partial diversion of BAs from enterohepatic circulation using BAS depletes the BA pool by approximately 40%, stimulating an increase in BA synthesis

from cholesterol (cholesterol catabolism) and increasing BA fecal excretion. The increase of BA synthesis results in a reduction of liver cholesterol content and up-regulation of low-density lipoprotein receptor (LDLR), with consequently increased uptake of low-density lipoprotein (LDL) from circulation.[23,29,69] This mechanism of a typical BAS is illustrated in Figure 1.4.

The first-generation (1G) BAS comprised copolymers containing amine/ammonium groups, represented by the commercially available colestipol (a polyamine cross-linked by epichlorohydrin) and cholestyramine (a cross-linked copolymer of styrene and divinylbenzene possessing covalently bound quaternary ammonium salts). The relatively high recommended doses of colestipol (16–20 g/day) and cholestyramine (16–32 g/day) required to reduce total cholesterol level by ca. 20% suggest their poor efficacy in competition between the resin and active BA reabsorption from the GI tract[29]. *In vitro* studies on both resins suggested that their low sequestration potency could be due to (i) low activity of the resins to bind trihydroxy BAs in the duodenum and jejunum and (ii) dissociation of the bile acids from the sequestrants in the terminal ileum, where free BAs are readily reabsorbed by the gut.[29] Colestimide (not available in Canada) and colesevelam belong to the second generation (2G) of BAS, distinguished (compared to the 1G) by a high content of hydrophobic aliphatic chains and a higher degree of quaternary ammonium cations, which are responsible for enhanced binding affinity to BA.[29]

Except for their low therapeutic efficacies, and GI side effects discussed earlier, currently, the BASs are contraindicated in pregnancy, and patients with significant hepatic dysfunction, constipation, malabsorption syndromes, and severe hypertriglyceridemia. Although the 2nd generation of BAS offers some advantages (decreased daily dose requirement,

improved efficacy), there exists strong motivation to develop new and more efficient polymer-based BASs for patients who cannot use statins or must take high statin doses.[29,71]

2.4 Concurrent polymeric BA sequestrants (BAS) from literature

Most of the literature on the evaluation of new polymeric bile acid sequestrants has depended predominantly on *in vitro* experiments.[72] These publications claimed that the binding measurements were performed under conditions that are likely to be encountered in the GI tract and therefore these *in vitro* results should predict a true *in vivo* situation. In contrast, such *in vitro* experiments are unlikely to predict *in vivo* conditions. Firstly, these *in vitro* experiments were conducted at equilibrium, while *in vivo* conditions in the GI tract are transient. Furthermore, in addition to the presence of pH and ionic strength gradients in the GI tract, active uptake of bile acids is known to be mediated by transporters in the GI tract.[72] None of the earlier *in vitro* experiments in the literature have taken this transporter-mediated uptake into consideration, which would significantly affect the *in vivo* bile acid binding efficacies of the sequestrants.[72] Considering these possible shortcomings of *in vitro* studies, in the following subsections the biopolymers (mostly) and dietary fibres based nonsystemic BAS from the published literature are being discussed that were evaluated through *in vitro* and animal model/clinical trial studies. Such discussion would also include a brief summary of findings from literature where direct scavenging effects of BA/BS were not discussed but reported the cholesterol reduction and impact of change in body weight (reduction of the diet–induced obesity, DIO).

2.5 Biopolymer-based BA sequestrants (BAS)

Biopolymers are naturally occurring polymers produced by living organisms due to their intriguing properties and inherent characteristics. Like any other polymers, the biopolymers are chain-like polymers/oligomers produced from renewable resources and they decompose in the environment (biodegradable).[32,33] Due to their S.M.A.R.T.© properties (Sustainable, Modifiable, Active, Renewable, and non-Toxic/natural), the biopolymers have a plethora of applications in biomedical sciences, pharmaceutical technology, medical devices, food applications including packaging, textiles, automotive and aviation technology, building materials, environmental sensors, electronics, and energy.[32–37] These biopolymers can be broadly classified as polysaccharide-based and protein-based compounds[38] based on the sources they are obtained/extracted as shown in the scheme presented in Figure–1.3 in the previous chapter. But, for this doctoral research, the cellulose, chitosan, and chitin-based systems were selected among the vast selections of bio–PSs from which the NPs were planned to functionalize to develop newer BASs for hypercholesterolemia treatment. Figure 2.3 below represents specific parts of the chemical structures of some selective biopolymers that are commonly used in drug delivery applications reported in the literature.

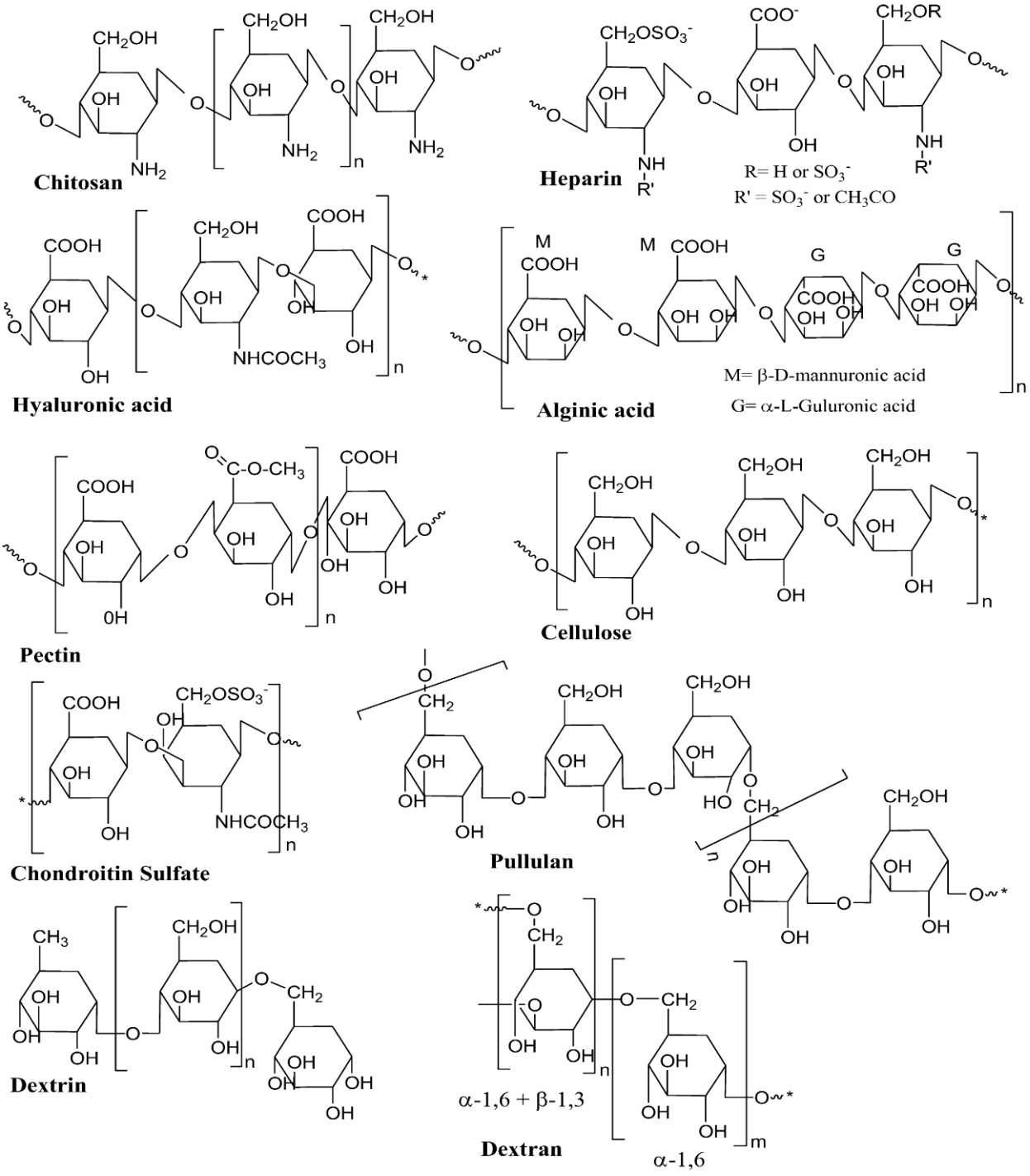
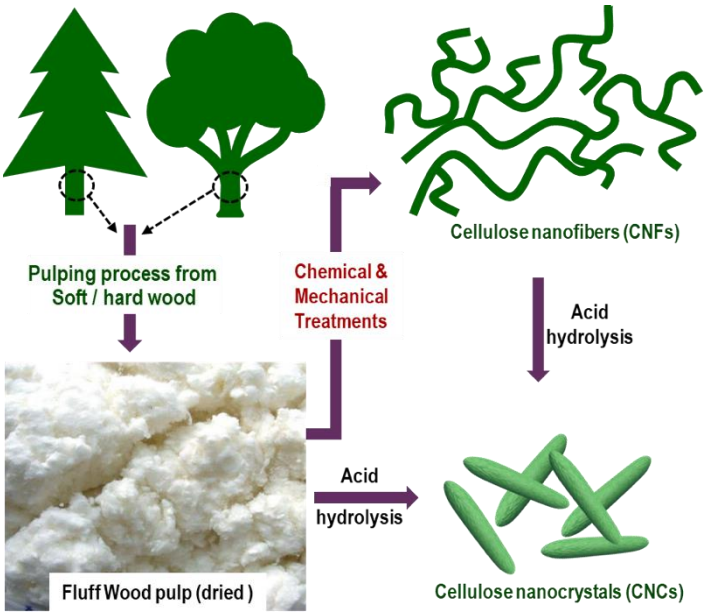


Figure 2.3: *Some examples of natural polysaccharides commonly used in biomedical applications. Reused from.*[73]

2.6 Cellulose and derivatives as the BASs

Cellulose is one of the most ubiquitous and abundant renewable biopolymers on earth and has a wide spectrum of applications. Since 1838, when cellulose was first discovered, a large body of research on cellulose and its' derivatives (mostly cellulose nanocrystals, CNCs) from various disciplines were studied for biomedical applications, such as targeted drug delivery.[74] Although the soft and hardwood from higher plants is the most commercially exploited source of cellulose, numerous other sources had been reported. Cellulose microfibrils, the structural units in higher plants, contain highly ordered (crystalline) domains alternating with disordered (amorphous) regions.[74] From these microfibrils, it is possible to extract the cellulose nanofiber, CNF, also called the nano-cellulose (NC) and cellulose nanocrystal, CNC, and Figure 2.4 illustrates the schematic of CNC extraction.[74]

CNC can be modified chemically to achieve the target-specific application. Herein, we will discuss the application of cellulose-based systems for bile acid removal/sequestration.



Source	L (nm)	d (nm)	Aspect ratio (L/d)
Bacterial	100–1000	10–50	2–100
Cotton	100–300	5–10	10–30
MCC	~500	10	50
Ramie	50–150	5–10	5–30
Sisal	100–500	3–5	20–167
Tunicate	100–several 1000	15–30	3–67
Valonia	>1000	10–20	50–100
Wood	100–300	3–5	20–100

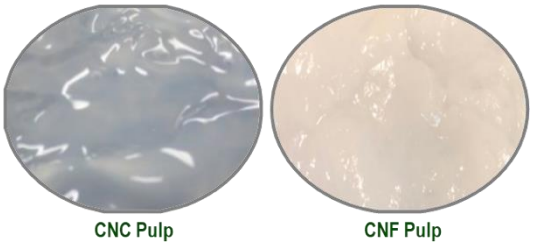


Figure 2.4: *Schematic of extraction of CNCs from a cellulose source (here, it is hardwood). CNCs can be extracted through mechanical, chemical or combination of mechanical, chemical and/or enzymatic (endoglucanase) treatments. Sulphuric acid (H_2SO_4) mediated hydrolysis is the most common and widely used technique for CNC production. The table was drawn from*[39–41].

Zhu *et. al.*[75] (2016) reported on the synthesis of a hyperbranched polyethylene amine-based cellulose system (hPEI–CE), and examined the adsorption on dyes, instead of BSs. Later, Shen *et. al.* (2020)[55] evaluated the hPEI–CE system for the adsorption of BS, as shown in Figure 2.5. They utilized the periodate ($NaIO_4$) mediated oxidation to convert its dialdehyde derivative (dialdehyde cellulose, DAC) and grafted the hPEI onto the DAC yielding hPEI–CE system to remove cholesterol. The authors investigated the sorption capacities of their BAS for sodium cholate (SC), examining factors such as concentration of SC, contact time and electrolytes.[55] Based on the evolution of coloured analogs of SC when reacting with 42% (w/w) sulphuric acid (H_2SO_4), the UV-Vis was used to quantify the SC in aqueous samples. This

novel BAS, *i.e.*, the hPEI–CE possessed a maximum adsorption capacity (Q_{max}) of 569.7 mg/g which was higher than cholestyramine[55] (Table 2.1).

Table 2.1: Comparisons of maximum adsorption capacities (Q_{max}) of novel hPEI–CE with both controls at an equal weight (700 mg/mL, 37^0C, 120 rpm). Reused from.[55]

Sorbents	Adsorption capacity (mg/g)	Adsorption percent relative to cholestyramine (%)
Cellulose (negative control)	5.67 ± 1	1.0 ± 0.18
DAC (negative control)	198 ± 10	36.1 ± 1.8
hPEI–CE	569.7 ± 20	104 ± 3.6
Cholestyramine (positive control)	548 ± 20	100 ± 3.6

Such interactions with their BAS to SC may be attributed to the two different binding forces namely: i) electrostatic interactions between the surfaced cationic amino groups of hPEI–CE and ii) the non-electrostatic interactions (hydrophobic, hydrogen bonding etc.) between the BAS particles and SC molecules. The binding phenomena were fitted to the Langmuir isotherm model and pseudo-second-order kinetic model, confirming the homogenous monolayered chemisorption with BAS and SC. They observed excellent cytocompatibility and anti-interference for their BAS based on the studies of MTT assay and adsorption tests in varying ionic strength, respectively. Most of the binding with SC occurred within the first hour before the BAS's adsorption sites were saturated or occupied, as predicted by the adsorption kinetic studies.

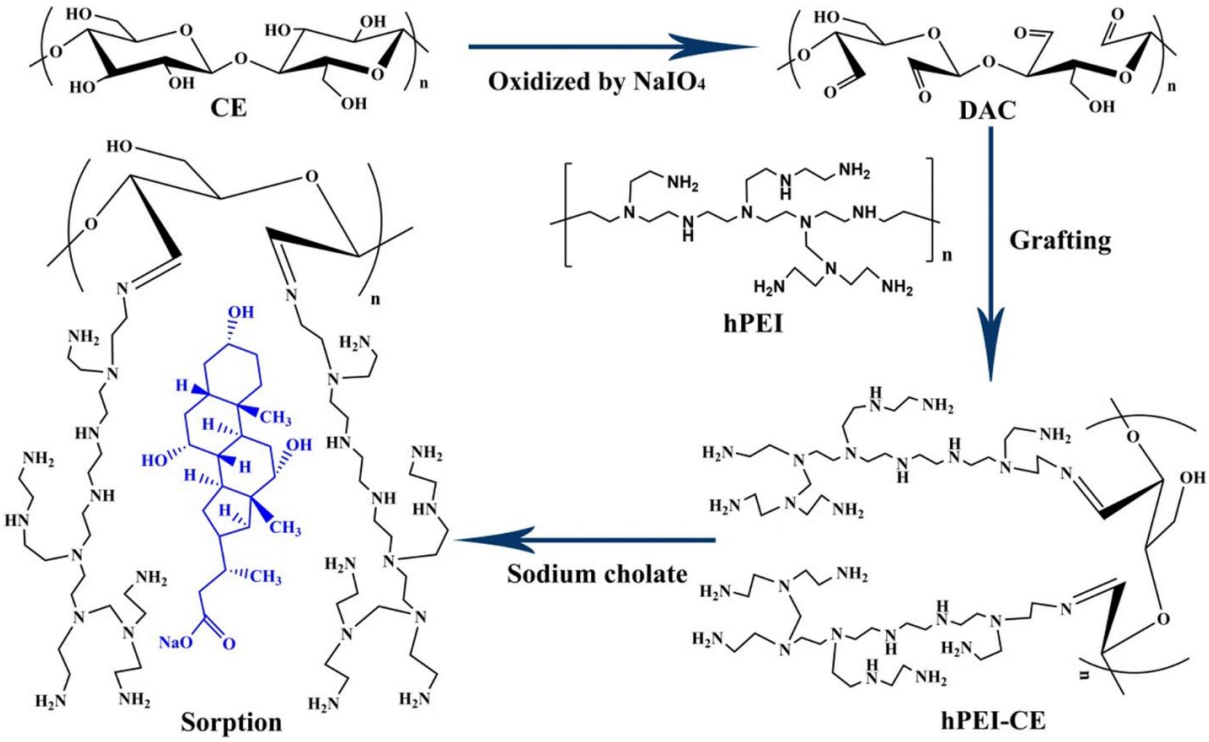


Figure 2.5: *Schematic of hPEI-CE preparation and the sorption of sodium cholate (SC). Reused from.*[55]

The micro-fibrillated celluloses (MFCs) were also modified and investigated for BS scavenging by Zhu *et. al.*[76,77], where they modified the MFC with a small quarternary ammonium (QAG), and GTMAC/EPTMAC (Glycidyl-trimethyl-ammonium chloride/2,3-Epoxypropyltrimethylammonium chloride) groups. The SC adsorption capacity of SC at various salt concentrations, contact time and concentration of initial SC were examined, and the Langmuir adsorption isotherm described the monolayer binding of SC onto the cat-MFC with a Q_{max} of 416.67 mg/g.[77] Additionally, the adsorption kinetics was best fitted to a pseudo-second-order suggesting that chemisorption controlled the surface adsorption of SC. The

significant disruptions of binding in the presence of salts during the sorption tests indicated the interaction between sodium cholate and CMFC was electrostatic in nature. Table 2.2 provides a summary of the binding of cationic MFCs relative to cholestyramine.

Table 2.2: Comparison of adsorption percent relative to cholestyramine of hPEI-CE with other adsorbents for bile acid. Adapted from.[55]

Adsorbents	Adsorption % relative to Cholestyramine[a]	References
*LMW β-Glucan	27.2	Ref.[78]
Cationic MFC	29.74	Ref.[77]
Cationic amphiphilic MFC	53.34	Ref.[76]
L. Japonica polysaccharide	68.29	Ref.[79]
Ultrafine β-glucan	86.20	Ref.[80]
Ultrafine guar gum	92.30	Ref.[80]
Ultrafine inulin	97.85	Ref.[80]
hPEI-CE	104	Ref.[55]

[a] *Only the BA binding relative to cholestyramine is listed here.*

[*] *LMW = Low molecular weight*

Kazlauske *et. al.*[81] (2014) studied the binding capacity of BAS with different kinds of cellulose modified with diethylaminoethyl (DEAE), namely macroporous (DEAE-Granocel), commercial microgranular cellulosic anion-exchanger (DE52), cotton fibre (DEAE-CF), and microcrystalline (DEAE-MKC). They investigated the scavenging efficacy of sodium deoxycholate (NaDCA), sodium glycocholate (NaGCA), and sodium taurocholate (NaTCA) as a function of pH and BS concentrations. A significant increase of several-fold in the Q_{max}

for BSs over that \ of cholestyramine, especially at pH 4. Most of the binding approached their saturation point within the initial 30 minutes (rapid adsorption) of treatments, compared to 1 hr (slow adsorption) for cholestyramine.[81] Table 2.3 summarizes the Q_{max} values obtained from a specific pH for cholic acid adsorption tests with BASs.

Table 2.3: Maximum cholic acid sorption capacity at pH of 4 – 6. Reproduced from.[81]

Adsorbents	**Max adsorption capacity (Q_{max}) recorded**	
	mg/g	**mmol/g**
DEAE-Granocel	84.0	0.206
DEAE-MKC	25.3	0.062
DEAE-CF	46.0	0.113
DE52	11.0	0.027
Cholestyramine	12.5	0.031

DeLoid *et. al.*[53] examined the use of nanocelluloses (CNF) for reducing intestinal fat adsorption by reducing the systemic high cholesterol level to also address diet-induced obesity (DIO). They concluded that the reduction of systemic absorption of ingested fat at the brush borders of small intestines is mainly the outcome of two principal mechanisms[53] (illustrated in Figure 2.6): i) coalescence of small fat droplets on NCs/CNFs till saturation, resulting in a reduction of available surface area for lipase chemisorption leading to a lower binding of lipase with the fat droplets and increased chemisorption of lipase with the CNFs, and ii) scavenging of bile salts, which are necessary for the emulsification of lipase mediated fats, resulting in interrupted interfacial dissociation of proteins at the lipid droplet surface and reduced the

solubilization of the fatty acids (FFA) from TGs. The findings indicated that the NCs could be the potential food additive/supplement to reduce the absorption of ingested fats and to have control over the management of DIOs.[53]

The interactions of NCs with fatty foods led to the disruption of the activity of pancreatic lipase reducing fat digestion and absorption. This was evaluated using heavy cream as the high-fat food model in the presence or absence of NC via the following experimental designs: (1) acellular simulated gastrointestinal tract (GIT) digestion with pH-Stat titration and fluorometric analysis to measure free fatty acid (FFA) release during small intestinal digestion; (2) *in vitro* biokinetics experiments using a triculture model of the small intestinal epithelium to measure translocation of FFA and TG from digesta produced by the GIT simulator; and (3) an *in vivo* rat gavage with heavy cream with or without NC, followed by measurement of postprandial serum TGs.[53]

From the obtained results (some illustrated in Figure 2.6), the authors observed a reduction of hydrolysis of TG present in heavy cream was very significant due to adsorption of the pancreatic lipase onto NC. With the addition of 0.75% (w/w) cream to the food, about 48.4% and 40.1% less FFAs were produced in the simulated GIT experiment, from titration mode and fluorometric analysis respectively.[53] Additionally, the presence of 0.75% w/w NC in the food reduced the translocation of TG across the intestinal epithelium (*in vitro* cellular experiment) by 52%. From the *in vivo* experiments, the measured level of the serum TG was reduced by 36% in presence of 1.0% w/w NC.[53]

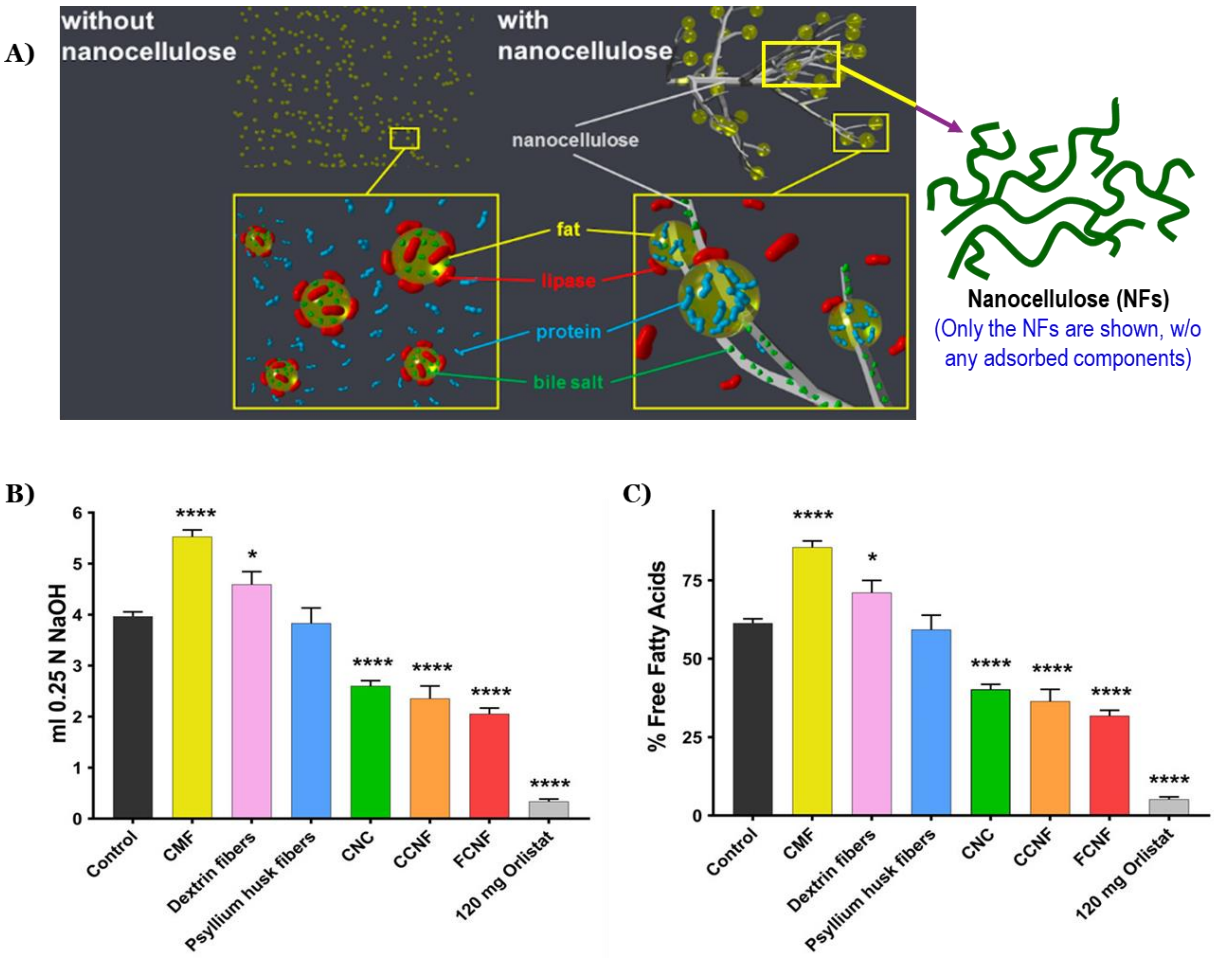


Figure 2.6: A) *Schematic illustration of the efficacy of NCs/CNFs on modulation of fat digestion leading to the reduction of raised LDL-C from the outcome of scavenging BSs and interruption in the increasing trends of the DIO. Graphical representations of the effect of cellulose and other fibres on in vitro triglyceride digestion:* ***(B)*** *Total NaOH (0.25 M) titrant used during small intestinal digestion of heavy cream.* ***(C)*** *Total percentage of FFA released during small intestinal digestion of heavy cream. Reused and adapted from.*[53]

Abbreviations in the image: *CMF = micrometer scale cellulose fibrils; CNC = cellulose nanocrystals; CCNF = 80 nm CNF (coarse), FCNF = 50 nm CNF (fine), Orlistat = commercially available lipase inhibitor (4.8 mg/mL).*

2.7 Other bio-PS based BAS:

2.7.1 Functionalized Paramylon

Paramylon, also known as the linear β-(1,3)-D-glucans is a group of chemically heterogeneous polysaccharides with long- or short-chain polymers of (1→3)-β-linked glucose moieties (Figure 2.7). These β-(1,3)-Glucans are widely distributed in bacteria, algae, fungi, and plants as components of the cell wall structure and other cellular functions. They have been found beneficial over a remarkable range of health conditions, such as cholesterol and blood glucose/sugar levels (BG/SL) regulation and enhancing immunity for the body's immune-suppressed conditions (like various cancers).[82]

Paramylon extracted from *Euglena gracilis*, a single cell flagellate eukaryote is stored as water-insoluble micrometer-sized spheroidal particles inside the euglenoid cells.[83] Shibakami *et. al.*[84] (2019) described the 4-fold benefits of the use of paramylon as sequestering agents that included their resistance (due to the linkage of glucose units by β-1,3-bonds) to enzymatic decomposition. After cationization, the solubility of paramylon is enhanced due to the random-coil conformation with hydrophobic interactions through the helical structures that facilitate the binding interactions with the analyte.[84]

In the study, different grades of HTAPs with varying the molar ratio of GTMAC were synthesized[85] and two cationic paramylons, namely HTAP1 (ZP = +59 mV) from naturally occurring paramylon and HTAP2 (ZP = +65 mV) from chemically defibrated paramylon HTAPs were examined. *In vivo* studies were conducted on the efficacy of HTAPs for weight reduction (and antidiabetic effects) of the high-fat diet-induced obese C57BL/6 J mice after a

5-week treatment with the high-fat diet (D12492) supplemented with 2% (w/w) powdered HTAPs.[84]

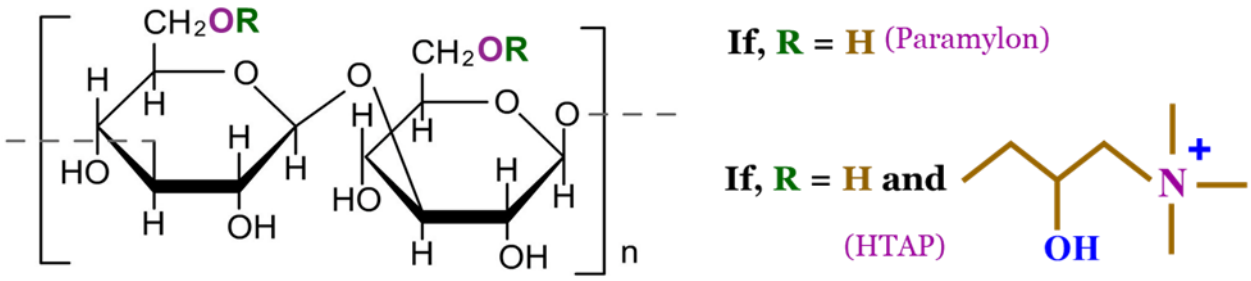


Figure 2.7: *Illustration showing the chemical structure of Paramylon. Here, if the R group is H, then it is paramylon. And if the R is H and/or glycidyl trimethylammonium chloride / (2,3-Epoxy-propyl) trimethylammonium chloride GTMAC/EPTMAC, then it is 2-hydroxy-3-(trimethylammonio) propyl paramylons (HTAPs).*

The *in vitro* BATs for the adsorbents with the mixture of all the BSs *i.e.*, NaC, NaDC, NaGC, and NaTC in PBS buffer (pH 6.8) showed selective adsorptions by the HTAP except for NaDC. As the pK_a of NaC, NaDC, NaGC, and NaTC were 5.2, 6.2, 3.8, and 1.9, respectively, the NaC, NaGC, and NaTC were present exclusively in the ionic form, while the NaDC was in both ionic and a nonionic form in the PBS solution during the experiments[84]. The pristine paramylon in its pristine state with no surface charges should not display any scavenging, except for a limited binding with the NaGC and NaTC due to non-electrostatic interactions between the adsorbent and the analytes. Tables 2.4 and 2.5 show the summary of their findings on the BS scavenging effect from BATs and TG reduction/weight change from the *in vivo* treatment on mice.

Table 2.4: Comparison in % of BSs bound to the adsorbent. BAT was conducted in PBS (pH 6.8) and an enzyme kit/UV-Vis was used to quantify the free BSs. Reproduced from.[84]

Adsorbents	Adsorbate (Bile Salts, BSs)[a]				
	BS mixture (%)	NaC (%)	NaDC (%)	NaGC (%)	NaTC (%)
HTAP1	43.1 ± 1.5	37.0 ± 2.1	83.0 ± 2.6	19.5 ± 1.5	41.3 ± 0.8
HTAP2	56.0 ± 0.8	51.9 ± 0.1	68.0 ± 1.1	36.4 ± 3.2	42.0 ± 0.6
Paramylon	~ 0	12.0 ± 1.6	~ 0	7.2 ± 3.3	16.4 ± 6.7
Cholestyramine	95.7 ± 0.6	96.4 ± 1.8	92.6 ± 1.7	92.2 ± 1.3	90.7 ± 1.2

[a]*Data are presented as means ± SE (n = 3/adsorbent)*

Table 2.5: Bodyweight change of high-fat diet-treated C57BL/6 J mice after a 5-week treatment. Adapted from[84].

Group	Bodyweight (g)		Bodyweight change (g)
	Initial	Final	
Cellulose	28.7 ± 0.7	37.3 ± 0.9	8.6 ± 0.6
HTAP1	27.1 ± 0.5	31.6 ± 0.6	4.5 ± 0.4
HTAP2	28.4 ± 1.2	33.2 ± 1.6	4.8 ± 0.5
Paramylon	28.5 ± 0.7	38.0 ± 1.0	9.5 ± 0.5

The HTAP mediated sequestration of BSs during the BATs shown in Table–6 is attributed to two major underlying interaction mechanisms: 1) ionic/electrostatic interactions between the cationic QAGs on the HTAPs particles and anionic moieties on BSs, 2) hydrophobic interactions between HTAPs hydrophobic skeleton and the steroid nucleus of

BSs.[84] The binding interactions were also affected based on the micellar sizest[84] of the BSs as the available hydroxyl groups which participated in the formation of H–bonds.

From the *in vivo* results, it was reported that HTAPs could be potential candidates in food additives to control weight gain. Here, cellulose, being structurally analogous to paramylon (β-1,4 linkage, whereas paramylon possesses β-1,3-bonds), was used as one of the negative controls. As shown in Table–7, the body weight changes in the HTAP-treated groups (gained weight ~17%) were reduced to ~50% of the cellulose-treated groups (gained weight ~30%) indicating that the β-1,3-bonds on the HTAPs were resistant to any *in vivo* enzymes and HTAPs retained their effects. In contrast, for paramylon without QAGs, no statistically significant effects on controlling the body weight gain were observed (gained weight ~33%).[84]

The plausible explanation for the weight gain by the HTAPs was postulated to be related to BS removal. The BSs as anionic exchange resins (AERs) have been reported to possess antidiabetic effects, where their efficacy for glycemic control was probably related to their efficiencies of sequestration of BSs and lipid micelles. Such alteration of the BSs' EHC induced by AER administration enhanced the release of glucagon-like peptide-1 (GLP-1), where the hormone that induced insulin secretion, from intestinal L cells.[86] Furthermore, the GLP-1 also reduces glucagon secretion, promotes satiety by delaying gastric emptying, and increases peripheral glucose disposal.[86] These multiple effects have resulted in the development of GLP-1 secretagogues, as well as the discovery of long-lasting agonists of the GLP-1 receptor for the treatment of type 2 diabetes.[84,86]

Recent studies concluded that the interruptions in the EHC of BSs caused by the AER administration increase the agonistic activities of TGR5 (Takeda-G protein-receptor-5), a

membrane-type bile salt receptor, and consequently the GLP-1 is then secreted by those activated TGR5.[87–89] The HTAP induced BS sequestration triggering the stimulation of GLP-1 release (secretagogues effect) subsequently promotes appetite suppression and leads to the control of the body weight gain.[84]

2.7.2 Functionalized Ulvans

Despite the many emerging environmental problems like “green tides” and “biofoulings”[90], the green macroalgae (*Ulva pertusa*, Chlorophyta) Ulva is considered a probiotic, an edible seaweeds with high dietary fibre and possessing several bio-PSs that are beneficial to human health.[91,92] The principal component of high growth Ulva is the soluble fibre ulvans, which are gelling sulphated polysaccharides with biological activities, such as immunoregulatory, cellular signalling modulators, anticoagulant, antibacterial antiviral, antioxidant, antihyperlipidemic and anticancer.[91–95] Like glycosaminoglycans (GAGs), these water-soluble cell walls’ polysaccharides, ulvan have a repeating disaccharide structure predominantly comprised of a uronic acid linked to a neutral sulphated sugar (illustrated in Figure 2.8). More precisely, ulvans are chemically composed of sulphated L-rhamnose, D-xylose, and uronic acids (D-glucuronic acid and its epimer L-iduronic acid),[91–93] and they have potential applications in biomaterial science (wound dressings, tissue engineering, biofilm prevention, and excipients), nutraceuticals (antiviral, antioxidant, antihyperlipidemic, anticancer and immunostimulatory), functional foods and agriculture.[91–95]

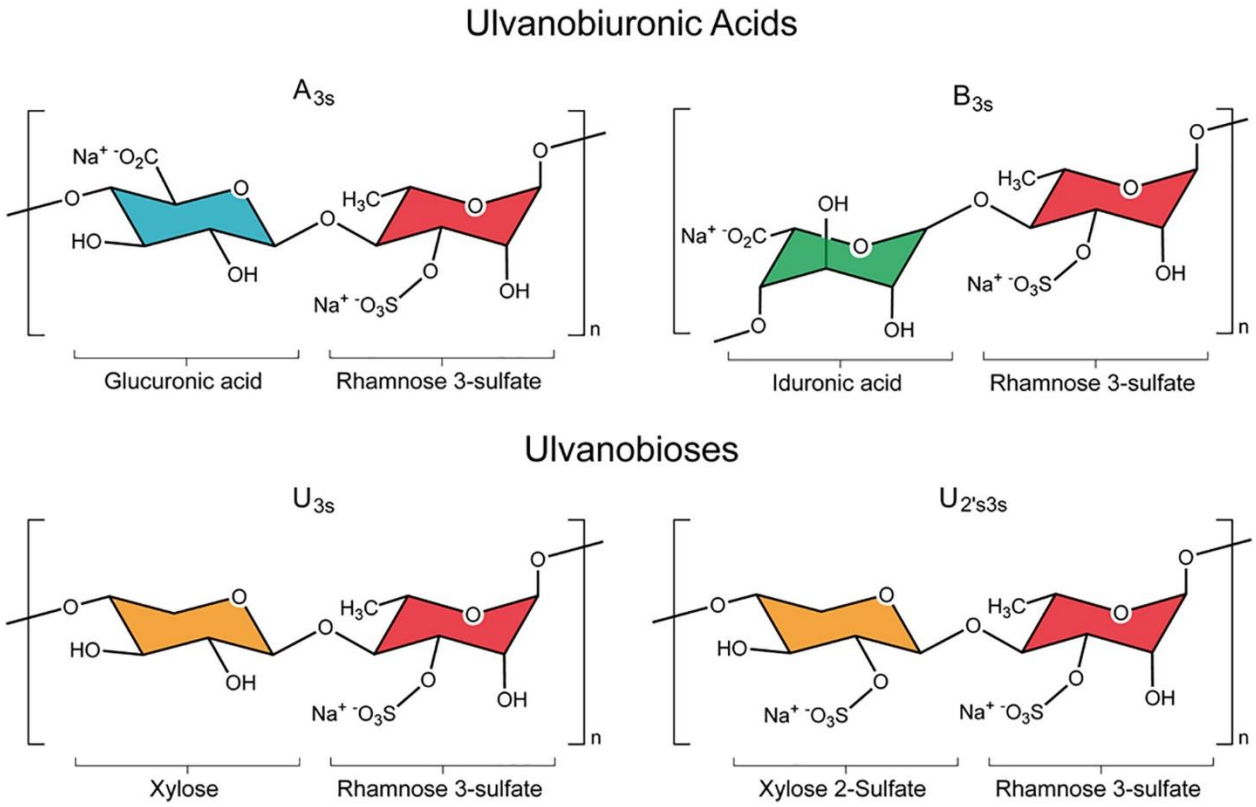


Figure 2.8 *Nomenclature and structure of the major repeating disaccharide units that comprise ulvan. Ulvanobiuronic acid A_{3s} contains glucuronic acid (blue) attached to rhamnose 3-sulphate (red), while the similar B_{3s} also contain rhamnose 3-sulphate but has iduronic acid (green) in the place of glucuronic acid. Ulvanobioses are comprised of rhamnose 3-sulphate attached to xylose (orange). Xylose can contain a sulphate group, as seen in $U_{2's,3s}$. Reused and adapted from.*[91,96]

Li *et. al.* (2020)[97] and Qi *et. al.* (2012)[98] reported the BSs sequestration mediated serum cholesterol reduction efficiencies of high sulphate (—OSO_3^-) content ulvans (HU) from *in vivo* studies in Kunming mice (male/female) models. The HU was synthesized using the sulfation agent, SO_3—DMF followed by the purification of the final product (HU) via regular dialysis. In the studies, 84 mice were fed with inositol nicotinate (positive control), ulvan (U,

negative control), chow-fed (normal control) and HUs at varying doses for 21 days, supplemented with water and feed. In the post-study periods, the mice were not fed for 12 h, and they were weighed and blood samples were collected from the eyeballs to obtain a complete lipid profile through enzymatic detections with the results summarized in Table 2.6.[97]

Table 2.6: Effects of U, HU, and inositol nicotinate (commercially available standard antihyperlipidemic drug) on serum lipid profiles (HDL-C is not shown here) in mice supplemented with a cholesterol-rich diet (composition: 2.0% cholesterol, 8.0% lard, 0.3% sodium cholate and 89.7% commercial chow). Adapted form.[97]

Animal study group	Dose (mg/kg)	TC (mmol/L)	TG (mmol/L)	LDL-C (mmol/L)
Normal control	–	2.47 ± 0.41	0.66 ± 0.08	0.64 ± 0.11
Hyperlipidemia	–	3.75 ± 0.17	0.93 ± 0.15	0.95 ± 0.23
Ulvan (U)	250	3.29 ± 0.49	0.83 ± 0.13	0.77 ± 0.15
HU (low dose)	125	2.75 ± 0.42	0.75 ± 0.20	0.64 ± 0.10
HU (middle dose)	250	3.07 ± 0.55	0.66 ± 0.25	0.69 ± 0.21
HU (high dose)	500	3.22 ± 0.31	0.87 ± 0.12	0.66 ± 0.13
Inositol nicotinate	500	3.33 ± 0.57	0.85 ± 0.10	0.74 ± 0.33

Li *et. al.* (2020)[97] observed that the mean body weight was reduced by 15.2% for the HU (250 mg/kg dose) treatment group, compared with the hyperlipidemia group. In terms of lipid profile, they found the HU-fed group (250 mg/kg) had an optimal effect on TG reduction (29.0%) compared to the hyperlipidemic group, but a lesser impact on LDL-C. Interestingly the antihyperlipidemic activity of HU at the dose of 125 mg/kg was found to be the strongest,

compared to the hyperlipidemic group, the TC and LDL-C concentrations were significantly decreased by 26.7% and 32.6% respectively.

Similar efficacies for the HU on overall lipid profiles were also reported in a study conducted by Qi *et. al.* (2012).[98] They concluded the antihyperlipidemic activity of HU at a dose of 250 mg/kg was the strongest, compared to the U-fed group, TG and LDL-C concentrations were significantly decreased 28.1% and 28.4%, respectively. Both findings confirmed that the antihyperlipidemic activity was not concentration-dependent for HU-fed mice.[97,98] In another study conducted by Qi *et. al.* (2012),[99] the authors synthesized acetylated ulvan (AU) with acetic anhydride in N, N-dimethylacetamide and investigated the effects of AU on the serum lipid profile through animal studies. Although there was no harmful effect observed in the net weight gain on the subjects (Kunming mice), the antihyperlipidemic activity of AU at the dose of 125 mg/kg was the strongest compared to the U-fed group, TG and LDL-C concentrations were significantly decreased by 25.3% and 20.6% respectively.[99]

2.7.3 Polysaccharides from sea cucumber, *Apostichopus japonicus* (AJP)

Liu *et. al.* (2012)[100] reported *in vivo* antihyperlipidemic activities (on Male Wistar strain rats) of polysaccharides from sea cucumber, *Apostichopus japonicus* (designated as AJP), which was mainly composed of glucosamine, galactosamine, glucuronic acid, mannose, glucose, galactose and fucose, with an average molecular weight of about 36.2 kDa. The disruption of the EHC of the BS pool led to enhanced catabolism of the serum cholesterol, where AJP at a dose of 400 mg/kg could significantly reduce the serum total cholesterol (TC),

triglyceride (TG) and low-density lipoprotein (LDL-C) by 17.23%, 20.78% and 31.18%, respectively compared to hyperlipidemic groups.[100]

2.7.4 Amino-bio-PS based BASs: Chitosan and Chitin/derivatives

A myriad of applications has been reported for chitosan and chitin-based NMs.[101–105] Recently, Xu *et.al.* (2020)[106] studied the *in vitro* bile acid sequestration resulting in the reduction of cholesterol for the BASs like chitin, chitosan and chitooligosaccharides (COS) extracted from lobster shells. They designed the BA binding study using sodium cholate (SC), sodium chenodeoxycholate (SCDC), sodium deoxycholate (SDC), and conjugated bile acid, sodium taurocholate (STC) where both their BASs's samples and BA's solutions were prepared in phosphate buffer (pH 7.0). The quantification of the post adsorption samples was conducted using the BQ Total Bile Acid Colorimetric Assay Kit followed by the absorbance at 540 nm through UV-Vis.[106] Although the authors did not report the max adsorption capacity for their BASs (Chitin, Chitosan and COS), they denoted the percent adsorption capacity of their BASs at three different concentrations, where COS was found to be the most effective BASs among the three, showing approximately 50% adsorption at 50 mg/mL for the dihydroxy BA, the SDC. The more efficacious binding of the COS was due to the aqueous solubility (phosphate buffer) of the COSs leading to enhanced viscosity, the indirect force of which was believed to be the underlying reason for the binding with Bas in addition to electrostatic interactions.[106] The chitosan and chitin were found to be insoluble or poorly dispersed in the phosphate buffer's neutral pH. For the *in vitro* adsorption test, the hydrophobic chitin (50

mg/mL) displayed better binding with BAs due to the hydrophobic interactions leading to the aggregation of BAs/BSs on the surfaces.[106]

From the above discussion, it is evident that the bio–PS based compounds have the capabilities to be considered for application in cholesterol reduction and hampering or reducing diet-induced obesity (DIO). And to the best of my knowledge no other literature, short communications or book chapters have reported on cellulose or nanocellulose (NC) – based (either CNFs or CNCs) or their derivatives or any other amino-bio–PS (other than chitosan and chitin) for use as either BAS or reducing LDL–C/body weight gain. CNCs (also known as nano-whiskers, CNWs), or other bio–PS based NPs systems for this BS scavenging applications leading to cholesterol reduction are fairly recent, and it is expected that more publications on these bio–PS materials will appear in the future. In a few of the literature, some other bio–PS based compounds like the dextran, alginates, dietary fibers, cyclodextrins, polyphenols, several hydrogels, etc. were reported to have efficacies in improving the total cholesterol profile, reducing the LDL–C level, and decreasing the body weight or stopping the weight gain (DIO) after feeding a heavy fat diet during the treatment period of conducted experiments. To discuss all the bio–PS based systems for such application is beyond the scope of this doctoral thesis and thus, readers are encouraged to navigate corresponding literature for gathering knowledge on their topics of interest.

Chapter 3: Cellulose nanocrystals (CNCs) based BAS

3.1 Introduction

Cellulose is a long-chain, high molecular weight polysaccharide (an isotactic homopolymer) composed of repeating units of dimers or disaccharides of anhydro-D-glucopyranose unit (AGU), known as cellobiose, where each anhydro-D-glucopyranose unit is connected by a β-1,4 glycosidic linkage and every other monomer is rotated 180^0 with respect to its neighboring unit,[74] as shown in Figure 3.1 (A). Regardless of its source, each cellulose chain is chemically asymmetric as one terminus has a reducing functionality, and the other end is non-reducing.[74,107]

Cellulose microfibrils are the structural units in higher plants formed by a biogenetic bottom-up process leading to the formation of cellulose fibres to produce hierarchical systems [Figure 3.1 (B)]. These microfibrils contain highly ordered (crystalline) domains alternating with disordered (amorphous or para-crystalline) regions. These crystalline domains can be separated and extracted from a cellulosic source through a "top-down" deconstruction process by mechanical, chemical or combination of mechanical, chemical and/or enzymatic (endoglucanases for example) treatments, yielding cellulose nanocrystals (CNCs).[74,107–109] In literature, a wide range of terminologies has been used to categorize cellulose nanocrystals, such as nanocrystalline cellulose (NCC), cellulose nanocrystal (CNC), cellulose nanowhisker (CNW), bacterial cellulose and/or bacterial nanocellulose (BNC) etc.[74,110] Throughout the thesis, the CNC and CNW is used interchangeably. In most of the cases, the base material is the anionic CNC supplied by CelluForce, Canada with a tradename of NCC™. Since one of

the major goals of this Ph.D. research is to prepare highly cationic NP systems, thus the removal of most of the surface sulphate half ester ($–OSO_3^-$) groups is a desirable outcome in the development of the desired nanoparticles. Without desulfation, the net cationic charge densities for the NP synthesized from NCC^{TM} would be lower and reduce the performance to bind and remove BS.

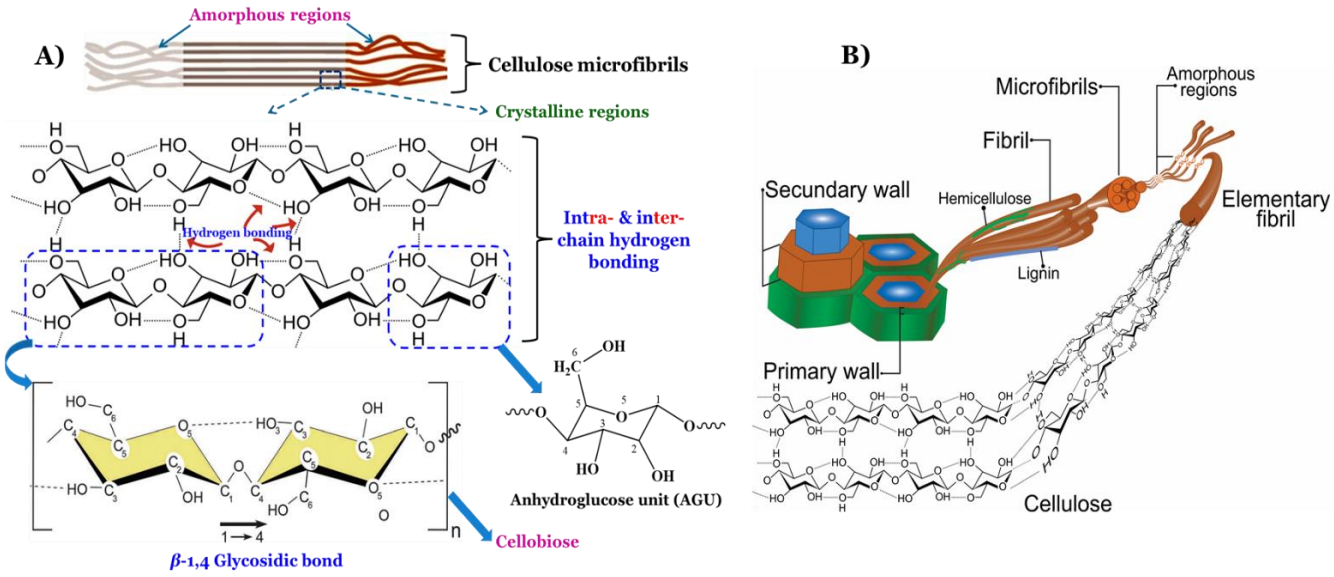


Figure 3.1: A) *Illustration of cellulose showing the intra and inter-chain H-Bonding for the individual microfibril and the molecular representation of β1,4 glycosidic linkages between the AGU units.* ***B)*** *Hierarchical structure of cell walls from which the elementary fibrils and the CNC can be obtained. Drawn from.*[111]

3.2 CNC Extraction and notable properties

In the extraction of CNC, the most widely employed process involves acid hydrolysis, where concentrated sulfuric acid (H_2SO_4) and hydrochloric acid are commonly used.[74,112] Due to such treatment, the disordered or para-crystalline regions of cellulose are disrupted by the

cleavage of accessible glycosidic linkages, whereas crystalline regions (the characteristic rod-shaped nanocrystals) that are more resistant to acid treatment are preserved. Sulfuric acid (H_2SO_4) hydrolysis imparts abundant anionic sulfate half ester (SHE) groups (—OSO_3^-) onto the CNC surface that induces electrostatic repulsion of CNC particles in aqueous solution.[74] Hydrochloric acid (HCl) hydrolysis introduces minimal surface charge while preserving a larger quantity of reactive primary hydroxyl groups[113–115] that enhance the grafting of small molecules onto the CNCs allowing for a wide array of chemical modifications. For this reason, several batches of CNCs were from the commercially available microcrystalline cellulose (MCC) via HCl-mediated hydrolysis.

CNCs have received unprecedented attention in the materials science community due to their unique properties, namely the S.M.A.R.T.© properties which are sustainable, modifiable, active, renewable, and natural/non-toxic. Other than this, these NPs also possess high specific surface area, high aspect ratio, high crystalline order and chirality, superior mechanical strength, and controllable surface chemistry.[74] The dimensions of CNCs typically range from 2−50 nm in width and 100−2000 nm in length. Owing to their nano-size and low density, CNCs have a large surface area of 150–250 m^2/g. They possess excellent mechanical properties, where the axial elastic modulus (Young's modulus) of native CNCs ranges from 110–220 GPa, and the tensile strength range from 7.5−7.7 GPa, which is comparable, and within the range of other reinforcement nanomaterials, such as carbon nanotube (CNT).[74]

3.3 Development of cationic CNC

From the structure at a molecular level, it is evident that each AGU of a cellulose chain contains three hydroxyl groups which can be categorized into two chemical classes namely primary and secondary alcoholic groups.[74] In most instances, the hydroxyl groups at the C2 and C3 positions behave as secondary alcohols while the hydroxyl group in the C6 position acts as primary alcohol. Although, the relative reactivity of the hydroxyl groups has the following order[116]: (C6)–OH >> (C2)–OH > (C3)–OH, most of the modification predominantly occurs at the (C6)–OH.[74] Thus, the grafting of QAGs will mainly occur at the C–6 position of —CH_2OH to yield an ether linkage. As the NCC^{TM} was desulfated through alkaline and acid-mediated hydrolysis to produced more 1^0 alcoholic groups, where the grafting ratio of the cationic groups would be increased. Additionally, to compare the efficiencies of the final products, the CNCs were also extracted from MCC[117,118] via HCl-mediated hydrolysis so that the —CH_2OH groups protruded from the surface of the extracted CNCs could be utilized for the grafting of QAGs.

3.4 Materials and Methods

3.4.1 Materials

Spray-dried cellulose nanocrystals (NCC^{TM}) extracted from wood pulp (via sulphuric acid hydrolysis method) with an average charge density and molecular weight (MW) of 0.26 mmol/g and 4460 kDa was provided by CelluForce Inc., Canada. All the reagents, & chemicals, such as microcrystalline cellulose (MCC, cellulose powder, 20 μ), glycidyl-

trimethylammonium chloride/ (2,3-epoxypropyl) trimethylammonium chloride (GTMAC/EPTMAC, MW = 161.6 g/mol, d = 1.13 g/mL), Tetrabutylammonium hydroxide 30-hydrate (TBAH, MW = 799.93), DOWEX® Marathon™ C ion exchange resin beads (diameter = 550 µm), were purchased from Sigma-Aldrich (MilliporeSigma) unless otherwise stated and were used as received without any further purification. HPLC grades of the solvents, like dimethyl sulfoxide, DMSO (boiling point, b.p.= 189^0C), tetrahydrofuran (THF, b.p. = 66^0C), 2–Propanol or isopropyl alcohol (IPA, b.p. = 82.5^0C), ethanol (EtOH, 78.4^0C), methanol (MeOH, b.p. = 64.7^0C), acetic acid (AcOH, b.p. = 118^0C) etc. were also purchased from the MilliporeSigma and were used as received without any further purification. The fine (150 µm) nylon fabric filter (mesh# 100) was purchased from a commercial vendor. Purified water (Milli-Q water) from a Millipore system (>18 MΩcm) was used to prepare the samples. Hydrochloric acid (HCl 1M) solution and sodium hydroxide (NaOH 1M) solution were diluted from freshly prepared standard solutions (highly concentrated) and were used for pH adjustments where applicable.

3.4.2 Desulfation of NCC™

As discussed earlier, the majority of the surface primary (1^0) alcoholic groups on C6 protruding from the CNC rods are occupied by sulphate half-esters ($–OSO_3^-$) groups (reported[119] S contents = 0.86 %, w/w), and thus are strongly negatively charged (reported[43] zeta potential value was –39 mV, laboratory data in 1 mM KCl provide a range of –48 mV to –58 mV). For the desulfation of NCC™, alkali or acid-catalyzed hydrolysis are commonly used. It has been reported that the removal of surface sulfate half-ester (SHE) groups ($–OSO_3^-$

groups) via desulfation using high concentrations of the alkali or acid may degrade or depolymerize[120] the CNC and destroy the integrity of the pristine rod shapes. Although the alkali catalyzed desulfation is most widely used, the use of concentrated alkali may result in the 3:6- and 2:3-anhydride structure of the CNC.[121] Thus, this thesis focuses on the preparation of different degrees of desulfated CNCs (DS-CNCs) using different strengths of NaOH and only one grade of DS-CNC via HCl-mediated hydrolysis. Furthermore, another grade of CNC, i.e., almost neutrally charged CNC was produced by extraction from the MCC via HCl mediated hydrolysis (illustrated in Figure 3.2).

For alkaline desulfation, the existing surface SHE ($–OSO_3^-$) groups of the NCC^{TM} were removed using a modified procedure described in the literature.[122,121] Briefly, 4 g of CNC was added to 100 mL MQ water (4% CNC dispersion, w/v) and the mixture was dispersed for 5 min at 15,000 rpm using a homogenizer, then sonicated for 10 minutes. About 250 mL of the dispersion was added to a 1000 mL round bottom flask (RBF). The gradient desulfation was achieved by varying the NaOH concentrations. 70 mL of freshly prepared concentrated NaOH was added slowly with stirring (1000 rpm @the hotplate or using a motorized mixer of two-blade propeller) for each gram of NCC^{TM} kept in the RBF, with the concentration of NaOH kept at 3 M, 4 M, 5 M, and 6 M in the RBF. Each of the graded desulfation reactions/batches was allowed to react for 5 hours at 65^0C under stirring at ≥ 1000 rpm. During the reaction, the mixture turned slightly yellowish (illustrated in Figure 3.2), and this phenomenon occurred much faster at the highest concentration of the NaOH (the 6M mixture).

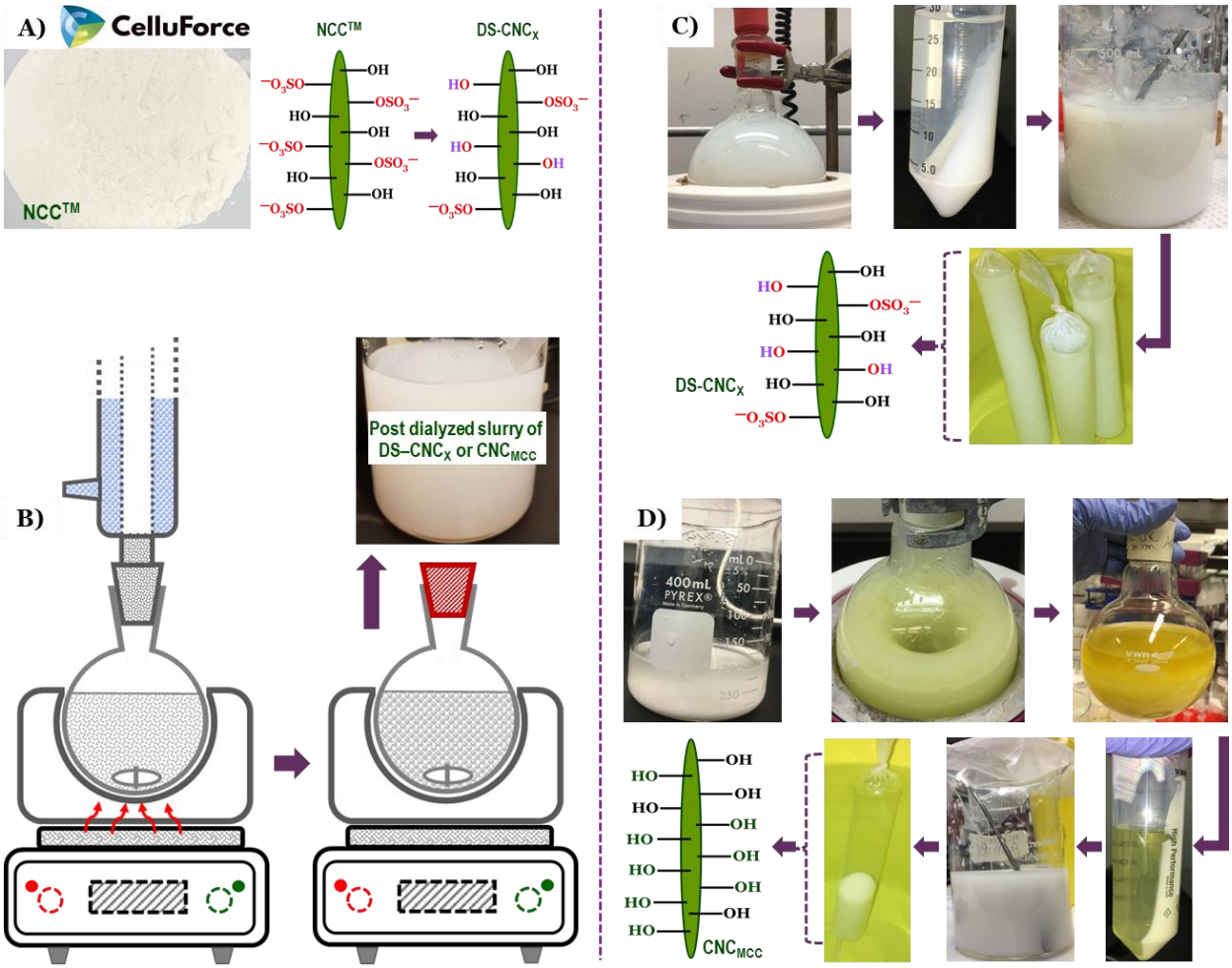


Figure 3.2: A) *NCC™ supplied from CelluForce, Canada, and the desulfation reaction scheme. After the surface desulfation, the primary alcoholic (1^0) groups may get converted to alkoxy-sodium form after alkali-mediated desulfation (if HCl is not used for NaOH neutralization).* ***B)*** *Schematic representation showing the reaction set up for the desulfation of NCC™ or extraction of CNC (the CNCmcc or CNC_{MCC}) from MCC.* ***C)*** *Schematic of the desulfation reaction setup. After the reaction, the colour changed, and bigger lumps of precipitates were observed.* ***D)*** *Extractions steps of CNC from MCC (20 μ powder) during which a more pronounced colour change was observed. During dialysis, the extracted CNC_{MCC} was found a bit unstable in aqueous dispersion and settle at the bottom within a few hours.*

As the desulfation was progressing, the partially desulfated cellulose nanoparticles in the suspension began to aggregate due to the induced interparticle attraction (Van der Waals force or hydrogen bonding) resulting from the removal of surface $–OSO_3^-$ groups. Similarly, for the HCl mediated hydrolysis, the same process was adopted but at a higher temperature of 80^0C, and the concentration of the HCl was kept at 6 M. Based on the reaction conditions, the produced DS–CNCs were designated as DS–CNCx, where 'x' refers to the strength of NaOH. Likewise, the CNC_{MCC} or the CNCmcc indicates the CNC extracted from the MCC in 6 M of HCl.

Now for the alkaline desulfation, after 5 hours, each reaction was stopped by adding an appropriate amount of concentrated HCl (37%, w/v) to neutralize the NaOH in the dispersion. And placing the round bottom flask in an ice bath was done for quenching the desulfation reaction[123,124] and for the rapid cooling to room temperature. The neutralization step using concentrated acid was also expected to convert the remaining surface sulfate groups in the sodium form of the partially desulfated CNCs (DS–CNC) to their protonated forms.[125] At room temperature, the reaction mixture was diluted with a large excess of Milli Q water and centrifuged at 10,000 rpm at 4^0C[126] for 10 min. The supernatant was discarded after centrifugation and the DS–CNC sediment was re-dispersed in Milli Q water. The redispersed suspension was dialyzed (molecular weight cut off, MWCO 12–14 kDa) against deionized water for 7 days, with continual water change until the effluent remained at neutral pH. The partially desulfated CNC was then concentrated by centrifugation and the sediment was redispersed in a small amount of M.Q. water for storage. A small portion of the DS–CNC powder was prepared by freeze-drying using a FreeZone 2.5L ($–50^0$C collector) benchtop

freeze dryer (Labconco, Kansas City, MO) for FTIR analyses, and overall, the yield was within 75–90% determined by gravimetric analyses (GA).

We encountered difficulties in redispersing the freeze–dried DS–CNCs due to very strong particle–particle[127–129] cohesion (the cohesion conforms to the DLVO theory[130,131]), especially the DS-CNC_6 powder obtained from a pilot batch. Thus, all subsequent batches of DS–CNCs (by alkaline/acidic hydrolysis) and the CNCmcc were kept as never-dried suspensions and stored in the fridge (4 – 8^0C) for the future ready-to-use condition while recording their individual concentrations of the suspensions through the GA.

3.4.3 Grafting of GTMAC onto CNCs

The quaternization of DS–CNCx, CNCmcc (also designated as CNC_{MCC} throughout the thesis) and NCC™ samples were conducted using the modified procedure reported previously.[132–134] The grafting of GTMAC onto the surface of DS–CNC_x or CNCmcc/NCC™ is an etherification process based on the nucleophilic substitution reaction (S_N2) reaction[119] where the grafting occurred at the primary alcoholic groups (—CH_2OH) protruding from the surfaces of the NPs.[119] When quaternization with GTMAC was performed in an alkaline solution, the epoxy ring would be hydrolyzed to yield non-reactive species, 2,3-dihydroxy-propyl-trimethylammonium chloride via an undesirable side reaction.[134] To avoid this side reaction, quaternization was conducted in organic or polar solvents, such as DMSO[135] (b.p. 189^0C), isopropyl alcohol[136] (IPA, an alcohol; b.p. 82.5^0C), and tetrahydrofuran[136] (THF, a cyclic ether; b.p. 66^0C) instead of water, either with TBAH (dissolved in a minimum

stoichiometric amount of M.Q. water) or with NaOH as the catalyst to activate the surface hydroxyl groups facilitating the S_N2 reactions.[119]

In a typical procedure, an equivalent volume of 0.6 g of the CNC aq. dispersion (kept in a fridge) was dispensed into an RBF and the solvent exchange with DMSO was performed via the Heidolph™ Hei-Vap™ rotary evaporator. For IPA & THF (b.p. < b.p. of water), the CNC aq. dispersions were concentrated by the rotavap and then individual solvents were added to the almost dry CNC mass, dispersing the mixture using the Ultraturrax T25 homogenizer (IKA, Germany) at 15000 rpm for 5 minutes at 25^0C. Following the same procedure as described for DMSO, the quaternization reactions were performed, purified, stored, and the yield% determined via gravimetric analysis (GA).

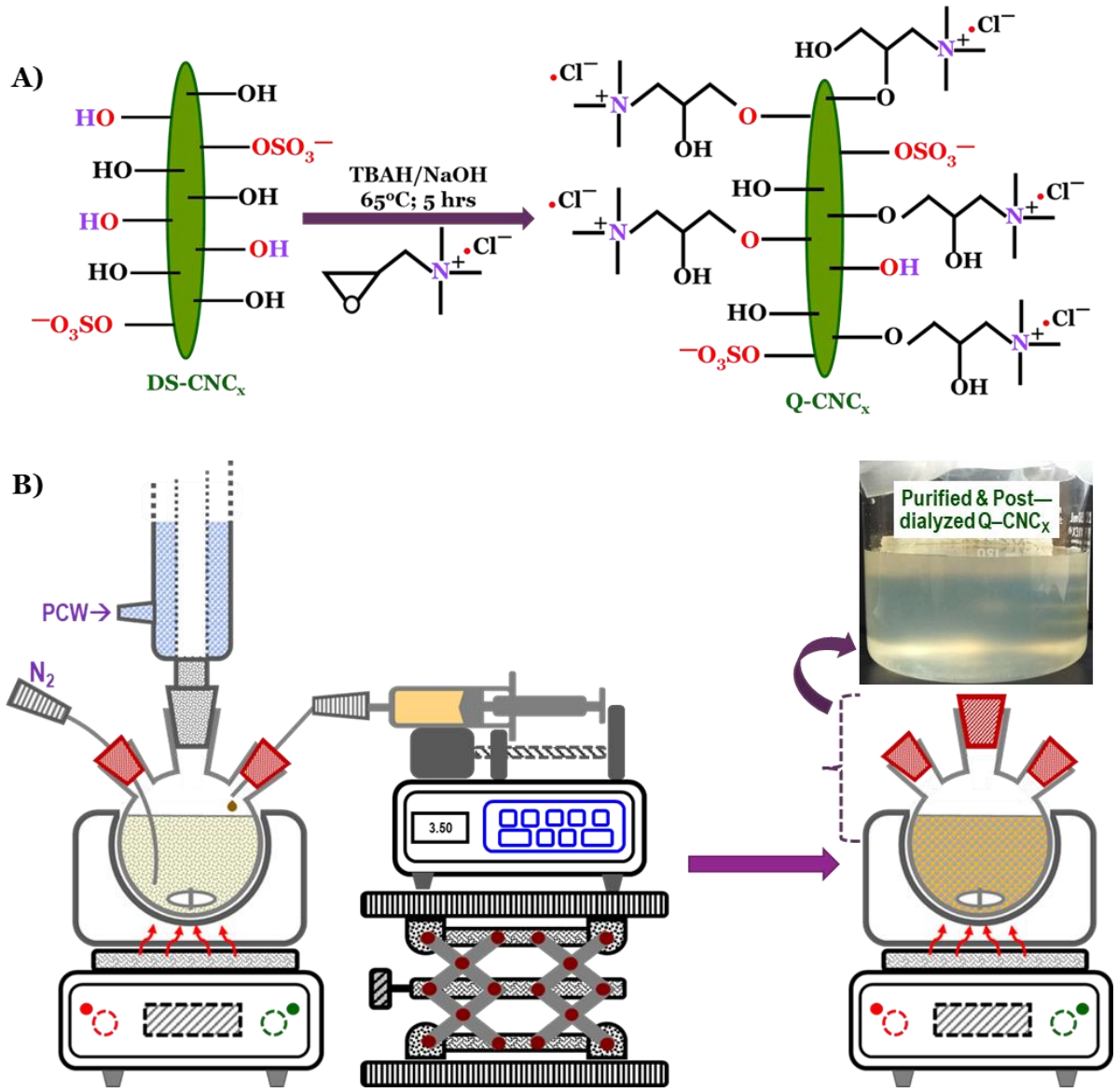


Figure 3.3: A) *Schematic showing the quaternization reaction for the CNC systems with GTMAC, added dropwise. Such reactions are S_N2 etherification reactions and if not done in organic media, then the degree of quaternization, DQ and the yield % get drastically low due to the occurrence of undesired side reactions. And the obtained Q–CNCs from the NCC^{TM}, DS–CNCs or CNC_{MCC} were structurally considered as Zwitterionic of different degrees, where NCC^{TM} leading Q–CNC was the most Zwitterionic and the CNC_{MCC} leading Q–CNC was the least Zwitterionic.* ***B)*** *Schematic of the quaternization reaction setup. After the reaction was completed, the colour of the mixture was found to be a bit darker yellowish in DMSO media.*

After 30 minutes, while the degassing was progressing, the heat was increased to 65^0C, and an equivalent volume of GTMAC solution (for CNC : GTMAC = 1 : 10 ratio) was added dropwise using a syringe pump and the mixture was allowed to react for 5 hours. The reaction mixture turned brownish at 5 hours and an unpleasant sardine odour was reported due to the reduction of DMSO to dimethyl sulphide (DMS)[135]. The reaction was then quenched by placing the reaction vessel in an ice bath[123,124]. Once at room temperature, the mixture was dialyzed (MWCO 12–14 KDa) against deionized water for 7 days (illustrated in Figure 3.3) with continual water change and the post dialyzed collected quaternized CNCs, Q-CNCs (chemically known as hydroxypropyl propyl-trimethyl-ammonium Chloride-CNC, HPTMAC-CNC) were stored as the never dried samples in the fridge for future use. A very small portion of the Q–CNCs were dried for FTIR characterization.

As mentioned earlier, a similar procedure was followed for the quaternization reaction conducted in IPA and THF[136]. For catalyst, where TBAH was not used, a few drops of conc. NaOH solution (15 M) was used, and the pH of the solution was adjusted to ≥ 13 to activate the surface primary alcoholic groups, —CH_2OH. By the dropwise addition of GTMAC, the reactions were then conducted similarly as mentioned above. Like the DS–CNCs, a similar pattern of nomenclature was used for these cationic CNCs, by replacing the pre-fix with Q– (meaning quaternized).

Table 3.1: Reaction parameters for the desulfation of NCC™, extracting CNC from MCC and quaternization of CNCs with GTMAC to prepare Q–CNCs.

NPs	Time (hrs.)	Temperature (T^0C)	Reagent Used	Reaction media
DS-CNC_3	5	65	3 M NaOH	MQ
DS-CNC_4	5	65	4 M NaOH	MQ
DS-CNC_5	5	65	5 M NaOH	MQ
DS-CNC_6	5	65	6 M NaOH	MQ
DS-CNC_a	4	85	6 M HCl	MQ
CNC_{MCC}	4	85	6 M HCl	MQ
Q-NCC™	5	65	TBAH; GTMAC (1:8)	DMSO : MQ = 90 : 10
Q-CNC_3	5	65	TBAH; GTMAC (1:8)	DMSO : MQ = 90 : 10
Q-CNC_4	5	65	TBAH; GTMAC (1:8)	DMSO : MQ = 90 : 10
Q-CNC_5	5	65	TBAH; GTMAC (1:8)	DMSO : MQ = 90 : 10
Q-CNC_6	5	65	TBAH; GTMAC (1:8)	DMSO : MQ = 90 : 10
Q-CNC_a	5	65	NaOH; GTMAC (1:10)	DMSO : MQ = 90 : 10
Q-CNC_{aa}	**8 — 10**	65	NaOH; GTMAC (1:10)	IPA : MQ = 80 : 20
Q-CNC_{ae}	**14**	**55**	NaOH; GTMAC (1:10)	THF : MQ = 80 : 20
Q-CNC_{MCC}	5	65	NaOH; GTMAC (1:10)	DMSO : MQ = 90 : 10

3.4.4 FTIR Characterization of DS–CNCs and Q–CNCs

The Fourier Transform Infrared Spectroscopy, FTIR was used to confirm the presence of the functionalities on CNC after the modification of NCC™. Test pellets were prepared by grinding and compressing approximately 2% of the freeze-dried samples in KBr, and the measurements were conducted using a Tensor 27 BRUKER machine at a resolution of 4 cm^{-1}, with a scan time of 32 s, from 4000 to 400 cm^{-1}. The FTIR spectra were acquired and analyzed using the OPUS software.

3.4.5 Elemental Analysis of DS–CNCs

The sulfur (S) content (in %) of NCC™ and DS-CNC samples were determined using a 4010 Elemental Analyzer (Costech Instruments) coupled to an Isochrom (Micromass UK) continuous flow isotope ratio mass spectrometer (CFIRMS). The SHE contents (—OSO_3^-) were then calculated from these measurements.

3.4.6 Potentiometric/Conductometric titration of DS–CNCs

Potentiometric titration was performed using a Metrohm 809 Titrando Autotitrator System equipped with a water bath to control the temperature. The titrator was controlled by the Tiamo software that dosed µL of titrants in each injection/dosing. Measurements were performed in triplicate in a closed jacketed vessel at 25ºC while stirring at a medium rate of 4 rpm. The conductivity was measured using a conductivity electrode.

The surface sulfate half ester, SHE (—OSO_3^-) content was also measured through conductometric titration with the freshly prepared and standardized NaOH.[43,137] The titration was performed as outlined by Beck *et. al.*[138] Before the titration, the CNC samples were treated with Dowex® Marathon™ C, hydrogen form (DM–C), a strong cation exchange resin, to convert the SHE groups from the **sodium** form (—OSO_3**Na**) to the **protonated** form (—OSO_3**H**). The conductometric titration indirectly measures sulfate groups by assuming a 1:1 ratio of H^+ ions to sulfate half esters, therefore, the ion exchange is a critical step.[138] In a typical procedure, the DM-C ion exchange resins were thoroughly washed with ethanol until the filtrate became colourless and it was dried under vacuum. A 1.0 to 1.5%(w/v) CNC suspension was mixed with DM-C (12 g DM-C/g dry CNC) in a sealed glass vessel, gently stirred and left

for 30 minutes. The resins were removed via filtration through a GF/F grade (0.7 µm pore size) glass microfiber filter. This treatment process was repeated a total of six times (6x) to ensure complete ion exchange with fresh DM-C,[138] as illustrated in the Figure–3.4.

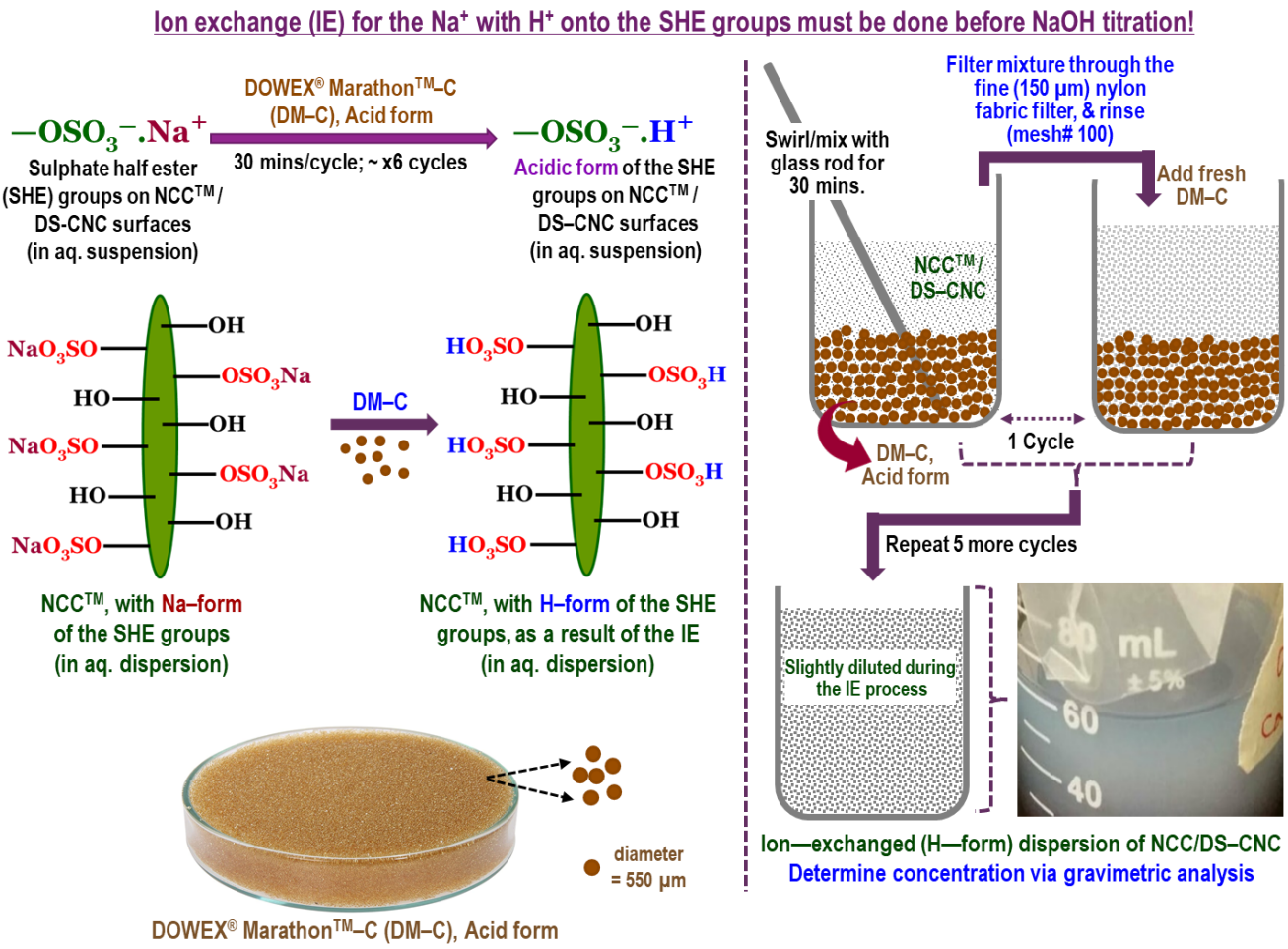


Figure 3.4: *Ion exchange steps for the conversion of **Na**–form of sulfate half ester, SHE (—OSO_3**Na**) groups to acidic forms of the SHE (—OSO_3**H**) groups done by the cation–exchange resin, Dowex® Marathon™ C, hydrogen form (DM–C). Literature suggested conducting multiple cycles of ion–exchange can ensure complete exchange of the targeted ion onto the surfaces of the nanoparticles (NPs). During the exchange process, the known starting concentration (conc.) of the dispersion gets diluted due to rinsing the beads with MQ water each cycle, and the final conc. can be determined through gravimetric analysis (GA).*

Following ion exchange, the titrations were performed using the Metrohm 809 Titrando Autotitrator by diluting a sample containing 150 mg of dried DM-C treated CNC to 80 mL and adding 0.8 mL of a 0.1 M NaCl solution to raise the conductivity to a measurable level. Additionally, the pH of the suspension was adjusted to ~ 3 – 4 with a few drops of 37% (w/w) HCl, and 1 to 10 mM standardized NaOH solution was used in the titration to determine the sulfate content. The NaOH solution was added in aliquots of 100 μL over 20 to 60 minutes, and the conductivity and pH were continuously measured throughout the titration. The conductivity was corrected for dilution effects and plotted against the volume of NaOH. From this plot, the equivalence point was determined from the interception of the linear regression of the two linear sections of the graph. For precise and accurate reading during titration, it was important to use a fresh NaOH solution and to standardize it against the primary standard potassium hydrogen phthalate (KHP) immediately before titrating the sample. The pH meter was also calibrated with fresh pH standards before standardizing the NaOH.

3.4.7 Potentiometric/Conductometric titration of Q–CNCs

Conductometric titrations with $AgNO_3$ were performed to determine the quaternary ammonium content of the quaternized CNC samples. In a typical procedure, a 60 mL of Q–CNC aqueous suspension was prepared at various concentrations of between 2 – 6 mg/mL from the concentrated stock solution stored in the fridge. 30 mL of the prepared suspension was added to the conical double jacketed vessel and the content was gently stirred during the titration. A 1 to 10 mM solution of $AgNO_3$, depending on the degree of cationization was used to titrate the chloride counter ions of the quaternary ammonium groups. The titration was

performed using a Metrohm 809 Titrando Autotitrator and 50 μL aliquots were added every 30 seconds until two clear linear sections were visible in the Conductivity–$AgNO_3$ volume plot. The plot was corrected for dilution effects[139] and the equivalence point was determined from the interception of the linear regressions of the two linear sections of the graph. The quaternary ammonium contents and degrees of substitution were calculated.

3.4.8 Aggregates sizes (D_H) and zeta potentials (ZP) of NPs

The zeta potential (ζ-potential) of a particle can be calculated from[140] $\zeta = \frac{3\eta\mu}{2\varepsilon f(ka)}$, where ζ is the zeta potential (mV), η is the viscosity of the solvent, μ is the electrophoretic mobility, ε is the dielectric constant of sample and *f* (*ka*) is Henry's function. Henry's function is a function of k, the inverse of the Debye length (thickness of the electric double layer) and the particle radius (a). Therefore, (ka) is the ratio of the particle radius to the electric double layer. When the electric double layer is thin (ka>1), Smoluchowski approximation[140] is used and Henry's function has a value of 1.5, thus simplifying the equation to $\zeta = \frac{\eta\mu}{\varepsilon}$. The point where the zeta potential is zero is known as the isoelectric point (IEP), where the colloidal system is the most unstable. However, a zeta potential value of between –20 to 20 mV is generally considered unstable and aggregation has often been reported.[140]

In this study, both the size (hydrodynamic diameter, D_H, in nm) and zeta-potential (ZP, in mV) analyses were performed using a Malvern Nano-ZS90 zetasizer. The measurements were done with 0.1%, 0.05%, and 0.01% (w/v) of appropriate samples of pH ranging from 2 to 10 (where applicable) at 25^0C and the reported results were the average of three

measurements for DLS and 10 repeated measurements for zeta potential. A minimum of 700 μL sample was loaded into the DTS 1070 folded capillary cells/cuvette to measure the ζ-potentials, and the Zetasizer software of version 7.13 was used to control the instrument. The size measurements of NPs were measured by dynamic light scattering (DLS, where $\theta = 173°$). Regular disposable polystyrene (PS) cuvettes, DTS0012 were used for the D_H measurements of the NPs, unless otherwise mentioned elsewhere for a specific cuvette.

3.4.9 Transmission electron microscope (TEM) images of NPs

TEM images were obtained using a Philips CM10 electron microscopy with an acceleration voltage of 60 keV. In preparing the samples for TEM characterization, the re-dispersed (after sufficient dilution) aqueous dispersions (0.001– 0.01 wt.%, depending on the NP systems), were sprayed (through a lab-made venturi tube for spraying) or pipetted drop(s) onto FCF#200-copper grids (FCF#200, Formvar/Carbon Film which has 200 mesh/grid), and allowing them to dry at ambient temperature overnight before imaging. Samples with hard-to-find good resolution images were stained by either $FeCl_3$ or lead citrate (trilead dicitrate, $C_{12}H_{10}O_{14}Pb_3$) & uranyl acetate $\{[UO_2(CH_3CO_2)_2H_2O)]\mathbf{.}\ H_2O\}_n$ double staining.

3.4.10 Batch Adsorption Tests (BATs) for binding efficiencies of NPs

A variety of analytical methods have been developed for the separation, detection, and determination of bile acids and their metabolites.[141–145] The most often used methods for the quantification of bile acid include chromatographic (LC, GC, HPLC, LC-MS), electromigration, and enzymatic techniques.[146–153] HPLC with supercritical fluid extraction

and pulsed amperometric detection has been applied for the determination of bile acids in feces. To the best of our knowledge, there are only a few reports[154] on the indirect spectrophotometric determination of cholic acid where the colic acid is converted to a new entity by enzymatic treatment,[155,156] or by reacting with furfural[157] (i.e., 2-Furaldehyde, or Furan-2-carboxaldehyde; an organic aldehyde) and sulfuric acid. Due to the lack of chromophore(s) (e.g., an aromatic ring), BAs do not have any UV absorbances unless they are converted to a compound having chromophore(s) or an aromatic ring.

Due to the lack of a tool within the resource available, here we are reporting the binding efficiencies of the developed NPs through the following three (3) categories of BATs based on detection/quantification techniques:

1) BATs of the NPs with a surrogate marker for which a negatively charged dye (e.g., methyl orange, MO) was chosen. MO has a pKa value of 3.5 and displays a max absorbance at the wavelength (λ_{max}) of 464 nm.[158–160]
2) BATs of the NPs with sodium cholate (NaC/SC), where unbound/free SCs were detected/quantified through the conductance measurement.[161] Although the sensitivity and accuracy of the conductance measurement are not as precise, being more sensitive and accurate over the surface tensiometry, this conductivity method was considered as the more suitable method for this project.
3) BATs of the NPs with SC where the unbound SC were detected/quantified through the conversion of SC to intermediate furfural–cholate followed by the UV-Vis detection. The furfural–cholate has a λ_{max} of 620 nm.[157]

All the three modes of BATs mentioned above require the use of calibration plots for quantifying the unknown ligands (MO, SC etc.) in aqueous solutions. Additionally, polyvinylidene difluoride (PVDF) hydrophilic membrane filters (Durapore™ Membrane Filters, 0.45 or 0.8 μm; MilliporeSigma™) were used to filter the post-BAT mixtures. Thus, for the MO via UV–Vis and SC via conductance, the calibrations curves were constructed for both filtered and unfiltered reference standard solutions. For the furfural–cholate, being inconvenient, time-sensitive reaction/measurement, and tedious process, no filtration was done in this case and the calibration plot was conducted using unfiltered reference solutions.

Each of the BATs with MO/SC was performed by stirring 20 mL mixture at 250 rpm for 2.5 hrs as shown in Figure–3.5 [20 mL mixture = 5 mL of the CNCs' dispersions at a specific concentration + 15 mL of MO/SC solution of a specific concentration]. At least 5 different concentrations of MO/SC were used in the Langmuir model fitting and all BATs were conducted at neutral pH and at RT (25^0C). For the BATs with MO, 100 ppm, 250 ppm, 500 ppm, 750 ppm, and 1000 ppm aqueous solutions were used, and two vials of the BATs (a set) were conducted simultaneously based on these MO/SC concentrations. For each set of the MO/SC concentrations as well as for the NP samples, a blank (20 mL of the MO solution for that conc. only, without any NP added) vial was always run to eliminate the likelihood of mechanical/instrumental/operator errors so that determined/calculated Q_{max} values possessed the desired accuracy. And for the construction of the calibration curve, a conc. range of 0 – 25 ppm was utilized, both for the filtered (PVDF membrane filters, 0.2 μ) and unfiltered solutions.

Similarly, for BATs conducted with SC for quantification using conductometry as well as UV-Vis (furfural–cholate, the coloured analog of the SC), the 5 selected conc. were 1 mM,

5 mM, 10 mM, 20 mM, and 25 mM. Similarly, for each set of samples, a blank (20 mL of the SC solution without any added NP; also considered as a blind test) vial was always run to eliminate the likelihood of errors. And in the case of detection via conductance, the calibration curve was constructed for a conc. range of 0 – 30 mM of the SC, and for the detections via UV-Vis method, the corresponding calibration curve was constructed for the conc. range of 0 – 27 μg/mL. The initial and final concentration of the ligand was measured using a Cary 100 UV–Vis spectrophotometer and the conductivity probe of the Metrohm 809 titrator for MO and SC, respectively.

Once the BATs were completed for MO, no visible aggregates were observed for the lower conc. of MO (i.e., the conc. < 250 ppm), and thus a few mL of the post–BAT MO mixtures were filtered and diluted appropriately with a known dilution factor (DF) before proceeding with the absorbance measurements @464 nm.[158–160] Visible aggregates were seen distinctly for any of the BATs conducted with the SC. But due to the formation of unstable sediment/precipitates after centrifugation of the post–BAT mixtures, the filtration method was adopted. Once the filtrates were ready for the measurement of either conductance or absorbance, appropriate dilutions were made wherever necessary, and the measurements were recorded along with the dilution factor (DF) for further data analyses. The respective calibration curves and the fitted equations were used to convert the absorption or conductance values of the ligands for unknown conc. to its corresponding conc.

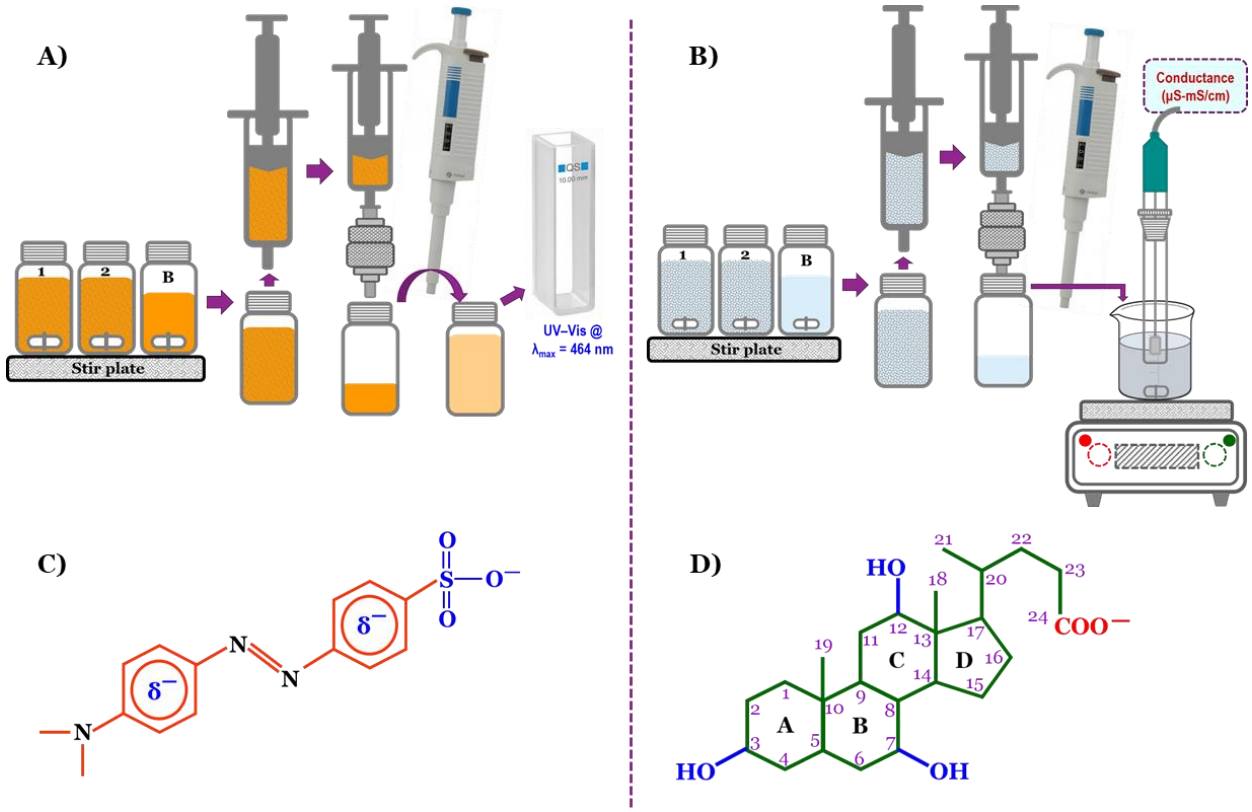


Figure 3.5: *Schematic of the experimental setup for the BAT of NPs* ***A)*** *with Methyl Orange (MO), an anionic dye, and* ***B)*** *with Sodium cholate (SC), one of the primary bile acids in the human body. Here, the 1 and 2 represent the vials of two trials for the same conc. of ligands (and the NPs) to minimize the manual/experimental error, and the B vial stands for blank for each set of conc. For simplicity, the set of two vials for only one conc. of the ligands are shown here. For Langmuir adsorption isotherm nonlinear fitting model, a min of five (5) conc. of the ligands were chosen to conduct the BAT with constant conc. of the NPs/adsorbents.* ***C)*** *and* ***D)*** *represent the chemical structures of MO and SC, respectively in aq. solutions.*

The furfural-cholate was synthesized,[157] both for constructing the calibration curve and during quantification of the unbound SC from the post-BAT samples, by reacting 1 mL of the reference NaC solution with 6 mL of 16 N sulfuric acid (H_2SO_4), 1 mL of freshly prepared furfural (1%, w/v) for 13 minutes at $65^0C \pm 0.2^0C$ (reaction scheme shown in Figure-3.6). Once

the reaction was done (turned into a slightly pink colour), the mixture was placed on an ice bath for rapid cooling followed by the addition of 5 mL of glacial acetic acid to the mixture (turned out to be a slightly greenish blue colour, darker for higher SC conc. of the reference standard solutions). The UV measurements were then conducted at λ_{max} and recorded.

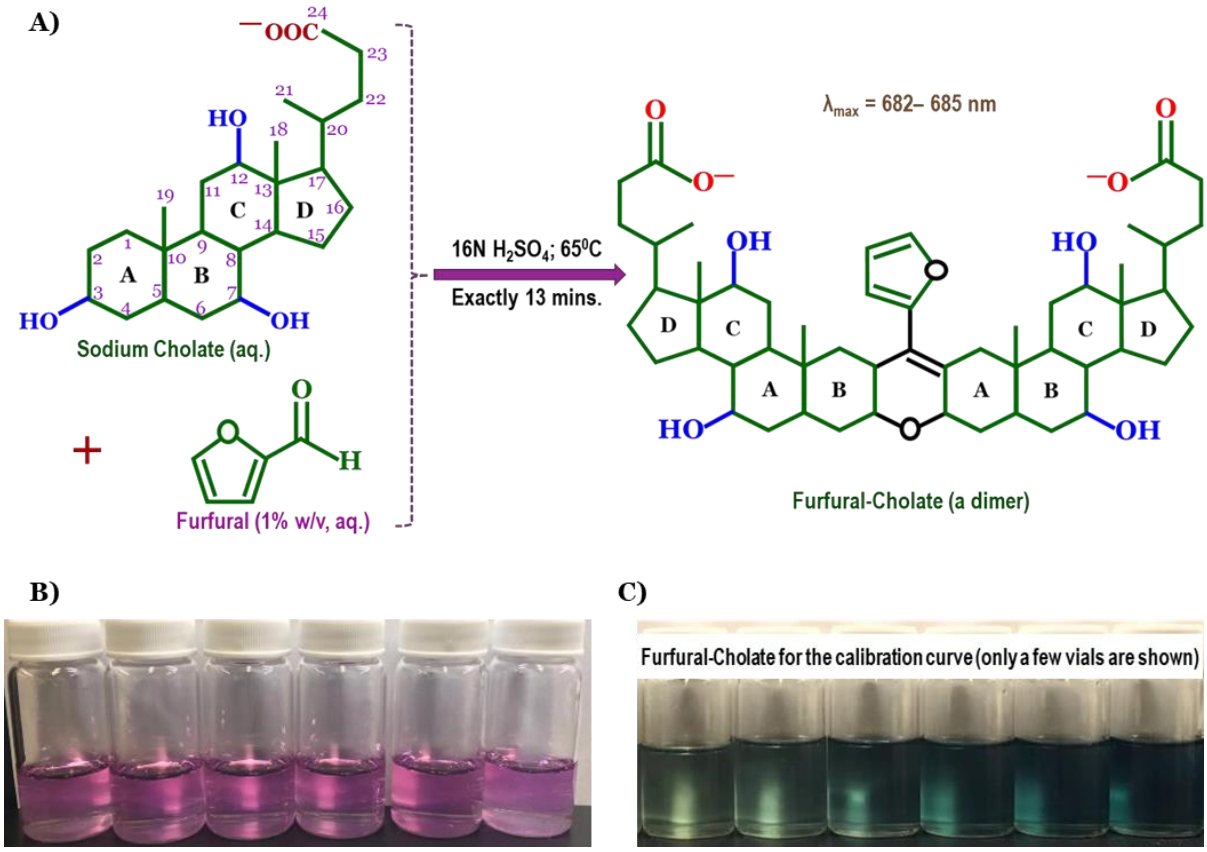


Figure 3.6: A) *Reaction scheme between furfural and sodium cholate.*[157] ***B)*** *Color produced after 13 mins of reaction.* ***C)*** *Color produced after the addition of acetic acid as the final step.*

For all the BATs, the ligand (dye & NaC) removal % and amount of ligand adsorbed (qe) on the substrate/adsorbent (the developed NPs) were calculated using the following equations[162–164] (3.1) and (3.2):

$$Percentage\ removal = \frac{C_0 - C_e}{C_o} x\ 100 \tag{3.1}$$

$$Q_e = \frac{(C_0 - C_e)V}{m} \tag{3.2}$$

The Q_e for the Langmuir Isotherm could be expressed in the linearized form (Eq. (3.3))

$$Q_e = \frac{K_L * Q_{max} * C_e}{1 + (k_L * C_e)} \quad and \quad \frac{1}{Q_e} = \left(\frac{1}{k_L * Q_{max}}\right) * \frac{1}{C_e} + \frac{1}{Q_{max}} \tag{3.3}$$

$$Now, for\ \frac{1}{Q_e} = \left(\frac{1}{k_L * Q_{max}}\right) * \frac{1}{C_e} + \frac{1}{Q_{max}}$$

$$Here, the\ intercept = \frac{1}{Q_{max}}\ and\ the\ slope\ is = \frac{1}{k_L * Q_{max}}$$

where Q_e is the amount of ligand adsorbed by 1 g of adsorbent (mg/g), C_e is the equilibrium concentration of free ligand molecules in the solution (mg/L), C_0 is the initial ligand concentration (mg/L), V is the volume of solution (L), m is the mass of adsorbent (g), k_L is the Langmuir constant, and the Q_{max} is the max adsorption capacity (unit mass/g) for the adsorbent for that ligand at equilibrium–concentration of ligand and temperature (T^0C).

3.5 Results and Discussion

3.5.1 Percentage yield and Desulfation of NCC™

After the DS–CNC was synthesized, purified, and collected as the never-dried concentrated slurry, the conc. was recorded, and by carefully measuring the volume of the slurry, the percentage yield was determined which is presented in the bar chart in Figure 3.7. As discussed earlier in section 3.4.2, a longer reaction time and higher temperature during the desulfation reaction could drastically reduce the yield[165] and this was evident for the alkaline desulfation process showing the lowest yield % when 6 M NaOH was used.

The possible reason for such a decreasing trend in the yield% of DS–CNCs with increasing concentration of NaOH was associated with the polymorphic conversion of native cellulose allotrope-I to allotrope-II due to mercerization[43,166,167] of highly concentrated alkali treatments. Literature suggested that when the concentration of NaOH exceeded the threshold (approx. 15-20%, w/v of NaOH) cellulose-I swelled, and dissolved cellulose-I yielding disordered or amorphous cellulose.[43,166,167]

Regardless of the yield, it was found from the titration and elemental analysis (EA) that a ‘gradient desulfation’ (i.e., an increasing pattern of desulfation with the increasing strength of NaOH used for desulfation) of NCC™ for all the four alkalis mediated DS-CNC was achieved (Figure 3.7 C, D) and this was one of the expected outcomes. Although the data were not in total agreement with published literature[168] results (CNC extracted by H_2SO_4 hydrolysis of native cotton fibre), the different starting CNC used for desulfation in our experiments was the most likely reason for the observed variations.

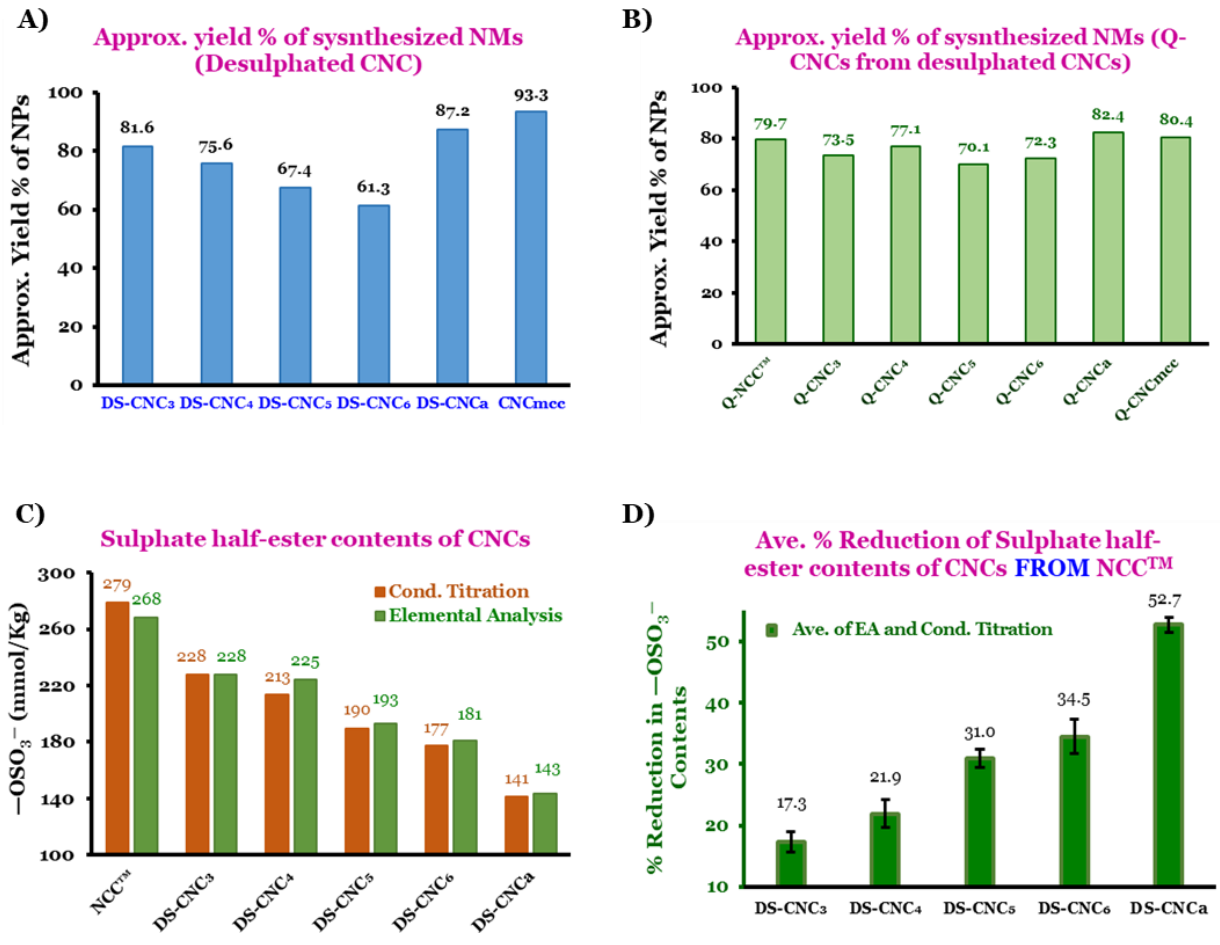


Figure 3.7: *Yield % obtained for the* ***A)*** *DS–CNCs and* ***B)*** *the corresponding Q–CNCs (except the Q–NCC™ and Q–CNC$_{MCC}$, which were not synthesized from any DS–CNC)* ***C)*** *Column chart representing the sulfate half ester groups (—OSO$_3^-$) contents for different DS–CNCs determined via conductometric titration and EA.* ***D)*** *Average % reduction of surface —OSO$_3^-$ contents based on the two methods.*

For the synthesis of the DS–CNC with gradient desulfation content, our data showed that the expected trend of sulfate half ester (SHE) groups (—OSO_3^-), i.e., the DS–CNC_6 possessed the lowest amounts of —OSO_3^- groups among all the 4 alkali-mediated DS–CNCs, i.e., desulfation degrees: DS–CNC_6 > DS–CNC_5 > DS–CNC_4 > DS–CNC_3.

The yield of DS–CNC_a obtained via the desulfation through the HCl acid-mediated hydrolysis was higher compared to the yield in DS–CNC_3. Furthermore, such form of desulfation also produced the highest DS–CNC and approx. 53% of the —OSO_3^- groups were removed from the NCC^{TM} for HCl acid-mediated desulfation. However, for the CNC_{MCC} the yield% was found to be the highest which was in the range of 93%. As the MCC did not have any surface —OSO_3^- groups (obtained from the certificate of analysis, *CofA* report of the supplier), the CNC_{MCC} were without—OSO_3^- groups and consequently, was not considered as a candidate for the titration and EA for the measurement of —OSO_3^- contents.

Here, the gradient desulfation processes gave rise to new primary (1^0) alcoholic groups (—CH_2OH) on the surfaces of the nanocrystals that were initially occupied by —OSO_3^- groups in NCC^{TM} prior to desulfation, and thus further chemical modifications were now feasible on the 1^0 alcoholic groups. As the sulfate half ester groups displayed a decreasing trend due to gradient desulfation, the repulsive forces from the surface —OSO_3^- groups were reduced, resulting in the inter-particle aggregation of the nanocrystals. Such forms of aggregations of the DS–CNCs were also evident from the aqueous dispersions (Figure 97, in appendix) prepared even at the lowest concentration (0.05%, w/v).

Based on these gradient DS–CNCs, the corresponding Q–CNCs were also synthesized, purified, and stored for future use (a representative example is shown in Figure 3.8). The average yield % for these Q–CNCs was found within the range of 70 — 80% indicating that the grafting of GTMAC was successful (all parameters for the reactions in this chapter are summarized in Table-3.1). Here, the highest yield was recorded for the Q–CNC_a (obtained from DS–CNC_a) which was ~ 83%. Additionally, as these Q–CNCs were mostly prepared from the partially DS–CNCs, the quaternized–NPs were highly cationic and more hydrophilic, yet trace amounts of sulfate half-ester, SHE groups (—OSO_3^-) were still present on the surfaces making the NPs zwitterionic (schematically represented in Figure 3.8).

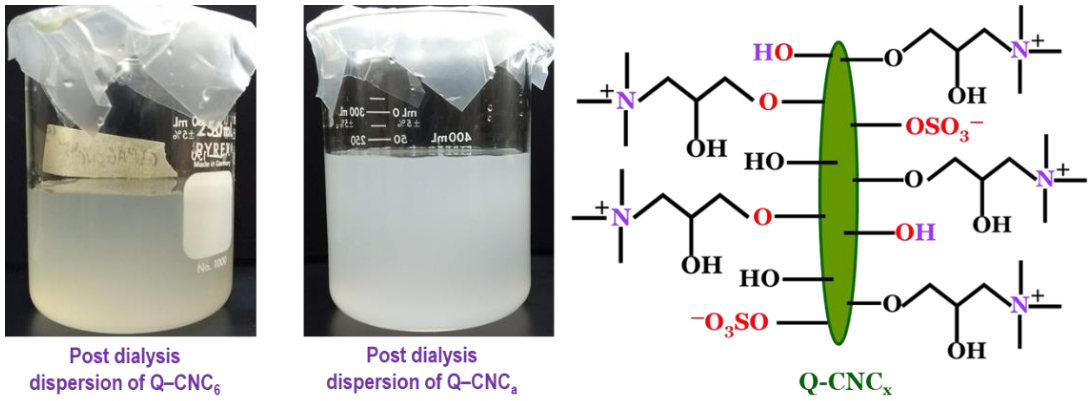


Figure 3.8: *Post dialysis suspension (concentrated) of quaternized CNCs, Q–CNCs where the leftmost indicates the Q–CNC_6 and the next to the right refers to the Q–CNC_a. The rightmost image is the schematic representations of the synthesized Q–CNCs which are also the Zwitterionic NPs. All the Q–CNCs developed thus far for this chapter, being more hydrophilic, were found very easily dispersible in water. In aq. suspensions, both the counterions, the Cl^- for the grafted QAG groups and the Na^+ for the leftover/trace SHE groups (—OSO_3^-) are ionized making them Zwitterionic but overall cationic. These phenomena of Zwitterions also shed light on why and how the Q–CNCs exhibit some degrees of aggregations in colloidal suspensions.*

3.5.2 FTIR characterization of DS–CNC and Q–CNCs

The FT-IR peaks of the DS–CNCs (Figure–3.9C) correspond to the peaks described in the literature[134,168–171] (Figure–3.9 A, B). The broad band at 3600–3000 cm^{-1} corresponds to —OH; a strong band due to hydroxyl (—OH) stretching appeared at 3413 cm^{-1}. The absorbance at 2902 cm^{-1} is due to symmetric C—H vibrations. The peak at 1430 cm^{-1} is associated with CH_2 scissoring motion; the band at 1113 cm^{-1} represents the stretching of the glucopyranose unit; a small peak at 815 cm^{-1} corresponds to symmetric stretching of the S–O–C linkage. The absorbance peak at 2902 cm^{-1} is due to the symmetric C—H vibration; an intense band at 1644 cm^{-1} from absorbed moisture; the C—H deformation mode of glycosidic linkage is assigned to absorbance at 897 cm^{-1}; and absorbance between 1030 and 1163 cm^{-1} is attributed to C—O stretching in major ether bands in CNC. The asymmetrical S=O vibration should have a peak at 1250 cm^{-1}. The peak at 1033 cm^{-1} has been attributed to the stretching vibration of —OSO_3^- groups. A peak at 1427 cm^{-1} corresponds to —CH_2 bending; and at 1203 cm^{-1}, the peak corresponds to C—OH bending in-plane at C–6.

From the combined FTIR spectra (Figure 3.9C), due to the gradient desulfation of NCC™, the —OSO_3^- groups were partially removed, thus the peak at 1033 cm^{-1} was altered, which is also in agreement with published literature.[169] The FTIR characterization confirmed that the DS–CNCs were successfully prepared and the gradient removal of the surface —OSO_3^- groups were achieved, and the remaining surface —CH_2OH would be the preferred sites for the grafting of QAGs.

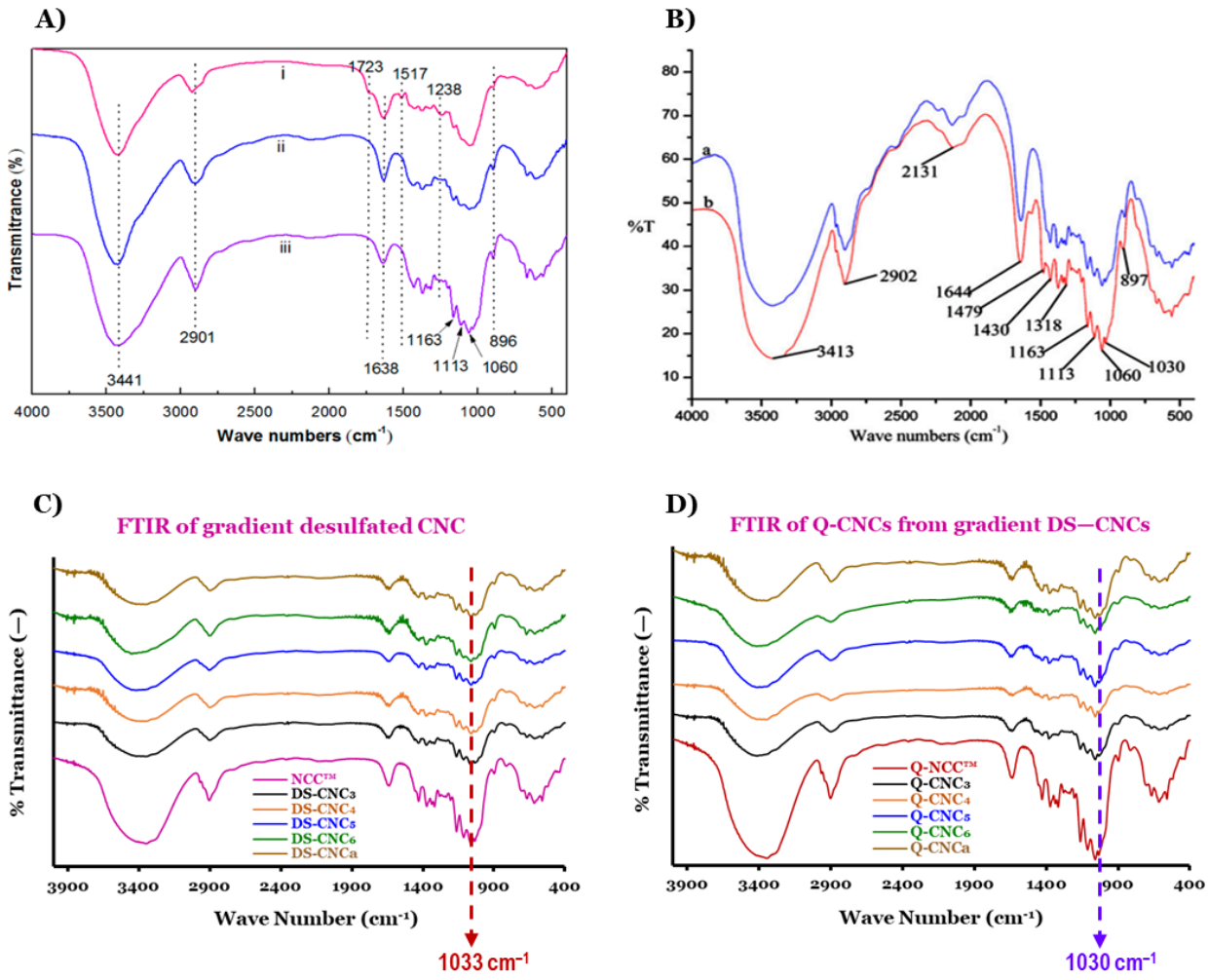


Figure 3.9: A) *FTIR spectra of (i) raw material (corn stalk); (ii) the extracted cellulose; and (iii) the CNCs. Reused from.*[134] ***B)*** *FTIR spectra of (a) unmodified sulfuric-acid-hydrolyzed CNCs and (b) GTMAC-CNCs. Reused from.*[134] ***C)*** *FTIR spectra of NCC™ and the corresponding DS–CNCs showing the reduction of the peak heights @ 1033 cm^{-1} which is reported to be for the —OSO_3^- groups (very subtle, and discernible easily if zoomed in).* ***D)*** *FTIR spectra of all the corresponding Q–CNCs based on the gradient DS–CNCs. Literature reported the peaks would be more intense than its precursors and we had such agreement for the synthesized Q–CNCs. Individual plots (not presented here) of DS–CNC$_x$ and respective Q–CNC$_x$ showed the distinct difference of peaks' intensities although no new peaks were discernible.*

Similarly, for the structural characterization and identification, the FTIR of all the corresponding Q–CNC samples were also performed (Figure–3.9 D). For the Q–CNC, an increase in the intensity of ether bands was observed between 1030 cm^{-1} and 1163 cm^{-1}, in addition to a prominent band at 1479 cm^{-1} attributed to CH_2 bending mode[134] and methyl groups of the cationic agent, all of which was in agreement with published literature.[134,168–171]

3.5.3 Grafting efficiencies and QAG contents of the Q–CNCs

The synthesized Q–CNCs NP systems were also characterized and evaluated by conductometric titrations to determine the amounts of quaternary ammonium groups, QAGs [**—$N^+(CH_3)_3$**]. The determined QAGs are listed in Table–3.1 and shown in Figure–3.11, where the QAG contents increased with an increasing degree of desulfation.

Table 3.2: The quaternary ammonium groups (QAG) contents, degree of substitution (DS), and the cationizing reaction efficiencies (CRE%) of the cationic CNC NPs (Q–CNC_X).

Cationic NPs	QAG (mmol/g)	Experimental pH	DS	CRE%
Q-NCC™	0.21	6.73	0.03	3.6
Q-CNC_3	0.79	6.42	0.15	15.6
Q-CNC_4	1.03	6.77	0.20	21.1
Q-CNC_5	1.63	6.63	0.35	37.5
Q-CNC_6	1.79	6.32	0.40	42.6
Q-CNC_a	2.17	6.63	0.52	55.9
Q-CNC_{MCC}	2.03	6.52	0.48	50.7

And Figure–3.10 represents the outlook of the typical conductometric titration plots (both NaOH and $AgNO_3$ titration) and the equations utilized to calculate the QAGs, DS, and CRE%.

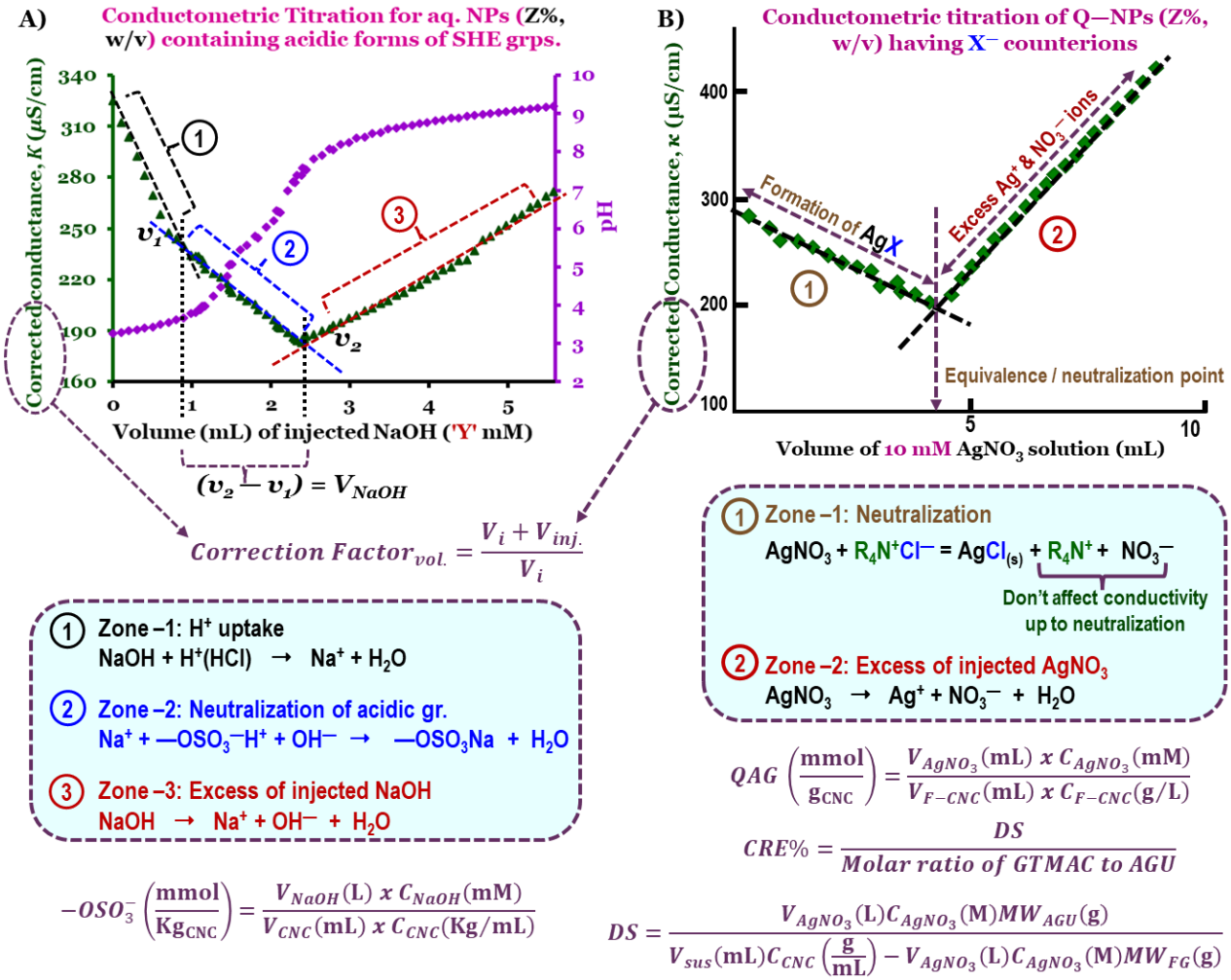


Figure 3.10: A) *An acid–base conductometric titration curve & the equation utilized for determining the sulfate half ester (SHE) contents (mmoles/Kg of the CNC). Usually, three distinct zones are observed in such forms of conductometric titration plots, and in this case, the volume (mL) required to neutralize the acidic forms of the SHE groups in the zone–2 is the number considered for calculation.* ***B)*** *$AgNO_3$ mediated conductometric titration plots for determining the QAG contents and the equations used to determine various parameters.*

Due to the gradient desulfation process, more surface 1^0 alcoholic groups were exposed/accessible for the grafting reaction. As a result, the highest QAG contents among the Q–CNCs were observed for the most desulfated CNC. The DS–CNC_a and the QAG were found to be 2.17 mmoles/g (Q–CNC_a) and the degree of substitution (DS) was 52%. Although the CNC_{MCC} was assumed to have the low level of —OSO_3^- groups (and thus, consequently, most of the surface protruding —CH_2OH groups are free to participate in the cationization reaction), it was expected to have most grafting onto the NPs.

However, the Q–CNC_{MCC} NPs did not display the highest QAG contents, and the most probable reason would be the inter-particle aggregation during reaction caused by the Van der Waals force and hydrophobic interaction. Other than this NP, all the other Q–CNCs showed a trend of increasing QAG contents (gradient quaternization) which were consistent with the gradient desulfation degrees.

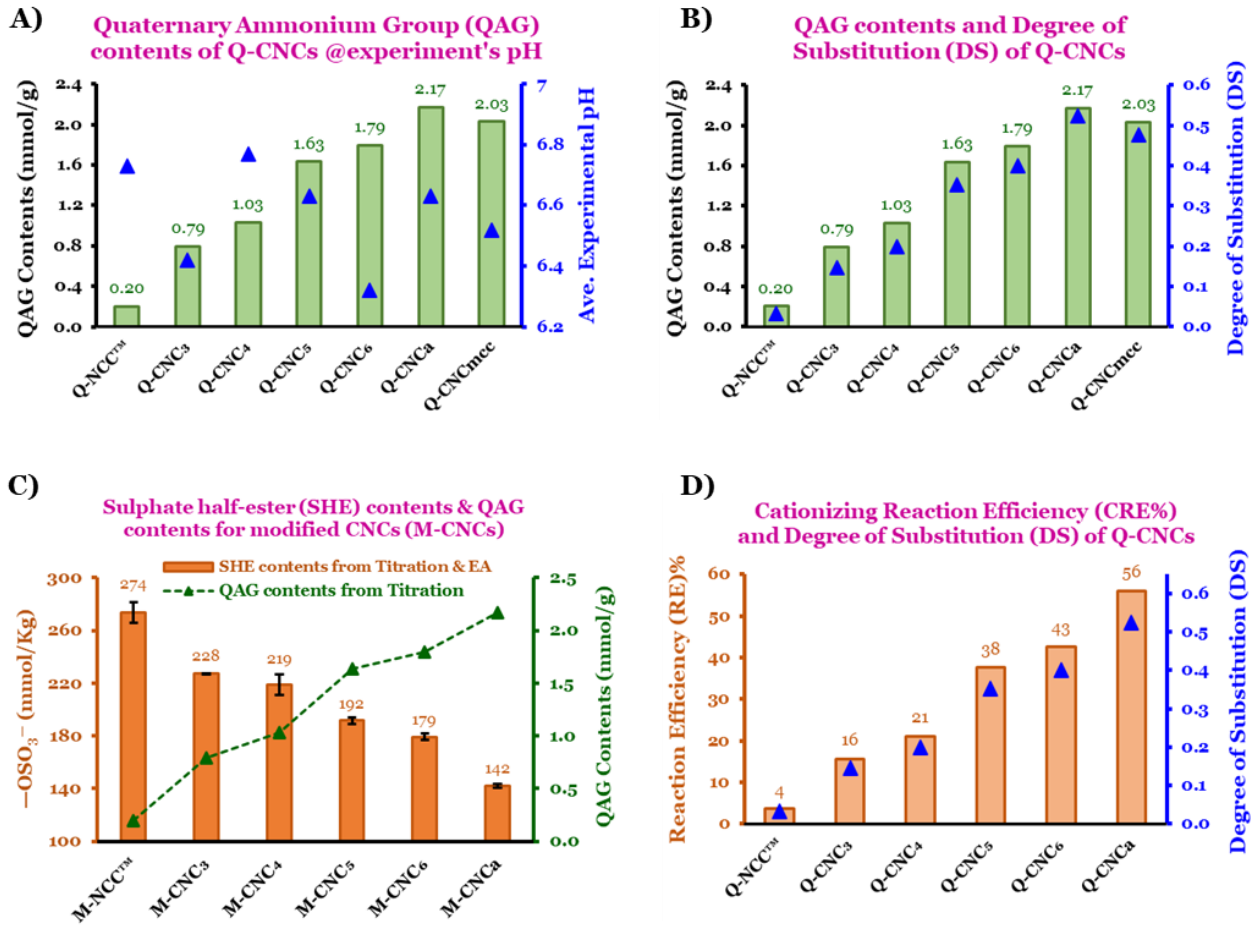


Figure 3.11: A) *The QAG contents of all the synthesized Q–CNCs which were determined from the equivalence (end) points obtained in the conductometric titrations of the 10 mM $AgNO_3$ with individual NPs.* ***B)*** *Comparison of the degrees of substitution of QAG onto the NPs' surfaces with the QAG contents. Essentially, a higher achieved DS from a higher reaction efficiency (RE%) usually ensures a greater amount of grafting of the QAG, which was one of the expected outcomes for the target-specific application.* ***C)*** *Comparison of SHE and QAG contents of the* ***modified CNCs (M–CNCs)****. The QAG contents exhibited a pattern of gradient increase over the Q–CNCs, especially for those that were synthesized from the gradient desulfated CNCs (DS–CNCs) with decreasing contents of surface —OSO_3^- groups.* ***D)*** *The DS and CRE% of all the Q–CNCs made from DS–CNCs.*

From the results obtained, we concluded that DS–CNC_6, DS–CNC_a and the CNC_{MCC} yielded Q–CNCs with higher contents of QAGs. Several literature suggested that it is possible to enhance the reaction efficiencies (RE%) for QAG grafting if organic solvents were adopted[136] as the reaction media for the cationization reactions with the GTMAC. The underlying reason for such an increase in the RE% was that the solvents such as isopropyl alcohol (IPA) and tetrahydrofuran (THF, a cyclic ether) reduced the likelihood of the degradation of the GTMAC before being grafted on the NPs. We utilized IPA or THF with trace amounts of water to cationize DS–CNC_6 and DS–CNC_a and the enhancement in the QAG grafting were evaluated.

Figure –3.11 summarizes the QAG contents of the Q–CNCs based on the solvent used as a media during the reaction. Higher QAG contents were recorded for the Q–CNC synthesized in THF (Q–CNC_{6e}, QAG = 2.51 mmol/g; and Q–CNC_{ae}, QAG = 3.02 mmol/g) rather than Q–CNC produced in IPA media (Q–CNC_{6a}, QAG = 1.96 mmol/g; and Q–CNC_{aa}, QAG = 2.57 mmol/g). Obviously, the most desulfated DS–CNC_a yielded the highest QAG containing Q–CNC when the THF was used as the reaction media (the Q–CNC_{ae}). Such investigations from the pilot syntheses of these Q–CNCs were to demonstrate that the grafting efficiency could be improved, and our findings conformed with previously reported findings.[136] The achievement of strongly cationic NPs via the higher extent of grafting, and the DS–CNC being the intermediate for synthesizing all the Q–CNCs, the degree of desulfation (DD) and the desulfation reaction efficiencies (RE%) were not determined. Due to the time-consuming grafting reaction and tedious method of slow addition of GTMAC, any further plan to produce a larger batch of Q–CNCs using IPA and THF solvents was not considered.

3.5.4 Sizes and Zeta potentials of DS–CNCs and Q–CNCs

Zeta potential and size characterization of 0.05 % (w/v) aqueous suspensions of desulfated–CNCs (DS–CNCs) were conducted to evaluate the DS–CNCs. Table–3.3 summarizes the average sizes (D_H) and zeta–potentials (ZPs) of the DS–CNCs and the corresponding quaternized–CNCs (Q–CNCs).

Table 3.3: The average sizes (D_H) and zeta–potentials (ZPs) of the 0.05% (w/v) aqueous suspensions of DS–CNCs and their corresponding Q–CNC, determined from the zetasizer.

Nanoparticles (NPs)	ZP @ Experimental pH (mV)	$ZP_{STDV.}$	Size, D_H @ Experimental pH (nm)	Size, $(D_H)_{STDV.}$
NCC™	– 42.0	0.7	107.4	9.1
DS-CNC$_3$	– 37.3	1.4	147.4	6.1
DS-CNC$_4$	– 36.2	3.1	180.7	11.8
DS-CNC$_5$	– 33.9	0.6	247.3	4.3
DS-CNC$_6$	– 24.1	2.3	273.9	5.7
DS-CNC$_a$	– 11.9	0.9	224.8	21.5
CNC$_{MCC}$	– 6.4	1.1	1057	48.9
Q-NCC™	13.4	7.6	127.4	10.9
Q-CNC$_3$	27.1	3.2	152.0	16.4
Q-CNC$_4$	31.4	2.4	198.9	23.6
Q-CNC$_5$	36.2	3.3	228.0	10.1
Q-CNC$_6$	43.3	1.6	231.3	33.6
Q-CNC$_a$	35.8	2.6	132.6	10.3
Q-CNC$_{MCC}$	38.8	3.6	826.2	39.7

Based on the gradient desulfation process, the surface charge of the DS–CNCs was reduced. Since the surface —OSO_3^- groups were removed due to the gradient desulfation of NCC^{TM}, it should result in a reduction of the negative charges on the surface of CNCs. Possessing lower negative ZP values, the interparticle repulsions in their aqueous suspensions were reduced leading to the formation of aggregates driven by Van der Waals interactions. The increasing trend of the average hydrodynamic diameters (D_H) of the aggregates further confirmed the aggregation of the suspended particles, and Figure–3.11 shows the trends of size and ZP of the DS–CNCs obtained through the gradient desulfation that yielded DS–CNC_{MCC}.

The D_H and ZP data for the Q–CNCs at 0.05 % (w/v, aq. unfiltered) are also reported in Figure–3.12, where Q–NCC^{TM} refers to the cationic CNC synthesized from the CelluForce CNC (NCC^{TM}), without further modification. The gradient increase in the surface cationic charge densities, evident from the ZP values, reinforced the fact that unoccupied or free surface 1^0 alcoholic groups were necessary for further modifications or grafting to yield cationic CNCs. The more the desulfation of NCC^{TM}, the more will be the surface cationic charge densities after grafting with GTMAC. As all the DS–CNCs were partially desulfated, the Q–CNCs appeared to be zwitterionic nanoparticles, and thus, they were prone to aggregate in aqueous suspension at low concentration, even at 0.05% (w/v). Due to such aggregation, the suspensions were cloudy and especially the Q–CNC_{MCC} was found to be unstable and sedimented to the bottom of the storage container (in as is concentrations of the post-dialysis samples).

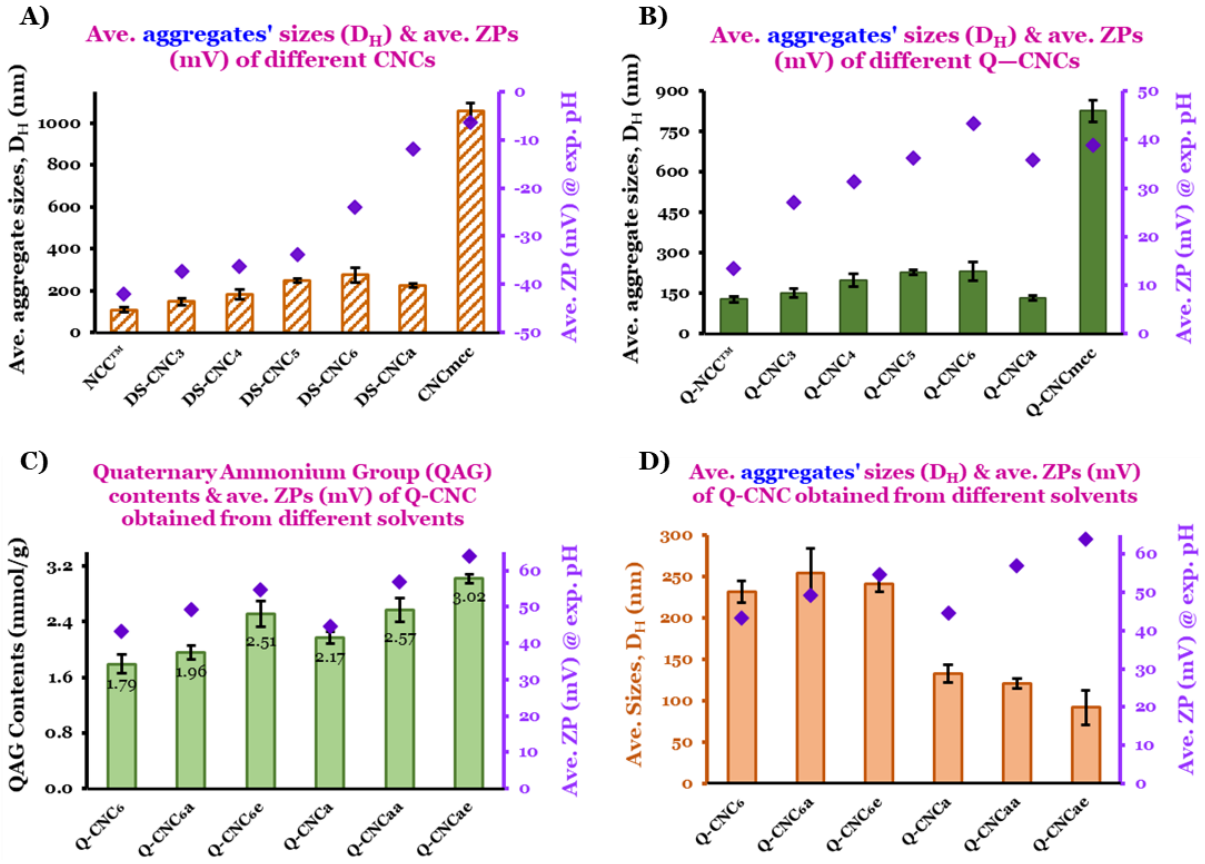


Figure 3.12: A) *Summary of the average sizes (D_H) and ZP of all the DS–CNCs and the CNC_{MCC}. Here the gradient reduction of the surface negative charges of these NPs also establishes the fact of gradient removal (desulfation) of surface SHE groups (—OSO_3^-). Due to such phenomena, interparticle repulsions got reduced and aggregations of the NPs were seen from the D_H data.* ***B)*** *Gradient increasing trend of surface cationic charges of the Q–CNCs obtained from the corresponding DS–CNCs. In this case, being the Q–CNCs Zwitterionic, inconclusive trends of aggregation of the NPs were seen from the D_H data.* ***C)*** *Effect of organic solvents as the media of cationization reaction, giving the highest cationization for the DS–CNC_a in THF solvent (an ether).* ***D)*** *Summary of D_H and ZP of the Q–CNCs obtained from different cationization reactions done in DMSO, IPA, & THF solvents.*

3.5.5 Sizes and Zeta potentials of the chosen Q–CNC @ different pH ranges

The gastrointestinal (GI) pH, transit time, and temperature profiles are variable throughout the human GI tract (GIT), and such fluctuations in temperature, pH, transit times, and motility (peristalsis) can affect the drug delivery,[172] or in this case the binding interactions of cationic CNCs with the secreted bile acids in the duodenum. The gastric pH ranges from 1.7 to 4.7 with an average gastric emptying time of 30 minutes (ranging 7–202 mins). During the small bowel transit, which had a duration of 67–532 min (median: 247 min), the pH increased slightly from 5.9–6.3 in the proximal to pH 7.4–7.8 in the distal section. Colonic pH conditions were characterized by values fluctuating mainly between pH of 5 and 8.[172,173]

Keeping this in mind, the Q–CNCs systems that possessed the highest cationic charges *i.e.*, the Q–CNC_6, Q–CNC_a, and the Q–CNC_{MCC} were evaluated by the size and zeta potential over the pH range of 2–10 and the results are summarized in Figure–3.13.

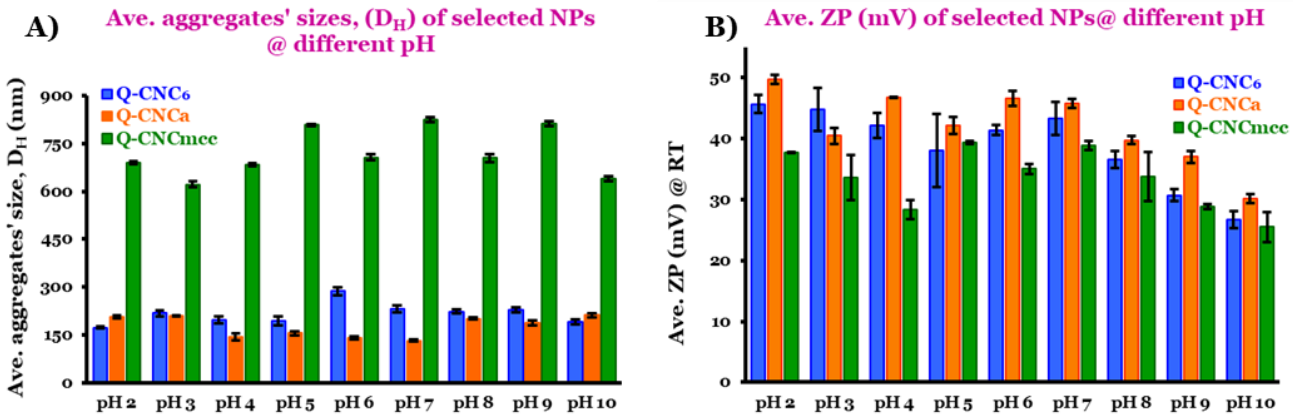


Figure 3.13: *Summary of the average aggregate sizes (D_H) in **A)** and the average ZPs in **B)** of the three chosen Q–CNCs for which the ZPs were found highest discussed earlier.*

From the pH data of the highest Q–CNCs, it was found that the aggregate sizes remained in a stable state over the GI pH ranges, although at lower pH (pH ≤3), the Q–CNCs seemed aggregated compared to those at pH 4 or 5. But, the Q–CNC_{MCC} were inherently larger, over 600 nm regardless of the pH changes due to the larger sizes of the extracted NPs from the MCC. Although there were no significant aggregations at a specific pH, no precise conclusive trend could be drawn from the DH data. Being Zwitterions, some aggregations were evident for these NPs due to the interparticle electrostatic interactions of opposite charges on the surface of adjacent NPs. In the case of ZP, the lowest pH, like in the gastric pH, possessed the highest ZP for the Q–CNC_6 and Q–CNC_a Zwitterionic NPs. Whereas the ZPs were found to be slightly in a lower range at higher pH, especially if the pH > 8.

From the literature, it is evident that the surface charge of NCC^{TM} or DS–CNCs was dominated by the covalently linked sulphate ester (SHE) groups (—OSO_3^-) on the CNC surfaces[174], the reported pKa[174] of which is 1.9. Thus, the change in pH (in the range of 3–8) did not significantly alter the ionization state and the SHE groups on the CNC surfaces remained almost fully dissociated for the Zwitterionic Q–CNC aqueous dispersions. However, at pH below 2, the protonation of SHE groups should commence, thereby decreasing the net negative charge on the DS–CNC / Q–CNC surfaces. When the pH of the Q–CNC dispersions increased to 8 or higher, some of the covalently bound SHE groups on the surface of CNC were dissociated. Thus, there is a greater possibility that several available QAGs on the Q–CNC surfaces would be neutralized by the ionized SHE groups leading to an overall reduction in ZP.

3.5.6 TEM images of DS–CNCs and Q–CNC

The TEM studies were performed to evaluate the morphology of the synthesized NPs. As discussed in the methods section, the Cu-grid was prepared and dried before the experiments were conducted. After careful analysis, we observed evidence of aggregation (as shown in Figure–3.14) for almost all the modified NPs (DS–CNC and the Q–CNCs) that were attributed to the drying phenomena during the sample preparation.

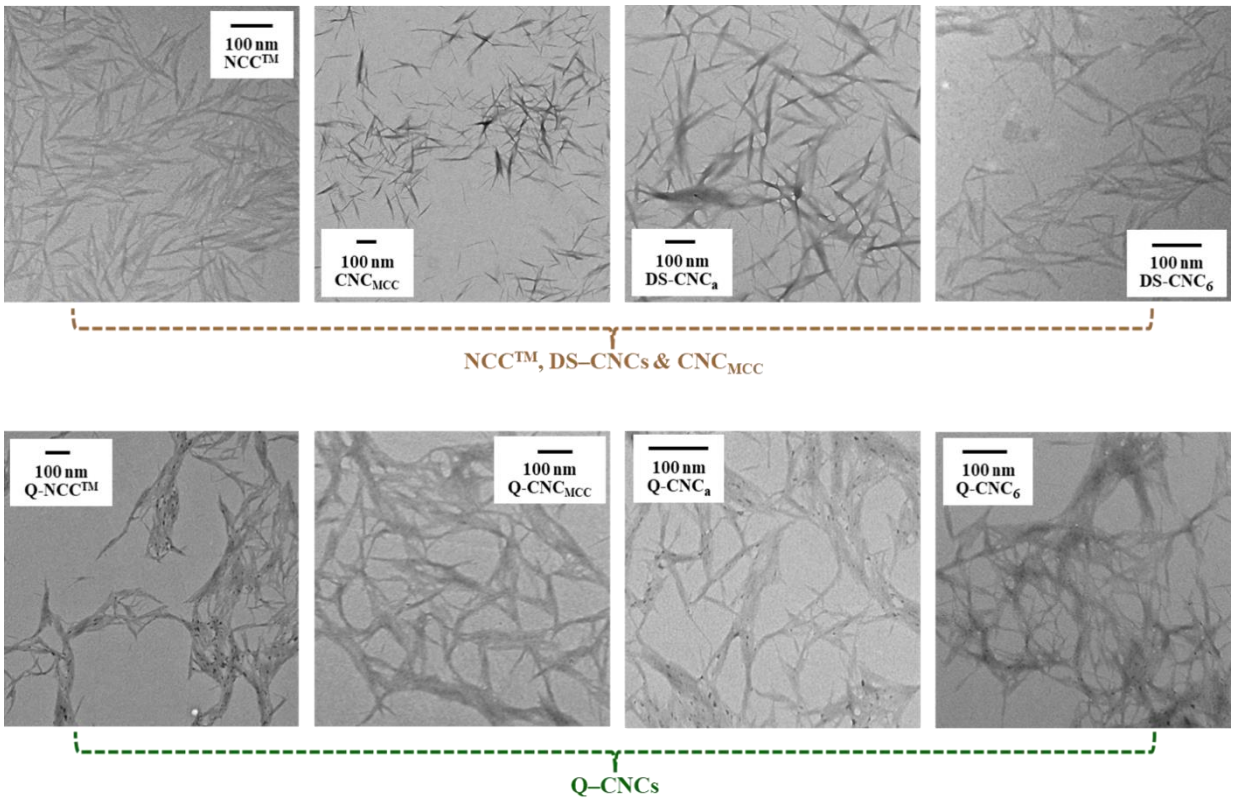


Figure 3.14: *TEM images of pristine CNCs (NCC^{TM}), the DS–CNCs and the CNC$_{MCC}$ shown on the top row. Although the aqueous suspensions of the samples were made in diluted concentrations and sonicated prior to pipette onto the CFC grids, they showed interparticle aggregation due to drying. The bottom row shows the TEM images of representative Q–CNCs samples made and dried similarly to the other NPs as mentioned above.*

This drying mediated aggregation was typically evident for the NCC^{TM}, although the colloidal suspensions were very stable with the ZP as well as the D_H values within the colloidally stable ranges (ZP $\geq \pm$ 25 mV). Thus, the CNC_{MCC} and, the DS–CNCs showed interparticle aggregations due to the H-bonding and Van der Waals forces which were evident from the TEM images as well as the D_H data, regardless of the drying mediated aggregation for the TEM grid preparation. Since all the Q–CNCs were Zwitterions, aggregation could be induced during the drying process on the TEM grid, thus the findings were in contrast to the D_H determined in aqueous solution via DLS. As for the gradient desulfation as well as for the gradient quaternization, there were no structural changes on the surface except for the removal of SHE (—OSO_3^-) groups (for desulfation) or higher extent of grafting (for cationization), thus TEM images could not differentiate the NPs of the same category.

3.5.7 Batch Adsorption Tests (BAT) for chosen/selected NPs

The evaluations of the binding efficiencies of the synthesized NPs were conducted using the Langmuir monolayer adsorption isotherm (LAMI) via linearized fittings, as described in the method section. As the literature suggested that such physicochemical adsorption of ligand onto the substrates is mostly monolayered[175–177] and being the most widely reported mode of analyses, only the Langmuir isotherm was considered for the analysis of the data. And, as described in the method section, the BAT was subclassified into three different experimental modes based on the detection techniques and the ligands (adsorbate/analyte) used namely: NPs + MO via UV-Vis, NPs + SC via Conductometry and lastly NPs + SC via UV-Vis (converting the SC into colored analogs).

3.5.7.1 BAT with Methyl Orange (MO) via UV-Vis method

All the Q–CNCs were examined to evaluate their binding/adsorption efficiencies for the anionic organic dye, MO which has a λ_{max} of 464 nm[158–160] in the UV-Vis absorption spectrum. MO, with a MW of 327.33 g/mole, is highly soluble in water (5 g/L @ RT) and it displayed a red color in acidic medium and yellow in basic medium with a pKa of 3.47. Figure–3.15 explains the possible physicochemical adsorption of MO.

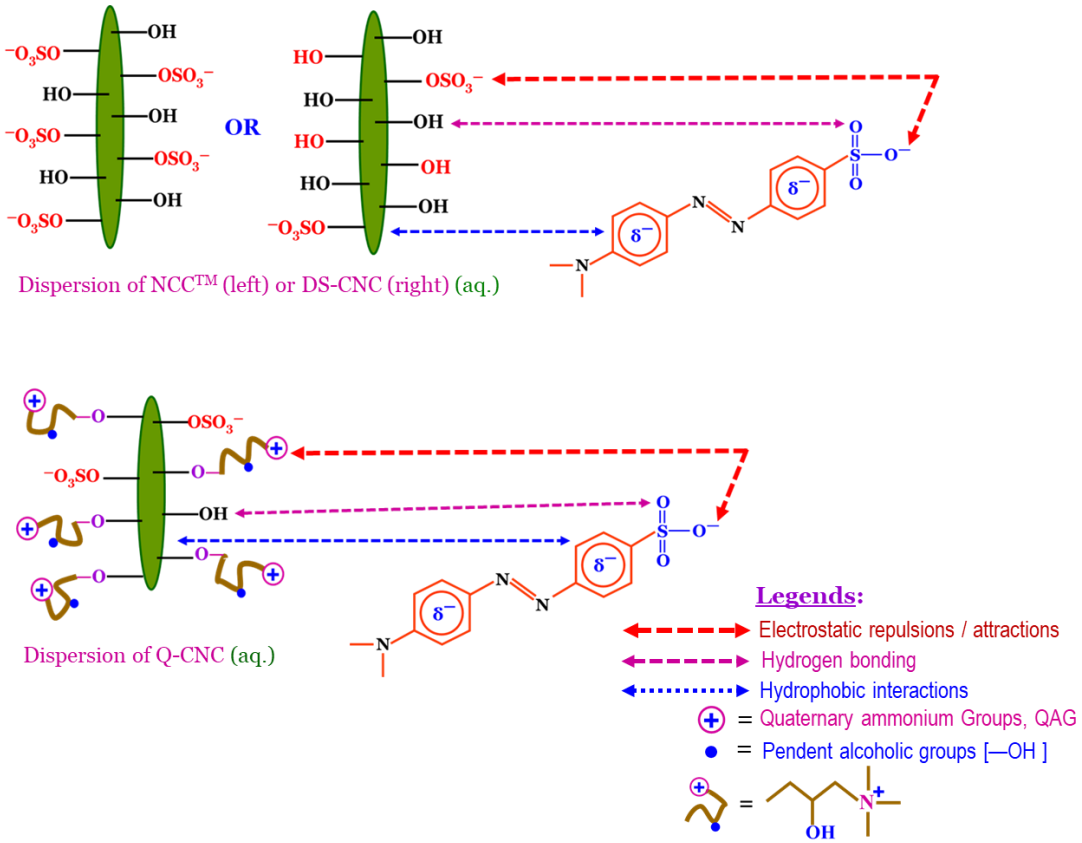


Figure 3.15: *Schematic representations of all probable interactions of MO with NP systems. The figure explains a fraction of the overall adsorption @ the surfaces is still possible even though the NP is negatively charged, and this is feasible due to the existence of other non-electrostatic binding forces (hydrophobic interactions, H-bondings etc.). A strong complex of NP–MO is possible for the cationic NPs even though the NPs are happened to be Zwitterionic.*

In this study, the selected highly anionic NCC^{TM} NPs were considered as the negative control and one of the partially desulfated CNCs, which is the least anionic (in this case, the DS–CNC$_a$), was considered as the positive control. The CNC$_{MCC}$ was also included in this study as a positive control of the BAT experimental design. Both the experimental controls herein would provide us with the information to determine the adsorption/binding or the parameters (effect of nano-sizes and partial negative charges on adsorption) that should be important in developing the next generation S.M.A.R.T.© bile acid sequestrants (BASs). The max. equilibrium adsorption (Q_{max} values) obtained through the linearized fitting of the Langmuir Monolayer Adsorption Isotherm (LMAI) is presented in Table–3.2 and Figure–3.16.

Table 3.4: Summary of the Q_{max} values obtained from the BATs with MO with the control and non-control NPs, and their corresponding aggregate sizes, D_H and ZPs. The sodium salt of the MO of MW of 427.33 g/mole was used for the BATs in this section.

NPs	Q_{max} (mg/g)	Q_{max} (mmol/g)	K_L	ZP (mV)	Size, D_H (nm)
NCC™	35.3	0.11	0.018	– 43.7	107.4
DS-CNC$_a$	82.1	0.25	0.043	– 11.9	147.4
CNC$_{MCC}$	86.4	0.26	0.061	– 6.38	1057
Q-CNC$_3$	118.7	0.36	0.098	27.1	152.0
Q-CNC$_4$	129.1	0.39	0.109	31.4	198.9
Q-CNC$_5$	163.2	0.50	0.122	36.2	228.0
Q-CNC$_6$	203.1	0.62	0.131	43.3	231.3
Q-CNC$_a$	235.2	0.72	0.151	35.8	132.6
Q-CNC$_{MCC}$	206.4	0.63	0.123	38.8	826.2

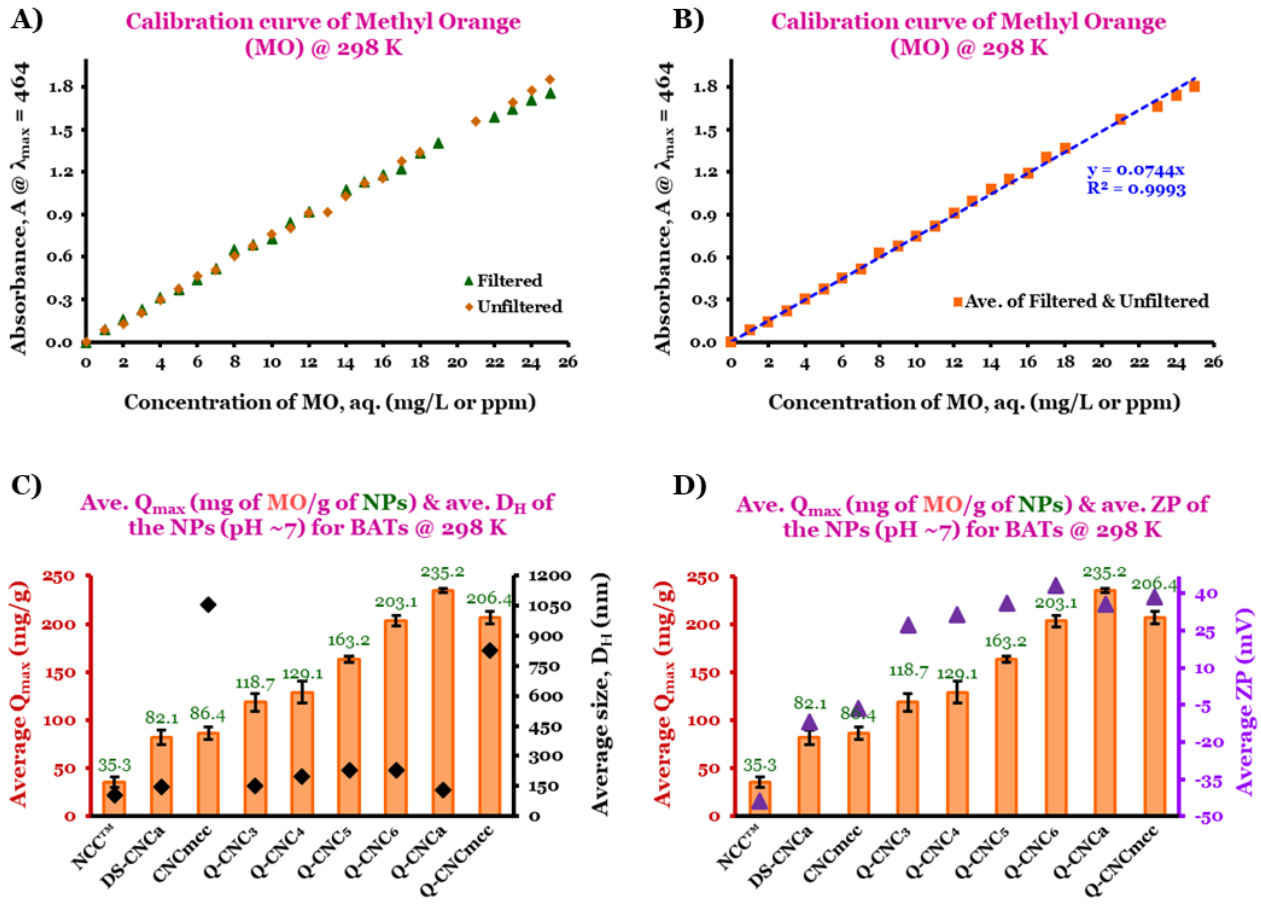


Figure 3.16: A) *The calibration curves of filtered and unfiltered MO reference stock solutions.* ***B)*** *Average of the two calibration curves obtained for the filtered and unfiltered ref. solutions of MO.* ***C)*** *Average D_H and the calculated Q_{max} from the BAT with MO for the chosen NPs. The BATs were done in RT, in inherent (neutral) pH, and the amount/mass of the individual NPs added into the BAT vials was the same for all conc. of the MO. and for the D_H measurements, the conc. of the individual NP was at 0.05% (w/v) aq. suspension.* ***D)*** *Average ZP and the calculated Q_{max} from the BAT with MO for the chosen NPs.*

From the above data, it is apparent that cationic NPs displayed potential for the removal/sequestering of anionic dyes. The highest Q_{max} for the MO adsorption was found to be 235.2 mg/g for Q–CNC_a NPs, where the measured D_H was found to be the lowest and the ZP displayed the highest positive values among all the Q–CNC systems. The Q_{max} for the Q–

CNC_6 and the Q–CNC_{MCC} were quite similar which was slightly over 200 mg/g, although the aggregate sizes (D_H) of these two NP systems were different (as the Q–CNC_{MCC} was synthesized from the CNC_{MCC} NPs which possessed a D_H of ~1053 nm), where the average D_H of the Q–CNC_{MCC} was 826 nm compared to 231 nm for Q–CNC_6 NPs. From the plot, the presented D_H data did not correlate with the Q_{max} values for MO, but a conclusive inference could be drawn from the ZP data, where the surface cationic charges were more descriptive for the adsorption of oppositely charged ligands.

But the effects of nano-sizes are not negligible either, as the negatively charged pristine CNC, the NCC^{TM}, which is the negative control, provided some degrees of adsorption of MO over the BATs. Such adsorption was due to the high surface area of the NPs, as well H–bond-at the exposed surfaces. To validate the negative control, two positive controls were considered for the BATs, namely the DS–CNC_a and CNC_{MCC} NPs. The Q_{max} of DS–CNC_a clearly explained the effect of 'nano' sizes on the adsorption of an analyte, where the ionic charges were similar. Whereas the Q_{max} data of the CNC_{MCC} indicated that in addition to particle size, surface functional groups capable of forming H–bonds with the analytes were also an important factor for the physicochemical adsorption.

To further establish the effect of surface charges and sizes, the charge shielding of NCC^{TM} and DS-CNC_a NPs were conducted by adding highly conc. (50 mM and 100 mM) NaCl and then BATs were conducted (Figure–3.17). Due to the charge shielding, aggregation of the particle occurred, and the aq. suspension turned cloudy. The average D_H data presented in Figure–3.17 confirmed that the interparticle aggregation was due to the H–bonds/Van der

Waals interactions since surface charges were almost neutralized based on the obtained ZP data.

The NCC^{TM} NPs (negative control) were significantly shielded at the salt conc. of 100 mM NaCl which was found ~ – 10 mV and the D_H obtained was 540 nm. For the positive control, the DS–CNC_a NPs were almost fully shielded as the ZP was found to be < –2 mV, with an aggregate size of ~ 1200 nm. From the Q_{max} values of the plot **C)** and the plot **D)** of Figure–3.17 that after the surface negative charges were screened, the adsorption capacities increased several folds indicating that the presence of opposite charges on the surfaces induced stronger adsorption for the NP systems.

From the results, the following conclusions could be determined:

- The physicochemical adsorption of negatively charged NPs offered some degrees of adsorption due to the extensive surface area (SA). Such surface area was the major factor promoting the physical adsorption due to non–electrostatic interactions (Van der Waals, H–bonds etc.).
- Possessing opposite surface charges is the most important factor for monolayer adsorption driven by ionic interactions of the substrates and ligands. The electrostatic interactions are long-range attractive forces that mainly establish the formation of irreversible complexes between the NPs and the analytes.

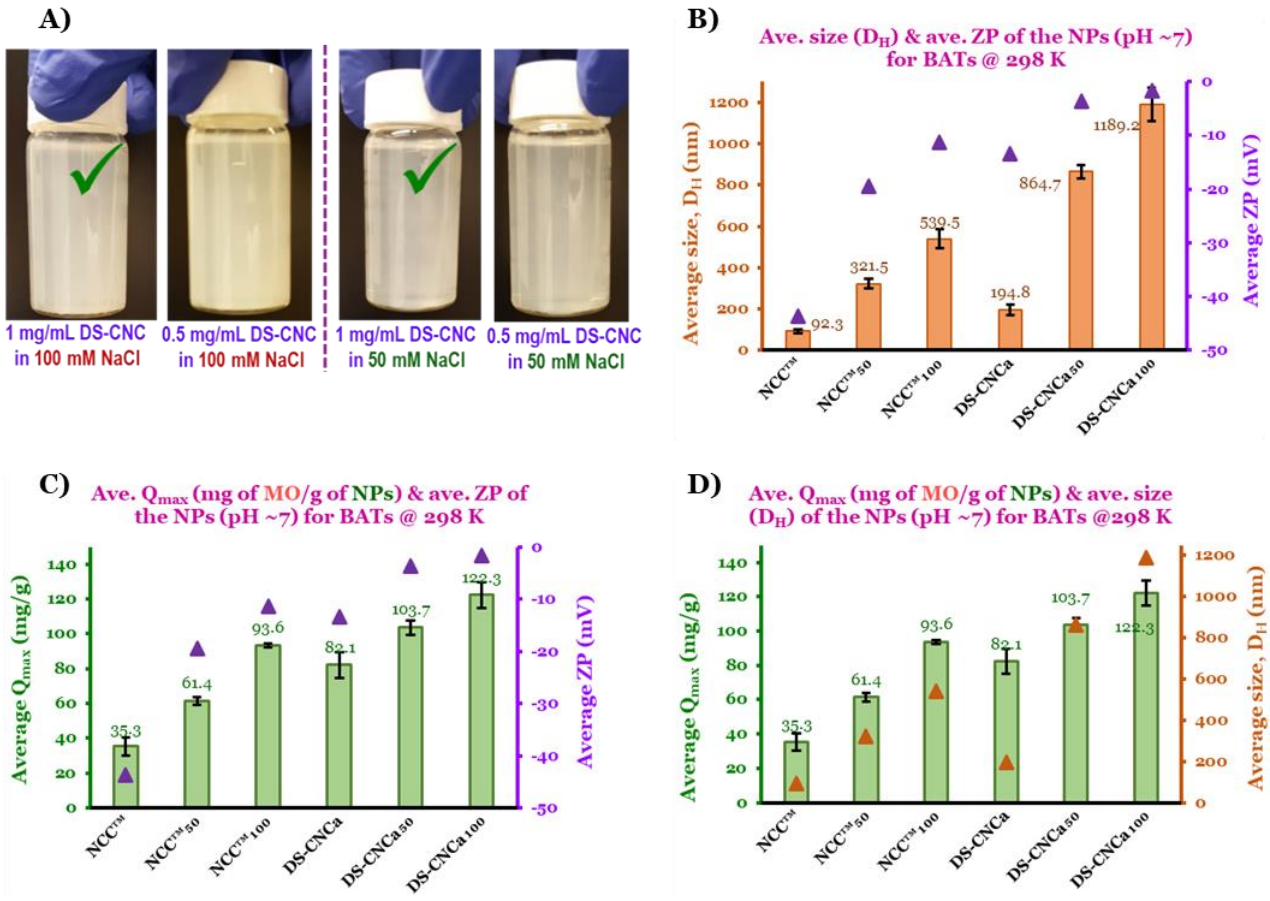


Figure 3.17: A) *The outlook of sonicated aq. DS–CNC$_a$ at two different conc. (0.05 & 0.1 %, w/v) in 50 mM and 100 mM NaCl solutions. All the suspensions became cloudier after the dispersions were made in the NaCl solutions due to the significant extent of aggregation as a result of the charge shielding. Such aggregations are evident from the D_H and the ZP data presented in the plot–**B)**. Both controls (NCC^{TM} and DS–CNC$_a$) at a conc. of 1 mg/mL (0.1%, w/v) were considered for conducting the BATs in charge shielded state with the MO. **C)** Plot comparing/summarizing the ZP, and the Q_{max} values obtained from the BATs with MO through the LMAI linear fitting model. **D)** Plot summarizing the D_H and Q_{max} values of the charge-shielded controls.*

3.5.7.2 BAT with Sodium Cholate (SC) via Conductance and UV–Vis method

For the conductance measurement method and UV-Vis method after converting the SC into coloured analogs, the BATs were conducted on NPs based on the QAG contents, D_H, and the ZP values. Among the library of Q–CNCs, only the Q–CNC_6, Q–CNC_a and Q–CNC_{MCC} were selected for the BATs of SC to evaluate their adsorption efficiencies. Similarly, as mentioned previously, the NCC^{TM}, the DS–CNC_a were considered for conducting the BATs as the negative control and the positive control, respectively. Figure –3.18 shows the possible mechanisms between the SC molecules and Q–CNC NPs and the calibration curves constructed through the conductance method and UV–Vis methods.

Sodium cholate (SC), the sodium salt of one of the primary bile acids in the human body, is highly soluble in water and becomes completely ionized leaving the conjugate base as strongly anionic. Now during the BATs, once the aq. dispersions of the cationic NPs were added, significant electrostatic interactions between these oppositely charged components (NPs and the SC) induced the binding of the molecules onto the surfaces of the NPs. After the addition of the NPs' aq. dispersion into the BAT vessels/vials, all the suspensions instantaneously became cloudy, and as time passed, visible aggregates started appearing for almost all the Q–CNC systems. The other feasible binding mechanisms for such adsorbent–adsorbate complex formation were through the formation of H–bonds, hydrophobic interactions/Van der Waals interactions, all of which are schematically illustrated in Figure–3.18 A).

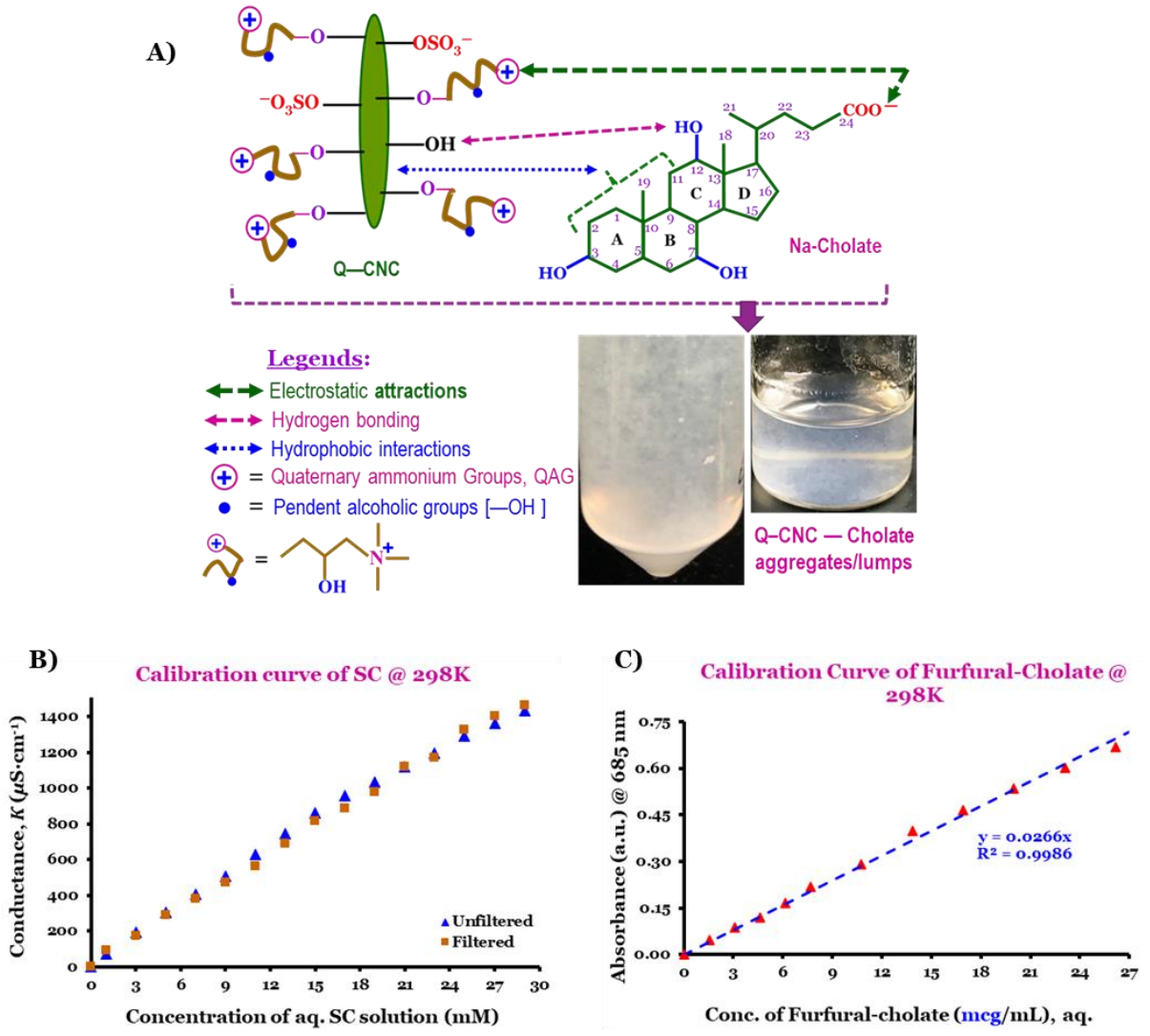


Figure 3.18: A) *The possible mechanisms of physicochemical adsorption of SC onto the surface of a Q–CNC system. During the BATs, most of the Q–CNCs showed distinct and visible aggregates and the commencement of such lumps started appearing slowly the moment after adding the NPs into the vessel containing the aq. solutions of SC. Although the mixture got a bit cloudy for NCC^{TM}, cloudier for DS–CNCs or CNC$_{MCC}$, no distinct aggregates were visible for such NP systems.* ***B)*** *&* ***C)*** *Calibration curves of aq. reference solutions of SC constructed through conductance and UV–Vis measurements, respectively.*

The Q_{max} determined through the Langmuir Monolayer Adsorption Isotherm (LMAI) linear fitting model is shown in Figure–3.19. The negative control, NCC^{TM}, showed some adsorption through the non-electrostatic interactions discussed in section 3.5.7.1 (BATs with MO) and the Q_{max} values were 96.3 mg/g for the conductance method and 42.7 mg/g using the UV–Vis method. In the positive control, DS–CNC_a, with most of the surface negative charges removed as well as many of the 1^0 alcoholic groups freed up, a significant amount of H–bonding and hydrophobic interactions occurred, yielding a Q_{max} of 151.2 mg/g (conductance method) and 186.2 mg/g (UV–Vis method). Among the Q–CNCs, the highest Q_{max} was reported for Q–CNC_a with a magnitude of 421.2 mg/g (conductance method) and 393.7 mg/g (UV–Vis method), although this NPs were termed as moderately Zwitterionic. For the least Zwitterionic NPs, the Q–CNC_{MCC} showed better adsorption for the SC, even though they exhibited interparticle aggregations leading to sizes greater than 800 nm (table 3.2) and the Q_{max} for these NPs was 319.7 mg/g (conductance method) and 361.1 mg/g (UV–Vis method). Lastly, for the Q–CNC_6, being moderately Zwitterionic, the adsorption capabilities were affected due to the interparticle aggregation, but the sorption profile was found to be similar to Q–CNC_{MCC}.

Except for the Total Bile Acid (TBA) Assay kit (Colorimetric; BioVision, Inc.), as there was no accessible and user-friendly tool to quantify SC, two ‘not widely used’ methods reported in the literature were utilized. Due to the nature of the reaction in the formation of furfural–cholate, and the strict time control, the obtained Q_{max} values for the SC displayed a large standard deviation/error making this technique less reliable than the conductance method. And for the conductance method for the BATs, the blank used was the 0.1 % (w/v) aq.

suspensions of the corresponding NPs so that the effect of counterions (mostly the chloride ions, Cl^{-}) on the specific conductance were accounted for during the measurement for the post–BAT filtrated solution.

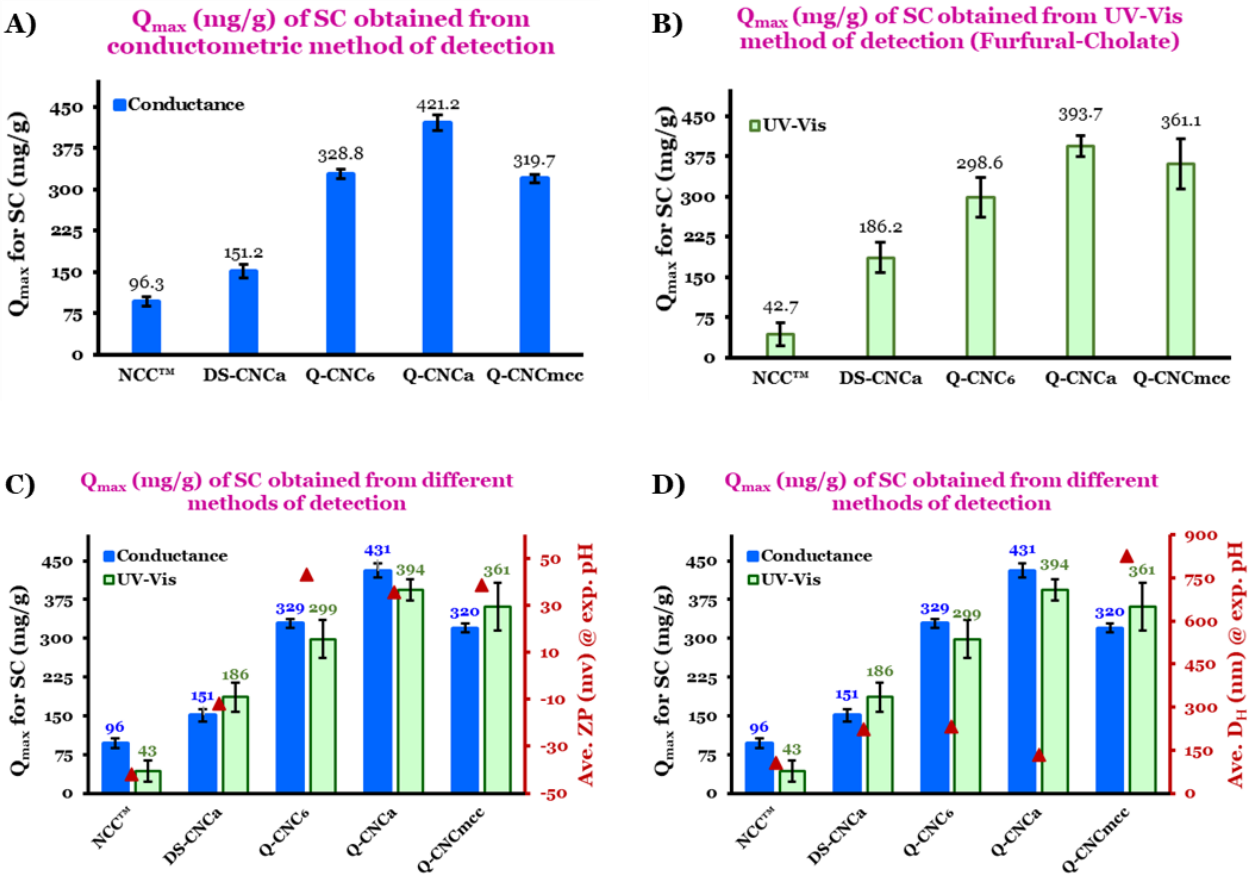


Figure 3.19: *The Q_{max} values obtained for SC through the LMAI linear fitting from the BATs via* ***A)*** *Conductance measurements, and* ***B)*** *UV–Vis measurements. Plots* ***C)*** *and* ***D)*** *summarized those Q_{max} values with the ZP and the D_H respectively.*

3.6 Conclusions

This chapter discusses the evolution and systematic development of CNC-based NP systems that possessed varying cationic charges with traces of negative charges from the SHE (—OSO_3^-) groups. Such Zwitterions NPs were more hydrophilic (thus easily dispersible in water) than their unmodified counterparts were capable of retaining the overall cationic charges over the GI pH ranges. As these 'green' NPs were produced from natural and sustainable sources (the CNCs; nontoxic, biocompatible), they are as attractive candidates for many different applications, such as effluent treatment or plasma cholesterol reduction by sequestering the bile salts.

After several physicochemical characterizations of these 'green' (natural) NPs using different tools, they were evaluated for their binding efficiencies with negatively charged ligands through the batch adsorption tests, BATs. In the BATs, the binding or adsorption efficiencies (determined by the Q_{max} values) of the NPs for the ligand/analyte offered insights on their removal efficiencies for the targeted analyte. The most cationic CNCs (C–CNCs) notably the Q–CNC_6, Q–CNC_a and the Q–CNC_{MCC} NPs were proven to have the capability of removing an anionic dye, MO from a solution confirming their potential use in effluent treatments. Due to the lack of a robust tool for the detection of bile salts, the MO was used as the surrogate marker for bile salts and the obtained data could be extrapolated to indicate the efficiency of their adsorption of bile salts.

Further studies on the Q–CNCs with SC revealed a huge breakthrough of their efficiencies to bind with (in other words remove/sequester) the bile salt (sodium cholate, SC is the representative molecule) from the solution. The determined Q_{max} of the Q–CNC_6, Q–CNC_a

and the Q–CNC_{MCC} NPs systems for the SC was almost 1.5 – 2 times higher than the MO. Such evaluation confirmed that the developed NP systems possessed significant capabilities to adsorb or conversely sequester/remove the bile salts from a bulk of samples, making them as efficient S.M.A.R.T.© BAS for use as the next-generation alternative to 'intolerable' cholestyramine.

Chapter 4: Hydrophobically modified PS based NMs as BAS

4.1 Introduction

The modified CNCs with the GTMAC molecules imparted the Q–CNCs NPs with more hydrophilic characteristics, which was discussed in Chapter 3. Additionally, BATs revealed the role of hydrophobic and electrostatic interactions between SC molecules and hydrophilic Q–CNCs. As one of the major objectives of this Ph.D. study is to achieve better PS (polysaccharide) based NMs that possess the capabilities to form irreversible NM–BS/BA complex. Hence, the modification of cationic CNC with a hydrophobic moiety could enhance the binding with SC molecules. From the discussion in Chapter 2, we noted that a hydrophobic group containing C–12 chain offers a balance between the overall hydrophilic–hydrophobic nature for the modified NPs. Based on this observation, a new hydrophobic molecule consisting of an epoxide moiety N,N-Dimethyl-dodecyl (1,2 epoxy propyl) ammonium chloride (DDEAC), (similar to GTMAC), with a C–12 chain, was synthesized. Modification of chitosan (CS) with such molecules are reported in literature,[178,179] but being *de novo* grafting for CNCs, we utilized the same reaction methodology similar to GTMAC grafting, for the quaternization of CNCs with the DDEAC which yielded NPs systems denoted as Q–C_{12}–CNC. For quaternization, DS–CNC_6 was used as the base material, and the NP was evaluated for the adsorption efficiencies for anionic ligands through methods described in Chapter 3.

In addition to the Q–C_{12}–CNC, a polymeric CNC-based system making the CNC amphiphilic (possessing both hydrophilic and hydrophobic domains) was considered in this chapter. The 2-(Dimethylamino) ethyl methacrylate (DMAEMA) monomer was grafted onto

the CNC surfaces via the atom transfer radical polymerization (ATRP) followed by quaternization reaction with methyl iodide (CH_3I) to impart permanently cationic charge (denoted as CNC–g–pQDMAEMA). The NPs were evaluated for their adsorption capacities of anionic molecules (e.g., methyl orange, MO & sodium cholate, SC etc.).

One of the most widely used bio–PS in the biomedical field, chitosan (CS), was also considered for the scavenging of BS/BAs. Here the commercially available (85% DD), chitosan (CS), is a linear polysaccharide composed of randomly distributed β-(1-4)-linked d-glucosamine and N-acetyl-d-glucosamine (structural representation in molecular level is shown in Figure–4.1) and is insoluble in water (green solvent) or most of the organic solvents.[180–183] It is the deacetylated derivative of α–chitin, which is the second most abundant bio–PS after cellulose.[48,184] CS and its derivatives (modified/functionalized CS) have long been approved by the US–FDA for commercial use in food, biomedical and pharmaceutical fields due to their safety, non-toxicity, biodegradability, biocompatibility and beneficial antimicrobial and antifungal activities.[180–183] However, their limited solubility in most solvents limits their application and hence modifications of CS had used to prepare water-soluble derivatives with permanent cationic charges. Such quaternized/cationic–CS (Q/C–CS) NPs or the block type binary (gemini) polymers via grafting the Q–CS onto the CNC systems (QCS–CNC) were then evaluated for their efficiency in the adsorption of MO/SC.

The *in vitro* evaluation of the adsorption efficiencies of the NP systems namely the Q–C_{12}–CNCs, CNC–g–pQDMAEMA, Q–CS, and QCS–CNCs will be discussed in this chapter offering insight necessary for the development of BASs with better adsorption profile. The discussion would also provide the reader with the information to compare the PS-based BAS.

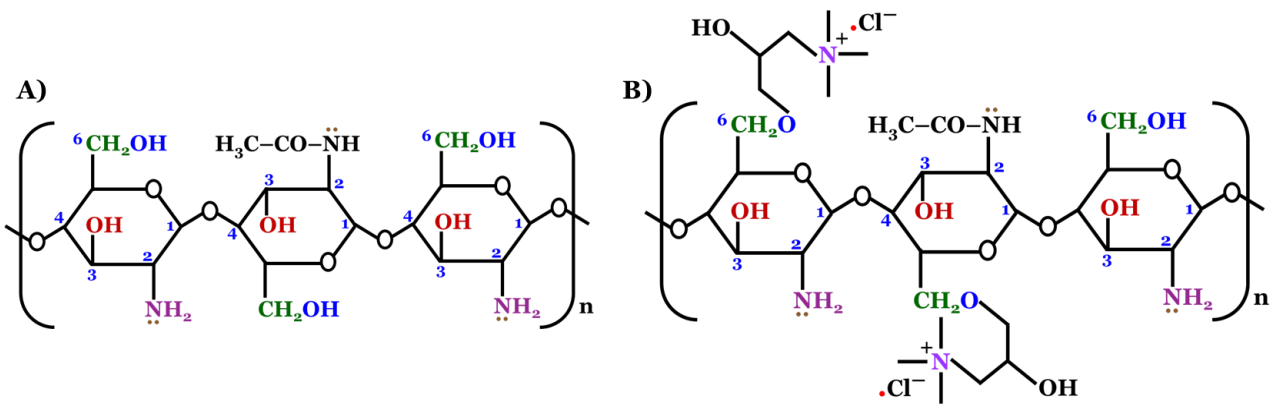


Figure 4.1: A) *Molecular structure of commercially available CS (DD = 85%) showing the groups/positions that can be functionalized: chemical modifications are feasible on the C–6 @ the primary alcoholic groups and on the —NH_2 groups @ C–2. Due to a very strong steric hindrance, no chemical modification is possible on the —OH groups @ C–3. The available free —NH_2 groups @ C–2 are the primary amines that always get protonated at any pH below ~8 (thus pH-responsive) to provide cationic functionalities of the molecule.* ***B)*** *A basic representative of cationic CS where many of the —OH groups (depending on reaction efficiencies) @ C–6 have been functionalized with GTMAC making the CS permanently cationic (the Q–CS), regardless of the pH.*

4.2 Materials and Methods

4.2.1 Materials:

The N,N-dimethyl-N-dodecyl amine, DMDA (MW = 213.4 g/mol, density = 0.79 g/mL), epichlorohydrin (1-Chloro-2,3-epoxypropane, MW = 92.5 g/mol, density = 1.18 g/mL), 2,2,6,6,-tetramethyl-1-(pyperidinyloxy) radical (TEMPO), sodium bromide (NaBr), sodium hypoclorite solution (NaClO; reagent grade, available chlorine 10-15 %), 1-ethyl-3-(3-dimethylaminopropyl) carbodiimide, EDC/EDAC (MW = 155.24, free base basis) and N-Hydroxysuccinimide (NHS), 2-(N-Morpholino) ethanesulfonic acid (MES) buffer, 2-

dimethylaminoethyl acrylate, DMAEMA (MW = 157.2 g/mol, density = 0.93 g/mL), methyl iodide (iodomethane, MW = 141.94, density = 2.28 g/mL, b.p. = 41–43^{0}C) were purchased from Sigma-Aldrich and used as received without any further purification. Chitosan, CS from shrimp shell (≥ 85% deacetylated, low MW ~ 90–125 KDa) was purchased from Alfa Aesar (part of Thermo Fisher Scientific) and used as received without any further purification. Purified water (Milli-Q water) from a Millipore system (>18 MΩcm) was used to prepare the samples. The GTMAC and all the other commonly used chemicals, such as NaOH/KOH, KCl, NaCl, potassium hydrogen phthalate (KHP), HCl acid (37% w/w), H_2SO_4 (98% w/w), glacial acetic acid (99.7% w/v) and all the other solvents like dimethyl sulfoxide, DMSO (boiling point, b.p.= 189^{0}C), 2–propanol or isopropyl alcohol (IPA, b.p. = 82.5^{0}C), methanol etc. were also purchased from the MilliporeSigma and were used as received.

4.2.2 Synthesis of DDEAC surfactant & Q–C_{12}–CNC_a NPs

The N,N-dimethyl-N-dodecyl-N-(1,2 epoxy propyl) ammonium chloride (DDEAC) was synthesized following the method described in the literature[178,185,186] with some modifications as shown in Figure–4.2. Briefly, 68 mL N,N-dimethyl-N-dodecyl amine (DMDA), 78 mL epichlorohydrin, [Epichlorohydrine **:** DMDA = 4 **:** 3 (weight ratio)] and 90 mL IPA (b.p. 82.5^{0}C) were added to a round bottom flask (RBF). The reaction mixture was stirred at 500 rpm for 30 hours at 30^{0}C under nitrogen purge to ensure an inert ambient environment inside the RBF. Then the IPA was removed using a Heidolph™ Hei-Vap™ rotary evaporator at 95°C, and the resulting semi-solid residue was repeatedly washed with large excess diethyl ether. After purification with ether, the DDEAC surfactant residue was dissolved in a minimum

volume of IPA, and the trace ether was then removed by further rotary evaporation at 60^0C to concentrate the soluble product. Finally, the yellowish liquid of the surfactant solution of moderate viscosity was stored in a container and the conc. was recorded through the GA denoting a 75% yield.

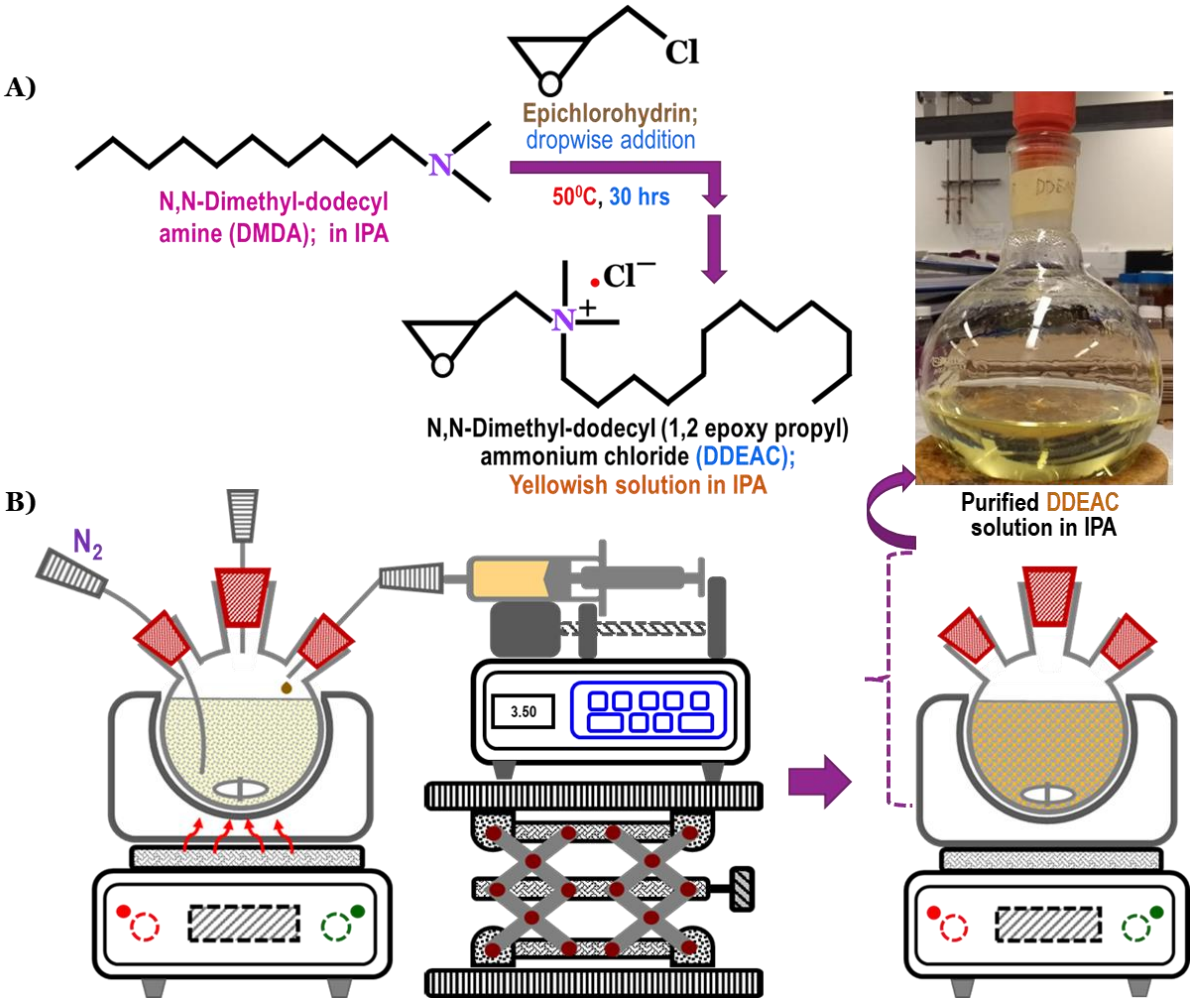


Figure 4.2: A) *Reaction mechanism of synthesis of DDEAC surfactant containing epoxide ring within the structure.* ***B)*** *DDEAC synthesis setup and outlook of the final product as in solution in IPA. Stored in RT after recording the conc. via the GA while the yield was also recorded.*

Once the characterization of the synthesized DDEAC was performed via Surface Tensiometry (ST), the quaternization of a selected DS–CNC with the DDEAC was conducted (illustrated in Figure 4.3), which was followed by purification as reported for the GTMAC mediated quaternization in the Chapter–3. For this reaction, the DS–CNC_6 was used for quaternization, where the stored DS–CNC_6, was redispersed in the IPA **:** H_2O mixture (90 **:** 10) to perform the quaternization reaction. The hydro–alcoholic mixture (IPA–Water) was chosen for this reaction as this reaction media has a better CRE% (cationization reaction efficiency) of the NPs as reported in Chapter 3 as well as the DDEAC was readily soluble in IPA.

After the synthesis of the Q–C_{12}–CNC_6, the purification was performed following the routine procedure as described earlier, and the concentrated suspension was then stored as a never-dried suspension at 4 – 8^0C (refrigerator) by recording the conc. and yield % obtained through gravimetric analysis (GA). Lastly, a small amount of the stored suspension was freeze-dried using the FreeZone 2.5L (–50^0C collector) benchtop freeze dryer (Labconco, Kansas City, MO) for FTIR characterization of the Q–CNC NPs.

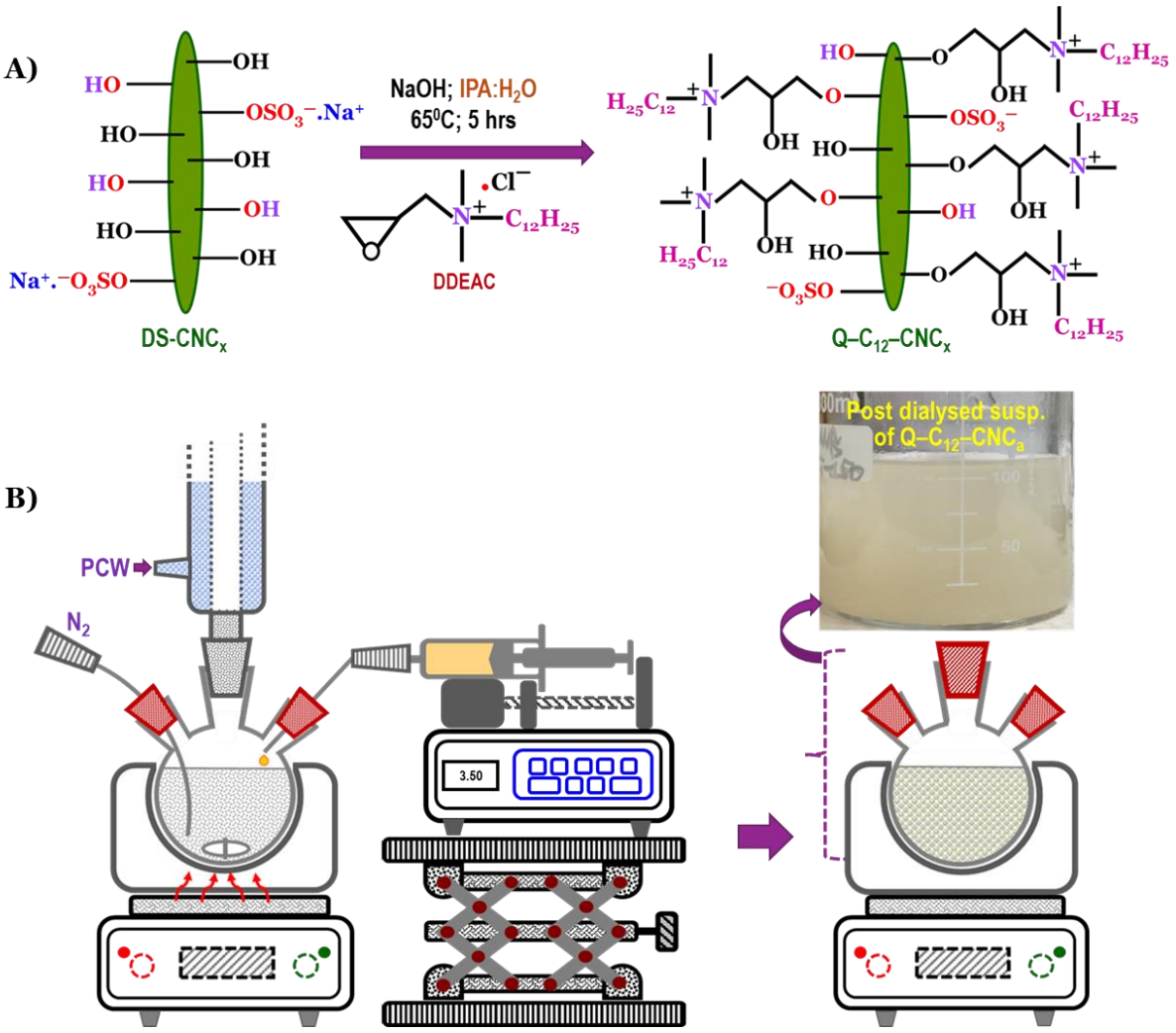


Figure 4.3: *Schematic representation of the quaternization (**a de novo synthesis**) of DS–CNC$_6$ with the synthesized DDEAC. **A)** Reaction steps showing the S$_N$2 reaction and the final Q–NP, structurally which is a Zwitterion having a C–12 hydrophobe (dodecyl alkyl chain) onto the grafted QAG. **B)** Schematic of the reaction setup at the laboratory scale, the insert represents the purified Q–C$_{12}$–CNC$_6$ Zwitterions which were then stored under refrigeration as the never dried suspension for further usage.*

4.2.3 Synthesis of quaternized chitosan (Q–CS)

The synthesis of QCS–g–CNC NPs were performed according to the three reaction steps:

i. Synthesis of a water-soluble derivative of chitosan [the quaternized chitosan (Q–CS)] with GTMAC, which is denoted as N-(2-hydroxyl) propyl-3-trimethyl ammonium chitosan chloride (HTCC)
ii. Synthesis of oxidized CNC (CNC_{OX}) with surface carboxylic acid groups (— COO^{-}) through 2,2,6,6-Tetramethyl-1-piperidinyloxy (TEMPO) mediated oxidation,
iii. Grafting of HTCC onto CNC_{OX}.

4.2.3.1 Synthesis of the quaternized chitosan (Q–CS), the HTCC

As the first step of the overall synthesis, the N-(2-hydroxyl) propyl-3-trimethyl ammonium chitosan chloride (HTCC), or quaternized chitosan (Q–CS) was produced from a one-step reaction with slight modification[187–189], and the reaction scheme is shown in Figure–4.4. Briefly, 2g of low molecular weight chitosan (CS) oligosaccharide (average MW ~110 KDa; degree of deacetylation, DD ~85 %) was dispersed in 100 ml of 1.0% (w/w) acetic acid (CH_3–COOH; or in short HAc./AcOH) solution, followed by homogenization with Ultraturrax T25 homogenizer (IKA, Germany) for 10–15 minutes to ensure the complete dissolution of the CS polymer with a pH of ~2.9. In the acidic solution, the CS was brownish-yellow in color, slightly viscous, and with the characteristic smell of HAc. [Viscosity: 50–500 cP for a 1% w/v solution in 1% acetic acid, information provided from supplier].

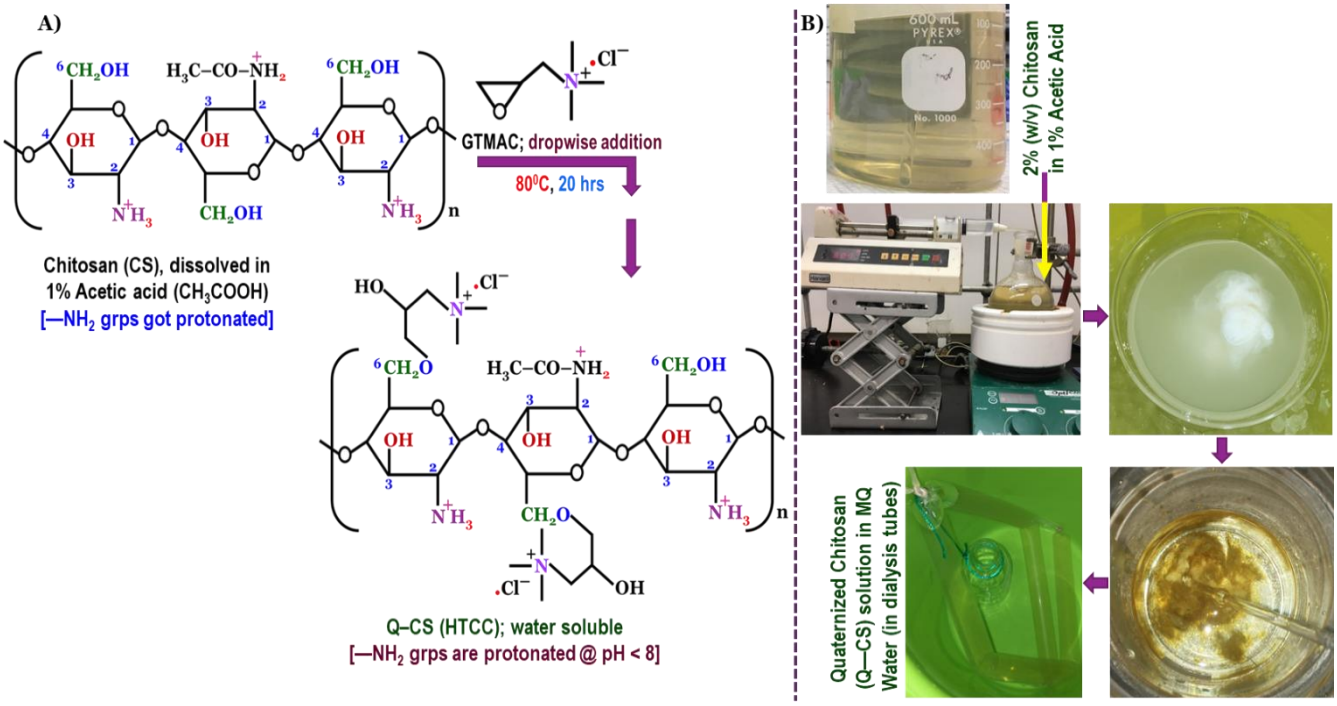


Figure 4.4: A) *Schematic representation of the reaction scheme for the synthesis of Q–CS (HTCC).* ***B)*** *The overall reaction setup and purification of HTCC. The purified HTCC was found completely water-soluble and was seen as slightly yellow/brown in aq. solution. The solution was stored at RT recording the conc. (obtained via GA) and was ready to use.*

The mixture was transferred to a round bottom flask, and GTMAC solution was added dropwise at a 1**:**12 molar ratio (glucosamine/GTMAC) when the temperature of the acidic CS solution approached 80^0C to achieve a higher (desired) degree of quaternization and stir at 600 rpm for 20 hours. The reaction was stopped after 16 hrs, and upon cooling to room temperature, acetone (4 – 8^0C) was added to the mixture at a 5**:**1 volume ratio. The addition of acetone coagulated the Q–CS as it sedimented to the bottom and recovered. It was then washed twice with excess acetone and dried in the vacuum oven to remove the trace amount of acetone. The solid was dissolved in water and dialyzed in DI water to remove unreacted GTMAC and trace

of acetone. The dialysis was (MWCO 12–14 KDa) conducted against deionized water for one week with continual water change until the measured water conductivity remained constant. The post-dialyzed solution of the purified Q–CS was stored in the refrigerator and a small amount of the sample was dried in the freeze dryer for FTIR characterization.

4.2.3.2 Synthesis of the oxidized CNCs (CNC_{OX}): TEMPO mediated oxidation

The surface hydroxyl groups of CNC can be oxidized to carboxyl groups using sodium hypochlorite (NaClO) assisted by 2,2,6,6-tetramethyl-1-(pyperidinyloxy) radical (TEMPO).[188,190,191] TEMPO is a stable and water-soluble nitroxyl radical and due to its steric hindrance, it can only oxidize the primary hydroxyl groups on CNC to carboxylic acids. After sonication of the refrigerated DS–CNC_a or the CNC_{MCC} in a Branson 1510 sonicator (Branson Ultrasonic Corporation, USA) for 10 min., an equivalent amount of suspension containing 1.3 g (8.02 mmol glycosyl units) of the CNC was transferred to the RBF. Then, TEMPO (20 mg, 0.128 mmol) and NaBr (400 mg, 3.880 mmol) were added to the CNC suspension and stirred for 30 min at room temperature. Then the pH of the solution was adjusted to 10 – 10.5 by adding 0.1 M NaOH. The oxidation was initiated by slowly adding NaClO 13% (9.8 ml, 17.114 mmol) over 30 min under gentle agitation. The pH was kept constant at 10, by continuous micro-addition of NaOH. The reaction was complete when no further reduction/change in the pH was observed, (approximately by 4 hrs). After 4 hrs, excess oxidant was quenched using MeOH or EtOH (10 mL) to terminate the oxidation and the pH was adjusted to 7 using 0.1 M HCl. To purify the oxidized nanocrystals, the solution was dialyzed against distilled water for at least 72 hrs. Figure–4.5 describes the overall reaction and synthesis protocols.

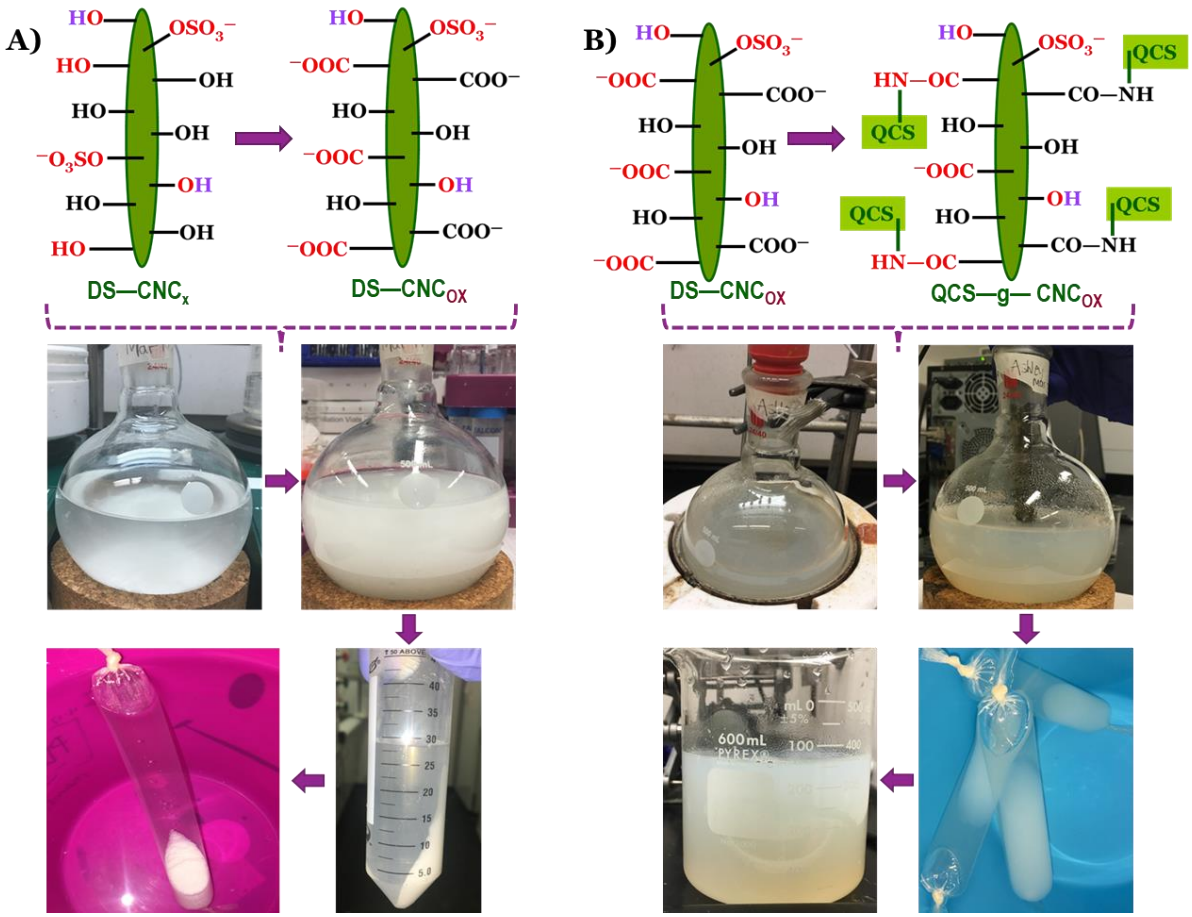


Figure 4.5: A) *Reaction scheme and laboratory setup for the synthesis of* ***A)*** *TEMPO-oxidized CNC from a selected DS–CNC or NCC™, and* ***B)*** *the QCS–g–CNC$_{OX}$ from the oxidized CNC NPs, which are structurally considered as a block type (M–N–M type) NPs and are Zwitterions having traces of both of the SHE groups (—OSO$_3^-$) and —COO$^-$ groups along with the grafted Q–CS fibers. This overall cationic NPs were stored in the fridge for longer storage as the never-dried suspensions, recording the conc. and yield%. In both cases of the syntheses, the NPs obtained were found less stable, especially the DS–CNC$_{OX}$ which readily settled down at the bottom from the dispersions. The QCS–g–CNC$_{OX}$ NPs were found a bit more stable than those of the CNC$_{OX}$ NPs.*

4.2.3.3 Grafting of QCS on the CNC_{OX} NPs using EDC crosslinker

For the last synthesis step,[188] an equivalent volume of 0.2 g CNC_{OX} was dispensed into an RBF. A 50 mL solution containing 1-ethyl-3-(3-dimethylaminopropyl) carbodiimide (EDC, 0.19g, 1 mmol) and N-Hydroxysuccinimide (NHS, 0.11g, 1 mmol) was then added to the CNC_{OX} suspension and stirred for 15 min. Another portion of the solution containing 0.36 g HTCC was dispensed and added to the first solution to yield a ~200 mL reaction volume. 2-(N-Morpholino) ethanesulfonic acid (MES) buffer (1.95g, 0.05 M) was added to the reaction medium and the pH was adjusted to 5 using 1 M NaOH or HCl. The reaction was stirred for 24 hrs at RT and dialyzed (MWCO: 12,000 Da) against D.I. water for 4 days until the conductivity of the dialysis medium remained constant.

4.2.4 Synthesis of pQDMAEMA–g–CNC NPs by Free Radical Polymerization[116]

Here the synthesis was done in two separate reaction steps as follows:

i. First, synthesis of the polymeric CNCs from the monomer DMAEMA producing the pDMAEMA–g–CNCs,[192] and
ii. Quaternization of the pDMAEMA–g–CNC using methyl iodide, MeI (CH_3I).[192]

4.2.4.1 Synthesis of pDMAEMA–g–CNC by ATRP

The reaction scheme of the synthesis of CNC-g-PDMAEMA and quaternization of pDMAEMA–g–CNC is shown in Figure–4.6. Briefly, an equivalent volume of 2 g DS–CNC was dispensed in an RBF, sonicated, and purged with nitrogen for one hour (1 hr) at room temperature (i.e., 25^0C). Then, 300 mg APS (or appropriate volume of APS dissolved in water,

freshly prepared) was added to the RBF under stirring at a temperature of 60^0C. About 10 – 15 minutes was allowed to raise the temperature up to 60^0C during degassing (10 – 15 minutes).[192]

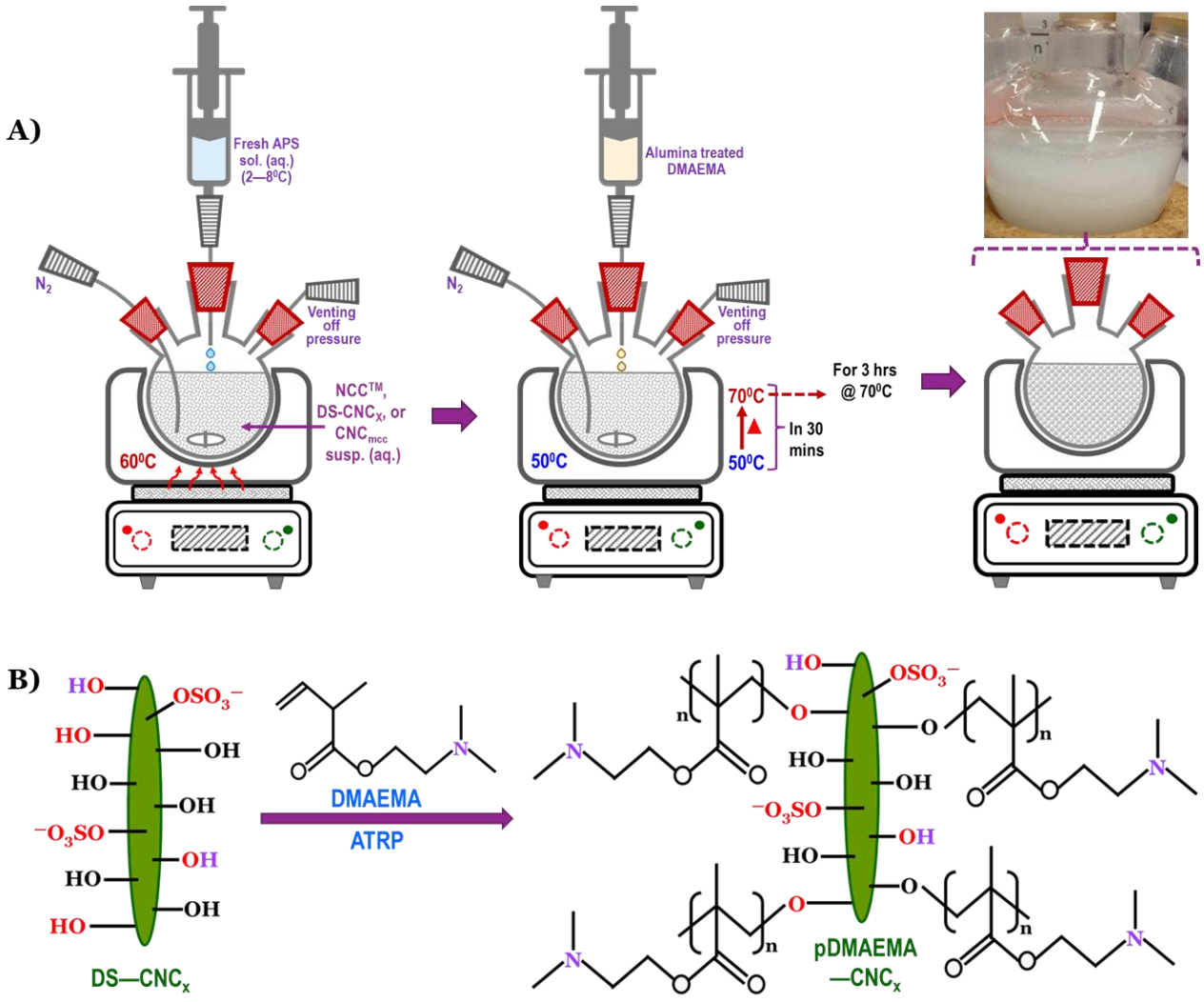


Figure 4.6: A) *Synthesis set up and steps of pQDMAEMA with the monomer DMAEMA.* ***B)*** *Corresponding polymerization reaction scheme of the synthesis from DS–CNC$_x$ via ATRP.*

Once the degassing was completed, the temperature was reduced to 50^0C, and 2.14 mL of alumina treated and degassed DMAEMA was added and the temperature was gradually raised to 70^0C over 30 min, and the reaction was conducted for 3 hr under continuous stirring. After completion, the product was centrifuged and washed with excess MilliQ water 3–5 times. Dialysis was conducted against DI water for 5 days followed by MQ, and the final product (pDMAEMA–g–CNC) with known concentration and yield (%) was stored in the refrigerator.

4.2.4.2 Quaternization of the synthesis of pDMAEMA–g–CNC by MeI[192,193]

The equivalent dispersion containing 300 mg of pDMAEMA–g–CNC and MeI (2 mL) were both dispensed in an RBF and stirred for 7 days (Figure-4.7). The crude p**Q**DMAEMA–g–CNC was purified by evaporating excess MeI under vacuum. After that, the quaternized NP dispersion was then purified via consecutive washing and centrifugation cycles in water (x 4) and finally stored under refrigeration (4–8^0C) while recording the conc. and the yield%. A small portion of the NPs was freeze-dried for FTIR characterization, and an off-white powder was obtained after drying.

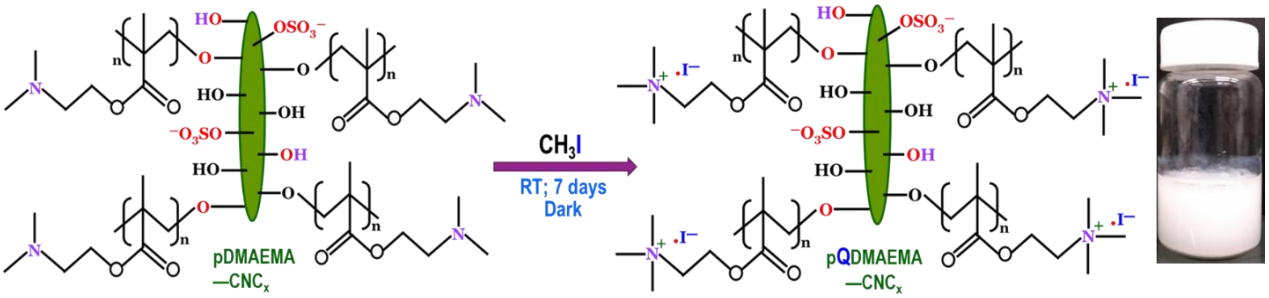


Figure 4.7: *Quaternization of the pDMAEMA–g–CNC using MeI at the RT*[192,193]*. The pQDMAEMA–g–CNC is structurally a Zwitterion, and a significant extent of aggregation was seen in the post-dialyzed suspension, which was stored at 4–8*^{0}*C.*

Figure–4.8 summarizes the NPs that were synthesized and discussed in this chapter.

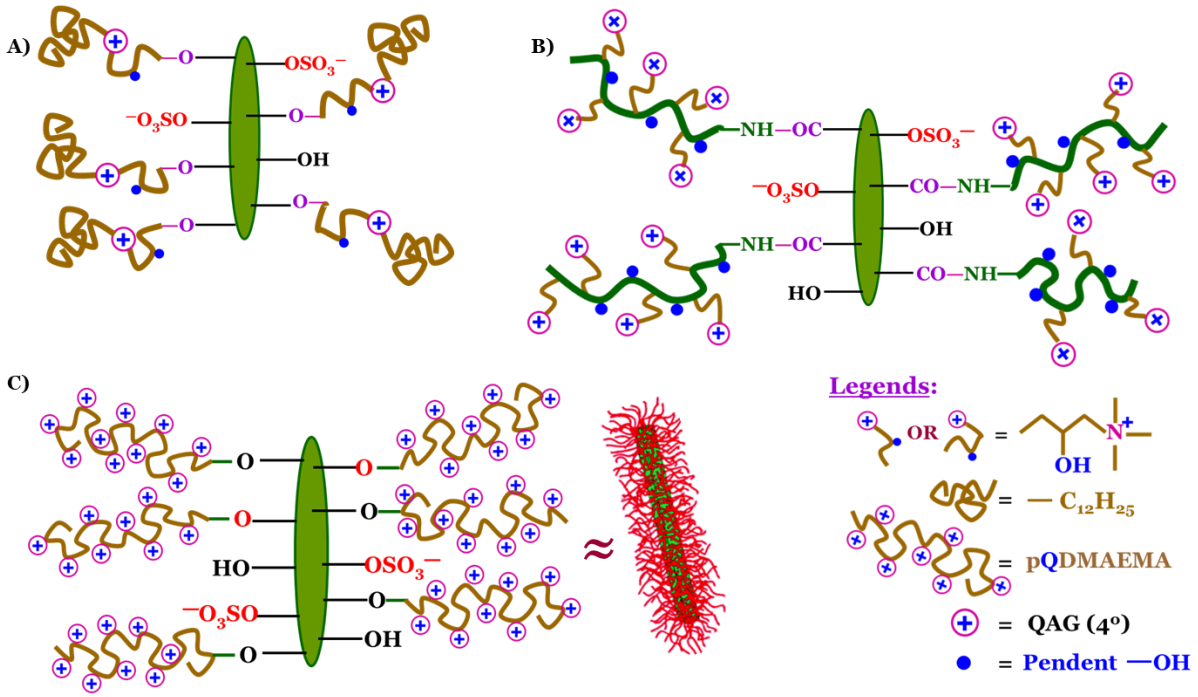


Figure 4.8: *Schematic structural representations of Zwitterionic NPs to be discussed in this chapter,* ***A)*** *the Q–C12–CNC*$_6$*,* ***B)*** *the QCS–g–CNC*$_x$*, and* ***C)*** *the pQDMAEMA–g–CNC*$_x$ *NPs which resemble like the bottle-brush. The associated counter ions for the QAGs are chloride (Cl*$^-$*) for* ***A)*** *and* ***B)****, and for the* ***C)*** *it is iodide (I*$^-$*)*

4.2.5 Method: ^{1}H NMR characterization

The ^{1}H NMR measurements for the synthesized surfactant, DDEAC was conducted at 25.0 ± 0.1^{0}C on a Bruker Avance NMR spectrometer operating at 300 MHz with the field strength of 7.0 Tesla. D_2O and CD_3OD (99.9 atom % D) were used to prepare the stock solutions (7-10 mg/mL) of the surfactants for ^{1}H NMR study. The peaks were referenced with respect to tertamethylsilane, TMS (δ = 0.00 ppm) when CD_3OD was used as a solvent and to 4,4-dimethyl-4-silapentane-1-sulfonic acid, DSS (δ = 0.00 ppm) when D_2O and/or DMSO was used as a solvent. In all NMR experiments, the number of scans (16 on average) was adjusted to achieve a good signal-to-noise and was recorded with a two-second relaxation delay in a digital resolution of 0.04 Hz/data point at a flip angle of 30^{0} of the pulse program. The following notation was used for the ^{1}HNMR splitting patterns: singlet (s), doublet (d), triplet (t), multiplet (m), and double doublet (dd). Data analyses were done through MestreNova (Mnova NMR) software.

4.2.6 Surface Tensiometry (ST)

Surface tension measurements for the DDEAC were conducted on a DCAT 11 (Dataphysics) tensiometer. Continuous dosing was performed by a liquid dispensing unit (LDU) that is capable of dosing microliters of titrants. The Wilhelmy plate method was used to measure the dynamic surface tension at the air-water interface to determine the critical micelle concentration (CMC) of DDEAC. A highly concentrated aqueous solution (12.5 mM) DDEAC was periodically titrated into the water to gradually increase the concentration to 3 mM, with surface tension measurements taken after each titration.

4.3 Results and Discussion

4.3.1 CMC determination of DDEAC

The % yield of the DDEAC was recorded as ~75%. The determined surface tension (SFT) of the DDEAC was found to be 1.79 mM which was in close agreement with reported values from literature[185] (1.88 mM). This confirmed that the synthesized DDEAC was produced successfully with high purity. Figure–4.9 shows the SFT plot and the point of intersection that corresponded to the formation of the micelles.

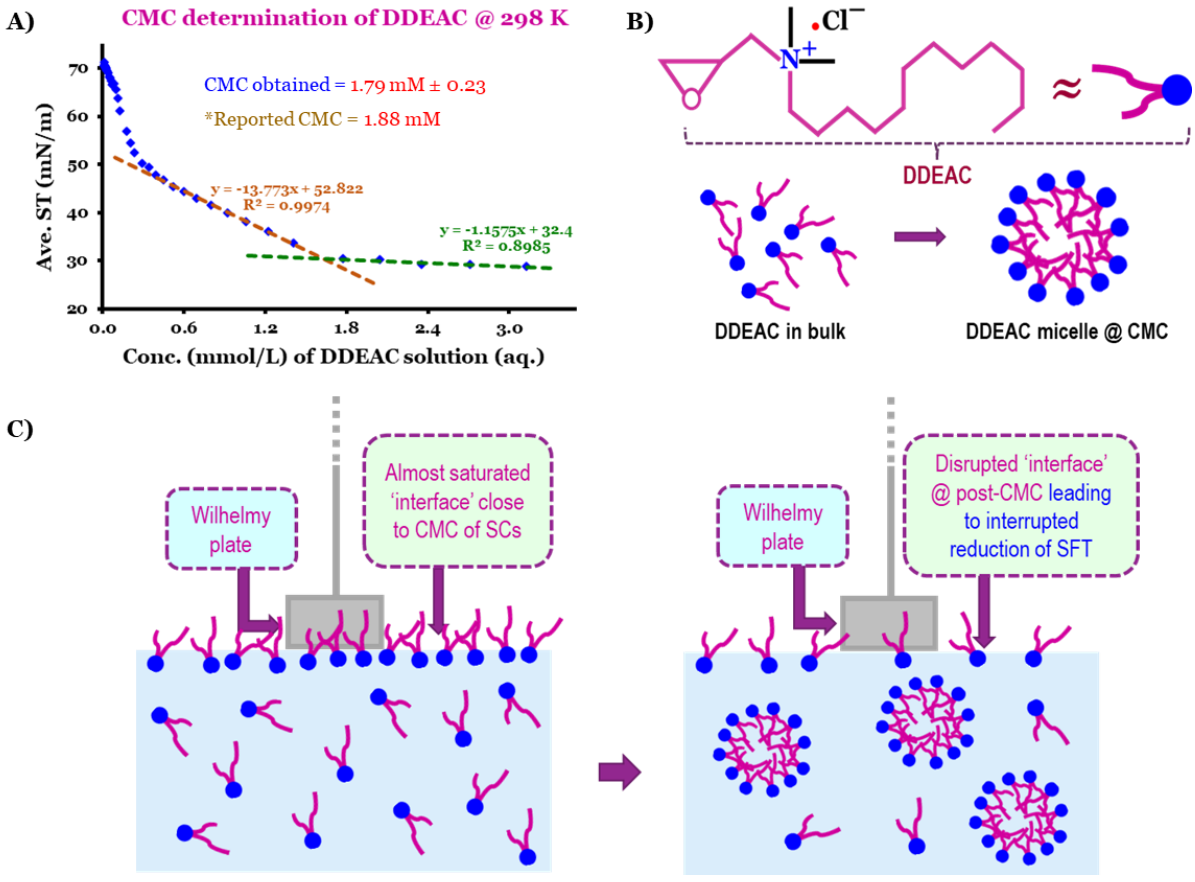


Figure 4.9: A) *SFT plot of DDEAC obtained from the Tensiometer.* ***B)*** *DDEAC molecule's chemical structure and schematic representation of the micelles.* ***C)*** *Fate of the DDEAC molecules at the water–air interface as the conc./no. of the molecules increases due to addition.*

It is well-known that the SFT reduction is significantly controlled by the monomer concentration and less on the aggregates/micelles. Additionally, a saturation of the surface layer (interfacial layer) corresponds to the interfacial saturation of the monomer. All excessive surfactant molecules form micelles and do not affect the surface layer, which participates to a limited degree in the SFT reduction. Such phenomena are schematically represented in Figure–4.9 (C).

4.3.2 Yield and QAG contents

From gravimetric analysis (GA) the corresponding concentrations were determined, and then the % yield was calculated. Here, the highest yield% was achieved for the Q–CS systems whereas the Q–CS grafted NPs (QCS–g–CNC_a) exhibited the lowest yield. For the selected NPs in this chapter, the second-highest yield was observed for the Q–C_{12}–CNC_6 which was ~76%, and Figure–4.10 shows the % yield and the QAGs determined from the conductometric titration.

The QAG represents the extent of cationic groups onto the surface of the NPs and was mostly determined to correlate with their adsorption efficiencies of anionic species or NPs. Among the NPs, the highest QAG content was ~2.4 mmol/g determined for the brush–CNCs i.e., the pQDMAEMA–g–CNC NPs where the majority of the pendent pDMAEMA chains were quaternized. For the non-quaternized pDMAEMA–g–CNC, the 3^0-ammonium content was determined to be 2.92 mmol/g, slightly higher than the QAG contents of their quaternized counterparts.

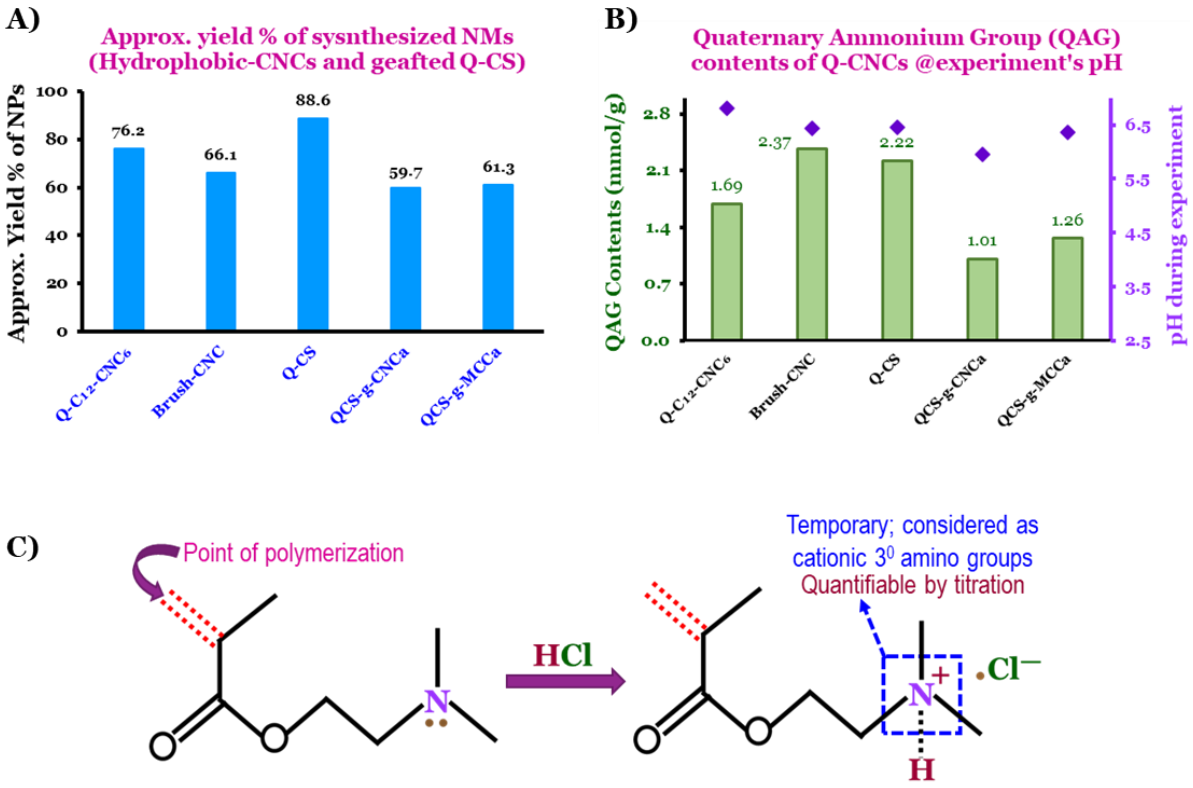


Figure 4.10: A) *Percentage yield of the selected NPs synthesized. Here, except for the Q–CS, all the NPs are structurally considered as Zwitterions where, the QCS–g–MCC$_a$ (or in another written format QCS–g–CNC$_{MCC}$) was the least or non-Zwitterions.* ***B)*** *The quaternary ammonium groups (QAG) contents determined from the $AgNO_3$ mediated conductometric titrations.* ***C)*** *The N,N-dimethyl-N-dodecyl amine monomer showing point of polymerization and the formation of tertiary (3^0) amino groups (due to protonation) that can be quantifiable by HCl—NaOH mediated conductometric titration.*

The degree of substitution (DS) and the % cationization reaction efficiencies (CRE%) were calculated for selected NPs. Both sets of data for the DS and CRE% are presented in the appendix.

4.3.3 FTIR Characterization

To confirm the presence of the DDEAC (the grafted QAG containing the C–12 hydrophobe) and the presence of PDMAEMA on the CNC surface, the FTIR of the precursor (CNC in this case) was also conducted. Figure–4.11 shows the FTIR spectra of all the NMs. The characteristic peak at 1030 cm^{-1} for the Q–C_{12}–CNC indicated the successful grafting of DDEAC onto the CNC surface via the ether linkage[134], —C–O–C—. The rest of the spectra, although very noisy, was similar to the CNCs with some new discernible peaks.

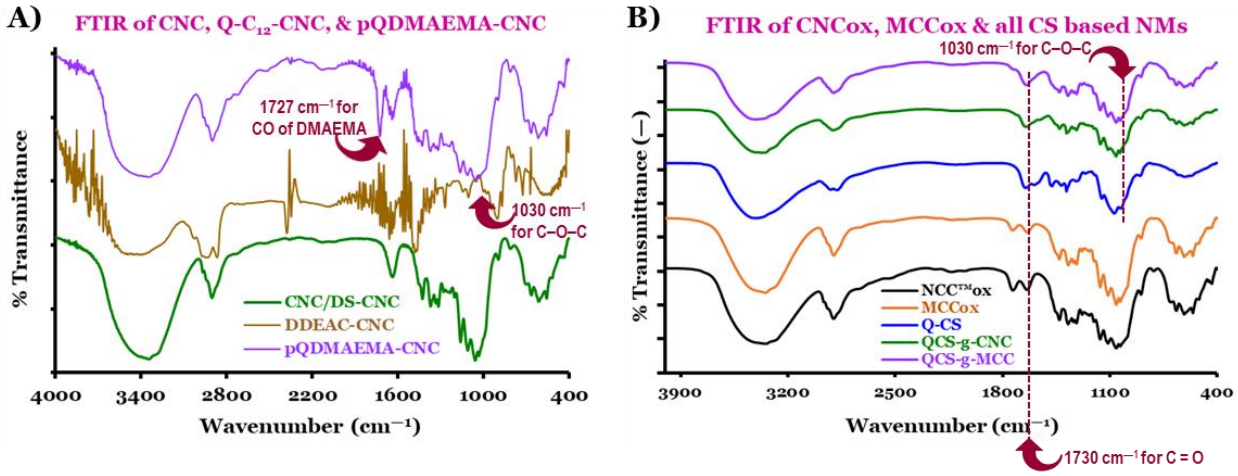


Figure 4.11: *FT–IR spectra of **A)** CNC, Q–C_{12}–CNC, and the p**Q**DMAEMA–g–CNC showing some characteristic peaks, and **B)** the CNC_{OX}, Q–CS, and the QCS–g–CNCs with notable characteristic peaks.*

Compared with the spectrum of pristine CNC, the pQDMAEMA–g–CNC displayed new small shoulders at 2761 and 2819 cm^{-1} corresponding to the symmetric and asymmetric stretching of methyl (CH_3) groups as well as another obvious new peak at 1727 cm^{-1} that is related to the stretching of the C═O bond on PDMAEMA chains. These bands are characteristic peaks of PDMAEMA.

In the case of CNC_{OX} or MCC_{OX} (figure–4.11 B), where the C–6 or the 1^0 alcoholic groups (—CH_2OH) were oxidized to —COOH groups, the C═O peak appeared at 1730 cm^{-1} which is the characteristic of the carboxyl group in their acid form.[188] Conversely, the presence of this peak further ensured that the oxidation at C–6 of most of the pendent/accessible surface —CH_2OH groups were successful. Due to the similar chemical composition of CS and CNC, no difference was observed for the Q–CS and the CNC_{OX}, except for the peak at 3200 cm^{-1} which corresponded to the —N–H stretching vibrations of the —NH_2 groups of the Q–CS.[188]

The C–O–C stretching vibrations for the ether linkage of GTMAC onto the CS were observed at 1030 cm^{-1}. In the QCS–g–CNC, the peak at 1730 cm^{-1} corresponds to C═O groups which were significantly reduced compared to CNC_{OX}, confirming the conversion of the carboxyl groups (—COO^-) in the grafting reaction with the free 1^0 amino groups (—NH_2) [188]. Due to the formation of new amide bonds (—C═O–NH—), the peak for the C=O groups shifted and were found buried under the water peak. But the C=O groups of the acetyl groups (CH_3C═O) of Q–CS chains (the 85% deacetylated CS was used as the starting material) was quite noticeable. The newly formed amide bonds were evident by the presence of the peak at 1696 cm^{-1} which was the C=O peak of the formed amide bonds.[188]

4.3.4 Aggregate sizes (D_H) and zeta potentials (ZP)

The aggregate sizes and ZPs were determined to understand the adsorption, i.e. removal efficiencies (RE%) of the anionic species for cationic NMs developed and presented in this chapter. Although during the measurement of the DH and the ZP of the NPs, the concentration selected (0.1% or 0.05% w/v, for instance) was way below that used for BATs, but the D_H and ZP of such concentration would give an idea to the reader for their corresponding RE% and thereafter to establish the possible trend(s) conclusion(s). The table below lists all the D_H and ZPs of the NPs.

Table 4.1: Average aggregate sizes (D_H) and ZP of the selected NPs

NPs	Zeta Potential (mV)	STDV_ZP	Size, D_H (nm)	STDV_D_H
Q-C_{12}-CNC_6	33.9	1.1	1033.3	43.5
Brush-CNC	29.1	1.7	1121.1	53.1
Q-CS	37.6	11.6	1739.3	61.5
QCS-g-CNC_a	27.5	1.1	447.4	25.5
QCS-g-CNC_{MCC}	41.9	2.3	1679.7	59.2

The effects of pH changes on the average D_H and ZPs were also investigated for several selected NPs among the library of NMs systems. As mentioned, and discussed earlier in Chapter–3, our gut has different segments of pH zones, and the expectations were to have the NPs' capabilities to retain their cationic charges over the range of pHs. From Figure–4.11 (C and D), it is obvious that ZPs of the selected NPs were less fluctuating or labile than the D_H at a specific pH. Due to the impacts of the pH change on the net surface charges, the inter–

particles aggregations occurred at a specific pH. For such forms of aggregations, the ionic interactions as well as the nonionic (H–bonding, hydrophobic or Van der Waals interactions) interparticle interactions are the most causative mechanisms. If the surface negative charges were screened in a low concentration of calcium chloride solutions ($CaCl_2$), the ZP fluctuations and the variations of the D_H were less frequent or dominant (data presented in the appendix), however, some aggregations occurred due to nonionic interparticle interactions. (Figure–4.12).

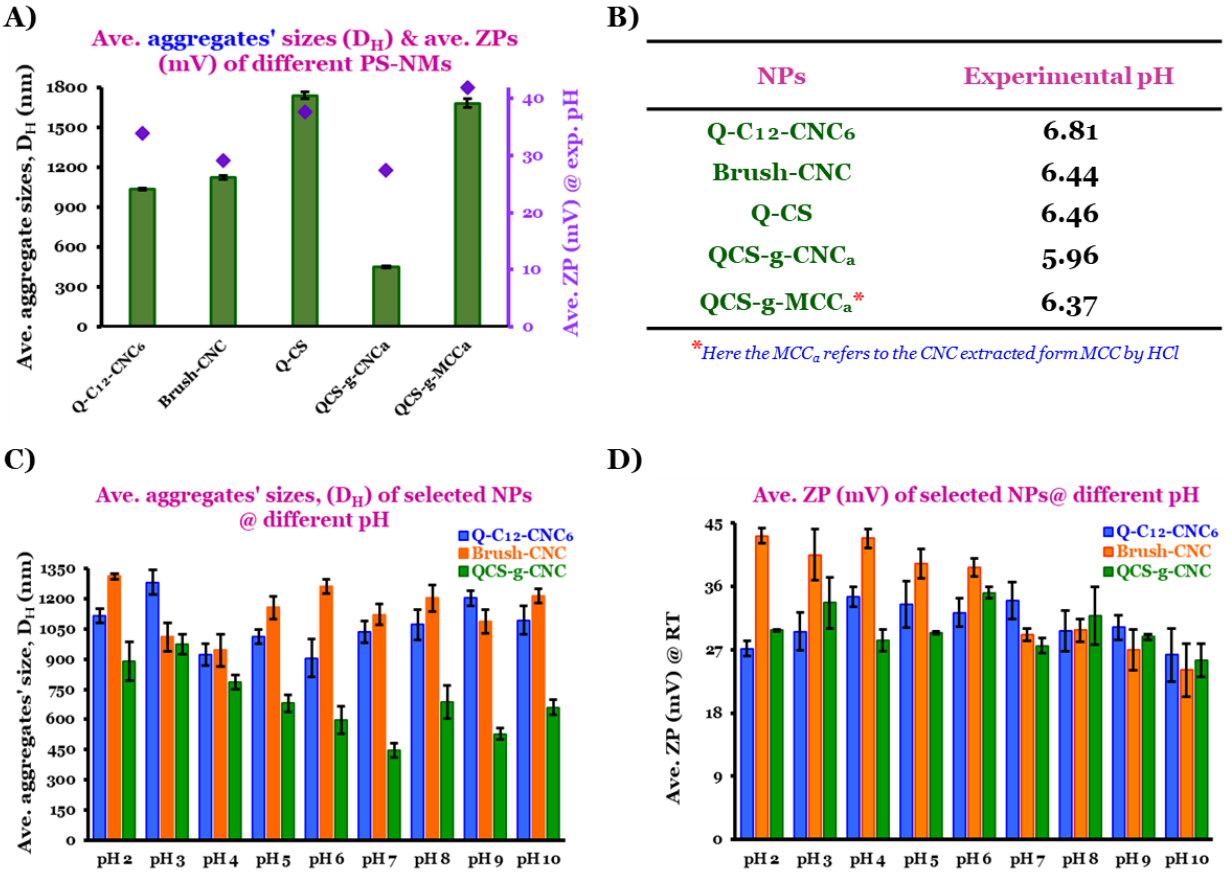


Figure 4.12: A) *Average aggregate sizes (D_H) and the ZP of selected NPs.* ***B)*** *Experimental pH of the aq. suspensions of the NPs. C) The ave. D_H – pH profile of the three selected NPs (Zwitterions), and* ***D)*** *The ZP – pH profile of the three selected NPs.*

4.3.5 TEM Images of the NMs

Figure–4.13 represents the TEM images of selected NPs, which illustrate the aggregation of the NPs. For NP systems, it is known that during drying of the sprayed (through the lab-made venturi tube) or pipetted NPs samples on the Cu–FCF#200 grids, aggregation occurred when the solvent (dispersion media) was removed. The densely packed aggregation was evident for the Q–C_{12}–CNC_6 Zwitterionic NPs due to the drying effect, and the enhanced hydrophobic interactions of the C–12 dodecyl chains on the grafted QAGs.

The CS was made hydrophilic and water-soluble due to the cationic groups on the Q–CS NPs, however, the TEM image showed aggregates of different aggregate sizes. Other than the drying effect, the most likely reason, in this case, was the formation of H–bonding between the pendent/protruded hydroxyl groups (—OH) of the 1^0 alcoholic moieties (—CH_2OH) as well as the partial hydrophobic interactions, even though the interparticle cationic repulsions were more pronounced. Similar aggregations were observed for the Q–CS grafted NPs due to the same reasons, especially for the QCS–g–CNC_6 systems whereas for the QCS–g–CNC_{MCC} systems, fewer aggregations were evident.

Lastly, the polymeric–CNCs, i.e., the brush–CNCs (pQDMAEMA–CNCs) also showed moderate aggregation, however, it was possible to capture an image of single or mildly aggregated NPs.

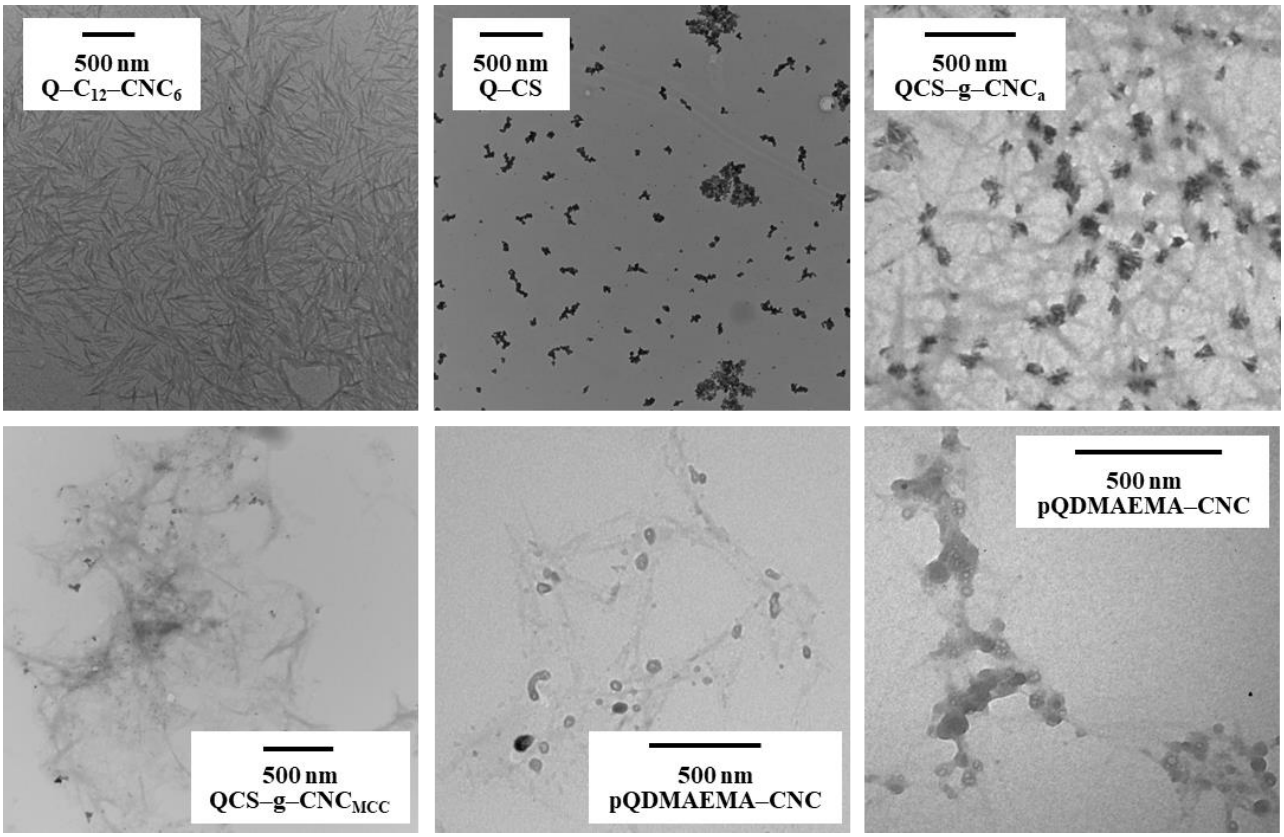


Figure 4.13: *Best possible obtained TEM images of the cationic (Zwitterionic) NMs systems; the Q–C12–CNC6, Q–CS, QCS–g–CNC$_a$, QCS–g–CNC$_{MCC}$, and the pQDMAEMA–CNCs.*

4.3.6 BATs for the NMs with MO and SC

The batch adsorption tests (BATs) were conducted for the NPs with both MO (anionic dye) and the SC (anionic bile acid, sodium salt), and the max adsorption efficiencies were determined from the linear fitting of the Langmuir monolayer adsorption isotherm (LMAI). One of the representative examples of binding phenomena is shown in Figure 4.14.

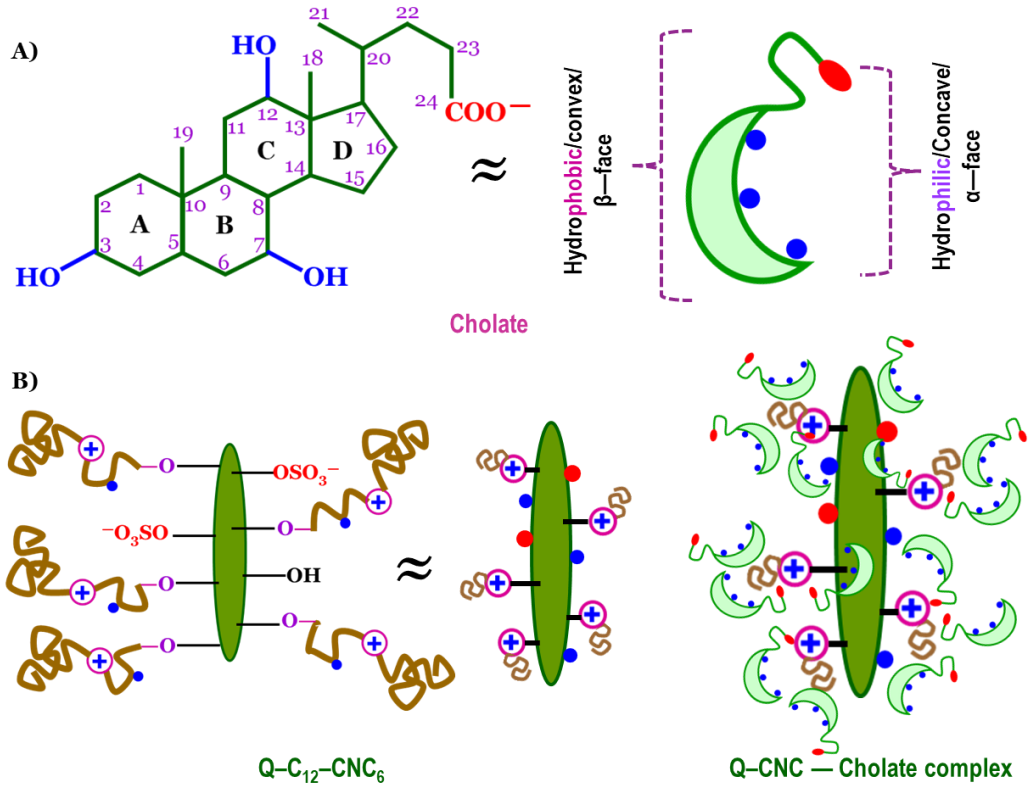


Figure 4.14: A) *The sodium cholate molecule and its two different faces in flat stereochemical conformation (schematic).* ***B)*** *Schematic illustration of the Q–C12–CNC6 and the complex formed with SC due to the physicochemical adsorption via ionic interactions (attractive long-range force, predominant, H–bonding as well as the hydrophobic interactions. Once the NP gets fully saturated as the monolayer formed, it is least likely to form another layer of adsorbates (the SC in this case) over the already formed monolayered complex. The dispersibilities of the NPs were seen drastically and significantly decreased right after the complexes were formed.*

In Figure 4.15, the calculated Q_{max} values for the NPs is described, where it is evident that the adsorption of MO onto the NP surfaces was not as strong compared to SC. The possible reason could be the compositional and stereochemical differences between these two molecules. As described in Chapter–3, the monovalent (single anionic charge) MO with two

phenyl rings in the structure possessed a pKa of ~3.5 and being in the sodium salt form, it was fully dissociated/ionized within the experimental pH. Due to the stereochemical conformation, the hydrophobic interaction with the hydrophobic domains on the NP surface was not as significant. The lack of H–bonds forming groups on the MO was another reason for the comparatively lower adsorption compared to SC.

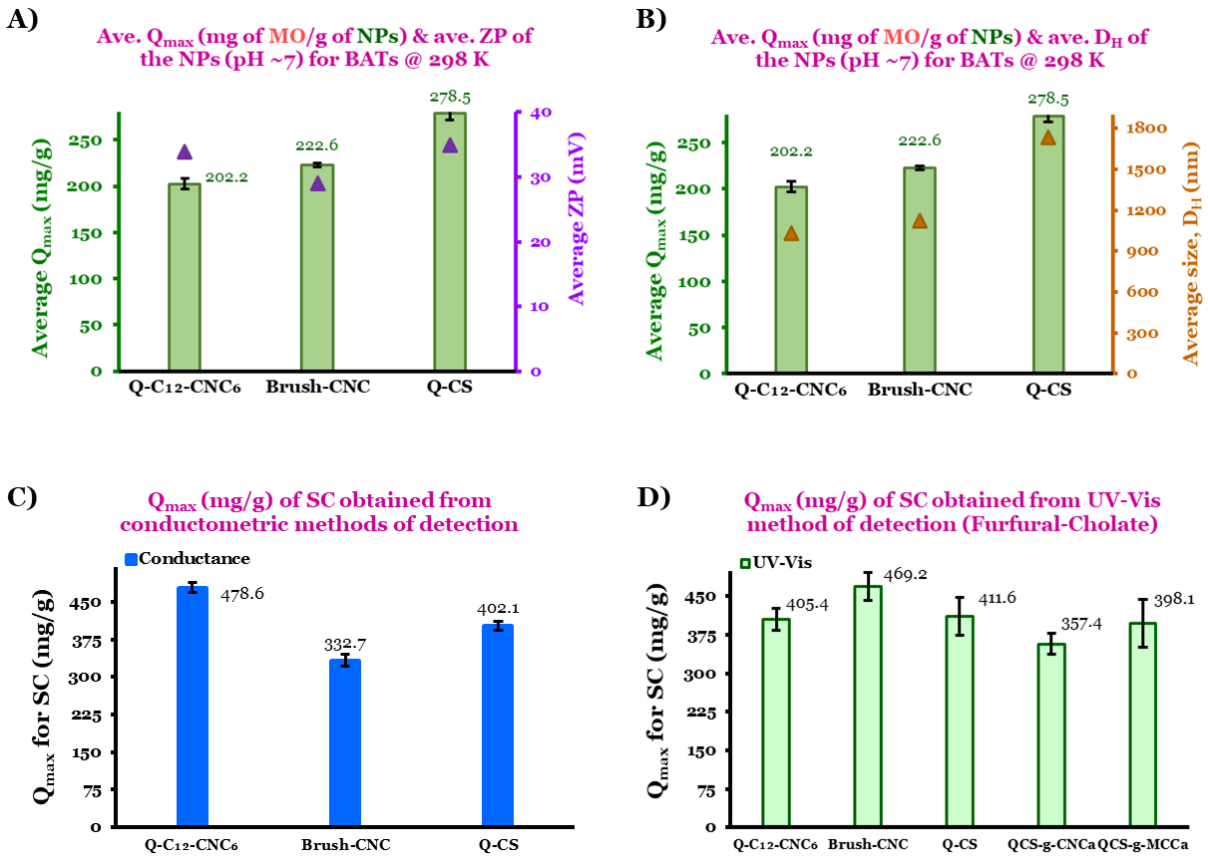


Figure 4.15: *Comparison of the Q_{max} values for the Q–C_{12}–CNC_6, brush–CNC, and the Q–CS with* ***A)*** *average ZP and,* ***B)*** *average D_H.* ***C)*** *The Q_{max} values of the three NPs obtained from the BATs where the quantifications were done via conductance measurements. For A), B), and C) the QCS–g–CNCs were under synthesis.* ***D)*** *Q_{max} values for all the NPs via UV-Vis method.*

In the case of the monovalent SC that possessed a steroid nucleus (CPPP ring) with three hydroxyl groups with a pKa of 5.13, the molecule was completely ionized to the sodium salt form at the experimental pH (~ 6.5—7.8). Stereochemically, the molecule possessed a flat conformation with two distinct faces (hydrophilic/hydrophobic) consisting of the steroid ring and the –OH groups, these molecules could participate in the H–bonding and hydrophobic interactions, in addition to the usual ionic long–range attractive forces. Furthermore, the specific surface areas (SA) offered by the NP systems would be an added benefit for such physicochemical adsorptions. These could be the likely reasons for a greater extent of adsorption onto the NP surfaces than those of MO.

Although the average D_H and ZP for the brush–CNCs were in micron size and ~ +29 mV respectively, these NP systems displayed the highest Q_{max} for the SC adsorption of ~ 469 mg/g (UV–Vis detection) NPs, but they did not seem as efficient for the adsorption of the MO. The possible entrapment of SC within the tentacles (pQDMAEMA chains) of the brush–CNCs could be the additional reason for better adsorption of SC. Furthermore, the dispersion of the pQDMAEMA was slightly more viscous (just visually observed and investigated, no experiment conducted on the U–tube viscometer) compared to other NP dispersion of the same concentration.

From the SC adsorption data (the Q_{max} values) from either of the detection techniques (Conductance or UV–Vis), it is evident that the presence of hydrophobic moieties could enhance the physicochemical adsorption of the SC. Such difference in the adsorption of SC between the hydrophilic (Q–CNC_6, chapter–3) and slightly hydrophobic CNCs (Q–C_{12}–CNC_6) was obvious when compared between their Q_{max} values (UV–Vis technique) (299 mg/g and

405 mg/g), where the data were sufficient to provide an explanation on the role of hydrophobic moieties.

4.4 Conclusions

This chapter discusses the hydrophobically modified CNCs, hydrophilic chitosan (Q–CS), brush–CNCs, and block type CNCs (QCS–g–CNCs) NPs systems and their efficiencies on adsorption (or removal efficiencies) of anionic species, such as MO and SC. The cationic (also Zwitterionic) NPs developed was found to be stable over a range of pH of 2–10, which lies within the GI pH ranges. Within the pH ranges, all the NPs retained their cationic charges (manifested by the ZP values) and the ZPs were colloidally stable (± 25 mV). The NPs suspensions were stable during the storage with little sediments at the bottom, however, if sediments were found, those were readily dispersible.

The significant extent of adsorption of SC by these nano-systems could be utilized as efficient BASs. However, once the biosafety of these NMs are evaluated on live cells, standardized animal testing (*in vivo*) or studies on human volunteers should be conducted to establish their efficiencies as the BAS. Additionally, these systems were effective for the adsorption of an anionic dye confirming their suitability as sustainable adsorbents for effluent treatment.

The NPs being based on the naturally resourced bio–PSs (cellulose and chitosan), possess S.M.A.R.T.© properties, and thus should not be harmful for human application or contaminate water, as the ions associated with the NPs were listed among the essential electrolytes.

Based on the results from this chapter it could be concluded that the availability of a sustainable and natural BAS with better efficiencies and minimal or no adverse effect is very close to reality, from the laboratory benchtop to the consumers at an affordable price.

4.5 Future Directions

It is very apparent that the presence of hydrophobe onto the NPs can affect the binding of SC with the NPs, and such evaluation should be conducted for hydrophobes present on the CS or the modified CS grafted CNCs. For all the NPs, the comparative studies for BATs with SC should be conducted for commercially available BAS, cholestyramine. And lastly, although it was assumed that these NPs should not be harmful to humans, the biosafety of all the NPs should be conducted via live healthy cells culture tests, either on microorganisms or on eukaryotic cells.

Chapter 5: Amino–PS, Chitin based NMs as BAS

5.1 Introduction

A myriad of applications has been reported in the literature on chitin-based NMs over the last few decades.[101–105] Chitin, the amino bio–PSs, is the second most abundant biopolymer found in nature after cellulose. It is a linear polysaccharide comprised of glucosamine (2-amino-2-deoxy-β-D-glucopyranose) and N-acetyl glucosamine (2-acetamide-2-deoxy-β-d-glucopyranose) monomeric units bound via β-(1→4) linkages[194] as shown in Figure–5.1.

Regardless of the sources, chitin exists in alpha, beta and gamma domain conformations, the difference being that the adjacent polymer chains are arranged in an anti-parallel, parallel, and mixed alignment/arrangement respectively. Chitin is found in fungal cell walls, in exoskeletons of certain marine invertebrates (e.g., sponges, coral) and in a variety of arthropods. The α-conformation is the most abundant in nature and is commonly extracted from the shells of crustaceans (e.g., shrimp, crab, lobster).[195–197]

A network of secondary electrostatic hydrogen bonds, formed among the hydroxyl, acetyl, and amino groups, produces the chitin's three-dimensional crystalline matrix. The α-chitin conformation forms a stronger structure (which is less prone to swelling) due to interchain bonds between hydroxymethyl groups which is not commonly observed in β conformation. The N-acetyl glucosamine monomeric unit forms multiple strong in**ter**- and in**tra**-chain hydrogen bonds due to its acetyl group and thus, a homopolysaccharide produced from this monomer is largely insoluble.

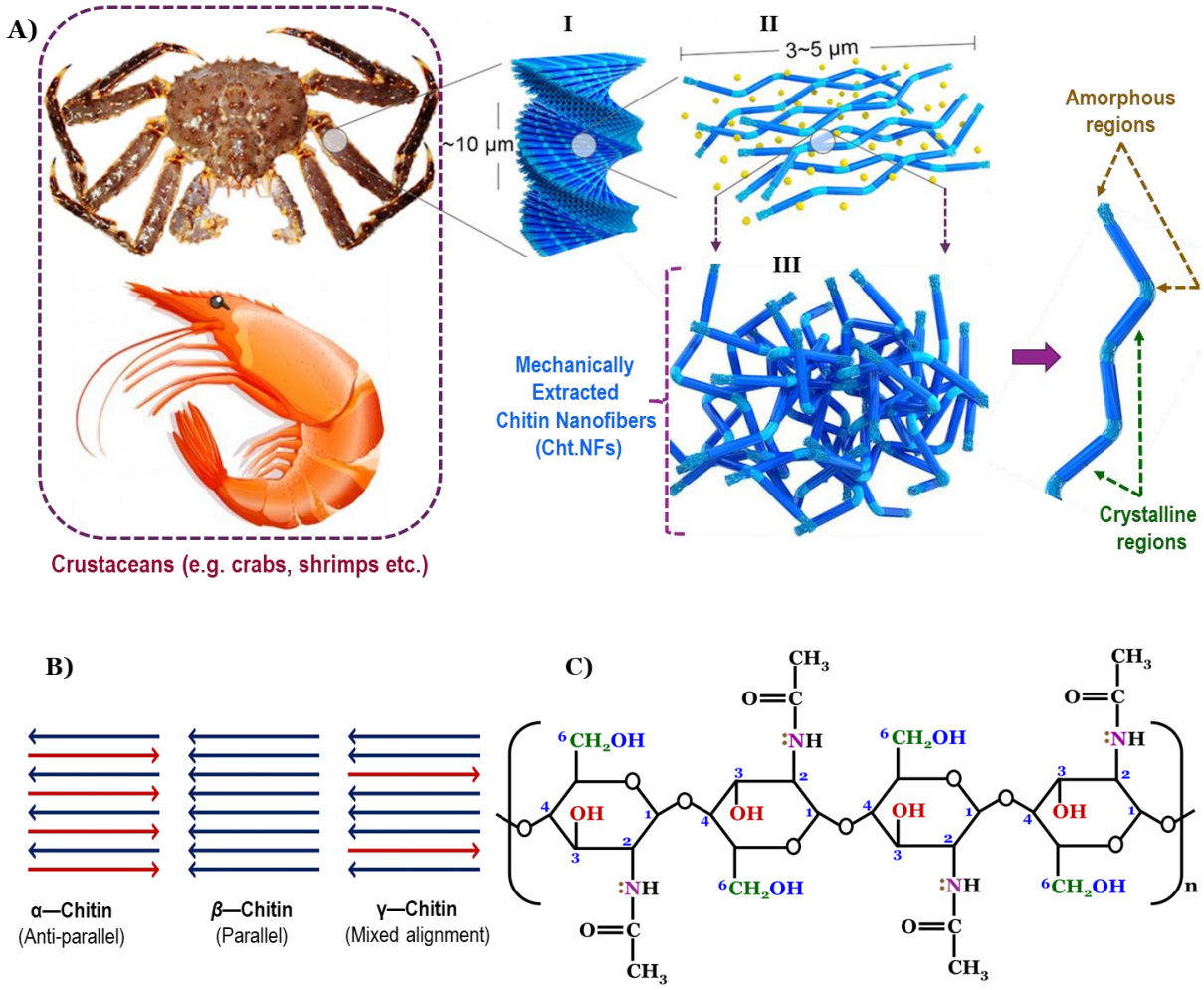


Figure 5.1: A) *Sources of chitin from sustainable sources and how chitin exists inside the exoskeletons. Here, I: Plywood structure of chitin, II: Ch-MFs in the matrix, and III: Mechanically extracted individual chitin NFs from the demineralized and deproteinized pure α–Chitin (powder). The insert to the right shows the crystalline (ordered, resistant to acid hydrolysis) and amorphous (disoriented/disordered, easily accessible for and prone to acidic hydrolysis) region of the individual bundle of chitin fibers.* ***B)*** *Parallel anti-parallel and mixed alignment polymorphs of chitin showing their different orientations of chains. The arrow indicates the reducing terminus/end.* ***C)*** *Basic chemical structure of the α–Chitin skeleton showing the glucosamine (GA) and N-Acetyl glucosamine (NAGA) attaching through the β-(1→4) linkages. Here the position 2 (C–2, for the acetamido groups) and position 6 (C–6, for the 1^0 alcoholic groups, CH_2OH) of the glucopyranose unit are the positions where most of the chemical functionalization occurs. A) & B) Adapted from.*[194,196,198,199]

Once deacetylated, the N–acetyl glucosamine unit becomes a glucosamine unit with increased hydrophilicity, where the primary amine becomes protonated at low pH generating a positive charge. The amount of positively charged amino groups is increased by deacetylation and the degree of deacetylation (DD) is determined from the ratio of glucosamine to N-acetyl glucosamine, thus a higher DD of the α–chitin (De-Chitin) would have more free amino groups (—NH_2) at C–2 position rendering it to be more positively charged. Because the free —NH_2 groups can be easily protonated[200] at pH below ~8, similar to the slightly acidic pH (4 — 6.3) of the small intestine. Due to the favourable pH-responsive cationic properties of deacetylated chitin, there is a possibility that it can interact with the anionic carboxylic group on bile salts via electrostatic forces making the chitin/chitin-based NMs (nanofibers and nanowhiskers) suitable for use as bile acid sequestrants, BAS.[201]

Thus, in this chapter the commercial α–chitin powder was modified via two different extraction methods from which chitin nanofibers (Cht.NFs), also commonly known as nanochitin in literature,[200,202–205] and the chitin nanowhiskers/nanocrystals (Cht.NWs/NCs)[206–211] were produced. The NWs were further modified by cationizing with GTMAC to produce NPs that are more cationic (the Q–Cht.NW_a) than their precursors. This is to enhance their capabilities of binding anionic species (SC, MO etc.), whereas the extracted Cht.NFs remained in their purified form that depended on the protonation of the surface 1^0 amino groups (—NH_2) for their cationic charges to be utilized as the adsorbents for anionic species (e.g., SC). The microscopic images in Figure–5.2 shows both types of chitin-based NMs.

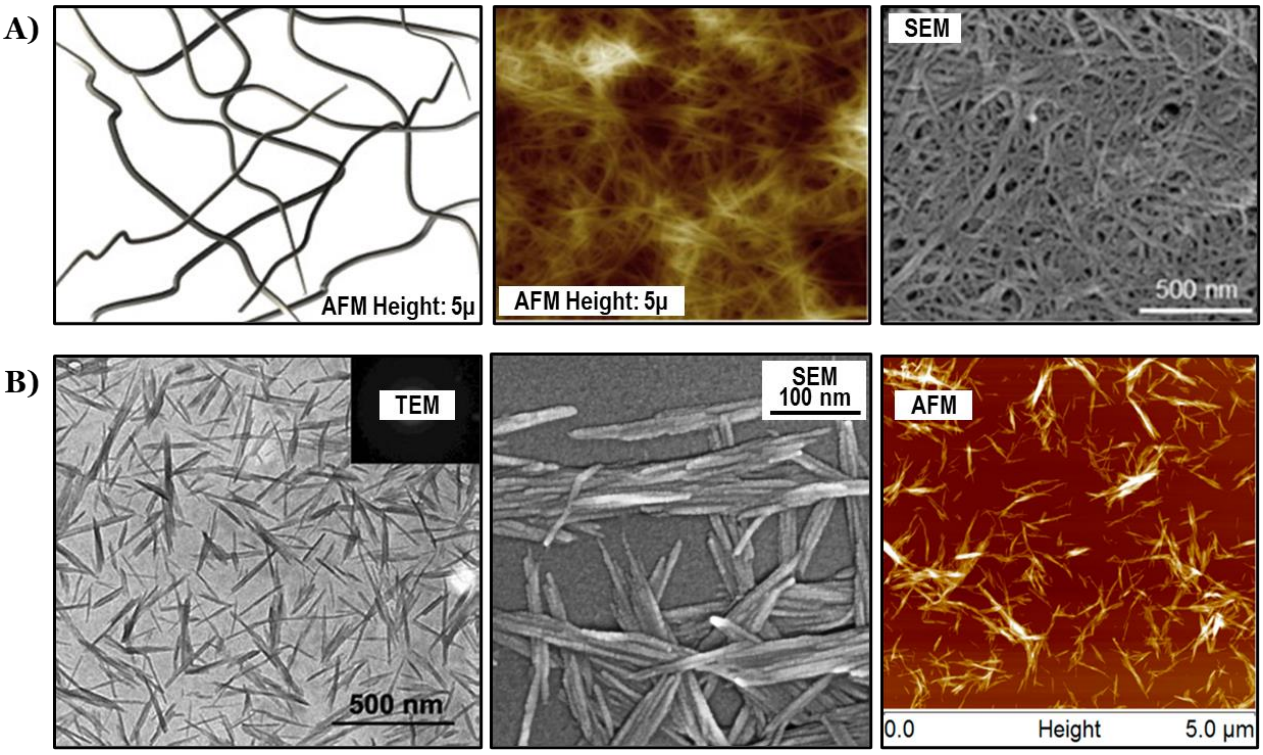


Figure 5.2: *Microscopic images of **A)** Chitin nanofibers or nanochitin (Cht.NFs), and **B)** chitin nanowhiskers or nanocrystals (Cht.NWs or Cht.NCs). Adapted from.*[198,211–214]

Chitin-based NMs were never explored in this lab (TAM lab) and being the newest addition to the list of NPs, several parameters were optimized to prepare the NPs. Several Cht.NFs were prepared based on the number of cycles or passes through the microfluidizer (µFD, details in the method section) namely, the Cht.MF_P_0, Cht.NF_P_1 to Cht.NF_P_5 where the Cht.MF_P_0 (MF stands for microfiber) indicates the deacetylated α–chitin (De–Cht.$_B$) where the deacetylation was conducted via alkaline hydrolysis. Cht.NF_P_1 corresponds to the extracted nanofibers (NFs) obtained by passing one cycle through the microfluidizer (µFD), whereas the P_5 refers to the NFs obtained by the consecutive passing of 5 cycles through the microfluidizer (µFD). Since the NWs were extracted via the HCl acid-mediated hydrolysis of

α–chitin by dissolving or cleavage of the amorphous regions, the produced NWs/NCs were denoted as Cht.NW_a/NC_a.

5.2 Materials and Methods

5.2.1 Materials

α–Chitin powder (practical grade, MW ~ 400 KDa) from shrimp shells was purchased from the MilliporeSigma (Sigma Aldrich) and used as received without further purification. Purified water (Milli-Q water) from a Millipore system (>18 MΩcm) was used to prepare the sample solutions. The GTMAC and other commonly used chemicals like NaOH/KOH, KCl, NaCl, potassium hydrogen phthalate (KHP), HCl acid (37% w/w), H_2SO_4 (98% w/w), glacial acetic acid (99.7% w/v) and other organic solvents were purchased from MilliporeSigma and used as received.

5.2.2 Alkali mediated deacetylation of α–Chitin followed by Cht.NF extraction

Complete deacetylation of α–chitin powder through hydrolysis using alkali is impractical and was not reported in the literature. By partial deacetylation, many of the surface acetyl groups (—$COCH_3$) of the acetamido groups (—$NHCOCH_3$) at C–2 of the chitin structure could be removed, leading to the exposure of new or free/unoccupied 1^0 amino groups (—NH_2). By doing so, such forms of De–Cht.$_B$ could be protonated in an acidic solution, which is expected to improve the dispersibility of the insoluble chitin/De–Cht.$_B$. Improved dispersibilities of the De-Cht.$_B$ is required or necessary as it would reduce the clogging of the interaction chamber of the microfluidizer (μFD). Furthermore, such dispersions would

facilitate the transmission of mechanically applied energies during the mechanical pre-treatment of the De.Cht.$_B$ dispersions prior to passing through the microfluidizer (μFD) cycle.[215]

The reported values of the optimal strength of NaOH varied from 33% – 60% (w/v) and 25 – 30 mL was commonly used for 1 gram of acetylated α–Chitin powder. For such deacetylation reactions, the reported temperature ranged from 95^0C – 107^0C and depending on the conditions, the time for the reaction was usually set from 2.5 hrs – 24 hrs.[216–223] In this study, the deacetylation reaction parameters were set at 35% (w/v) NaOH [= 8.75 M] and 25 mL of NaOH was used for1 g of α-Chitin powder, and the reaction condition was: time set at 2.5 hrs, temperature at ~ 95^0C under continuous reflux. A 0.03g of $NaBH_4$/1 g of α–Chitin was added to the reaction mixture as a catalyst/reducing agent to prevent the strong alkali-induced depolymerization,[220] formation of 3:6- and 2:3-anhydride structures, and & weight loss.

For the deacetylation, briefly, 15 g of α-Chitin powder was weighed into a 500 mL round bottom flask (RBF) and then 375 mL of freshly prepared 35% (w/v) NaOH was dispensed into the RBF. The mixture was homogenized for 10 min, as the temp of the oil bath was raised to ~100^0C. The mixture was then refluxed at 95^0C at 1200 rpm for 2.5 hrs. Once the reaction was completed, it was stopped (a change in color was observed for the mixture), and the RBF was placed in an ice bath and followed the usual procedure to purify the De–Cht.B. After purification, the post–dialyzed slurry was recovered and stored at RT in a storage bottle while recording the concentration via gravimetric analysis (GA), their pH, and the yield%. Figure–5.3 illustrates the overall steps of the deacetylation reaction of the chitin powder.

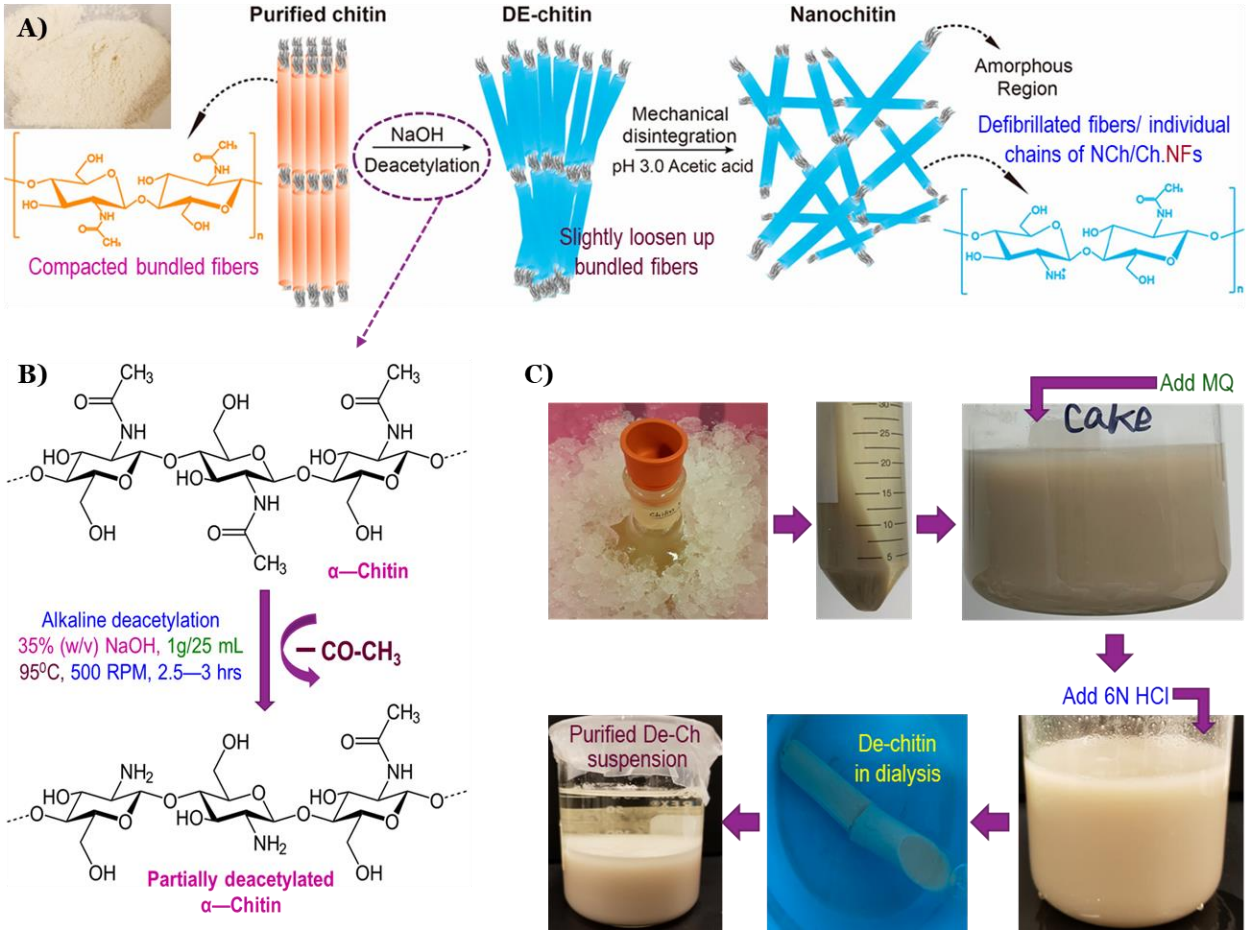


Figure 5.3: A) *Overall roadmap for the defibrillation of the chitin to produce Cht.NFs from the deacetylation of α-Chitin powder. Adapted from.*[215] ***B)*** *Deacetylation reaction steps at a molecular level showing the partial deacetylation giving rise to the* 1^0 *amino groups onto the surfaces. Drawn and adapted from.*[224] ***C)*** *Processing of deacetylation at laboratory scale from reaction to purification steps. The De–Cht.*$_B$ *was found very unstable and within a few hours, they form loosely settled sediments at the base of the container bottle or glassware. Several pilot batches of De–Cht.*$_B$ *were made and instantly non–using products were kept in the fridge (2–8*^{0}*C) for longer storage.*

5.2.3 Cht.NFs (nanochitin) extraction via mechanical treatment

Once the De–Cht.B was prepared, then individual Cht.NFs were extracted (defibrillated) following the literature[225,226] with some modification. For such defibrillation, a combination of aggressive mechanical treatments, namely homogenization & sonication for multiple times and passing it through microfluidizer (μFD) was conducted. A 0.22% (w/v) aqueous De.Cht.$_B$ suspensions acidified with glacial acetic acid to pH of ~ 2.7 – 3. were prepared. The concentration was thus fixed after several trial-and-errors so as to reduce clogging when it was passed through the μFD. As discussed in the introduction, the acidification protonated the available surface —NH_2 groups, which improved the aq. dispersibility of the cationic De.Cht.$_B$.

The in-house supplied air pressure did not go above 60 psi (4.16 bar) @ the air gauge. And for the μFD used in this case, the processed pressure (psi) = Supplied air pressure (psi) x 237, giving rise to max 14,220 psi or 980.4 bar of processed pressure [1 bar = 14.504 psi]. Available literature suggested that running the pre–treated pH adjusted dispersions at a higher pressure (1500 bar), thus it was planned to run through the in-house μFD to complete five cycles/passes so that five different sets of NFs could be achieved and collected.

All the five prepared dispersions of the De.Cht.$_B$ (for obtaining Cht.NF_$P_{1–5}$) were homogenized for 5 min followed by a total of 4 cycles of sonication in the ultrasonic bath where each cycle of sonication consists of 4 runs, and each run was 10 min long, having 15 min intervals between the runs, as shown in Figure–5.4.

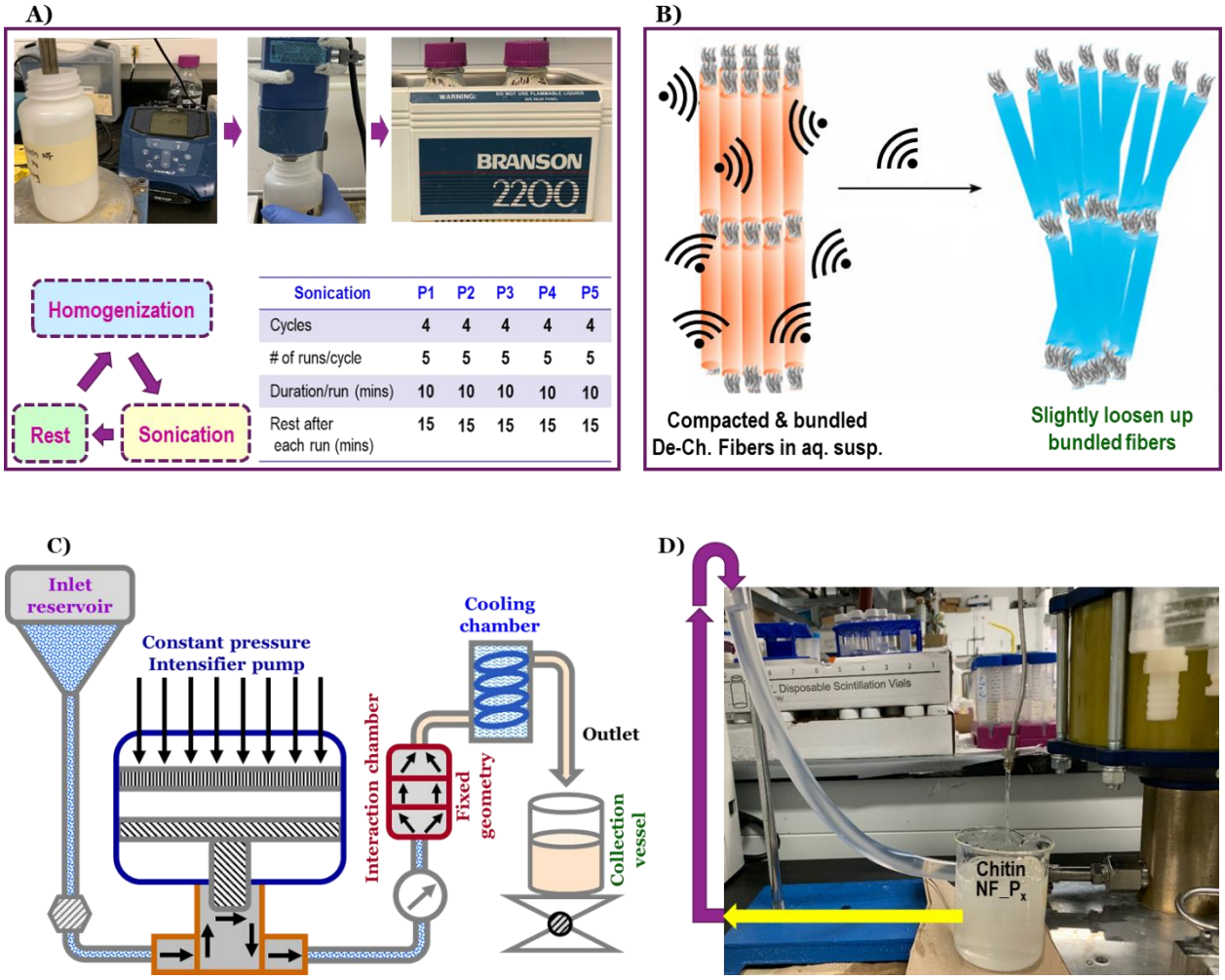


Figure 5.4: A) *The processing of the De–Cht.$_B$ dispersions for mechanical pre–treatment prior to run through the microfluidizer (μFD): from pH adjustment to multiple cycles of homogenization/sonication. The snapshot of table enlists a few specific parameters for the sonication steps.* ***B)*** *Schematic illustration for the impact of the mechanical pre–treatment steps on the bundled De–Cht.$_B$ fibers which get slightly loosened up as such. Drawn from*[206]*.* ***C)*** *Schematic of the operational principle of the μFD.* ***D)*** *The steps showing how the multiple cycles of runs passed through the in–house μFD to obtain/collect the Cht.NFs_P$_{1\text{-}5}$. For the pass–2 and above, the channels/pathway of the μFD was flushed, let bleed, and collected in the same vessel with only a few mL of MQ water (~5 mL) before the collected content was dumped into the feeding (inlet reservoir). Thus, gradually increased dilution effects (for conc.) were seen as expected for the Cht.NFs samples which are > pass–1.*

Literature suggests that such mechanical pre-treatments would ensure the loosening (as shown in Figure–5.4) of the compacted groups of nanofibers within the bundle structure[206] through numerous H–bonds. The pH was readjusted for all the completed pre–treated dispersions if there were any deviations of the observed pH. The mechanically pre–treated and pH adjusted (~3) aq. dispersions of the De–Cht. samples were then passed through the μFD, which transformed the suspended NPs into a clear dispersion due to defibrillation via the interaction chamber giving rise to individual and shortened NFs. All the received liquid were then centrifuged **@ 10,000 rpm for 4 mins** (only one cycle), and the **supernatants were collected** and denoted as Cht.NF_P_x, as shown in Figure–5.5 for the recovered pre–/post dialyzed NFs.

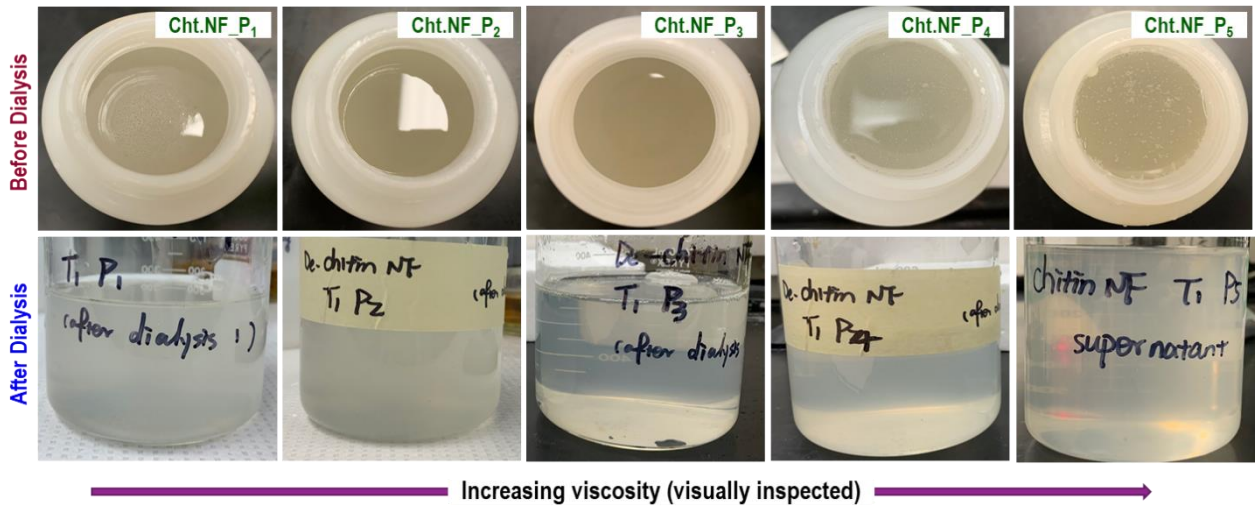


Figure 5.5: *The Cht.NF_$P_{1–5}$ solutions after the collections from the microfluidizer, μFD (the top row; before dialysis) and the purified solution after the dialysis. The relative viscosity was found to increase towards the Cht.NF_P_5 solution just through the visual inspection (glass rod assisted) by the experimenter.*

During the collections of the defibrillated chitins i.e., the Cht.NFs_P_x obtained displayed a very slight brown color which became more pronounced and noticeable for the Cht.NF_P_5 samples. The viscosity was increased from the pass–1 towards pass–5, and for the Cht.NF_P_5, where the recovered samples were thick and flowed readily even after the purification by dialysis. All the Cht.NF samples were dialyzed to remove the acetic acid and the post–dialyzed purified NF dispersion were then collected, stored in storage bottles recording their pH, conc. (through the gravimetric analysis, GA) and calculated the yield%. And all the solutions were stable during storage.

5.2.4 HCl mediated deacetylation of α–Chitin (Cht.NW/NC extraction)

As illustrated in the schematics shown in Figure–5.1, the chitin microfibrils possessed amorphous (disordered) and crystalline (highly ordered) domains. It was reported that mineral acid hydrolysis could dissociate such regions with low lateral order (the amorphous regions) to extract the water-dispersible, highly crystalline residue (the nano–whiskers/crystals) to yield a stable colloidal suspension. During such hydrolysis, the chain cleavage at the random locations along the microfibrils resulted in partially acetylated whiskers that are rod-like or spindle-like particles. Thus, the hydrolysis via HCl acid was performed following the method described in the literature[206–211] with minor modifications. Briefly, 1 g of α–Chitin powder was weighed and dispersed in a beaker containing 30 mL of 3M HCl acid using a homogenizer. The mixture was then placed in an RBF on a hot plate to perform the hydrolytic cleavage under reflux at a 95^0C for 1.5 hr and a mixing speed of 600 rpm. A slight darkening of the reaction mixture was evident at the end of the reaction, and the product was purified following the usual

steps using the methods described in the previous chapters. After five days of dialysis, the purified slurry was collected, homogenized, and the pH, conc. (via GA) and the % yield was recorded and stored. The NPs were slightly unstable, and sediments were observed at the bottom of the vessel after several hours. A small fraction of the aqueous slurry was freeze-dried for FTIR analysis. Figure–5.6 shows the synthetic and purification steps.

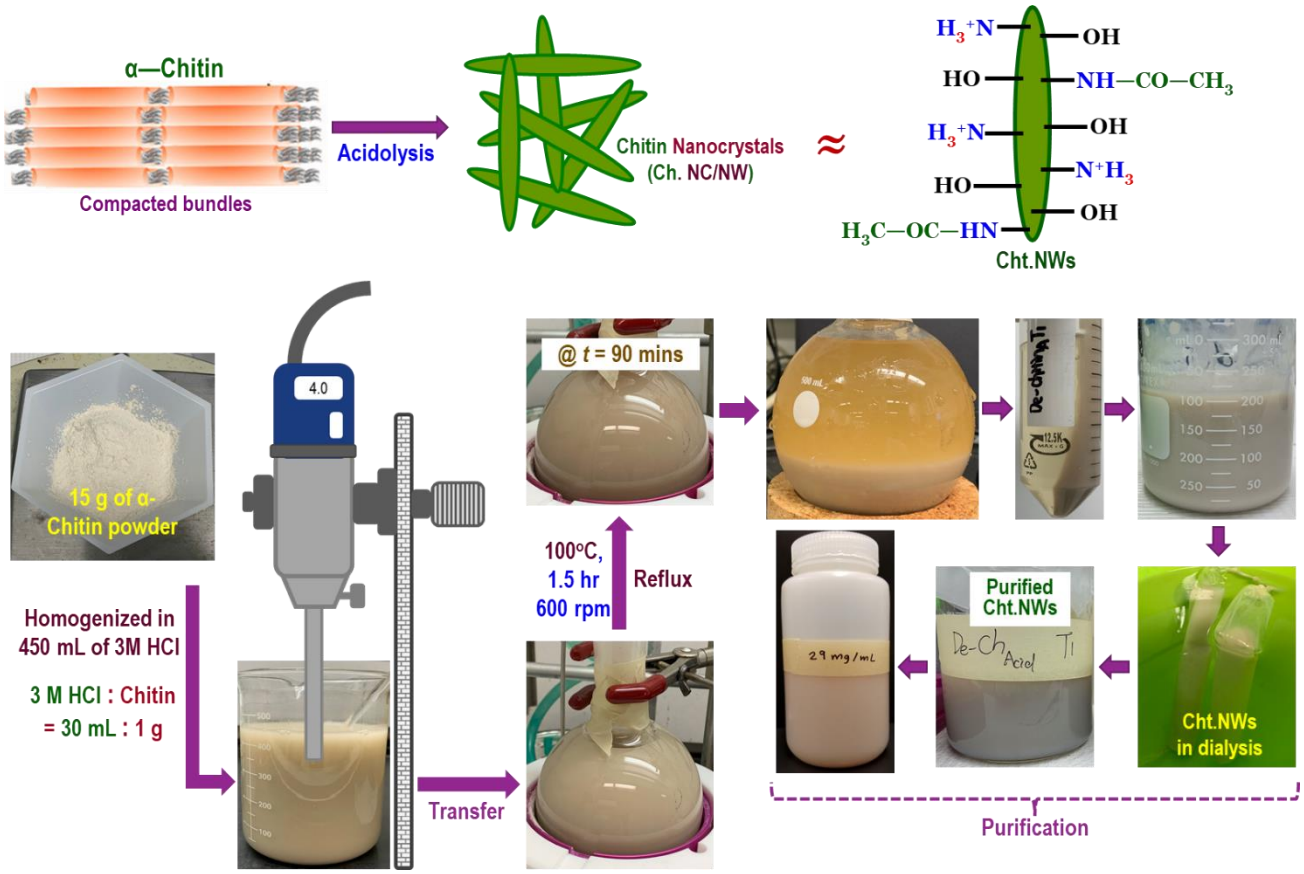


Figure 5.6: *Schematic representation of the acidolysis of chitin's bundled microfibrils*[206]*, and the particle structure of the Cht.NWs (to the right). The bottom row shows the extraction and the purification steps of the Cht.NWs from the commercially available –chitin powder. Several pilot batches of Cht.NWs were extracted, stored in the fridge, and utilized as required.*

The pH of the post–dialyzed slurry was within ~5.4, where the e surface —NH_2 groups would be protonated. Such pH-dependent protonation of the —NH_2 groups on the Cht.NW_a imparted positive charges (—N^+H_3) to the surface of the NPs that stabilized the colloidal dispersions of Cht.NW_a NPs due to the repulsive forces (thus pH-responsive) between the crystallites. As the NWs were extracted via the acid-mediated hydrolytic cleavage of the amorphous regions of the chitin microfibers, the NPs were denoted as Cht.NW_a.

The Cht.NW_a NPs were further deacetylated through alkaline deacetylation to impart larger numbers of free —NH_2 groups/NPs to the NPs (Cht.NW_{ab}), hence one pilot batch was performed. As the degree of deacetylation (DD) [which corresponds to the availability of the —NH_2 groups] achieved was only slightly higher than the Cht.NW_a, the Cht.NW_{ab} was **not** considered to be further quaternized with GTMAC molecules.

5.2.5 Quaternization of the extracted Cht.NW_a/NC_a

The post–dialyzed Cht.NW_a were then quaternized to introduce permanent, non–pH-responsive cationic charges to the surface of the NPs. Due to the lack of the suggested method in the published literature, and the similarity of the molecular structure/composition of the CS and chitin, the same quaternization method using GTMAC for the CS was used to quaternized the Cht.NW_a. Briefly, an equivalent volume of 1 g of Cht.NWa was dispensed into the RBF and diluted with ~200 mL of IPA:H_2O [= 90:10]. The pH of the mixture was then adjusted to ~13.8 with freshly prepared 6 M NaOH solution to activate the surface 1^0 alcoholic groups (—CH_2OH) for the etherification S_N2 reaction. By dropwise addition of the 1:12 molar ratio of the GTMAC, the reaction was completed in ~ 6 hr @ 65^0C and 500 RPM.

A similar routine procedure was used to purify the Q–Cht.NW$_a$ NPs and the post–dialyzed slurry (off–white coloured) was recovered with its pH, concentration (via gravimetric analysis, GA), and the % yield determined. Figure–5.7 illustrates the overall reaction and the synthesis steps.

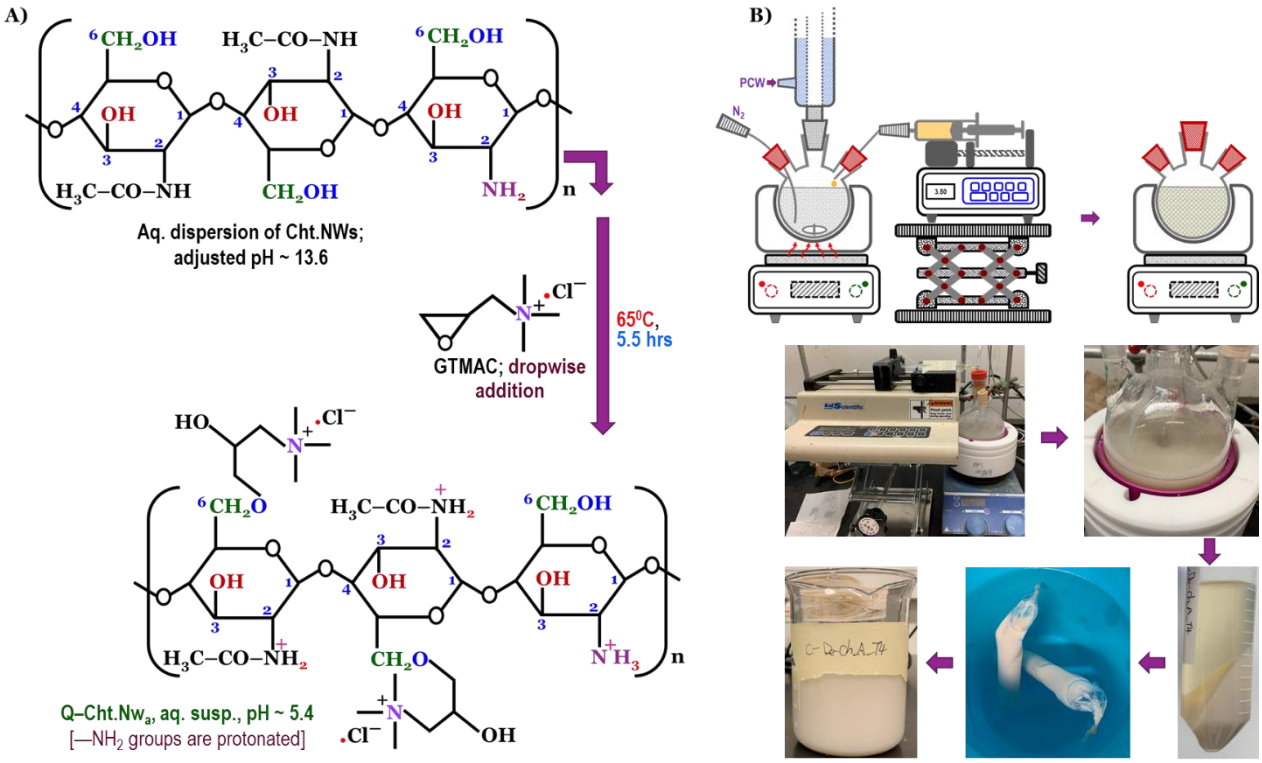


Figure 5.7: A) *The etherification S_N2 reaction for the grafting of GTMAC onto the surface 1^0 alcoholic groups (—CH$_2$OH) producing the Q–Cht.NW$_a$.* ***B)*** *The overall process of the synthesis and purification of the cationic chitin NWs (the Q–Cht.NW$_a$). The purified NWs were found to retain their stability up to ~24 hrs, as after that loosely formed and easily redispersible sediment was seen to form at the bottom of the container.*

5.2.6 Other methods

All the other methods for the characterization of NPs e.g., the FTIR, conductometric titrations, D_H and ZP measurements, UV–Vis measurement, and the TEM imaging were performed as discussed in Chapter–3. As there were a few modifications planned in the BATs conducted with the MO and the NPs, the methodology for the BATs would be discussed below.

5.2.7 Batch Adsorption Tests (BATs) of the NPs with MO

Some difficulties were observed for the fitting of the linearized plots of the Langmuir Monolayer Adsorption Isotherm (LMAI) for 6 data points, hence it was planned to increase the number of concentrations of MO for the BAT studies. Thus, a total of 10 concentrations of the MO, ranging from 50 ppm to 500 ppm was selected. For the planned BATs, all the freshly prepared MO solutions, UV–Vis absorbances (after appropriate/required dilutions) were measured right after their preparation, as well as after the BAT studies (to see if there are any differences). All the BATs for the NPs along with the individual *in situ* parallel negative controls were conducted on a speed-controlled shaker in 15 mL conical centrifuge tubes. The same calibration curve was used during the analyses for all the BATs conducted for the NPs developed here. Other than this, the rest of the experimental steps were performed according to the protocols described in Chapter 3.

As the quantification of free/unbound SC through the conductometric method and UV–Vis method (converting SC to its colored analogue) was tedious and lengthy, none of the BATs were performed with the SC molecule. In the next section, such detection protocol with MO

(which was mentioned above) would be introduced and be discussed. Figure–5.8 shows the schematic representation of the BAT tests with 10 different conc. of MO.

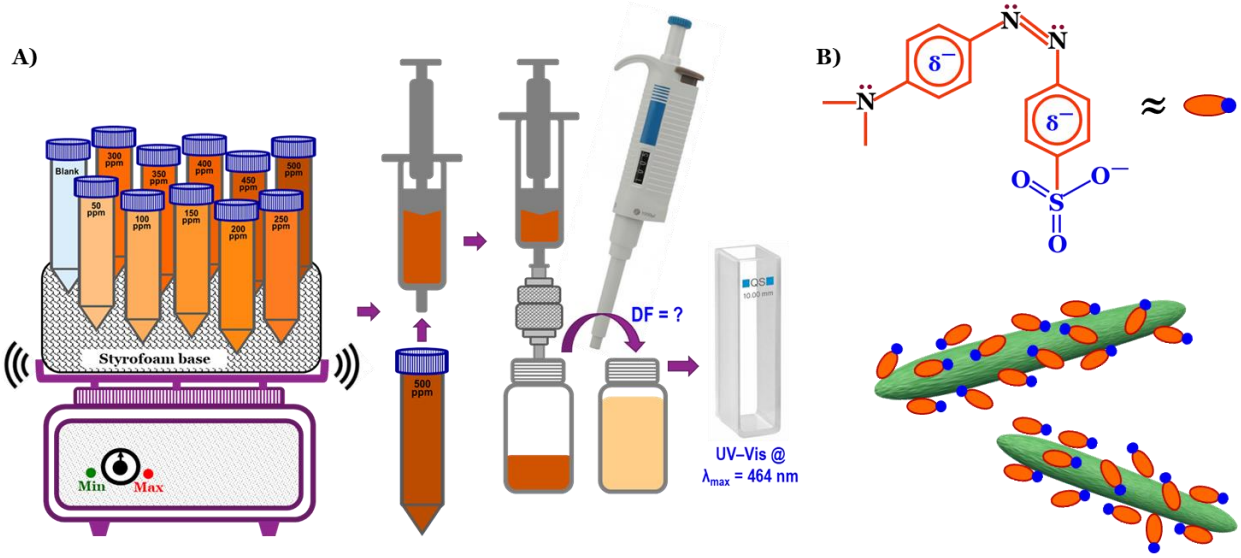


Figure 5.8: A) *The modified BATs done with Cht.NFs and Cht.NWs for MO of 10 different concentrations (50–500 ppm) at RT on a shaker. The data obtained from the UV-Vis measurement @* λ_{max} *(after appropriate dilutions as required) was then fitted through the linearized Langmuir Monolayer Adsorption Isotherm (LMAI).* ***B)*** *Molecular structure of MO and schematic representations of* ***monolayer adsorption*** *of the MO molecules onto the nanocrystals (NCs) of sustainable nanomaterials (e.g., Q–CNCs or Q–Cht.NWs).*

5.3 Results and discussion

5.3.1 Yield % of the developed NMs (chitin based)

Figure–5.9 summarizes all the chitin-based NPs developed in this study. The % yield of the NWs obtained by the acidolysis of α–chitin was lower as the amorphous regions of the α–chitin microfibrils were cleaved, dissolved and removed during the centrifugation process. For the NFs, it was seen with more cycles, the acidified and mechanically pre–treated De–Cht.$_B$ samples after passing through the microfluidizer (μFD) resulted in a higher yield.

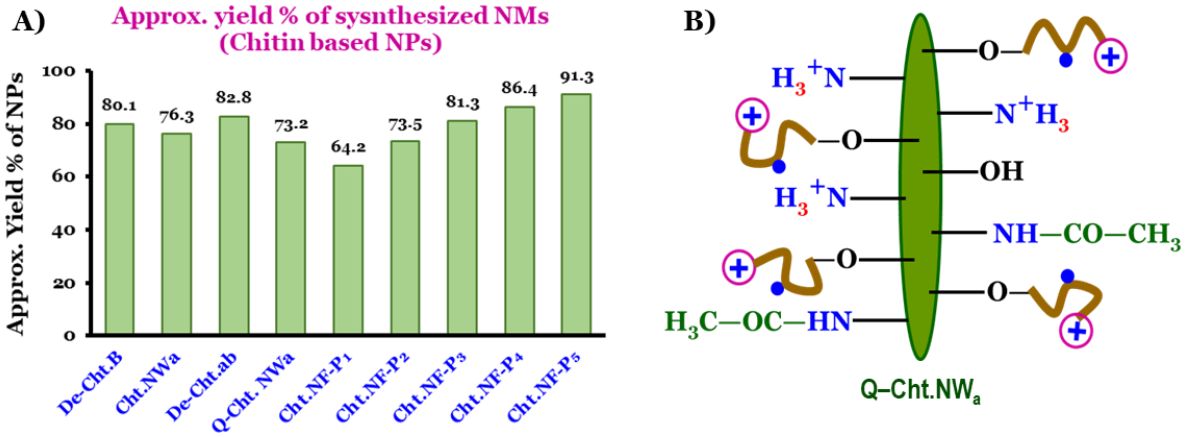


Figure 5.9: A) *The percentage yields of the chitin derivatives including NFs and NWs.* ***B)*** *The schematic representation of the quaternized Cht.NW$_a$, of which in aq. suspensions, the available surface (—NH$_2$) groups got protonated making them more cationic over the grafted QAGs at the protruded 1^0 alcoholic groups (—CH$_2$OH).*

5.3.2 FT-IR of the developed Chitin–NMs

For the De–Cht.$_B$, Cht.NW$_a$, and Cht.NW$_{ab}$, the freeze-dried mass could be grounded, but for the Cht.NF_P$_1$ to Cht.NF_P$_5$ samples, the dried mass could not be grounded (as shown

in Figure–5.10). Rather they were cut into finely small pieces to prepare the FT-IR pellets, and Figure–5.10 shows the FTIR spectra of all the derivatives of α–chitin.

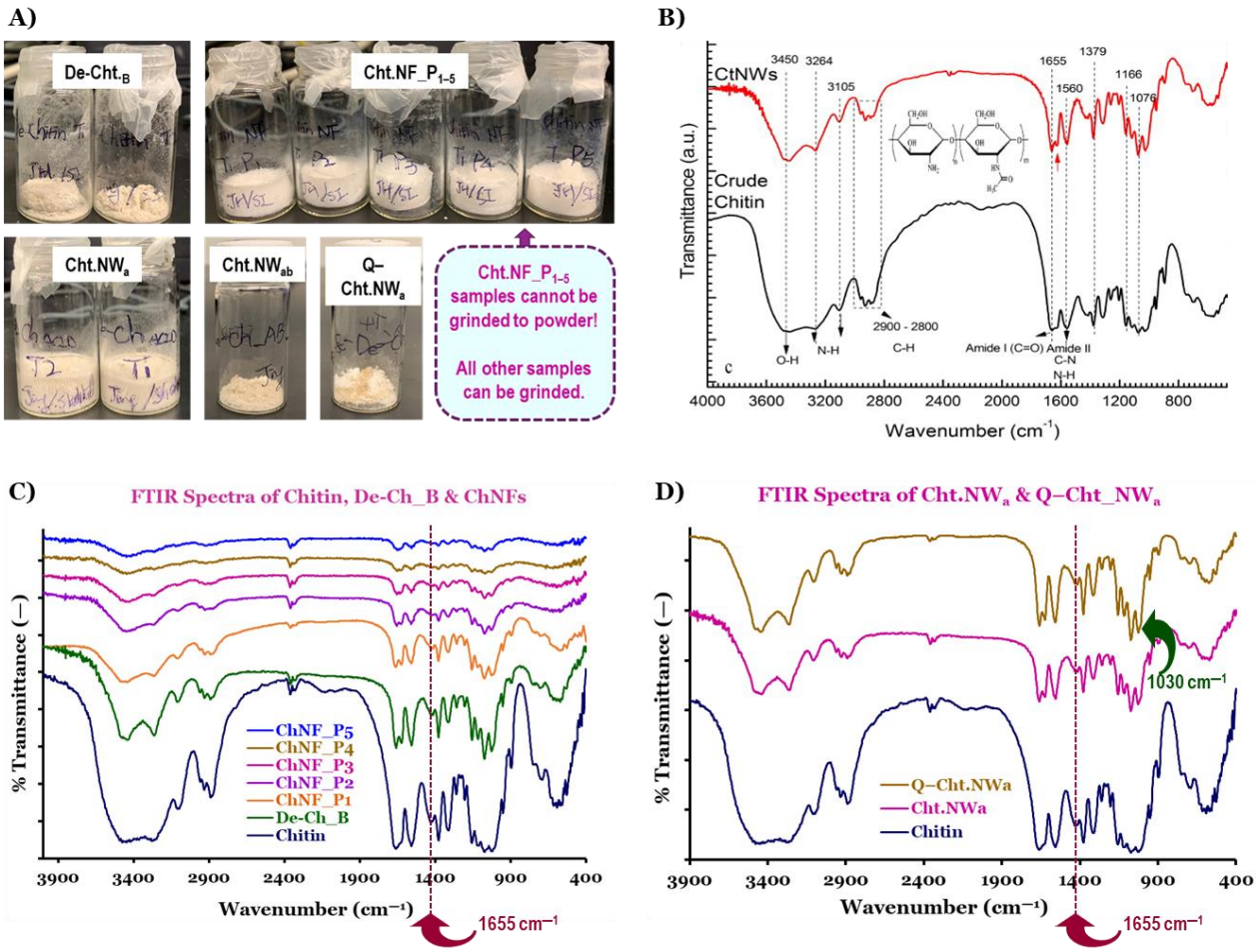


Figure 5.10: A) *Freeze–dried samples of the α–chitin derivatives.* ***B)*** *Notable peaks of Chitin and chitin–NWs from literature.*[227] ***C) & D)*** *FT–IR spectra of the α–chitin and all chitin derivatives, including the NFs, NWs, and the Q–Cht.NWs.*

Following are the notable peaks in the spectra[227–229]: the OH stretching at 3450 cm^{-1}, NH stretching at 3264 cm^{-1} and 3105 cm^{-1}, CH vibrations in the 2900–2800 cm^{-1} range, amide-I CO at 1655 cm^{-1}, amide II (a combination of C–N–H stretching and N–H bending) at 1560 cm^{-1}, CN stretching at 1166 cm^{-1}. The shoulder at 1655 cm^{-1} is due to inter molecular hydrogen bonding between acetylamide groups (—NH–CO–CH_3) and intra molecular hydrogen bonding between acetylamide C=O and C–6 hydroxyl groups (OH), reported to be associated only with α–chitin[228,229], indicating all the derivatives of α–chitin. Thus, the FTIR data confirmed that the chemical (alkaline/acid hydrolysis, quaternization etc.) or mechanical treatment of α–chitin to produce the derivatives did not alter the chemical nature of the native/commercial α–chitin.

5.3.3 QAGs and cationic groups contents via conductometric titrations

The QAG contents were determined by $AgNO_3$ titration through the conductance measurements, similar to the quaternized–chitosan (Q–CS) NMs discussed in the previous chapter (Chapter–4). However, for the NFs produced from the different passes which were not quaternized, they possessed surface 1^0 amino groups (—NH_2), and the protonated amino groups (thus cationically charged, the —N^+H_3) could be quantified by the simple acid–base titration with the corresponding conductances. Figure–5.11 shows the contents of quaternary ammonium groups (QAGs) and the cationic amino groups (—N^+H_3) obtained from the $AgNO_3$ and NaOH titrations, respectively.

From the data, it was evident that in the acidic pH of ~3, all the Cht.NFs possessed strongly protonated —NH_2 groups, which gradually increased after the protonated & pretreated De–$Cht._B$ samples underwent multiple cycles @ the microfluidizer (μFD). As such, the highest

protonated —NH_2 groups contents was observed for the Cht.NF_P_5 (1.70 mmol/g) followed by Cht.NF_P_3 contents (1.24 mmol/g) and then Cht.NF_P_2 (1.10 mmol/g). However, for the Cht.NF_P_4, a sharp transition was observed for the protonated —NH_2 groups contents (1.48 mmol/g) than those of the Cht.NF_P_3The possible exposure of some new 1^0 amino groups (PAGs, —NH_2) on the surfaces of the fragmented nanofibers (Cht.NF_P_X, obtained from multiple passes) could be the most likely reason for such a noticeable increase in the protonated–PAGs contents.

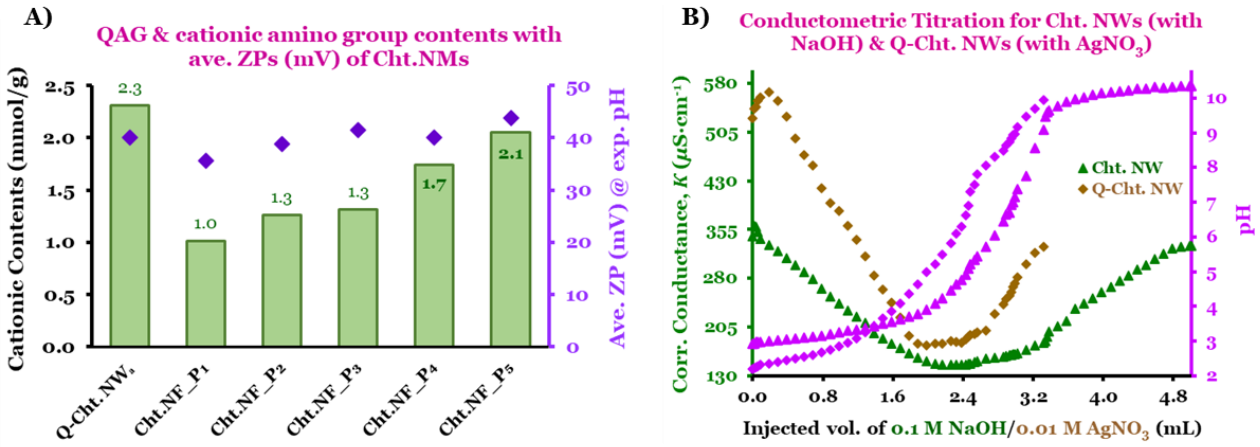


Figure 5.11: A) *The QAG contents and the protonated —NH_2 groups' contents of chitin-based NMs determined through conductometric titrations using 0.01 M $AgNO_3$ and 0.1 M NaOH respectively as the titrant.* ***B)*** *A representative plot where two modes of conductometric titrations were plotted in the same graph.*

As these NFs showed notable protonation of the —NH_2 groups @ C–2 at a pH below ~8, no further quaternization of these NFs was conducted. This would also provide an insight

into the role of quaternized and non-quaternized amino–PS based NMs for the adsorption (i.e., removal) of anionic analytes like the MO (or SC).

Now, in terms of QAG, the Cht.NW_a were grafted with GTMAC @ C–6 producing the Q–Cht.NW_a, and the determined QAG contents were found 2.31 mmol/g. As QAGs were resistant to pH changes, such grafting imparted the permanently cationic charges to the NPs. However, for the Q–Cht.NW_a since there were some free/unoccupied —NH_2 groups @ C–2 on the surfaces of NPs, they would display pH-responsive characteristics in terms of cationization and such phenomena could be an added benefit for sequestering the anionic species like the SC or MO.

5.3.4 Ave D_H and zeta potentials (ZPs) of the developed Chitin–based NMs

The average aggregate sizes (D_H) and the ZP of the samples of chitin based NMs were measured to elucidate the colloidal stabilities and their capabilities of sequestration of the SC (or MO) based on their surface cationic charges, respectively. Figure–5.12 describes the samples prepared for the size and zeta potential measurements. A total of four vials were prepared for the measurements: acidic pH (~3), inherent pH (the default pH of the post–dialyzed concentrated suspensions) (~5), neutral pH (~7) and alkaline pH (~10), to also check the NMs' stabilities over the GI pH range in different zones as well as to evaluate the characteristics of the surface charges in such conditions.

Due to the insoluble nature of the commercial α–chitin, the dispersions were prepared at 0.05% (w/v), whereas all the other chitin dispersions were prepared at 0.1% (w/v). The dispersions were slightly viscous for the Cht.NFs even at that low concentration, and an

increasing trend in the viscosities were evident with the number of passes for the production of the NFs (Cht.NF_P_5 > … … Cht.NF_P_1).

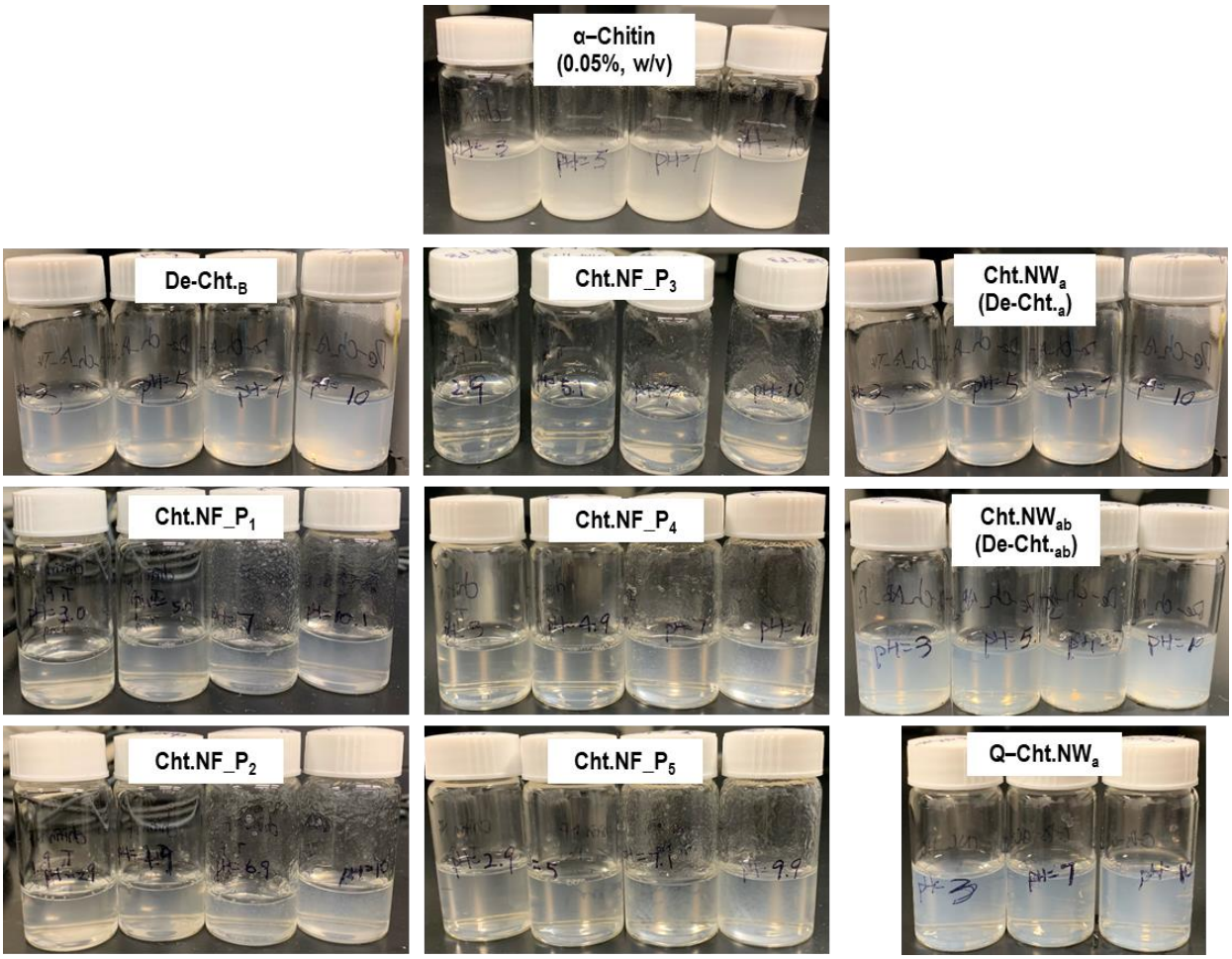


Figure 5.12: *The prepared dispersions of α–chitin and its derivatives. The commercial α–chitin is insoluble/non–dispersible in MQ water and thus a lower conc. (0.05%, w/v) of the suspensions was prepared and adjusted the pH. For the chitin NFs prepared (0.1%, w/v) derived from the 5 different passes @ µFD, more thick suspensions were seen for the vials having the adjusted pH of ~7 and ~10. The Cht.NW$_a$ and the further deacetylated NWs (Cht.NW$_{ab}$) were found stable at any pH without any precipitation or sediment/cake formation, but the latter were seen cloudier at the same conc. The ZP/D_H of any GTMAC grafted NPs were seen not so variant over pH changes in the previous chapters. The inherent pH of the post–dialyzed Q–Cht.NW$_a$ were found > ~5.6, thus only the three different pH adjusted suspensions were prepared in this case.*

The average D_H and ZP data of the chitin derivatives are shown in Figure–5.13. The commercial α–chitin possessed a size of ~ 4µm, and after alkaline deacetylation, the aq. dispersibility of the De–Cht.$_B$ was enhanced due to the available/unoccupied surface —NH_2 groups that were protonated @ the experimental/inherent pH (~ 7). Due to such protonation, the cationic charges of the —N^+H_3 groups induced the repulsion that increased their colloidal stability with a D_H of ~ 1.5µm. The development of the cationic charges was also evident from the increase in ZP for the De–Cht.$_B$ NPs over the ZP of the α–chitin.

The Cht.NW_a possessed significantly lower D_H than the De–Cht.$_B$ NPs with a D_H of ~527 nm for the Cht.NW_a and a ZP of ~ +26 mV. Further deacetylation of the NW_a (producing the Cht.NW_{ab} NPs) slightly increased the ZP to ~+29 mV with a D_H of ~425 nm due to reduced aggregation arising from more inter–particle repulsions between the cationic charges. A significant decrease in the D_H was observed after quaternizing the NWs, where the Q–Cht.NW_a displayed a ZP of ~ +40 mV and a D_H of ~119 nm. The reduction in the DH was attributed to the higher inter–particle repulsions between the cationic charges of QAGs and the protonated —NH_2 groups on the surface.

All the Cht.NFs obtained from different passes @ the µFD showed strongly cationic characteristics (manifested by the ZPs > +32 mV, figure–5.13 B) at their inherent pH (~5.5) of the corresponding aq. dispersions. For the NF_P_1, the aggregate size was found ~1.5 µm, and the other four NFs (P_2–P_5) possessed a D_H of ~1300 nm.

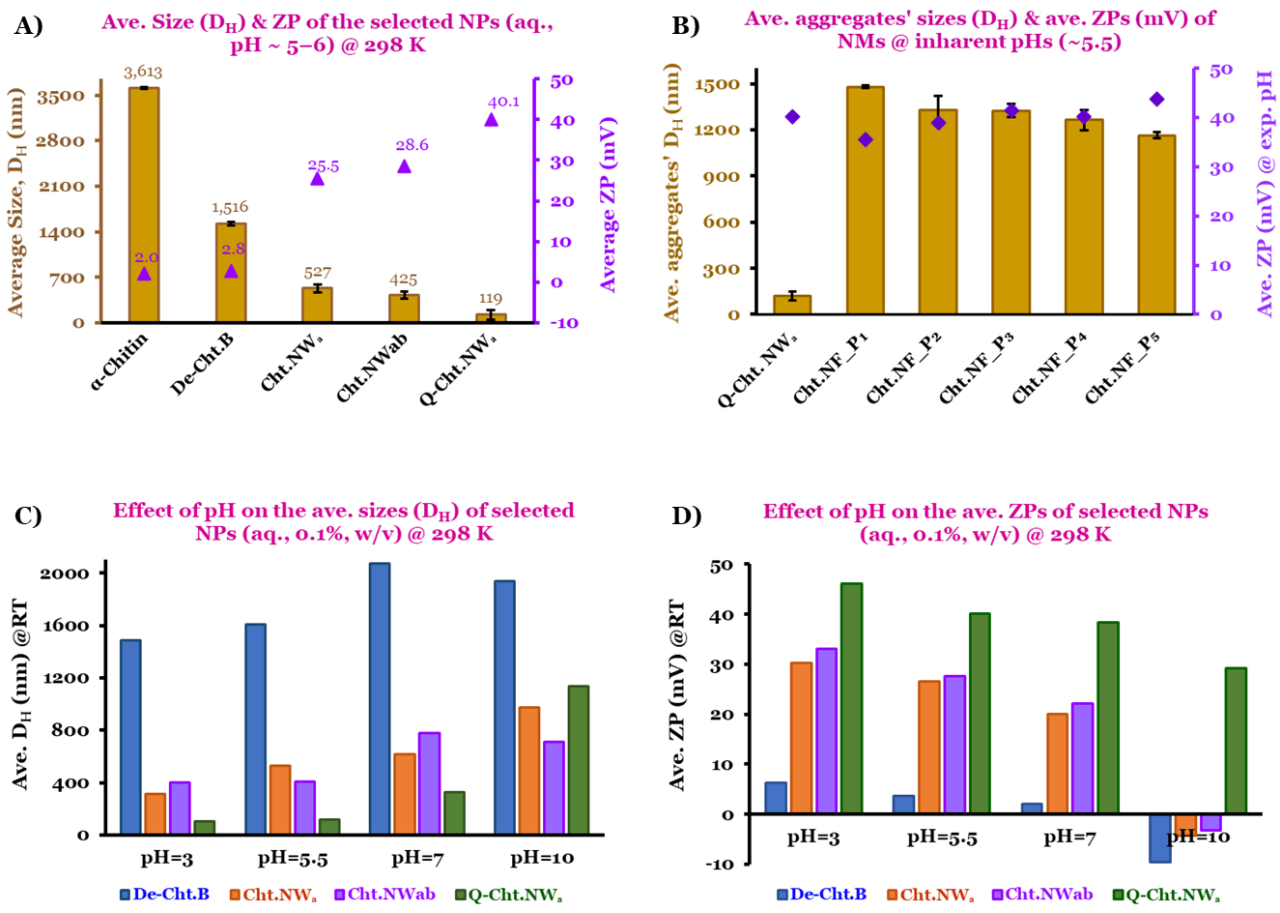


Figure 5.13: A) *Average aggregates' sizes (D_H) and the ZPs of commercial α-chitin and its derivatives: deacetylated chitin (alkaline; De–Cht.$_B$), chitin nanowhiskers (Cht.NW$_a$), deacetylated chitin nanowhiskers (Cht.NW$_{ab}$), and quaternized chitin nanowhiskers (Q–Cht.NW$_a$).* ***B)*** *Comparison of D_H and ZPs of Q–Cht.NW$_a$ and the Cht.NF_P$_x$ NMs along with the quaternized chitosan (Q–CS).* ***C)*** *and* ***D)*** *Effect of different pH on the D_H and the ZPs respectively for the chitin derivatives. The ZPs of the De–Cht.$_B$, Cht.NW$_a$ and the Cht.NW$_{ab}$ were found negative at alkaline pH (pH ~10) most probably due to the deprotonation of the primary alcoholic groups at C–6 producing the anionic alkoxy (—CH$_2$O$^-$) ions. At that strongly alkaline pH (~10), all the protonated amino groups (—N$^+$H$_3$) would be deprotonated and would thus revert to the uncharged primary amino groups, PAGs (—NH$_2$).*

The effects of changes of pH were also evaluated for the α–chitin and its derivatives and the D_H data (Figure–5.13 C) indicated that all the NMs (De–Cht.$_B$, Cht.NW$_a$, Cht.NW$_{ab}$ and the Q–Cht.NW$_a$) showed similar stabilities over the four different pHs (pH ~3, ~5.5, ~7, and ~10). Although there were some aggregations observed for the NPs in the aqueous medium, when the pH shifted from acidic to alkaline no sharp increase in the D_H of the NPs was observed, except for the De–Cht.$_B$. In terms of the ZP of the chitin derivatives, a notable reducing trend for the overall surface cationic charges were evident for all the NMs as shown in Figure–5.13 D.

The D_H and the ZPs of the Cht.NF_P$_x$ NMs were also evaluated with respect to the changes in pH of the dispersion media, as shown in Figure–5.14. As expected, the primary amino groups, PAGs (—NH_2) that were available on the surfaces of the NFs became protonated (—N^+H_3) @ acidic medium (pH ~3) and thus the ZP values became strongly positive. Due to the higher cationic charges that produced higher inter–fibrillar repulsions resulting in the size of the aggregates becoming smaller at acidic pH, especially for the NFs P_2–P_5 with D_H of less than 1µm. Once the pH of the dispersion was increased from inherent pH (~5) to neutral pH (~7), no significant changes in the D_H of the NFs were observed except for the NF_P_1 which displayed a sharp increase in size due to aggregation. Such phenomenon is also evident, and it could be explained based on the reduction of the ZPs from +36 mV (@ pH ~5), to +5 mV (@ pH ~7) as a consequence of the deprotonation of the protonated PAGs (—N^+H_3) of the surfaces. Like the other chitin derivatives described in Figure–5.13 C & D, all the NFs possessed negative ZPs @ a pH of ~10 due to the reason discussed earlier. From the

careful inspection of the vials of the NFs @ that at pH (~10) visible flocs suspended in the media was observed.

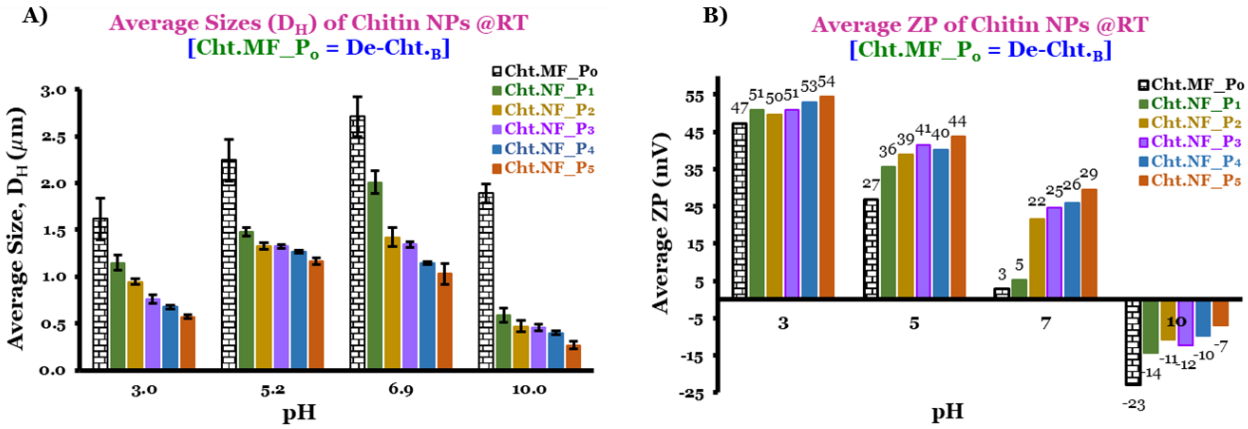


Figure 5.14: *Effect of various pH of the dispersion medium on the* ***A)*** *D_H of the De–Cht.$_B$ (Cht.MF_P_0) and the Cht.NF_$P_{1–5}$, and* ***B)*** *ZPs of the same NPs.*

5.3.5 TEM images of Chitin–based NMs

Due to the expected aggregation upon drying of the samples on the CFC grids, better quality TEM images were not obtained after multiple trials. Figure–5.15 shows the TEM images (@ poor resolution) of the NFs and NWs derived from the α–chitin. After several trials in making the TEM grids we were unable to find a better resolution images for the Cht.NF_P_x. As mentioned earlier, the NFs obtained from the pass–1 to pass–5 were found slightly viscous and after preparing the suspensions for preparing the grids, it was a bit concentrated and further aggregations occurred during drying the grids. Having the suspensions for the TEM in diluted concentrations failed to provide the acceptable TEM images.

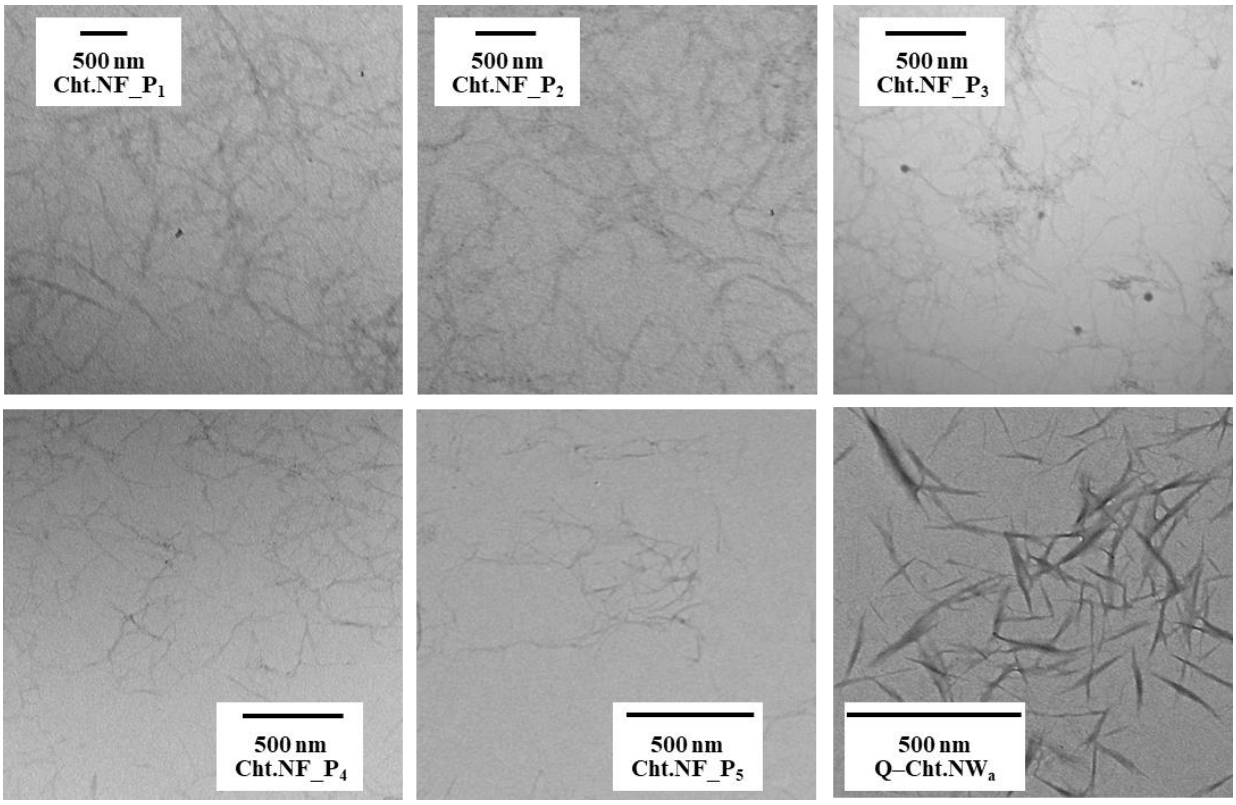


Figure 5.15: *The TEM images of the extracted Chitin derivatives: the Cht.NFs obtained from the microfluidizer through pass–1 to pass–5 (labeled as Cht.NF_P1, Cht.NF_P2, ……Cht.NF_P5) and the Q–Cht.NWs. The TEM image of the Cht.NWs was not acquired.*

5.3.6 BATs of Chitin–based NMs with MO

As discussed in the materials and methods section, due to the ongoing plan to develop the cholate sensor, these NMs were not evaluated for their capabilities to sequester SC from the BAT studies. Here, the NMs were evaluated for their adsorption capabilities of MO. The determined Q_{max} values are listed in Table 5.1 and the corresponding plots are shown in Figure–5.16, where reasonable comparisons could be made for some selected NPs described in the previous chapters.

Table 5.1: The determined Q_{max} values of some selected NPs (including the chitin-based NPs), from the batch adsorption tests (BATs) with methyl orange (MO), and the corresponding zeta potentials (ZP) and sizes (D_H) of the NPs.

Full names of NPs	Abbreviated form of NPs	Q_{max} (mg/g)	STDV _Q_{max}	ZP (mV)	Size, D_H (nm)
Nanocrystalline Cellulose (CNC)	**NCC™**	35.3	5.2	-43.7	92.3
Desulfated CNC (by HCl)	**DS–CNC$_a$**	82.1	7.3	-13.4	194.8
Commercial α–Chitin powder	**α–Cht.**	55.2	11.2	2.0	3613.0
Deacetylated Chitin (by NaOH)	**De–Cht.**	91.3	6.4	2.8	1516.3
Deacetylated Chitin (by HCl) / Chitin Nanowhiskers	**Cht. NW$_a$**	186.7	8.1	25.5	527.0
Deacetylated Chitin/~Nanowhiskers (1st by HCl, then by NaOH)	**De-Cht.$_{ab}$**	207.3	7.4	28.6	424.8
Chitosan (DD = 85%)	**CS**	82.6	4.1	21.6	2093.7
Quaternized Chitin Nanowhiskers	**Q-Cht. NW$_a$**	327.4	9.3	32.5	119.3
Quaternized Chitosan	**Q-CS**	278.5	11.6	35.0	1739.0
Quaternized Desulfated CNCs	**Q-CNC$_a$**	295.2	6.7	35.8	132.6

From the Q_{max} data and the ZP values of the chitin derivatives as shown in Figure–5.16 A), it was evident that the Q–Cht.NW$_a$ possessed higher adsorption capacities over other NP systems, even for the other Q–NPs, such as Q–CS and Q–CNC$_a$. From the earlier discussion on the adsorption capacities of the Q–CS, similar types of binding/interaction forces were observed for the adsorption of the MO on the surfaces of Q–Cht.NW$_a$. The Q–Cht.NW$_a$ NPs possessed additional cationic groups (the protonated PAGs, —N^+H_3) @ pH ~7 on the surfaces over the grafted quaternary ammonium groups (QAGs), as the primary (1^0) amino groups, PAGs (—NH_2) of the Q–Cht.NW$_a$ became protonated at that pH. Thus, stronger ionic attractive

forces were evident between the anionic MO molecules and the Q–Cht.NW$_a$, as shown in Figure–5.17. As discussed in the preceding chapters, as well as reported in the literature, the electrostatic attractive forces (long-range force) between the opposite charges were the most crucial factors, for the binding/chemi–adsorption of the system.

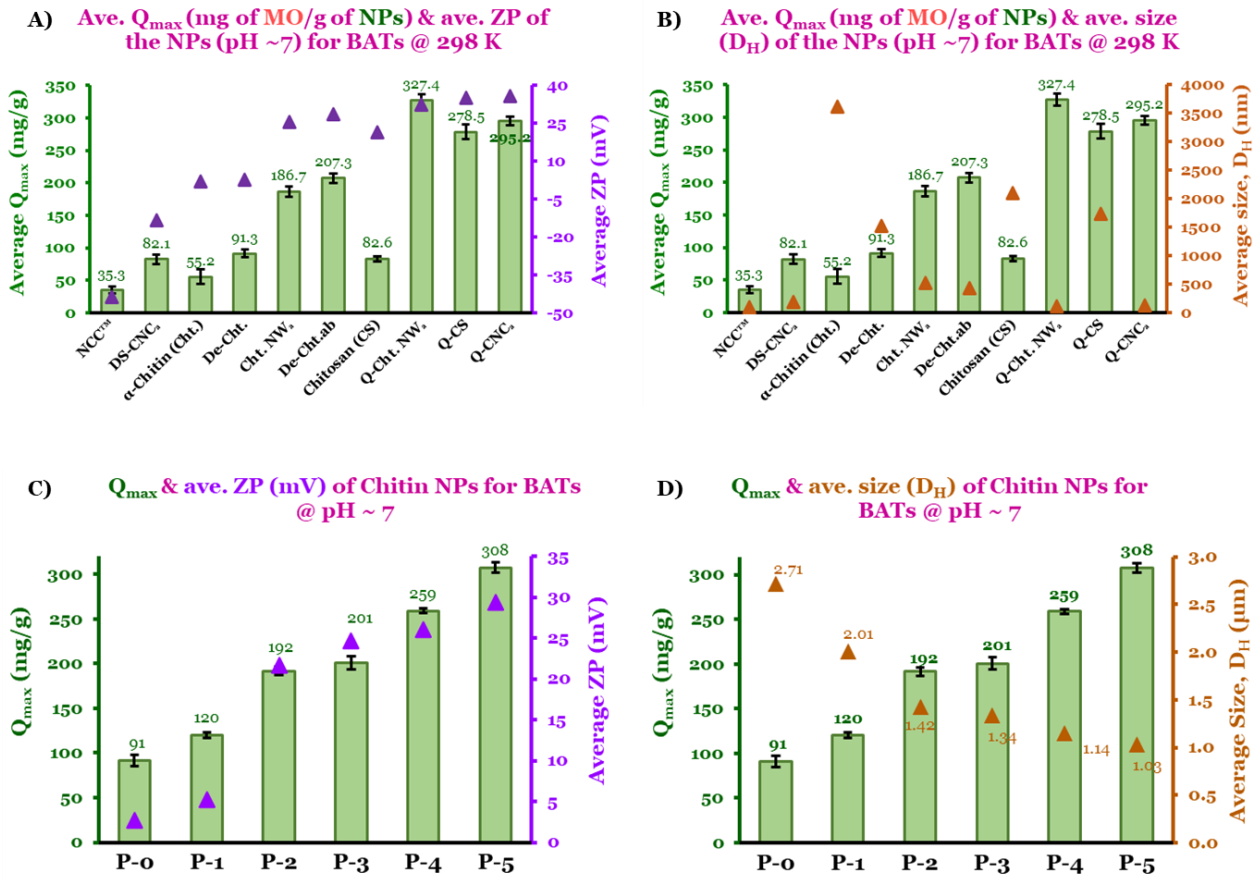


Figure 5.16: A) *The determined Q_{max} values obtained from the linearized Langmuir Monolayer Adsorption Isotherm (LMAI) of the chitin derivatives and comparisons of the Q_{max} values of some selected NPs with the chitin derivatives against the ZP values.* ***B)*** *Same data against the aggregates' sizes (D_H) explaining the possible relationship between the surface charges and the adsorption. The Q_{max} values of the five different Cht.NFs from 5 different passes are plotted against the* ***C)*** *ZP values and* ***D)*** *the aggregate sizes (D_H). Here, the P-0 is the De–Cht.$_B$.*

The Q–CS, derived/synthesized from the commercial chitosan (CS), are the nanofibers (NFs) that are hydrophilic, solvated fibers that were found completely soluble in water at low concentrations. Due to the inter–fibrillar/particle aggregation from the H–bonding, probably a few of the surface–QAGs (quaternary ammonium groups) became shielded. This could be the most likely reason for the lower Q_{max} (278.5 mg/g) of the Q–CS compared to the Q–Cht.NW_a. But due to their complete water solubilities, the Q–CS nanomaterials showed comparable adsorption of the MO with other NPs, namely the Q–CNC_a and the Q–Cht.NW_a.

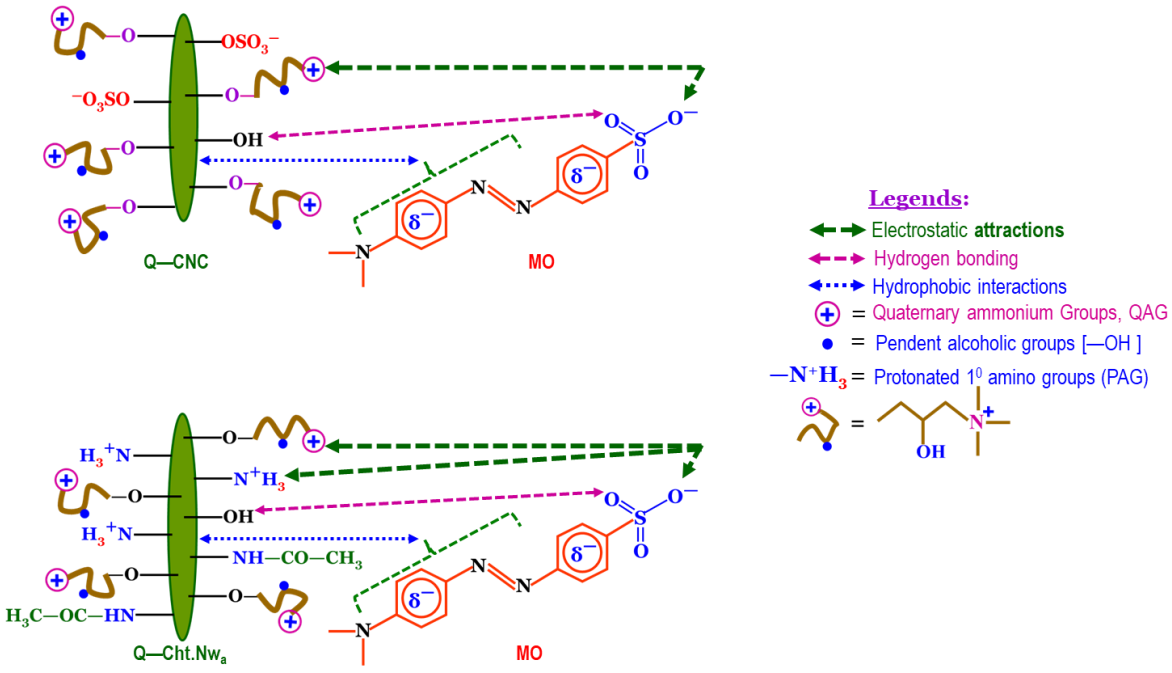


Figure 5.17: *The schematic representation of all the probable in-effect forces that are responsible for binding/adsorption between the cationic NPs and the anionic MO molecules. The top image is for the Q–CNC NPs and the bottom is for the Q–Cht.NW_a. The Q–Cht.NW_a possesses surface PAGs (—NH_2) that got protonated @ the pH of ~7 and thus are able to establish the additional ionic attractive forces between the —N^+H_3 groups and the sulfonate groups (—SO_3^-) of the MO molecule during the BATs. Such phenomena explain the most likely reason of the greater extent of MO adsorption by the Q–Cht.NW_a over the Q–CNCs.*

The De–Cht., Cht.NW_a and the Cht.NW_{ab} (here the De–Cht.$_{ab}$ on the plot) NP systems showed greater adsorption, especially both NWs i.e., the Cht.NW_a & Cht.NW_{ab} or the MO molecules over the NCC^{TM} or the DS–CNCs due to the presence of PAGs (—NH_2) which were protonated. In this case, due to the size and lower aq. dispersibilities, the De–Cht. showed very lower extent of MO adsorptions. For the commercial α–chitin and CS, which were completely insoluble in water resulting in an unstable dispersion, these two particles showed some degrees of MO adsorption (Figure–5.16 A/B), where the non–ionic forces (hydrophobic interactions/Van der Waals forces, H–bonds formation etc.) could be the most likely reasons for the interaction. During the batch adsorption tests (BATs), the post–adsorption mixtures of these two systems were precipitated, due to unstable dispersion.

Table 5.2: The determined Q_{max} values of the chitin nanofibers (Cht.NFs) from the batch adsorption tests (BATs) with methyl orange (MO), and the corresponding zeta potentials (ZP) and sizes (D_H).

Full names of NPs/NFs	Abbreviation of NPs/NFs	Q_{max} (mg/g)	STDV _Q_{max}	ZP (mV)	Size, D_H (μm)
Deacetylated Chitin (by NaOH)	**Cht.NF_P_0**	91.3	6.3	2.8	2.71
Chitin Nanofiber, Pass–1	**Cht.NF_P_1**	119.9	3.1	5.3	2.01
Chitin Nanofiber, Pass–2	**Cht.NF_P_2**	191.6	4.6	21.7	1.42
Chitin Nanofiber, Pass–3	**Cht.NF_P_3**	200.7	7.1	24.7	1.34
Chitin Nanofiber, Pass–4	**Cht.NF_P_4**	258.8	2.6	26.0	1.14
Chitin Nanofiber, Pass–5	**Cht.NF_P_5**	307.5	5.4	29.4	1.03

The determined Q_{max} values from the BATs with MO for the chitin nanofibers (Cht.NFs) obtained from multiple runs/passes through the microfluidizer (μ–FD) are listed in Table 5.2 and shown in Figure–5.16 C & D. For the cases of adsorption of MO by Cht.NFs, an increasing trend of the Q_{max} were observed with increasing passes to produce the NFs using the μFD, and the Cht.NF–P_5 showed the highest Q_{max} (308 mg/g) for MO. Such adsorptions were inversely proportional to the aggregate sizes of the Cht.NFs. Although, the zeta potentials (ZPs) were not significantly higher for the NFs compared to the ZPs of Cht.NW_a or the Q–Cht.NW_a, they showed comparable adsorptions for the MO, especially for the Q_{max} of Cht.NF–P_5, which was higher than the Q–CS or the Q–CNC_a NPs. The most likely reason for this could be the viscosity of NF dispersions as shown in Figure–5.12.

During the processing and purifications, all the NFs were more viscous (by visual inspection) than the NW dispersions of the same concentration. The dispersion viscosities were higher for the NFs obtained with higher passes in the μ–FD. Although none of the viscosities were measured for the NP system in this Ph.D. work, due to the viscosity, for example, for the Cht.NF_P_5, more MO molecules may have entrapped to the NF_P_5 vicinity leading to greater adsorption. Further studies should be conducted to examine the effect of the viscosities of the NFs on the adsorption of anionic species. Similar behavior for the dispersions' viscosities was also reported in the previous chapter (Chapter–4) for Q–C_{12}–CNC and brush–CNC NPs.

5.4 Conclusions

This chapter discusses the chitin and chitin-based NMs, where this natural bio–PS possessed the S.M.A.R.T.© properties with the additional structural benefit of the PAGs (—NH_2) on the surfaces that became protonated at a pH below ~8 making the overall systems more cationic. These cationic systems showed higher zeta potentials in acidic pH (~3) and the quaternized chitin NWs (the Q–Cht.NW_a) were stable at pH up to ~10. The NF systems obtained from higher passes (mainly the Cht.NF_P_4 and _P_5) through the µFD were more viscous at their inherent pH (~5.5) and their ZP or the D_H were not significantly changed until a pH of ~7. All the systems showed greater physico-chemical adsorption of MO demonstrating their potential as the adsorbent for effluent treatment and as the BAS to sequester the bile salts for treating hypercholesterolemia.

5.5 Future Directions

The relative viscosities of the NP dispersions were found to be one of the important factors for binding MO or anionic species. Thus, the measurement of viscosity of the NP dispersions should be conducted and further investigation should be carried out to determine their impact on the binding of ligands to the substrate. Before they can be considered for human application, the biosafety of such NMs should be determined.

Chapter 6: Development of Sodium Cholate detection System

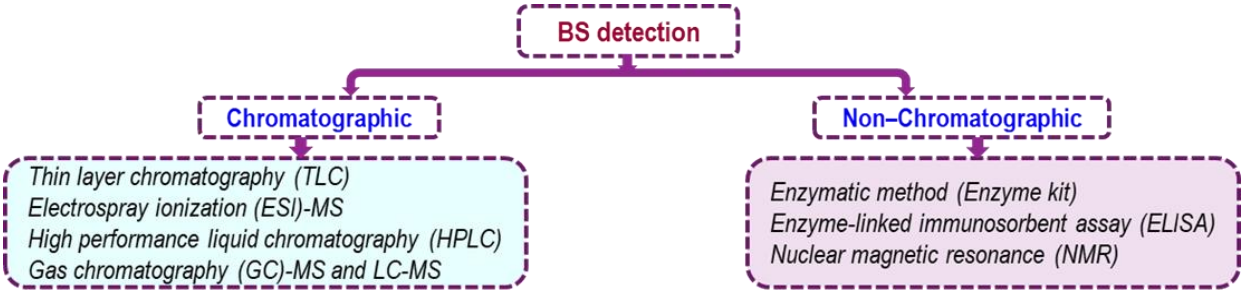
6.1 Introduction

The detections of BS in aqueous samples are non-user friendly and the current methods for such detections have many notable limitations[143] as shown in Figure–6.1. This challenge is due to the lack of availability of methods at the laboratory scale, such detections of BS from a benchtop instrument, which had been ignored for a long time. The bile salts do not have any UV–Vis absorbance (as shown in Figure–6.2) regardless of the conc. used for analysis and thus the UV–Vis technique was not suitable to directly measure the absorbance to determine the unknown concentration. The common tools/method used for the detection and quantification of BS along with their limitations (mentioned in the parentheses) are[146–153]:

- Enzyme Kits (widely used in many disciplines, accurate, UV–Vis detection, expensive)
- UV–Vis spectroscopy via producing intermediate-colored analogs[157] which have been discussed in Chapter–3/4 (troublesome, presence of artifact, quantitative)
- Conductivity Measurement[161,230,231] (acceptable & quantitative, but major artifact due to presence of counter ions)
- Isothermal Titration Calorimetry, ITC[232–237] (acceptable, but qualitative)

Due to the limitations or pitfalls for each of the individual lab-scale methods/tools, further research is necessary to develop a tool capable of measuring the concentrations of ions/analytes of interest (here SC) based on the ionic activities in aq. samples. In this regard, a membrane electrode selective to BS could be a gold standard, which was not taken into consideration and had long been ignored and unexplored. If a drug selective electrode (DSE) could be devised,

then it would unlock immense opportunities to the material and analytical sciences and could result in a significant breakthrough.



Methods	Advantages	Disadvantages
TLC	Easy operation, low cost; without sample derivatization	Only applicable to qualitative analysis but not samples containing impurities, generally used to detect a mixture of BAs standard substances.
ESI-MS	Without sample derivatization, qualitative analysis is allowed directly according to specific neutral or low-molecular-weight fragment ions	Only applicable to qualitative analysis but not distinguishing of substances with the same parent or fragment ions (e.g. conformational isomers)
HPLC	High sensitivity and specificity, applicable to hardly volatile substances.	Complicated sample treatment that requires derivatization to enhance the UV absorption of BAs, with the efficiency affecting detection results; long detection time that is unsuitable for a large number of samples
GC-MS	High degree of separation giving accurate molecular information, applicable to separation and quantification of mixtures of non-conjugated BAs	Requirement of derivatization that converts conjugated BAs into non-conjugated ones to decrease boiling points, complicated treatment process that is unsuitable for a large number of samples
LC-MS	Short analysis time, low limit of quantification allowing separation of conformational isomers; simple sample treatment, without derivatization, automatic detection suitable for high-throughput analysis	High cost, complicated instrumental operation, mostly applicable to basic research but not clinical use.
Enzymatic	Routine clinical detection method of TBA, simple operation, low cost, reflecting the overall characteristics of TBA.	Only applicable to C_{24}-steroids containing C_3-OH which, when substituted, causes detection failure; not applicable to low-content BAs
ELISA	Suitable for a specific BA.	Low accuracy, proneness of antibodies to cross reactions with metabolites or matrices to produce false positive results
NMR	Mainly applicable to a certain type of BAs	Requirement of sample derivatization, complicated operation, failure to detection of a specific BA.

Figure 6.1: *Common techniques utilized for detection of BS, their advantages and disadvantages. Except for the enzyme kit, all the methods are used at the industrial scale of detection. Table drawn and adapted from.*[143]

6.2 Ion-selective electrode (ISE)

There are a wide variety of commonly used names for the polymeric electrodes, such as ion-selective electrode (ISE), drug selective electrode (DSE), indicator electrode, flexible membrane electrode (FME), or the polymeric membrane electrode (PME).[238–250] The major developments in the history of ISE occurred over the last several hundred years. Gibbs (in 1875), Arrhenius (in 1887), Nernst (in 1888-1889), Ostwald and Planck (in 1890) have conducted studies on the properties of semi-permeable membranes, thermodynamic relationships of membrane equilibria and the theory of electrolyte solutions.[240–242] Herein, the concepts like diffusion potential, potential difference and ionic mobility have led to the evolution of membrane electrochemistry.[240–242]

An ion-selective electrode (ISE) is an analytical tool or a sensor (a half cell electrode) which can be used to determine the concentration of the analyte (ions/drugs of either cationic or anionic) of interest based on the activity of the analyte in aqueous solution by measuring the electrical potential (EMF, in Volts or mV) across a polymeric membrane designed as being selective or partially selective to the target analyte(s)[240,241,244,246–248]. Such ISE is a half–electrode (half–cell), and in combination with another reference half–electrode (RE, a half–cell), a full electrochemical cell is established. In terms of the RE, the Ag/AgCl or the saturated calomel electrode, SCE (Hg_2Cl_2) are the most common reference electrode. Figure–6.2 shows the basic fabrication of a full electrochemical cell consisting of an ISE and a RE.[240,241,244,246–248]

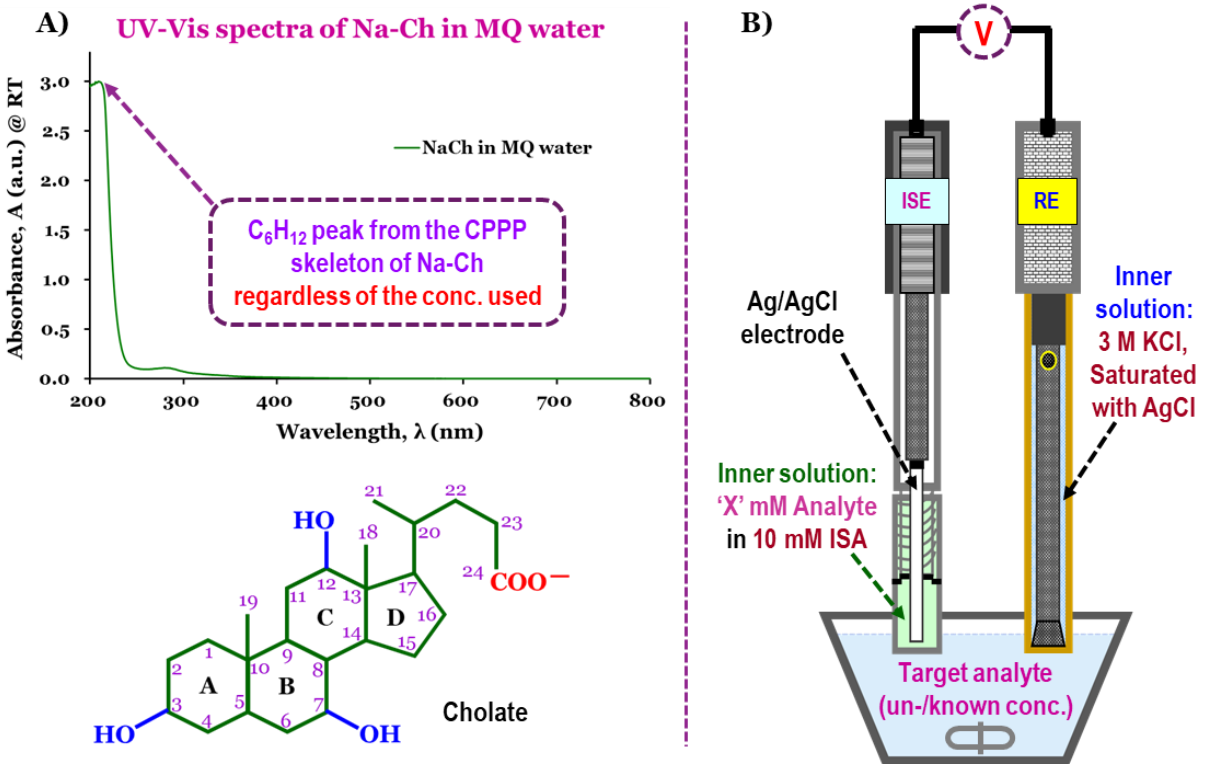


Figure 6.2: A) *UV–Vis spectra of the aqueous solution of sodium cholate (SC). The peak that appeared was for the cyclohexane ring and doesn't show any hypsochromic/bathochromic (blue/red) or hypo–/hyperchromic shift based on the changes in conc. The chemical structure of the SC is shown just below the spectrogram.* ***B)*** *A basic schematic of an electrochemical cell consisting of the ISE (half–cell) and the RE (a Ag/AgCl electrode, another half–cell) connected to a voltameter or a benchtop pH meter. For the RE, the inner solution used was the aq. 3M KCl saturated with AgCl for which the known half-cell potential is +0.2225 V (with respect to the standard H–electrode).*

ISEs can be classified according to the nature of the basic membrane material. The main requirement is that the membrane must be immiscible with respect to the solutions and solid contacts. There are four main types of ion-selective electrodes[240–242]:

- Solid-state membrane electrodes

- Liquid (or plastic) ion-selective electrodes
- Glass membrane electrodes
- Electrodes with suitable additional membranes

Such a benchtop model of the ISE offers several advantages, namely, (a) they are user friendly and easy to operate, (b) not so expensive to fabricate, (c) a higher conc. Can be determined through the dilution effect, (d) the real-time conc. determination based on the activity of ions is possible, (e) either anionic or cationic ions can be determined/quantified depending on how the ion-selective membrane (ISM) has been fabricated. However, there are some unavoidable and inherent limitations[251–255] for the ISE that may be difficult/impractical to circumvent, such as–

- The ISM allows more than one type of analyte (if present) to pass through it, producing artifacts to the measured potential due to the passage of other ions.
- The ISM fails to measure the potentials with precision or accuracy for analytes for which it was not made selective, which is inconvenient in many instances.
- The measured potentials by the ISM of the ISE are based on the conc. of the analytes/ions in equilibrium at the ISM's surfaces which is only ensured for diluted conc. of the sample solutions. At a higher conc. of analytes, say an amphiphilic (thus, can work like a surfactant) drug, micelles are formed resulting in a reduction of the mobilities of the free single molecules. Consequently, the conc. of the free drug molecules at the immediate vicinity of the membrane would be lower than that in the bulk causing significant inaccuracy in the measured potentials.

This chapter briefly discusses the development of a cholate selective/detecting membrane electrode and its application in the determination of the unknown conc. of the post–BAT samples. The idea of drug selective membranes (DSM) or the electrodes (DES) is a cliché and thus was being reported by many of the research bodies to detect/quantify drugs of interest. Herein, this study was conducted from the inspiration of Siegfried Lindenbaum's (R.I.P.) (1981)[243] and Luigi Campanella's (1982–83) works[247] on a bile salt electrode using a liquid membrane. In these studies, flexible polymeric membranes were not used, rather an ionophore solution sandwiched between two polytetrafluoroethylene, PTFE (Teflon) discs to 'mimic' a membrane was used.[243,244,246–248] Considering the facts, the cholate selective flex-membrane (CSM) based electrode (the CSE) offers a possible approach to quantify the concentration of sodium cholate continuously.

6.3 Cholate selective membrane electrode (CSE): Components

The CSE is a reference electrode (RE) consisting of a custom-made Ag/AgCl electrode with four components: the electrode body, inner Ag/AgCl probe, end cap or also known as electrode head or tip, and the drug selective membrane (CSM). The inner Ag/AgCl reference electrode probe was made by coating the silver rod with silver chloride through electrolysis in a 100 mL of 1 M NaCl for 20 minutes with Ag–rod as anode and platinum electrode as a cathode. Figure–6.3 shows the schematic of a drug selective electrode (DSE), here the cholate selective electrode, CSE, depicts all four components. The electrode head/tip is detachable, onto which the selective membrane, CSM is cut and glued at one of the ends.

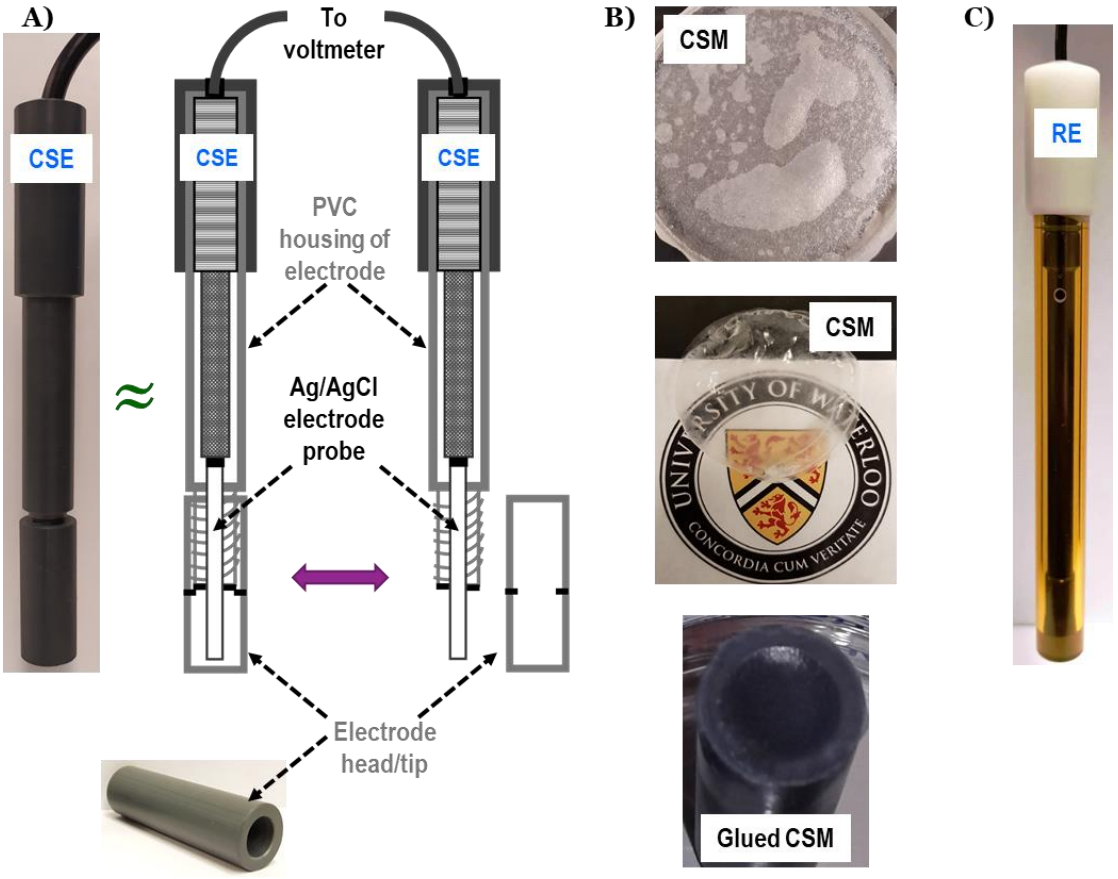


Figure 6.3: A) *The schematic illustration of the components of CSE showing all 4 parts of that half–cell.* ***B)*** *The success in preparing the unprecedented CSM for the 1st time after several trials and errors. During the working mechanism of the electrode system, this CSM is considered as the salt bridge.* ***C)*** *The Ag/AgCl reference electrode, RE (a half cell) to be used to construct a full electrochemical cell (E–Cell).*

Several numbers of electrode heads were fabricated from the in-house facilities at the University to run multiple quality assurance tests to confirm that they are working well. Once the glued CSM was secured at the tip, ~1.5 mL of the target analyte solution i.e., the sodium cholate, SC (NaCh.) solution prepared in an ionic strength adjustor (ISA, here 10 mM NaCl

was used) was pipetted into the housing before the tip was screwed into the CSE PVC housing. As outlined in Figure–6.4, the selective membrane that separates the CSE from the unknown samples, works as the salt bridge between the two half cells of the E–Cell. For the Ag/AgCl—RE, the inner solution used was the 3 M KCl solution saturated with the AgCl. Once the E–cell was connected to the voltameter, the shorthand notation could be written as follows—

CSE **I** 10 mM NaCl, 10 mM NaCh **II** Test solution **I** RE [where **II** is the CSM]

Here, Figure–6.4 shows the shorthand notation of the full E–cell setup using the CSE and the RE.

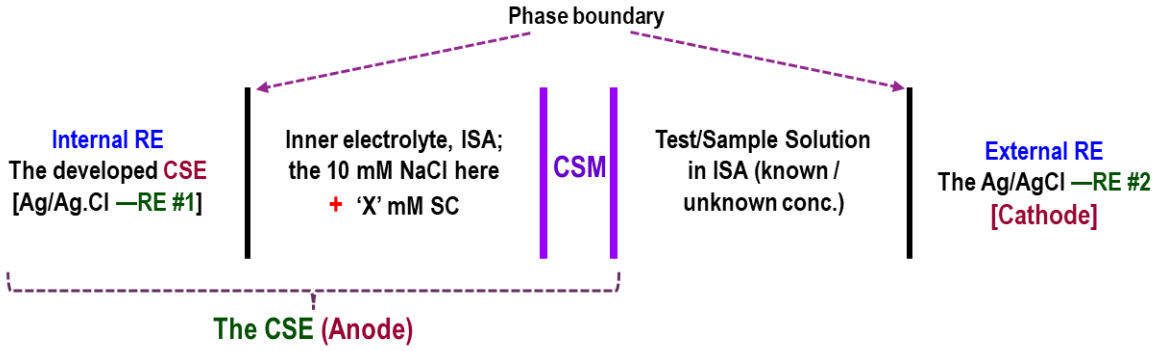


Figure 6.4: *The cell diagram (shorthand notation) of the E–cell to be used in this chapter's work which is the quantification of SC from unknown conc. of the samples obtained from the BATs conducted between SC and the selected developed NMs.*

In the cell diagram (shorthand notation) of the ISE mediated E–cell, the single vertical line indicates a phase boundary, such as between the metal electrode, M (s) and M^{+}(aq), or between X (s) and X^{-}(aq.) [the spectator ions are usually omitted]. The double vertical line represents the salt bridge or the ion/drug selective membrane, ISM/DSM (cholate selective

membrane, CSM in this case). By convention, the electrode written to the left of the cell diagram is the anode, while the right-hand side electrode is considered as the cathode.

6.4 Working principal of the CSE: Nernstian response

For the E–cell based on the ISEs/CSE there are no products or reactants since no redox exists.[256] Here, only the inner or outer solutions contain ions and the potential measured (E_{meas})[256] for a solution is the potential difference between the,

- Potential @bulk analyte/outer side of the membrane (E_{outer}), and
- Potential @the reference/inner side of the membrane (E_{inner})

$$\text{Thus,} \quad \mathbf{E_{meas} = E_{outer} - E_{inner}} \tag{6.1}$$

The potential @the membrane is related to the concentration of ions present on each side of the CSM and it can be expressed by the Nernst equation[256]:

$$\text{From the Nernst equation,} \qquad \mathbf{E = E_0 - \frac{2.303RT}{nF} \log \frac{1}{[C]}} \tag{6.2}$$

where R is the gas constant [8.314 (V.C)/(K.mol)], T is the temperature in K, n is the stoichiometric # of electrons involved in the process, F is the Faraday constant (96,485 C/equivalent), square brackets ([C]) represent concentrations in moles/L, and the **n** (sometimes denoted as '***z***') denotes the charge of the ion of interest (e.g., cholate, which is 1). Now, at 25^0C, the RT/F is equal to 0.0592V, and the Nernst equation for an electrode potential[256] becomes:

$$\mathbf{E_{outer} = E_0 - 0.0592\ V.log\frac{1}{[C_{unk}]}} \quad 6.3$$

$$\mathbf{E_{inner} = E_0 - 0.0592\ V.log\frac{1}{[C_{ref}]}} \quad 6.4$$

As C_{ref} and E_0 are both constant, and the E_{inner} (equation-6.4) is constant as well, thus by combining Eq.–6.3 & 6.4 and Eq.–6.1 gives—

$$\mathbf{E_{meas} = Constant + 0.0592\ V.log\ [C_{unk}]} \quad \mathbf{6.5}^{256}$$

To determine the unknown conc. of a sample, a calibration curve based on different known conc. of SC solution in ISA was determined and the slope of the linear section of the EMF $_{vs}$ Log [C] calibration plot is considered.[240–242] The EMF of the samples' unknown conc. were measured using a similar setup as the calibration curve and the obtained EMF was recorded along with the dilution factor, DF (if applicable). Once the slope (from calibration curve) and the EMF (mV) of the samples with unknown concentrations were measured, the conc. was determined using the procedures and equations[240–242] described below —

$$\mathbf{y = mx + c} \quad \text{[from the calibration curve]}$$

$$\boldsymbol{x = \frac{y - c}{m}}, \quad \boldsymbol{and} \quad \boldsymbol{x = log[C]}$$

$$\boldsymbol{[C] = antilog \left[\frac{y - c}{m}\right] \quad = \quad antilog \left[\frac{EMF - Intercept}{Slope}\right]} \qquad 6.6$$

Here in Eq.–6.6, both the intercept and the slope values were determined from the calibration curve.[240–242]

6.5 Mechanism of the developed potentials @CSM: Ion transduction

As discussed earlier, for the ion/cholate selective electrodes (ISEs/CSEs), the input signal is the activity of a specific ion, and the corresponding output is the electrical potential. In this regard, such overall signal transduction occurs at the interface(s) of the sample and the ion/cholate selective membrane (ISM/CSM). The known conc. of the inner filling solution of the indicator electrode (the CSE) contained a fixed species of the ion of interest (Cholate–).[257] When the electrode containing the CSM was placed in an unknown analyte solution (NaCh), at the solution–membrane interface, an ion-exchange equilibrium was established. The resulting charge separation at each interface resulted in a phase-boundary potential as quantified by a voltmeter.[257]

Although there are some disagreements on the mechanism of how the ISE/CSE works, a few of the literature suggest[240–242] that in an ISE/CSE, the ion/cholate selective membrane (ISM/CSM) works similar to a salt bridge (like in the Galvanic/Voltaic cells were redox exists)

which is made saturated with the ionophore molecules that are embedded or fixed within the PVC matrix of the membrane. The potential differences that are developed across the CSM when placed into the sample solution (unknown concentration) are then measured against a reference electrode (RE).[240–242] For the electrochemical cells constructed with the ISE/CSE and the RE, no 'redox' reactions take place and thus a lack of clarity still exists on the mechanisms of how the membrane potentials are developed.

The governing mechanism within the ISM/CSM in developing a phase boundary potential is important to gain a deeper understanding on the ISE's efficiencies. One of the literature mentioned[257], within the CSM, the charge carriers existed as ions and they are mobile. However, at some point between this membrane and the electrode (the Ag metal probe), the second half of the overall signal transduction occurs, i.e., the conversion of the charge carrier from ions to electrons.[257] A conventional ISE usually contains a AgCl-coated Ag wire as an inner reference electrode in contact with an inner filling solution that contains Cl− at a fixed concentration (from the 10 mM NaCl used as ISA). Consequently, ion-to-electron transduction is achieved by the ionization reaction of the $AgCl_{(s)} + e^- \rightleftarrows Ag_{(s)} + Cl^-(aq)$, which defines the interfacial potential between the AgCl/Ag electrode and the inner filling solution ($\Delta\varphi_{a3}$)[257] as shown in the Figure–6.5. For the bulk sample/ISM and the ISM /inner filling solution interfaces, the charge carrier is the target ions i.e., the cholates (Ch^-) in this case. For such polymer (PVC) based CSM, the potential differences across the two interfaces ($\Delta\varphi_{a1}$ and $\Delta\varphi_{a2}$, respectively) are governed by the distribution of the cholate (Ch^-) ions across the two immiscible phases.[257]

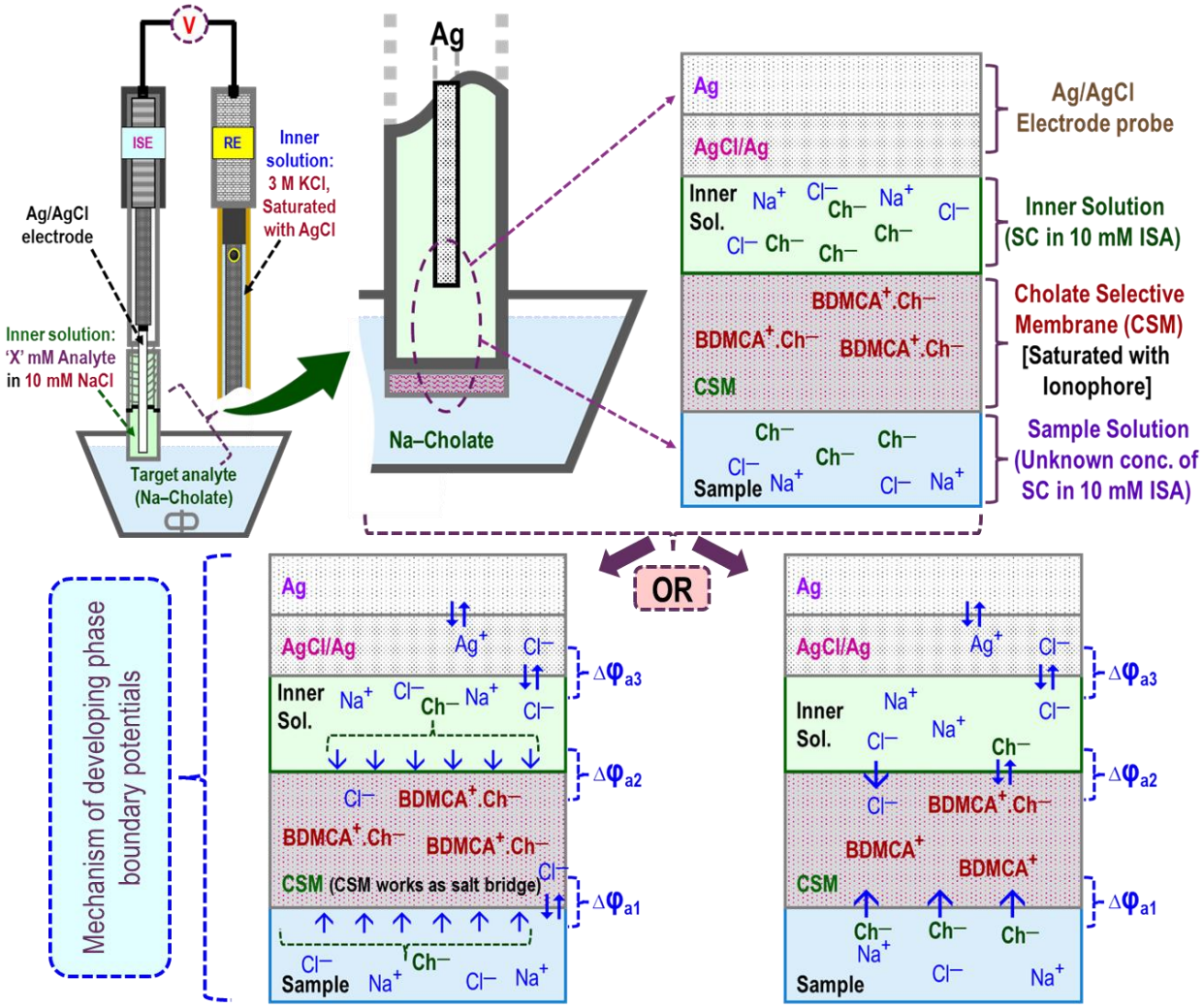


Figure 6.5: *The two possible mechanisms of electromotive potential (EMF) development at different phase boundaries: the bulk/CSM, the CSM/inner filling solution, & the inner solution/Ag–electrode. These two mechanisms of EMF development across the CSM (shown in the bottom part of the image)* ***are the most described in the literature****. Image not drawn to scale and proportions; the numbers of various arrows are* ***NOT*** *indicative of corresponding numbers of ions shown, wherever applicable.*

6.6 Materials and Methods

6.6.1 Materials:

The sodium cholate hydrate, SC/Na–Ch. xH_2O from bovine (MW: 430.6, anhydrous basis), PVC (high MW, ~60 KDa), benzyl-dimethyl-cetyl-ammonium chloride (BDMCA.Cl), or benzyl-dimethyl-hexadecyl-ammonium chloride [16-BAC (benzalkonium chloride), Cetalkonium chloride; MW: 396.09 g/mol], the plasticizer Bis(2-ethylhexyl) sebacate [Dioctyl sebacate (DOS), Di(2-ethylhexyl) sebacate (DEHS); MW: 426.67], NaCl, KCl, NaOH, phosphate buffer were purchased from the MilliporeSigma and used as received without any further purification. All the other commonly used solvents, Durapore® Membrane Filters and commonly used reagents were purchased from MilliporeSigma. Purified water (Milli-Q water) from a Millipore system (>18 MΩcm) was used to prepare the sample solutions.

6.6.2 Synthesis of ionophore

The CSE was made selective mainly for the CSM, where an ionophore was embedded. The ionophore is the molecule or the membrane component that is selective to cholate (Ch^-). Thus, the first step to fabricate the sensor or the CSM was to synthesize the ionophore from its structural components, namely the SC (water-soluble) and the quaternary ammonium group, QAG containing (cationic) lipophilic surfactants namely benzyldimethylcetyl-ammonium chloride (BDMCA.Cl). Although there was no clear reported protocol for the synthesis of the ionophore, we modified documented report[246–248] and developed a suitable and effective synthesis method for the ionophore. Figure–6.6 illustrates the development process of the CSE, synthesis of the ionophore, and the preparation of the CSM.

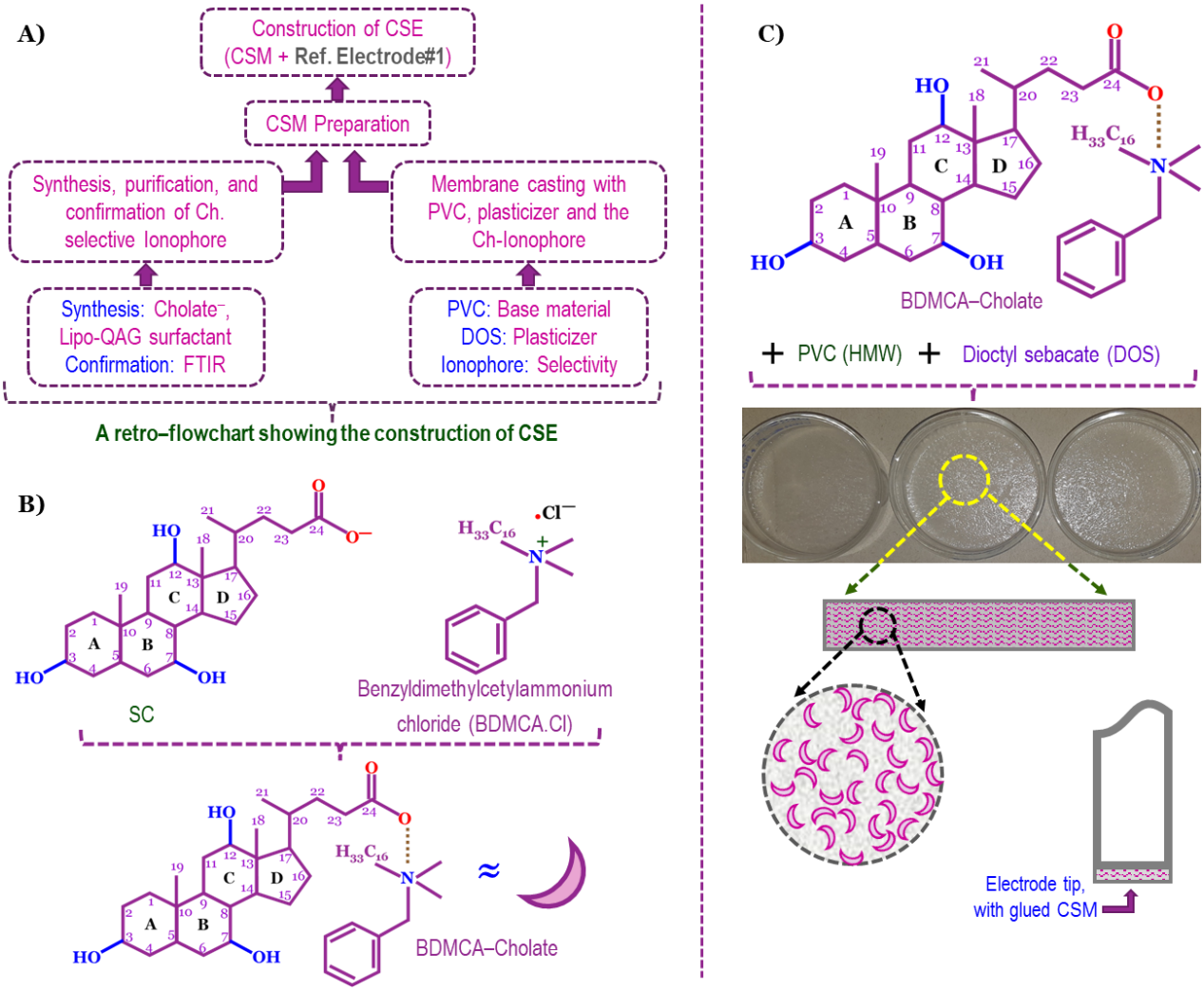


Figure 6.6: A) *A retrograde flowchart indicating the stepwise construction of a CSE starting from the synthesis of the ionophore.* ***B)*** *Molecular reactants for the synthesis of the ionophore called benzyldimethylcetylammonium–cholate (BDMCA–Cholate).* ***C)*** *Casting of CSM prepared from PVC, ionophore and plasticizer. The zoomed insert shows the outlook of the casted and dried flexible CSM where the ionophore molecules are embedded and distributed.*

Briefly, an equal volume of the aqueous solution of SC and BDMCA.Cl in chloroform ($CHCl_3$) was mixed overnight @RT and 450 rpm with a 2:1 molar ratio in an RBF. A large

excess of SC was used to ensure the complete formation of ionophore. Once the electrostatic complexation reaction was completed, the mixture was stopped and transferred to a cone shaped separating funnel to recover the chloroform phase, which was then then concentrated in the Heidolph™ Hei-Vap™ rotary evaporator. The ionophore was precipitated by cooling the concentrated liq. (the $CHCl_3$ phase) with larges excess of ether ($C_2H_5–O–C_2H_5$) followed by a second wash with ether before recovering the purified solid precipitates (the ionophore). The purified ionophore was dried in vacuum oven and analyzed with the FT–IR, and Figure–6.7 shows the overall synthesis and purification of the ionophore.

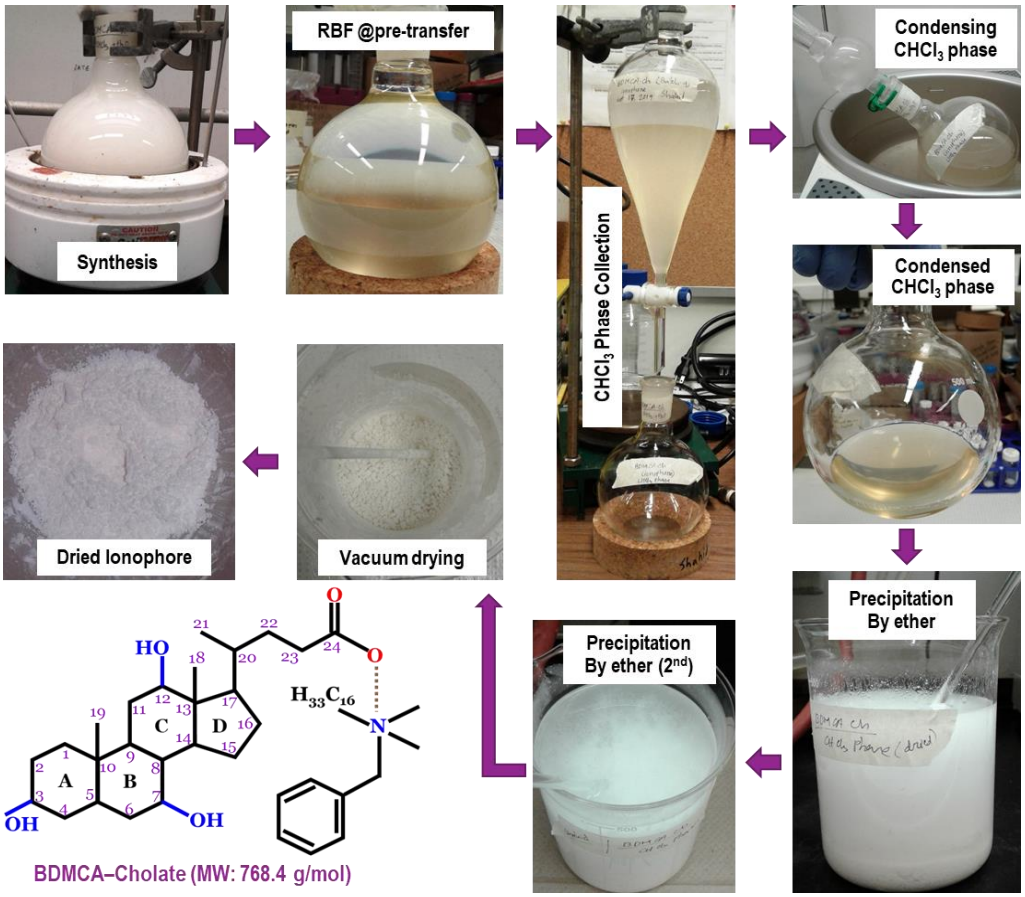


Figure 6.7: *Synthesis and purification of BDMCA–Cholate ionophore (lipophilic in nature).*

6.6.3 FT–IR of the ionophore

The KBr disc of the BDMCA.Ch ionophore was prepared following the usual procedure and the FT–IR test was conducted as discussed in Chapter–3.

6.6.4 Casting of CSM

Before casting the CSM, the solution mixture was prepared in a conical centrifuge tube (Falcon tube) according to the desired composition based on the reported literature (cite ref), with minor changes. Briefly, 165 mg of PVC (HMW), an equivalent volume of 330 mg plasticizer (dioctyl sebacate, DOS; density = 0.914 g/mL), and 5% of the total amount of the PVC and plasticizer were mixed. From several trials & errors, it was found that the resultant mixture precipitated. Thus, solutions with higher conc. were prepared for the PVC and the BDMCA.Ch in tetrahydrofuran, THF (b.p. 66^0C). The ionophore (BDMCA.Ch) was insoluble in water and only **partly** soluble in THF in RT @ a conc. of 20 mg/mL, but it became completely soluble in THF @ > 55^0C.

Here for each CSM, the ratio of the weight % of the three components was considered as —

PVC : DOS : Ionophore = 32 : 63 : 5

Figure–6.8 shows the schematic of the overall CSM casting procedure.

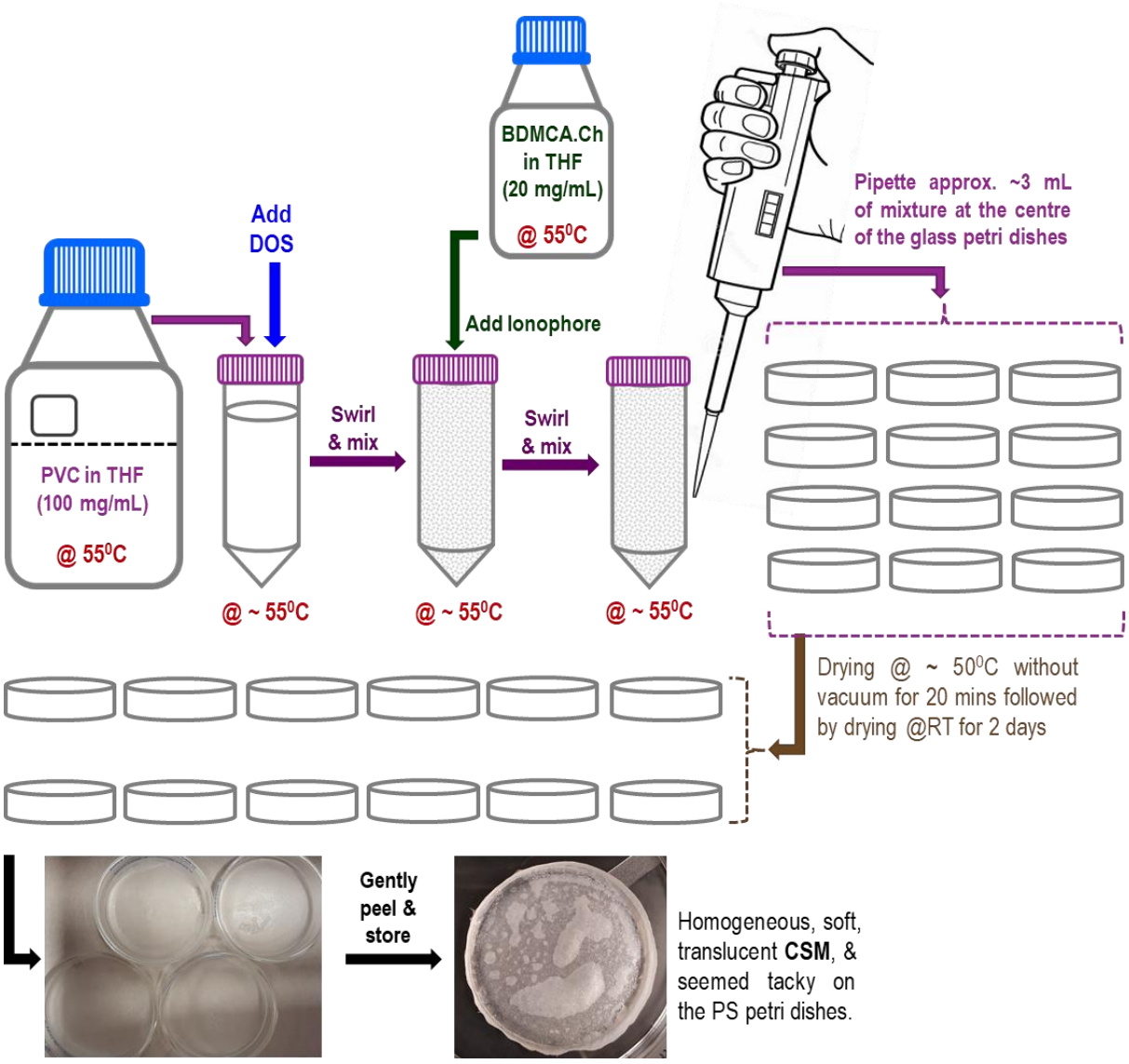


Figure 6.8: *The overall procedure of CSM casting. The CSM has three components: PVC (HMW) as the base material, DOS as the most used plasticizer with PVC, and the BDMCA.Ch ionophore which had been synthesized in-house. A ration of PVC : DOS : Ionophore = 32 : 63 : 5 (wt.) was followed per CSM. The ionophore solution (THF is the solvent) starts precipitating out gradually when solution temperature decreases below 55^{0}C (say, ~50^{0}C).*

To achieve the minimal wastage of the CSM, a higher conc. of PVC (100 mg/mL) and a moderately higher conc. of ionophore (20 mg/mL) was prepared in THF and both solutions were kept at 55^0C during the casting process (ionophore phase got separated < 55^0C). First, the calculated volume of the PVC was added to a Falcon tube and then the plasticizer was added, the mixture was then mixed under gentle swirling to minimize bubbles formation. Once completed, the tube was placed in a water bath set at 55^0C. Lastly, the calculated volume of the ionophore solution was added to the Falcon tube placed in a water bath, then gently mixed to minimize air bubbles formation.

The mixture became cloudy as the temp. was reduced from 55^0C to 50^0C. The required volume of the mixture was 'slowly' dispensed into the center of each petri dish (d= 6 cm, dimension 60 x 15 mm) to avoid bubble entrapment. All the petri dishes were then dried under ~50^0C inside an oven for 20 min followed by drying at RT for two days. The fully dried casted membranes were then peeled off and stored in PS petri dishes for future use. When needed, each of the CSM was hole punched to make tiny discs of diameter ~13 mm, which were then glued onto the electrode head before mounting the head in the electrode body.

6.6.5 Electrode head fabrication and conditioning

The electrode heads were made from PVC which partly dissolved in THF, which was utilized as adhesive to attach the 13 mm cut discs on the electrode head. Upon careful inspection of any possible leaks, the electrodes were then kept aerated in glass scintillation vials for curing for ~1.5–2 hr.

Conditioning is a procedure that is performed to re-sensitize the ISE to the target analyte before calibration.[255,257–261] ISEs stored over a prolonged time should be conditioned to resensitize prior to use. As the general rule, the conditioning achieved the followings:

- Re-establishes the permeation of ions.
- Is a necessary step for new electrodes that are being used for the first time, or that recently had membrane replacements; especially for very low conc. measurements.
- If not done properly the ISE/CSE might yield an inaccurate reading/drift (higher or lower) due to loss of sensitivity.

All the properly secured tips were first conditioned by soaking the tips in a conditioning solution for ~2–3 hr. The conditioning solution should be pure and either the MQ water or the solvent media used to conduct the experiments.[255,257–261] Here, the freshly prepared ionic strength adjustor, ISA (10 mM NaCl, in MQ water) was used as the conditioning solution. The tips were ready for use immediately after the conditioning was performed. Such conditioning was also applied to tips/CSMs that lost their sensitivities upon use during testing/experiments. Figure–6.9 describes the overall process of attaching the CSM onto the electrode tips and the conditioning process in the selected/chosen ISA (10 mM NaCl).

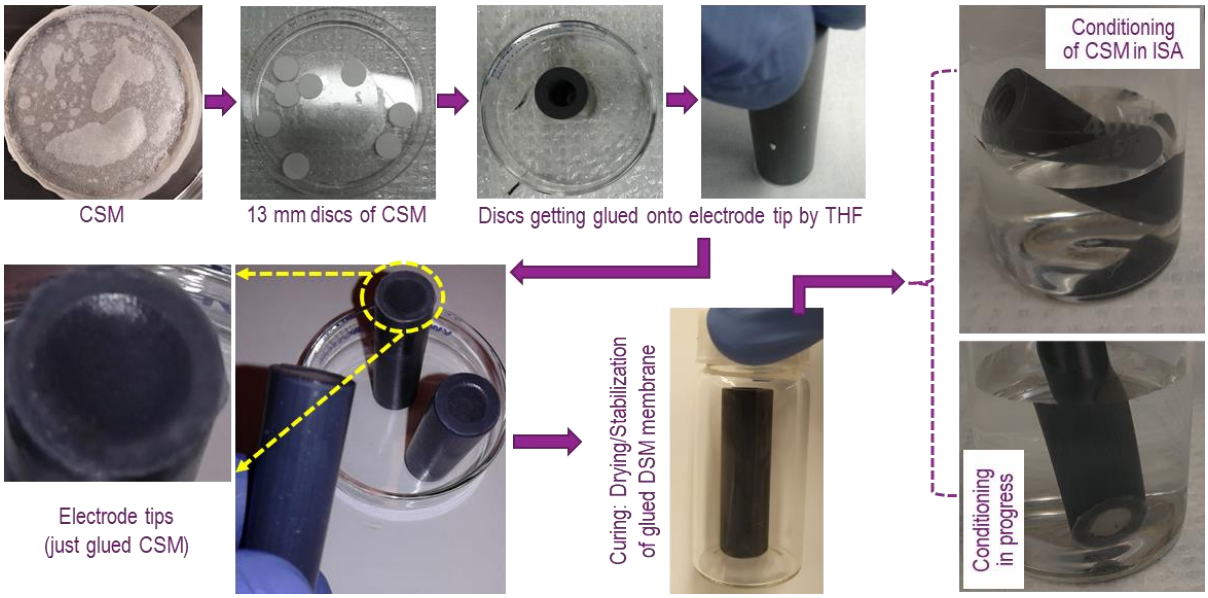


Figure 6.9: *Stepwise fabrication of the electrode heads with the cholate selective membrane (CSM) and curing of the glued CSMs, followed by conditioning. After analyses of several results, this conditioning step was discarded as it failed to revert the desensitized CSM/tips to their pristine conditions. Additionally, the usage of ionophore was meant to eliminate the conditioning steps for any ion-selective electrodes (ISEs).*

After, analyses of several results, it was concluded that the conditioning failed to restore the desensitized tips/CSMs to their pristine conditions (a few examples of data are presented in the appendix). Furthermore, it was found that conditioning before 1st-time usage of a tip usually has less effect on the EMF, however, the drifted EMF resulted in inaccuracies of the data (examples in appendix). For all these reasons, the conditioning step was discarded and immediately after curing the glued CSM, the tips were used instead.

6.6.6 Construction of calibration curve of SC with the CSE

Based on the discussion in Chapter–2 (Literature Review) on (a) the daily production and the enterohepatic circulation, EHC of bile throughout the body, and (b) the critical micelle concentrations (CMC) of sodium cholate (SC), the calibration curves within the range of 50 µM – 25 mM SC were constructed in multiple attempts though the continuous addition of the stock SC solution. In the continuous addition modes, 4 different concentrated solutions were prepared in ISA instead of more than 30 reference samples. Then pre-calculations were done to determine the corresponding stroke volume to be added from each of the 4 different vials to prepare more than 60 different concentrations (data points) within the range of 50 µM – 25 mM. After several trials and errors with the corresponding analyses of results (some examples in the appendix), it was concluded to use a fresh/unused electrode tip along with replacing both inner solutions of the ion/cholate selective electrode (ISE/CSE) and the reference electrode (RE) respectively, for each experiment conducted.

In the calibration experiments, ~1.5 mL of 10 mM SC in 10 mM NaCl (as the ionic strength adjustor, ISA) was pipetted into an unused tip and mounted onto the CSE. The standard 3 M KCl (saturated with AgCl) inner solution was added to the RE, and both electrodes were connected to the VWR Sym**pH**ony SB70P pH meter in mV modes. A 50 mL of the ISA was added to a crystallizing dish (capacity 80 mL; D x H = 60 x 35 mm), and this was considered as a blank for the experiments conducted with the CSE @ RT. A stopwatch was used to measure the mixing time to ensure homogeneity and equal duration of mixing after pipetting the concentrated SC into the blank. The blank reading was recorded and then precalculated stroke volume of the concentrated SC was added to the dish, mixed for 30 sec.

at 600 rpm, then the electrode set was dipped into the dish with the speed set at 100 rpm. Once the EMF (mV) reading stabilized on the pH meter, two more readings were recorded for the same conc., before adding the second stroke volume, and this process continued until a predetermined concentration was reached. Figure–6.10 illustrates the overall process of constructing the calibration curves through continuous addition modes.

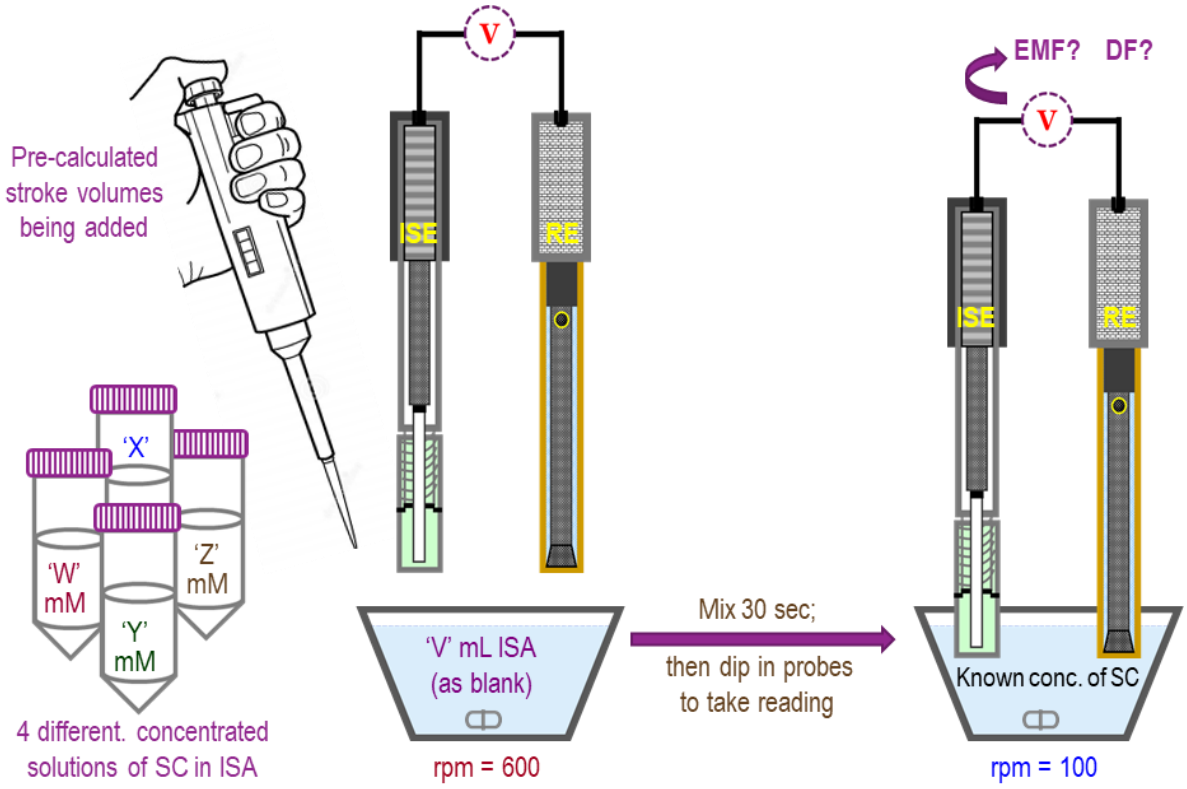


Figure 6.10: *A basic representation of the process of constructing EMF (mV) vs Log (C_M) calibration curves through continuous addition modes, conducted with the E–cell composed of CSE & a RE. The 10 mM NaCl (ISA) is used as the blank. The inner filling solution for the CSE was 10 mM SC prepared in ISA, and for the RE, it was the 3 M KCl solution saturated with AgCl. The calibration curves were conducted at RT and the EMF readings for each data point were taken at least in a triplicate manner to report the average.*

A total of 60 data points of EMF (mV) in triplicates corresponding to 60 different known conc. of SC were recorded manually and plotted as the EMF (mV) against the Log_{10} of molar (M) conc. For such plot(s), the break point(s) should correspond to the CMC of the SC in ISA at RT, where the range of the calibration curves was chosen to be from 50 µM – 25 mM.

Bile salts/acids (BSs/BAs) are endogenous surfactants and self–aggregating molecules. In solution, the BSs/BAs possess a unique identifier or parameter called critical micelle conc. (CMC), which is the conc. where a specific morphological aggregate (micelles) are formed. For the SC, the reported CMC in the literature was found to be within the range of 11–14.3 mM @ RT,[161,231,262,263] depending on the tools used for determining the CMC. From the EMF *vs* Log(C) plots, the CMC of the SC was determined. If the CMCs obtained from other instruments, such as tensiometer or conductivity meter were in close resemblance, then it could be concluded that the elementary model of the cholate selective electrode (CSE) was working well. The sensor's efficacy was also further evaluated through unblind, single–blind, double–blind tests (some data presented in the appendix).

6.6.7 Calibration curve of SC via Tensiometry & Conductometry

The calibration curves for the same concentration range as in the EMF (50 µM – 25 mM) were also constructed as part of cross-validation to justify if the fabricated CSE worked properly or not. In both cases, the same conc. of the four concentrated SC solutions, the same volume of blank and the same precalculated stroke volumes was added to the dish, similar to the protocol for the EMF calibration curve. However, as the presence of counter ions would

impact the conductance reading significantly,[264–267] for conductometry, all the solutions were performed in MQ water (not in ISA), including the blank. In both techniques, the manual addition of the assigned stroke volumes was followed and the resultant conductance or the surface tension (SFT) data in a triplicate manner were recorded @ RT. Figure–6.11 illustrates the basic method for constructing the calibration curve using the **tensiometer** and **conductometer**. Other details of both of the techniques were described in Chapter–3.

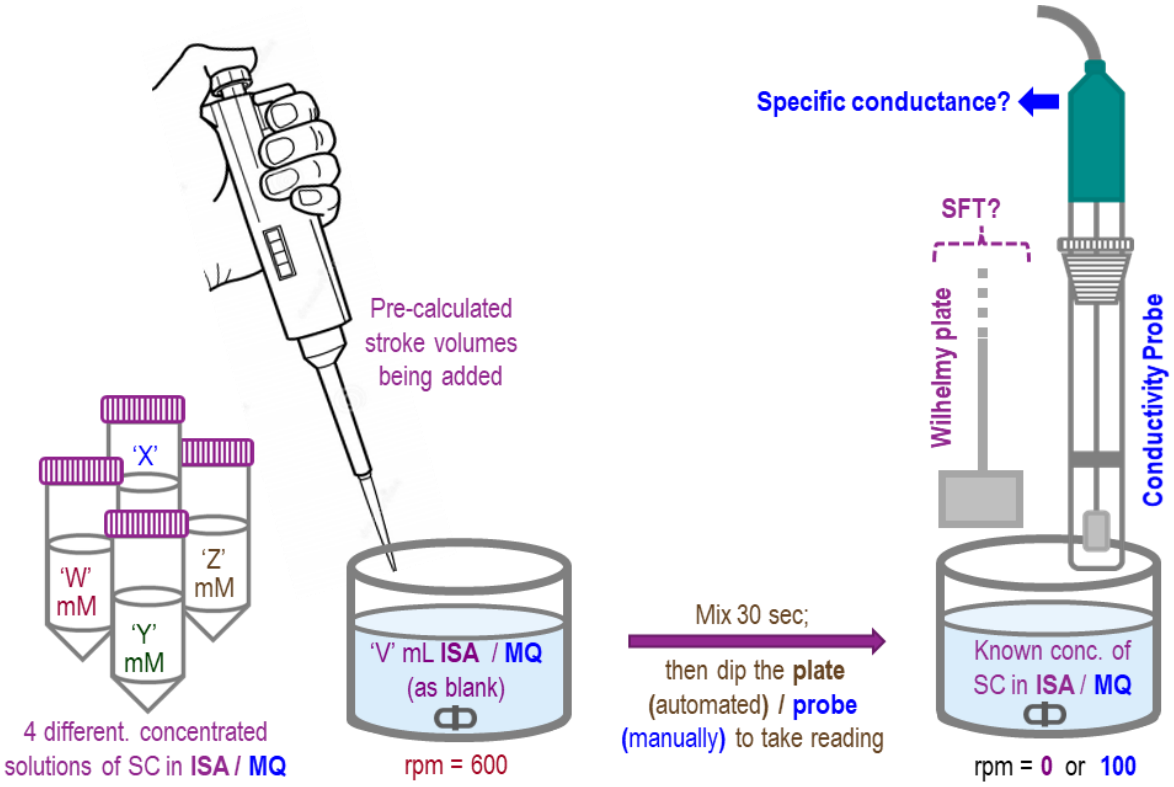


Figure 6.11: *Schematic illustration of the methods of producing calibration curve by Tensiometry and Conductometry. For the latter case, the whole experiment was conducted in MQ water including the preparations of the four concentrated reference solutions of SC. The 60 data points (SFT or the sp. conductance) obtained in a triplicate manner in both cases were baseline corrected and then plotted against Log (C_M) (for Tensiometry) or the C (for Conductometry).*

The data were baseline corrected before they were plotted against the conc. By convention, for the tensiometry, the data was plotted as surface tension (SFT) vs Log (C_M), and in the case of conductometry, the plot was as specific conductance *vs* C, where the C_M notation corresponds to the existing molar conc. of SC in the vessel. Any observed break point(s) of such calibration curves indicate the CMC value of SC @ RT for that solvent media.

6.6.8 BATs of SC for selected NMs and Q_{max} determination by the CSE

Based on the results of all the NMs developed and discussed in Chapters –3, 4 and 5, a list of NMs were selected to conduct the batch adsorption tests (BATs) with sodium cholate (SC) to evaluate their efficiencies as potential BASs. The choices were made depending on the NM sizes, surface charges, viscosity, efficacy on methyl orange (MO) adsorption, presence of hydrophobe, amino groups, and the structural shape of the NPs (e.g., bottle brush-like structures). Table–6.1 summarizes the rationale for the selections of NPs for the BATs conducted with SC followed by the quantification of the free SC with the fabricated cholate selective electrode (CSE). For all these BAT studies, only one trial was conducted due lack of the availabilities of the synthesized and purified NPs in the repository.

For the BATs, to mimic the human body's internal temperature, peristalsis (the wave-like muscle contractions that force the ingested stuffs to move forward along the gastrointestinal tract, GIT), and the GIT emptying time, a temperature of 38^0C @ 200 rpm for ~ 2.5 hr was selected. Briefly, 30 mL of 5, 7.5, 10, 12.5, and 15 mM of freshly prepared SC in ISA (10 mM NaCl) were taken in pre–labelled 50 mL Falcon tubes (conical centrifuge tubes) and 15 mL of 'x' % (w/v) NPs were then added in each of the tubes, as shown in Figure–6.12.

Table 6.1: Rationale for the selected NPs for batch adsorption tests (BATs) with sodium cholate (SC) followed by quantification of free SC with the cholate selective electrode (CSE).

NPs Name	Rationale to choose
NCC™ (CelluForce CNC)	Negative/regular control 1
DS–CNC_a (Desulfated CNC by HCl)	Negative/regular control 2
Q–CNC_a (GTMAC-DS-CNC_{HCl})	Highest ZP and lowest D_H among ALL the Q-CNC_x systems
Q–CNC_6 (GTMAC-DS-CNC_6; desulfation was by 6M NaOH)	Moderately high ZP and low D_H among ALL the Q-CNC_x systems where the desulfation of the NCC™ were done via alkaline hydrolysis.
Q–C_{12}-CNC_6 (DDEAC–CNC, with C-12 chain)	Only option for the Q-CNC with a C-12 hydrophobe
Brush–CNC (pQDMAEMA-g-CNC)	Low stock left for Brush-CNC_a; other Brush systems were not synthesized
Q–CS (GTMAC-Chitosan)	Only option for 1:12 synthetic ration [CS : GTMAC]
QCS–g–CNC_a	Greater ZP and better D_H profile over the QCS-g-NCC™
Cht. NW_a (Deacetylated Chitin NWs by HCl)	Only option for the chitin nano–whiskers (Cht. NWs)
Q–Cht. NW_a (GTMAC-Chitin NWs)	Only option for cationic chitin nano–whiskers
Cht.NF_P-5 (Chitin NF pass-5)	Greater ZP, better D_H profile, and most viscous over the other passes
Questran™ (Cholestyramine)	Positive control (commercial bile acid sequestrant)

After the NPs were added, all the tubes were placed in a pre–heated ($38^0 \pm 0.5$ C) water bath on a Styrofoam so that the stir bars could rotate. The adsorption experiments were conducted for each of the nanoparticles (NPs) for about ~ 2.5 hr, after which the vials were

placed in an ice bath for ~2–3 min to instantaneously bring the sample to room temperature (RT).

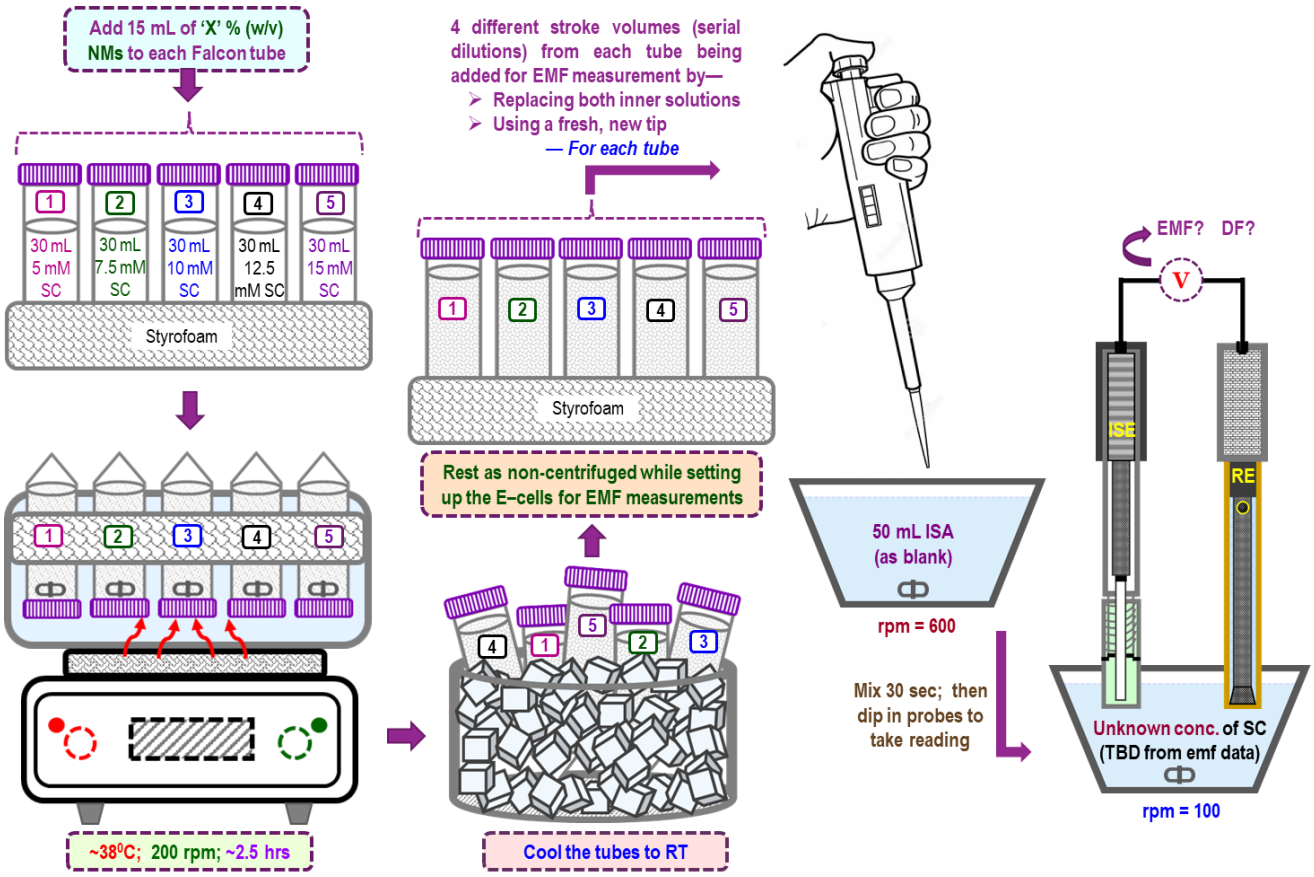


Figure 6.12: *Steps showing the overall BAT of a selected NM with SC followed by the detection of unbound/free SC left in the post–adsorption liquid. The BATs for all the selected NMs were done in the same way and for every Falcon tube in each test, the new/unused tip, as well as fresh inner solutions for both electrodes, were used to maintain consistency of results. Except for the anionic or neutral NMs, all the other NMs' BATs' tubes got cloudy during and after the adsorption tests, and visible aggregates/lumps were seen for all the tubes of ascending conc. of the SC. The quantification of the free SC from each tube was tedious & time-consuming, and thus at times, that portion was divided into two days, where applicable.*

Depending on the availability of resources, the quantification of the free/unbound sodium cholate, SC were performed the next day after the batch adsorption tests, BATs. Most of the nanomaterials (NMs) displayed visible aggregates in the sample after the BATs, but they quickly settled at rest before E–cells detection. Lastly, the direct immersion of the cholate selective electrode, CSE in concentrated solutions of the SC impacted the sensitivity of the cholate selective membrane (CSM), thus this was not done during the measurement of free SC from the BATs, except for the 5 mM and 7.5 mM labelled Falcon tubes.

6.6.9 Binding/Adsorption Kinetic Tests (AKTs) of SC with the NMs

During the batch adsorption tests (BATs) with the selected **cationic** NMs, it was observed that just after the addition of the NMs into the Falcon tubes containing 5 different concentrations of sodium cholate (SC), the mixture became cloudy, especially the tubes with higher conc. Thus, the adsorption kinetic (AK) was conducted for one of the NMs as a representative example and it was compared to the AK of the commercially available BAS, Cholestyramine (Questran^{TM}). Here, the Q–CNC$_a$ was chosen to be the NP of interest due to its overall evaluated parameters [like the size (D_H), zeta potential (ZP), quaternary ammonium groups (QAGs) contents, and the efficacy (Q_{max}) on the methyl orange (MO) adsorption]. Briefly, 200 mL of the 7.5 mM SC (prepared in the ionic strength adjustor, ISA) was added to the round bottom flask (RBF) and it was heated to 38^0C ± 0.5 under stirring of 250 rpm (600 rpm for cholestyramine due to the poor dispersibility of this BAS) and once the set temperature of the RBF's content was reached, 25 mL of the 1 % (w/v) of the Q–CNC$_a$ (and Cholestyramine, for another adsorption kinetic test, AKT) suspension prepared in ISA was

added slowly to the RBF. The AKT(s) were then conducted for ~2.5 hr during which a 5 mL aliquot was withdrawn from the 225 mL of the mixture at different time intervals without replacing the withdrawn volume with the fresh 7.5 mM SC, as shown in Figure 6.13. A total of 19 samples were collected in the 20 mL glass scintillation vials and in the Falcon tubes which were then tested (with dilutions or without) as shown in Figure–6.13. In this case, serial dilutions were not performed during EMF measurement due to a lack in the volume (5 mL) of the collected aliquots. For each collected sample with respect to (w.r.t.) the sampling times, a new tip for the cholate selective electrode (CSE) along with fresh inner solutions for both electrodes were used. And again, the measured EMF reading/sample was recorded as triplicate.

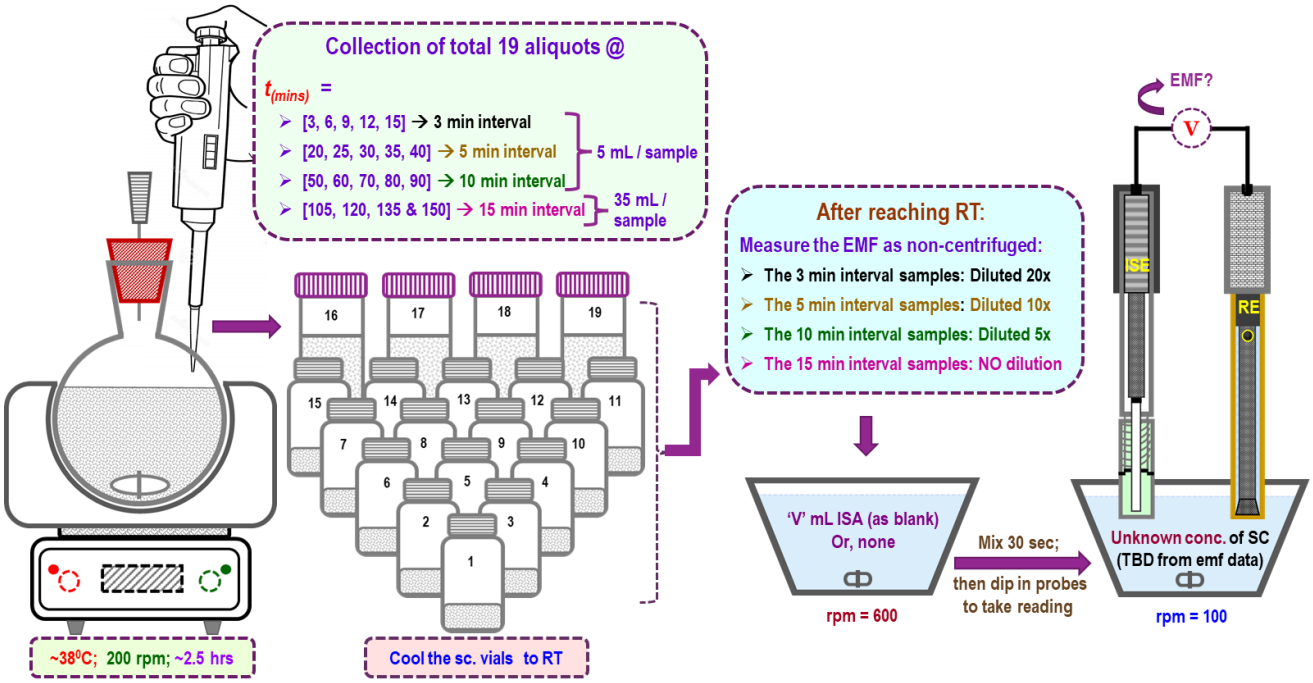


Figure 6.13: *Adsorption kinetic tests (AKTs) of NMs followed by quantification of the free SC in the collected samples at different time intervals.*

6.7 Results and Discussion

6.7.1 Yield and FT–IR of BDMCA–Cholate ionophore

The collected and dried ionophore (BDMCA.Ch) was weighed as the dry mass, and the % yield was determined to be ~71.6 %. The ionophore was stored in an air–tight container in a desiccator for further use.

Figure–6.14 shows the FT–IR peak of the ionophore which was compared to the spectra of its constituents. For any organic nitrogen compounds, the reported N–O **a**symmetric stretch[268] is from 1550–1475 cm^{-1}, and the N–O symmetric stretch is from 1360–1290 cm^{-1}. For this ionophore, the newly appeared peak at 1573 cm^{-1} (1541 cm^{-1} for N–O bond in literature[268]) confirms the successful bond formation between the QAG of the 16–BAC and the oxygen (O) of the carboxylate groups (—COO^{-}) of the SC molecules. The FT–IR result thus confirmed the successful formation of the BDMCA.Ch ionophore.

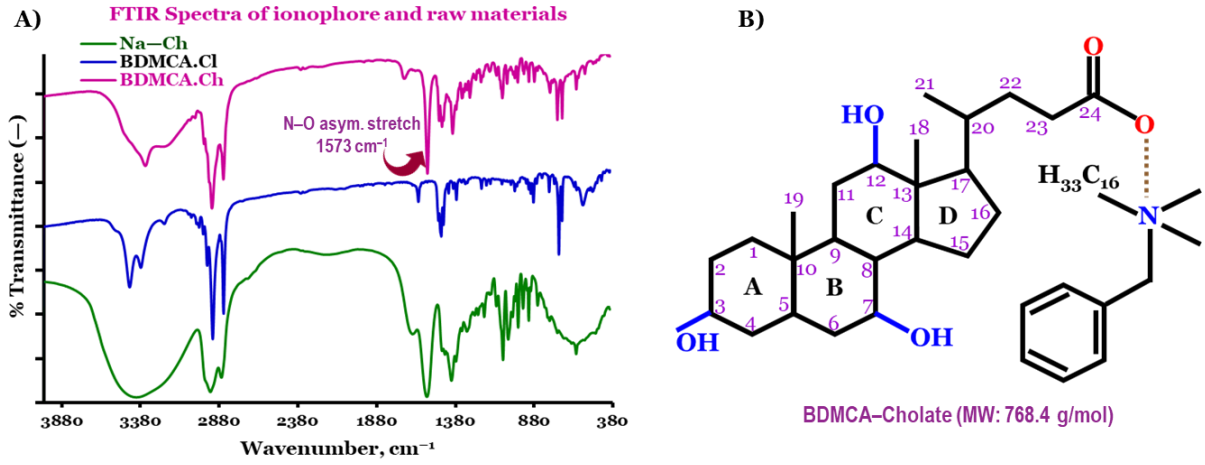


Figure 6.14: A) *The FT–IR spectra of SC, 16–BAC (the cationic detergent, BDMCA–Chloride), and the synthesized ionophore, BDMCA–Cholate.* ***B)*** *Chemical structure of the ionophore showing the newly formed bond* ***—N- - -O—*** *between the 16–BAC and the SC.*

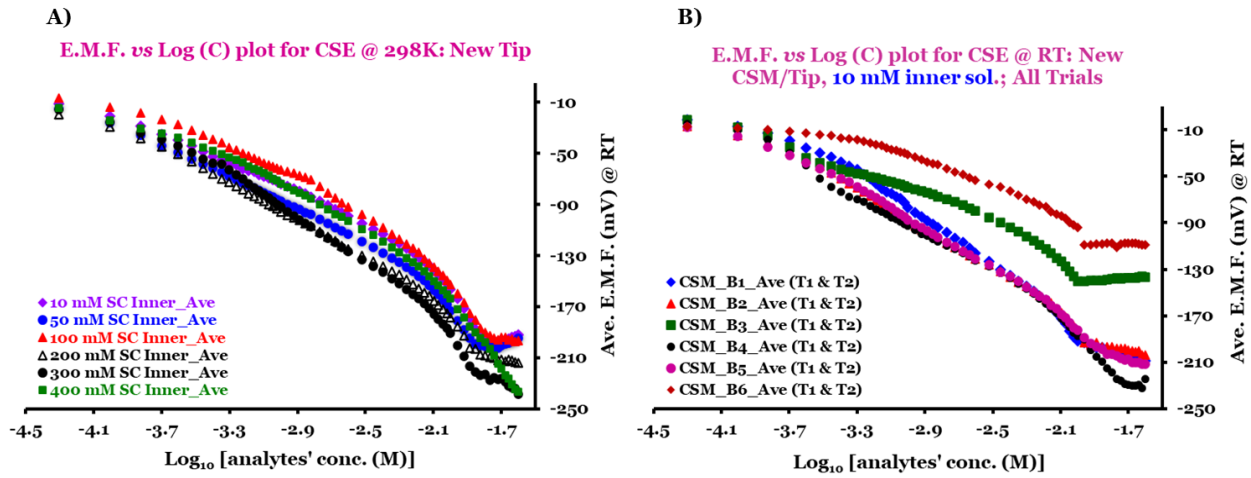
6.7.2 Calibration curves of SC via EMF technique from the CSE

The effects of the strength of an inner filling solution, conditioning the cholate selective membrane (CSM)/tip, used CSM/tips, inner solution in reference electrode (RE), and the presence of other anionic molecules on the EMF responses for known conc. of SC in ISA were evaluated. Here, only the effect of inner filling solutions on the calibration curve of the SC was discussed and a few examples of the rest were included in the appendix.

Figure–6.15 shows the effect of the strength of the inner solutions on the EMF responses over a range of conc. (calibration curves), and the CMCs obtained from the breakpoints of the plots were summarized below the figure. Although the effect of strength of the inner solution (freshly prepared SC in ionic strength adjustor, ISA) of the cholate selective electrode (CSE) was tested up to 300 mM, based on several reported studies[244,246–248] of similar electrode systems we decided to use 10 mM SC in ISA as the inner filling solution for future experiments. Additionally, the use of a 10 mM inner solution provided the closest resemblance of the CMCs obtained with the reported CMCs in the literature.[161,231,262,263]

For consistency and accuracy of results, a new tip was used for experiments conducted with the CSE. Thus, multiple batches of the cholate selective membrane (CSM) were casted, and for each casted CSM at least two calibration curves (trial–1 & 2) were constructed for a representative tip of that respective batch using the 10 mM SC in ISA as the inner filling solution. Figure–6.15 B summarizes all the average calibration plots as well as the corresponding CMCs, obtained from different batches of the casted CSM. Although there were some outliers probably due to the inconsistencies of homogeneity during the casting of the CSM, the average of the closest four calibration curves was considered for analyzing the batch

adsorption tests (BATs) and adsorption kinetic tests (AKTs) data, along with the unblind tests (UBT), single–blind tests (SBT), and double–blind tests (DBT) during the quality assurance phase of the CSE development (few examples of results in appendix).



Inner Sol. (mM)	Primary CMC (mM/L)	Secondary CMC (mM/L)
10	6.6	16.5
50	5.9	16.5
100	4.5	17.9
200	7.5	14.0
300	7.3	13.6
400	2.4	9.4

CSM Batch # (10 mM Inner sol.)	Primary CMC (mM/L)	Secondary CMC (mM/L)
CSM_Batch–1	6.6	10.1
CSM_Batch–2	6.8	11.9
CSM_Batch–3	5.4	10.9
CSM_Batch–4	6.0	9.7
CSM_Batch–5	5.6	14.4
CSM_Batch–6	5.2	13.4

Figure 6.15: A) *Effect of the strength of inner filling solutions for the CSE on the EMF responses over a range of conc.: 50 µM–25 mM SC prepared in ISA. The CMCs enlisted below the plot, were determined from the visibly distinct breakpoints of the calibration plots which are not easily discernible from this combined plot of the average data.* ***B)*** *The average (from T–1 & T–2) of calibration curves obtained from two of the representative tips from that respective batch of the casted CSM. Inconsistent results were seen for the CSMs from batches #3 and 6, probably due to the lack of homogenous distribution of the embedded ionophore. The CSMs from those two batches were seen a bit cloudier than the rest of the batches, and the most likely reason for this could be the partial precipitation (insolubilities) of the ionophore prior to proper drying. The determined CMCs from this data were also enlisted in the table presented just below the plot.*

6.7.3 Micellization and CMC determination of SC from EMF *vs* Log(C) plots

The SC, one of the primary BAs in human body is a planner molecule, self–aggregating and literature suggests that SC can form pre–micellar aggregates, primary (1^0) micelles, and secondary (2^0) micelles. The 1^0 micelles are formed mostly due to the inter–molecular (monomers) hydrophobic interactions at the hydrophobic faces and the reported numbers[269–274] of molecules in such 1^0 micelles were within 2–10 molecules, as shown in Figure–6.16.

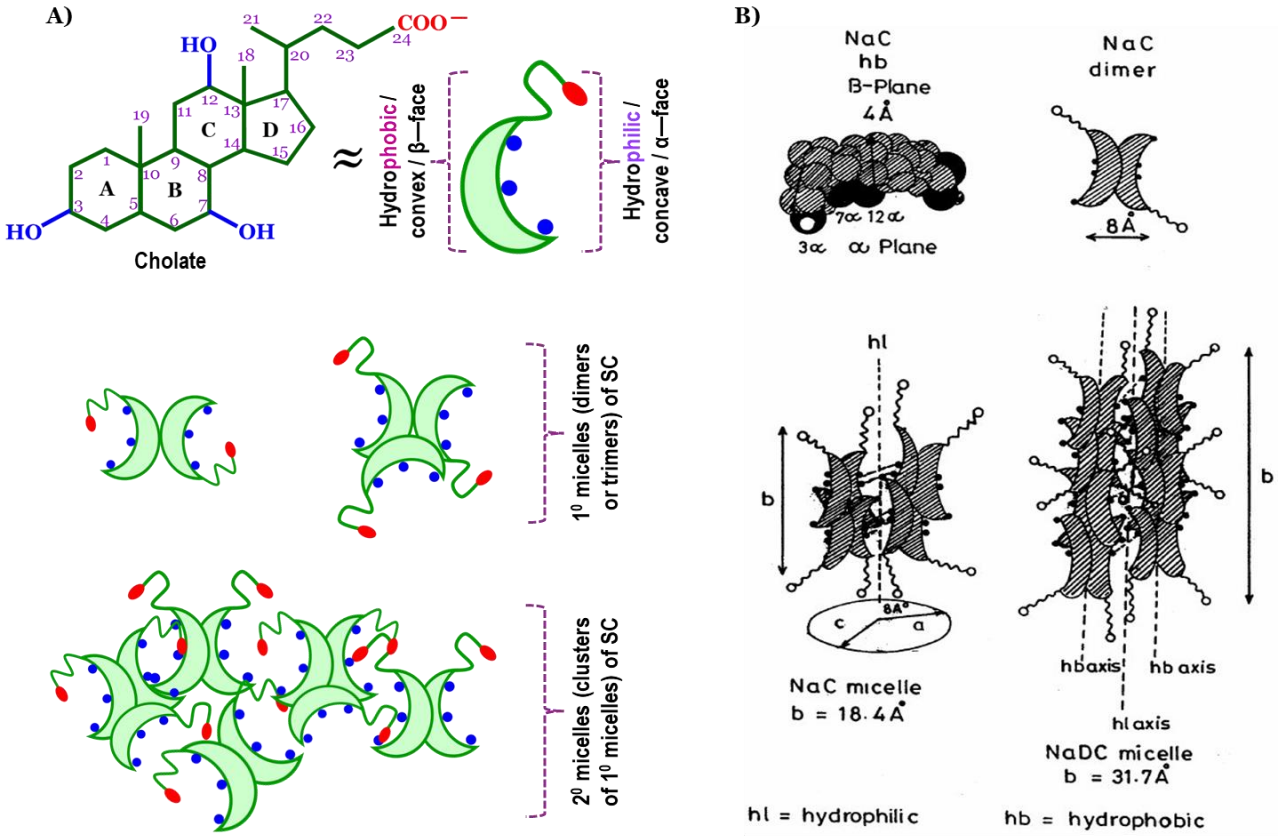


Figure 6.16: A) *Chemical structure of SC monomer molecule and its two faces: the hydrophobic and hydrophilic faces. Schematics of the 1^0 & the 2^0 micelles are also presented.* ***B)*** *Different micelle formations reported in the literature and their corresponding sizes (diameter) were investigated by small-angle neutron scattering (SANS). Reused from.*[270]

At RT, the sequential aggregation of SC induced the formation of the pre-micellar or early aggregates leading the primary (1^0) CMC at ~7 mM (no chiral selection) at low conc, followed by a secondary (2^0) CMC at ~14 mM as conc. of the concentration of the SC was increased[274]. The combined data from one-dimensional (1-D) proton-NMR (^{1}H-NMR), pulsed-field-gradient spin-echo (PFGSE)-NMR, and micellar electrokinetic capillary chromatography (MEKC)/ capillary electrophoresis from several studies also revealed such sequential preliminary (pre-micellar or early) aggregation, primary (1^0) and secondary (2^0) micelles formation.[272,273] Such forms of sequential aggregations discussed herein were evident from the breakpoints of the calibration curves obtained from the cholate selective electrode CSE as shown in Figure–6.17. This data also reinforced the fact that the CSM provided the EMF values exclusively based on the availabilities of free SC monomers in the bulk.

It was reported that the 2^0 micelles comprised of approx. 10–100 molecules where the inter–micellar (1^0) hydrogen bonds at the hydrophilic faces formed such clusters. The average radius of SC micelles in the aq. solution at a higher concentration range (~25–100 mM) was found to be 10.14 ± 0.01 Å.[271] Here, in terms of the reported sizes of the micelles, the Mean Spherical Approximation (MSA) Structure (a system of charged spherical objects in a dielectric medium) was reported.[271] And although the 2^0 CMC was reported in the previous paragraph, however the literature a range of the 2^0 CMC was between ~11–15 mM[161,231,262,263] @RT, depending on the techniques used, as well as the experimental media, and the presence/absence of accessory ions/salts.

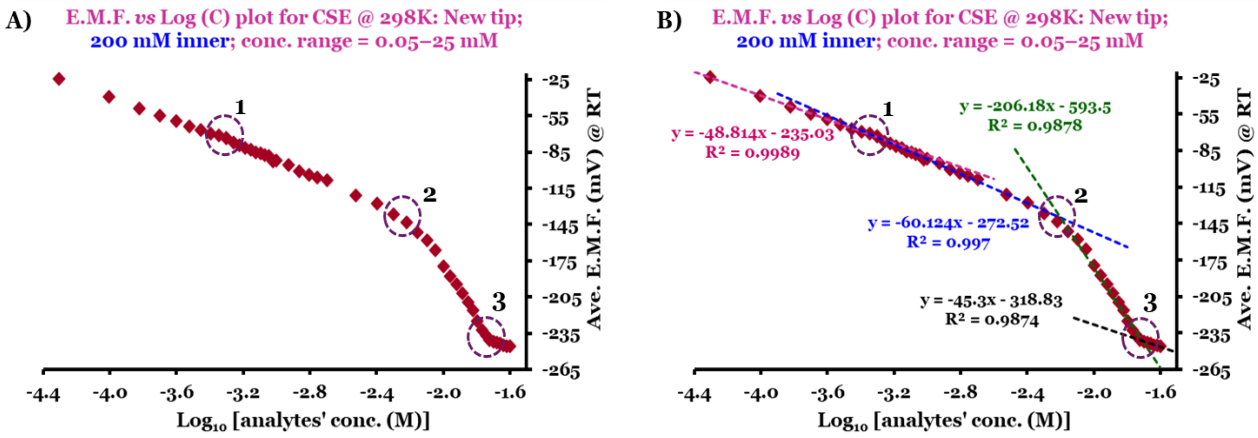
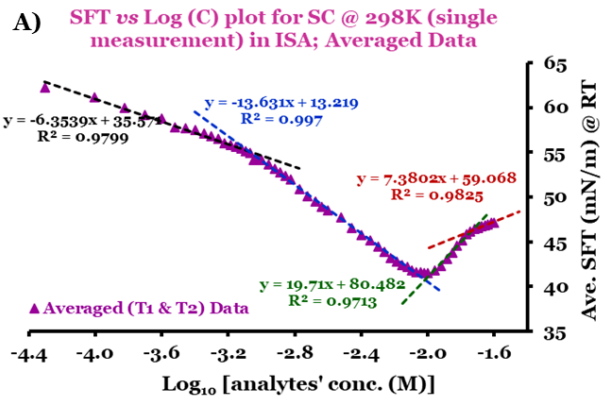
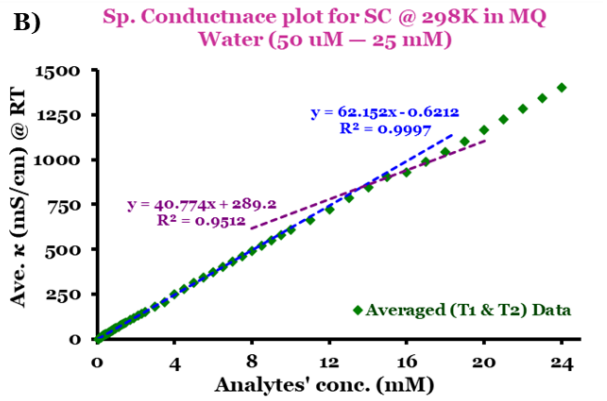


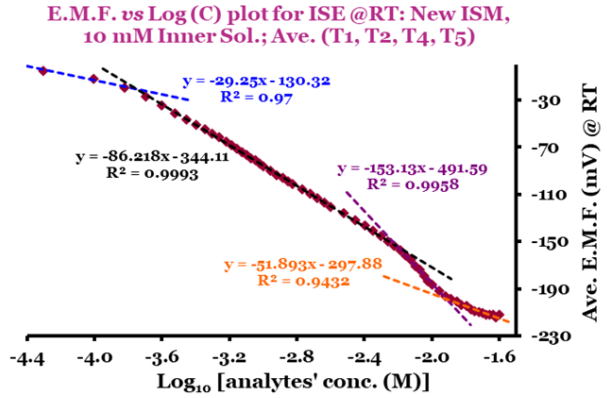
Figure 6.17: A) *One of the calibration plots within a range of 0.05–25 mM from the average (T–1 & T–2) data obtained by the CSE using 200 mM SC in ISA as the inner solution.* ***B)*** *The same plot of A) showing the 3 distinct breakpoints (point of intersections, POI) and the trendlines showing the major linear zones in the plot. Here, it is obvious that the POI–1, POI–2, and the POI–3 indicate the pre–micellar aggregations and the 1^0 & 2^0 CMCs respectively.*

6.7.4 Calibration curves & CMC of SC from Tensiometry and Conductometry

The CMC values of SC were also determined via the tensiometer and the conductivity meter to validate the efficacy of the CSE. The average surface tension (SFT) data from two trials were plotted against the Log (C) to obtain the calibration curve, and the break points in the SFT corresponded to the aggregate formation or micellization. At the lowest point in the SFT, the corresponding conc. of the SC is denoted as the 1^0 CMCs after which the SFT increased slightly. The most likely reason of such behaviour in SFT would be the consumption of the added free monomers (SC) for the progressive/successive formation of more 1^0 CMC past the 1^0 CMC point.







D)

Method of CMC determination	Primary CMC (mM/L)	Secondary CMC (mM/L)
*EMF (sensor), in ISA	6.6	16.5
SFT (in ISA)	8.6	18.3
Sp. Conductance (in MQ)	N/A	14.1

Figure 6.18: A) *Calibration curve of SC within the conc. range of 0.05–25 mM, constructed via Tensiometer @ RT in 10 mM NaCl media as the ISA. The premicellar aggregation point, the 1^0 & 2^0 CMC points: all of them are distinctly noticeable from this SFT vs Log(C) plot.* ***B)*** *Calibration curve of SC in the same conc. range (0.05–25 mM), constructed via conductance measurement @ RT in MQ water plotting the baseline-corrected specific conductance vs mM concentrations. In this case, only one breakpoint was distinguishable which represents the 2^0 CMC, depending on the position/location of the breakpoint.* ***C)*** *The average plot for the calibration curve obtained from the CSE via EMF measurement @ RT using the 10 mM SC in ISA as the inner filling solution.* ***D)*** *The enlisted values of the 1^0 and 2^0 CMCs of SC at RT obtained through different tools.*

**The CMCs were obtained from the calibration curve constructed based of the average of the four trials, as shown in figure 6.18 C.*

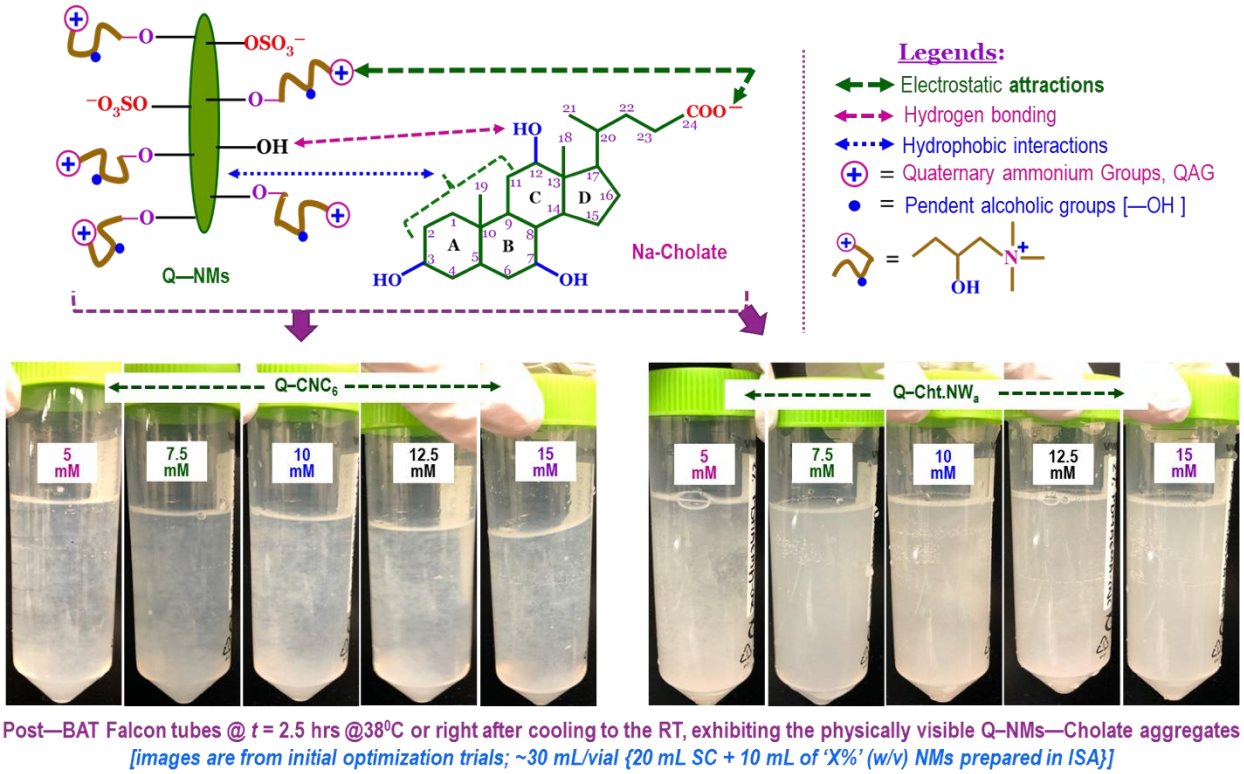
Once the numbers of 1^0 micelles exceeded a critical value, the 2^0 micelles were formed as evident from the last breakpoint at the end of the surface tension (SFT) plot. Figure–6.18 shows the calibration curves obtained by the two techniques and the average of multiple trials of the EMF calibration curve by the cholate selective electrode (CSE).

For the calibration curve obtained from the conductivity measurement, only a single breakpoint was distinguishable. The breakpoint was seen past the 11 mM region, which corresponded to the 2^0 CMC for the SC, concluded based on the reported 2^0 CMC values in the literature (11–15 mM). Conductivity measurement is dependent on the number of ions/cumulative ions or in other words, concentrations, present within the measurement vessel. Thus, a gradual increase in the conc. of SC proportionately also increased the dissociated Na^+ and cholate (Ch^-) ions in the solutions/liquid. In this case, the formation of the 1^0 micelles did not affect the conductance reading as in the 1^0 micelles, none of the anionic charges (Ch^-) were masked among the participant SC. This could be the most likely reason for not observing the break or change in the slope for the 1^0 micelle formation. Due to the inter–micellar H–bonds formation, the 2^0 micelles were formed when some of the anionic charges among the participant SCs associated with the micelles resulted in the slope change in the calibration curve, which corresponded to the 2^0 CMC.

Figure–6.18 C shows the average of four different averaged calibration plots obtained with four CSM tips, and the CMCs obtained are summarized in the table and Figure–6.18 D. Here, the close resemblance of the CMC values of the SC within a range confirmed that the CSE was working within an acceptable limit of accuracy and reproducibility.

6.7.5 BATs of selected NPs with SC and Q_{max} determination through CSE

The BATs of the selected NPs were conducted with SC in ISA to evaluate their sequestration abilities of SC from the body. The free/unbound SC was quantified by the CSE and Langmuir monolayer adsorption isotherm (LMAI) was used to quantify the Q_{max} from the linear fitting of the plots. Figure–6.19 explains the possible mechanism/adsorption or binding forces that could be in effect simultaneously during the BATs of NPs with SC.



Post—BAT Falcon tubes @ *t* = 2.5 hrs @38^{0}C or right after cooling to the RT, exhibiting the physically visible Q–NMs—Cholate aggregates
[images are from initial optimization trials; ~30 mL/vial {20 mL SC + 10 mL of 'X%' (w/v) NMs prepared in ISA}]

Figure 6.19: *Interaction mechanisms of a representative NM with SC for its physicochemical adsorption onto the surfaces of the NM. The resultant complexes (NM–SC) were easily visible within the Falcon tubes after the BATs were done for 2.5 hrs, regardless of the tubes be @ 38^{0}C or RT. The labels of the tubes indicate the initial conc. of the SC taken, NOT the conc. after adding the NMs' dispersions.*

As discussed in the Chapter–2 (Literature Review), the SC has a hydrophobic steroid ring, and stereochemically it can be considered as a flat molecule, where the hydrophilic and the hydrophobic faces of the molecule are at opposite planes. Such forms of conformation might be the most probable reason for the strong hydrophobic interactions, one of the predominant driving forces for physicochemical adsorption with the cationic NMs. After the principal binding force, the ionic interactions (long-range forces), the three hydroxyl groups on the hydrophilic face provide the ground to participate in the formation of significant numbers of H–bonds facilitating the adsorption. The existence of all these three forces enhanced the efficiencies of the NMs to scavenge the BAs/BSs from the human body and thus, could ensure their potential usage as the BAS in coming days.

Figure–6.20 shows the post–BAT Falcon tubes for most of the selected cationic NMs. The images were taken prior to the measurement in the E–cell with the cholate selective electrode (CSE)—Reference electrode (RE), or the next day. The determined max adsorption capacities (Q_{max}) of the NMs for SC are shown in Figure–6.21 showing the comparison of the Q_{max} values of the selected NPs with their corresponding ZPs and the aggregate sizes (D_H). A comparison of the Q_{max} with the ZP/D_H of the commercially available drug, Cholestyramine (Questran^{TM}) is provided together with the other NPs. From the results obtained from the BATs, it was evident that most of the cationic NPs developed in this study for use as BAS showed similar or higher Q_{max} values than the commercial brand Questran^{TM}.

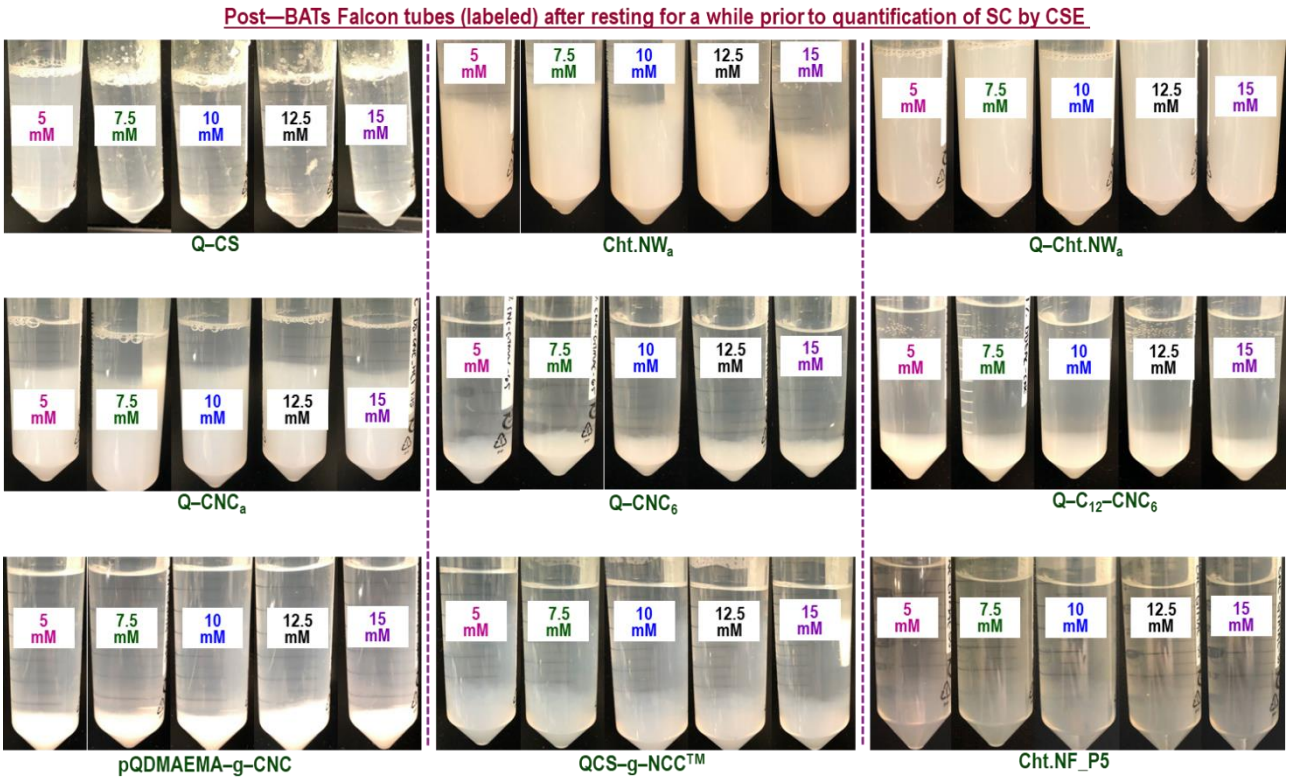


Figure 6.20: *The post–BATs tubes for most of the selected NMs on which the BATs were conducted with SC. The negative controls or the tubes for anionic NPs are not shown here.*

The Q–CNC_a NPs were found to have slightly more SC sequestration capability than the Q–CNC_6 NPs systems. This might be due to the higher ZP and slightly lower D_H sizes of the Q–CNC_a NPs compared to Q–CNC_6 NPs. The Q–CNC_6 were highly Zwitterionic due to the presence of SHE groups (—OSO_3^-) on the surfaces, while the Q–CNC_a NPs were moderately less Zwitterionic since the surfaces possessed fewer SHE groups compared to the Q–CNC_6 NPs. The presence of hydrophobic groups on the QAG (for Q–C_{12}–CNC_6 NPs; an unprecedented NP) or the hydrophobic polymeric CNC NPs (brush–CNCs) showed significant improvements in terms of SC binding/sequestration with a binding capacity of ~357 mg SC/g

of NPs for Q–C_{12}–CNC_6 NPs and ~493 mg SC/g of NPs brush–CNCs. Although the ZPs was slightly lower, the D_H were almost double in sizes of the hydrophilic–CNCs (Q–CNC_6, Q–CNC_a), and the prominent hydrophobic interactions (after the ionic interactions) with SC could be the most likely reason for the significant increase of the Q_{max} values.

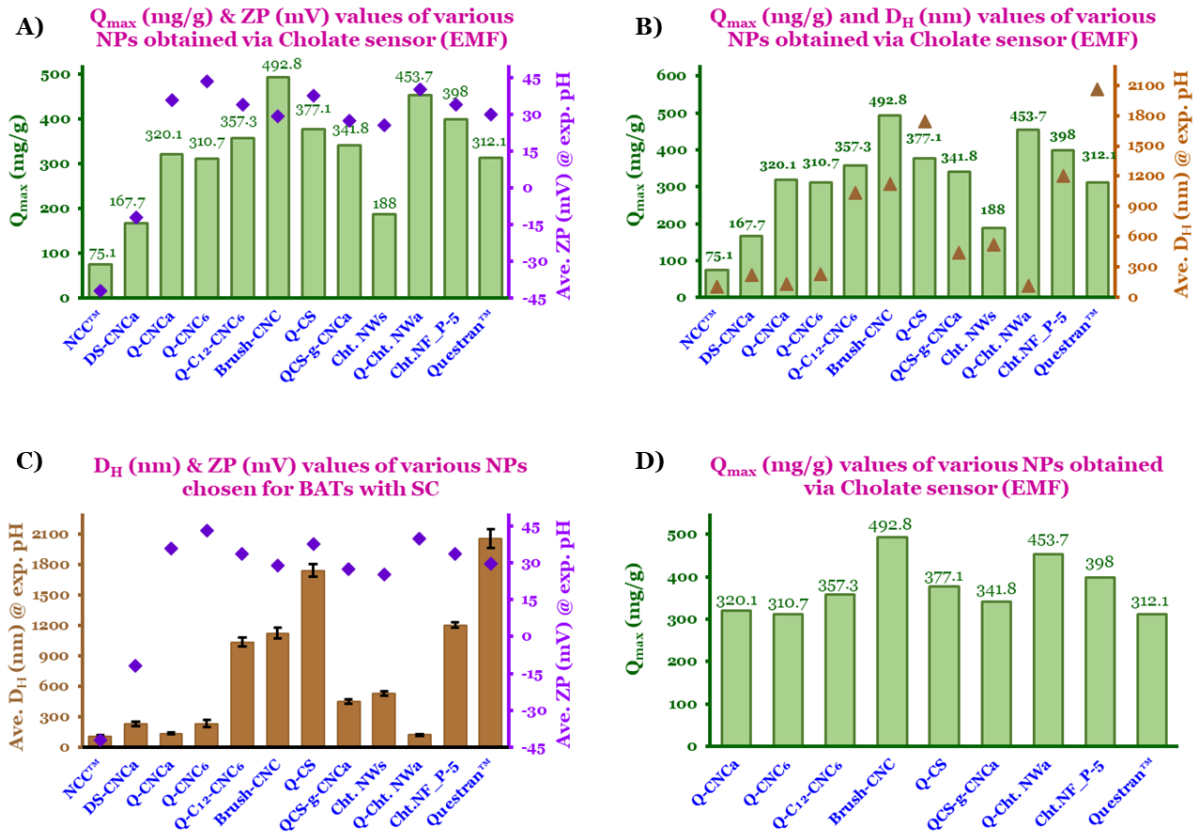


Figure 6.21: *Comparison of Qmax values of the selected NMs for SC with A) ZPs of the NMs, B) Aggregate sizes (D_H) of the NMs. C) The D_H and the ZP of the chosen NMs. D) The Q_{max} values of the cationic NMs among all the selected NMs (i.e., without the negative controls).*

P.S.: *Cholestyramine resins were purchased from MilliporeSigma, Canada, as powder form, and the US brand of the commercial drug, Questran™ (cholestyramine) is just used for the ease of writing on the plots.*

The Q–CS NFs, although having a D_H of more than 1.5 µm showed better binding profile (Q_{max} = 377 mg/g) over the QCS–g–CNC_a NPs systems. One notable reason for the higher Q_{max} for the amino–polysaccharide, Q–CS NFs could be their complete aqueous solubilities which is one of the key factors for physicochemical adsorption of molecules (e.g., SC here). In comparison, the QCS–g–CNC_a showed slightly lower aq. dispersibilities that might have been affected the adsorption of the SC during the BATs.

The determined Q_{max} values for the other amino—PSs, the Q–Cht.NW_a (454 mg/g) and the Cht.NF_P5 (398 mg/g) were significantly higher with the brush–CNCs possessing the second-highest Q_{max}. For the Q–Cht.NW_a NPs, the surface PAGs (—NH_2) were protonated (—N^+H_3) producing stronger cationic NPs, which was one of the additional factors that facilitated the overall adsorption of SC molecules as shown in Figure–6.22 A. The Cht.NFs were not permanently cationic, but they possessed pH-responsive properties and thus retained their cationic charges at the experimental pHs (< ~7). One of the important dispersion properties of Cht.NF_P5 was their dispersion viscosity and apparently the dispersions of the Cht.NFs from pass–1 to pass–5 were like dilute solutions. The resultant viscosity of the solution/dispersion of Cht.NF_P5 could be the most likely reason of the higher Q_{max} values for SC.

Cholestyramine is an indigestible resin and HMW cationic polymer which was almost completely insoluble either in MQ water or in ISA. Although it exhibited a very poor dispersion in ISA, the BATs were still conducted to evaluate their efficacy for SC sequestration and the results were used as the positive control. Figure–6.22 B represents dispersions in MQ water and in ISA showing its insolubility and the Falcon tubes of the conducted BATs right after the test in the bottom row.

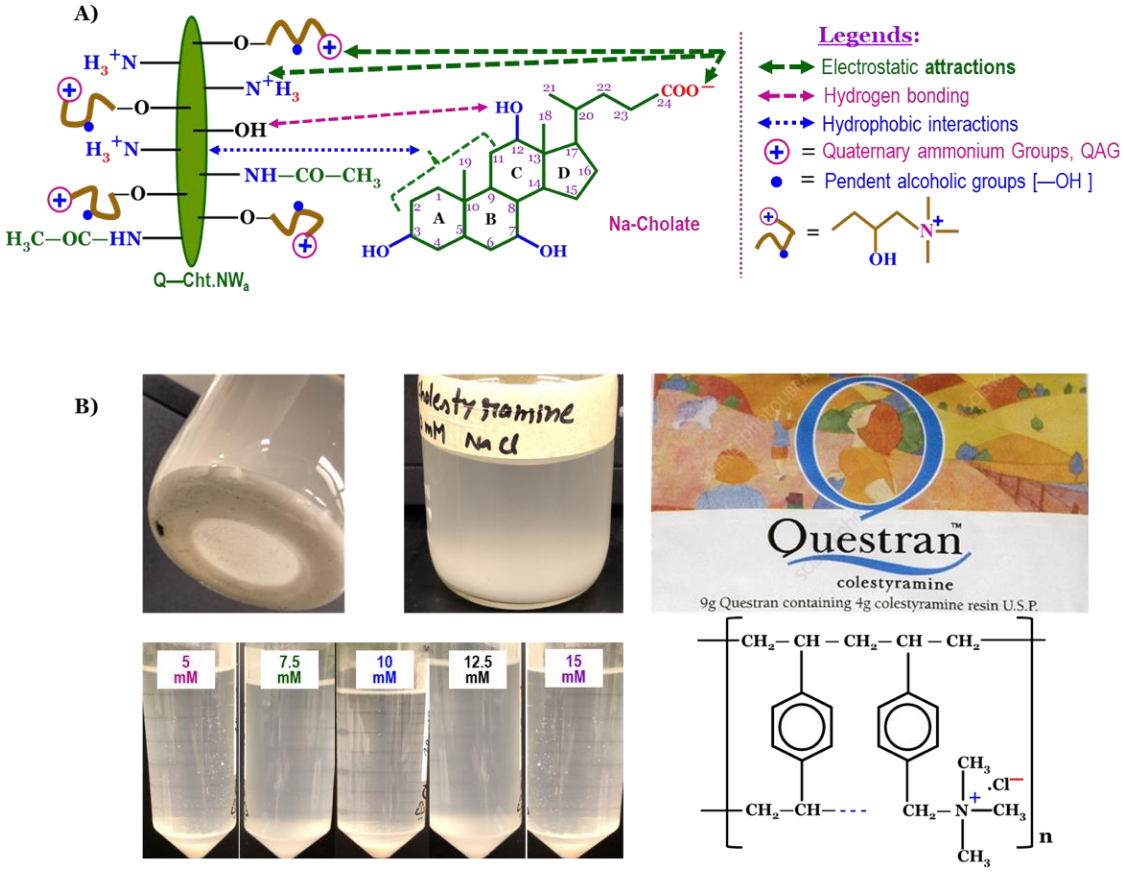


Figure 6.22: A) *Schematic representation of the possible simultaneous existences of all the binding forces between the Q–Cht.NW$_a$ (amino–PS based NMs, other examples include Q–CS, QCS–g–CNCs, Cht.NW$_a$ and the Cht.NFs) and the SC molecules.* ***B)*** *Cholestyramine resin's dispersions @ 0.5 % w/v (aqueous, top-left; and in ISA, top right) which were found almost insoluble and non–dispersible. In the bottom row, the Falcon tubes of the BATs are shown which are labelled as the initial conc. of the SC taken. And to the right-side column, the sachet of the cholestyramine is commercially available in the US market, and the chemical structure of the resin is given just below the sachet.*

Here, due to its low dispersibility, the D_H and ZP of cholestyramine were conducted at 500 ppm (0.005 %, w/v) of dispersion yielding a ZP of ~23 mV and D_H of ~ 2 µm. Although the BATs were conducted at a higher conc. of 0.8% (w/v), the determined Q_{max} obtained from

the BATs were found to be ~ 312 mg/g. Regardless of their poor aqueous dispersibility, the Q_{max} of cholestyramine was reportedly higher than the Q_{max} of Q–CNC_6 NPs or the Q_{max} of non–quaternized Cht.NW_a and the most likely reason would be the non–ionic (hydrophobic/Van der Waals) as well as the ionic interactions with the SC molecules.

Based on all the results presented here in Figure–6.21, it was concluded that overall, the surface charges of the NMs, the aggregate sizes, their dispersibilities/solubilities, and the viscosities of the intended dispersion (solution) are the controlling factors for the binding capacities of the NMs for SC. In all the cases, the non–ionic interactions were as important as the ionic interactions for the physicochemical binding or adsorption process of the SC onto the surfaces of NMs. However, the rate of binding might vary over time for the NMs of interest. Thus, in the next section, one representative example of adsorption kinetics will be discussed and compared with the binding kinetics of the positive control, cholestyramine.

6.7.6 Adsorption Kinetic Tests (AKT) for the NMs with SC

Due to time constraints, the AKT tests were only conducted for the binding of sodium cholate, SC with one of the selected concentrations of SC. Thus, one of the NPs were selected for conducting the AKT, and then compared to a commercially available drug, cholestyramine being a positive control. Here, considering the surface charges (ZPs), D_H, and the stability of the aqueous dispersion, the Q–CNC_a was selected as the NP of interest. As discussed in Chapter 3, the AKT for the Q–CNC_a and the Questran^{TM} (Cholestyramine) samples were conducted for 150 min during which samples were collected at different intervals. Here, right after the addition of the NMs as BAS to the RBF, the mixture became cloudier, similarly, when Q–

CNC_a was added to the SC, it turned cloudier faster than with cholestyramine. Figure–6.23 provides snapshots of the AKT with the Q–CNC_a NPs and the corresponding samples.

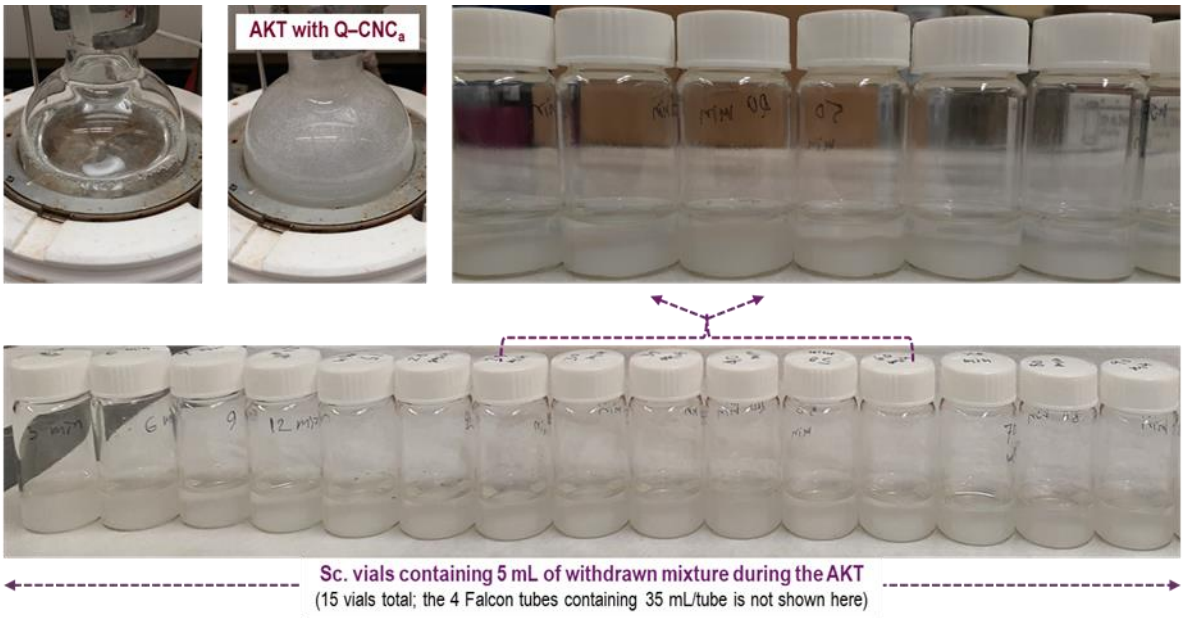


Figure 6.23: *The adsorption kinetic test (AKT) of a representative NM with SC and the withdrawn 5 mL samples in the scintillation vials at different time intervals. The SC–NP complexes were found sedimented at the bottom of the vials while the set–up of the E–cell was carried out.*

The contents of vials were then evaluated for the free SC contents to determine the amounts that were bound to the NPs. And the results thus obtained from each of the vials are shown in Figure–6.24. From the figure, it is evident that the Q–CNC_a NPs not only bind faster to the SC than cholestyramine, but they also approached to the saturation point (the point after which the adsorption rate and extent are very low) sooner than cholestyramine. The cholestyramine dispersion at 1% (w/v) was unstable and it rapidly precipitated in the container. Before adding the cholestyramine dispersion to the 200 mL of 7.5 mM SC in the RBF for the

AKT study, the dispersion was sonicated, and the required 25 mL were pipetted under sonication. Being the complex resin and HMW polymer, the resultant poor dispersibilities affected the rate as well as the extent of the sorption of SC @ 38^0C.

Figure–6.24 B shows the AKT of a novel BASs called SK&F 97426-A, which is a quaternary alkylammonium polymethacrylate described by Benson *et. al.* (1997)[275] and it was compared to the AKT of cholestyramine. In the study, the association rates of BAs were faster for cholestyramine than for SK&F 97426-A.[275] However, in the present study, an opposite scenario for the cholestyramine was observed compared to Q–CNC_a. The adsorption of the SC onto both cholestyramine and Q–CNC_a was much higher than SK&F 97426-A and the other BAs (TC, GC, TCDC). The detection and quantification of free BAs, as well as the structural variations over the BA molecules, could be potential reasons for such a variation in the observed binding capacities. Other possible reasons could be the variation in the formulations, like the glucose-free Krebs-Henseleit buffer ($MgSO_4$, $KHPO_4$, KCl, & NaCl) that might disrupt the BAS-BA binding.

Several factors could be the likely participating factors as the causative reasons for the faster rate and extent of association between SC and Q–CNCs over that of cholestyramine, i.e.:

- the active surface charges of NPs
- the D_H of NPs (NPs provide available surfaces for surface adsorption)
- the hydrophilicity/hydrophobicity of NPs and corresponding aq. dispersibility.

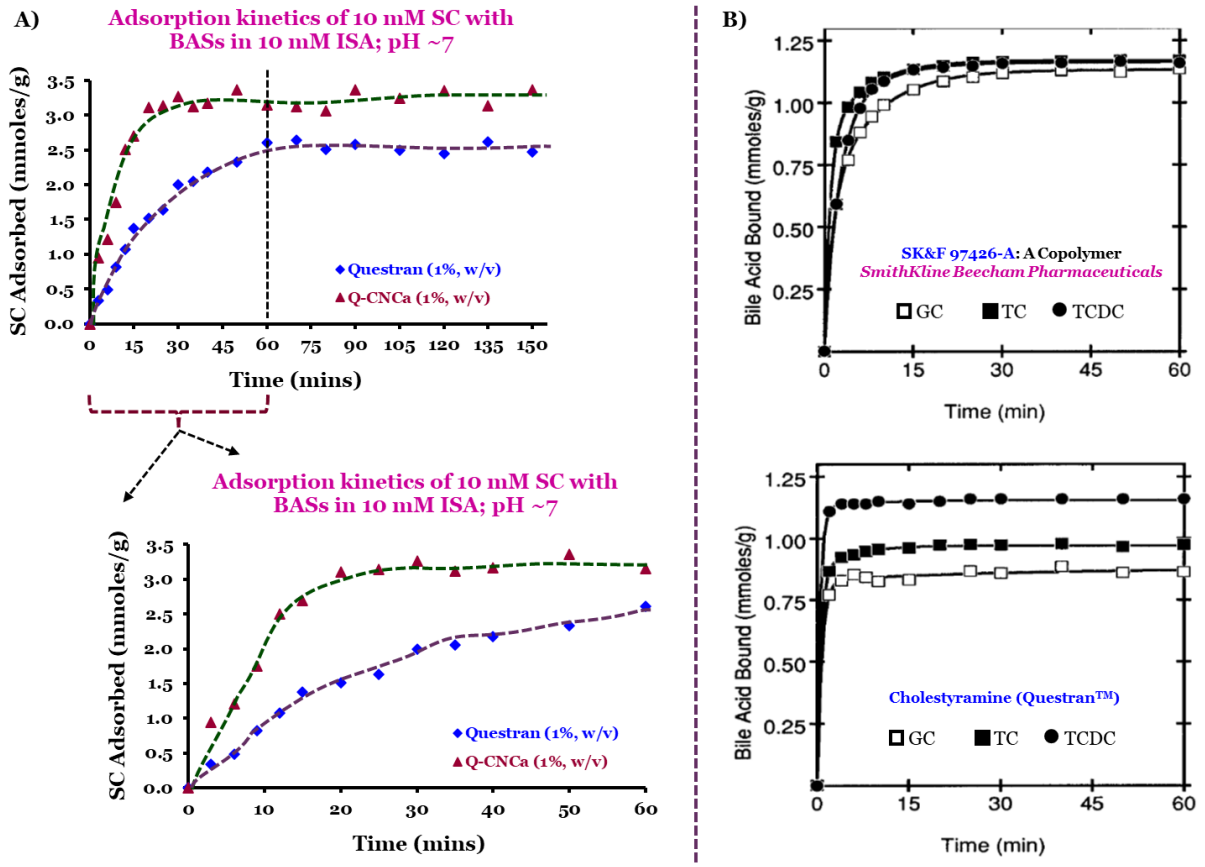


Figure 6.24: A) *Adsorption/binding/association kinetic tests (AKTs/BKTs) conducted for one of the developed NMs (here, the Q–CNC$_a$ NPs was chosen) and for Questran^{TM} (cholestyramine) as the BASs. The rate and extent of the sorption of the SC onto the Q–CNC$_a$ was found higher than that of the cholestyramine manifesting the Q–CNC$_a$ to be more efficacious BASs.* ***B)*** *The adsorption kinetics of a novel BAS named SK&F 97426–A and cholestyramine with the radiolabeled (^{14}C) – glycocholate (GC), taurocholate (TC), and taurochenodeoxy cholate (TCDC). Here the size of the cholestyramine used was mostly within the range 38–212 µm (measured by dry sieving) and the 0.4% (w/v) BASs' slurry prepared in glucose-free Krebs-Henseleit buffer was used for the 5 mM of the radiolabeled BAs for the AKT. The radioactivity was measured by liquid scintillation counting. Adapted from.*[275]

A better overall profile based on all the above properties was observed for the Q–CNC_a NPs. In the case of cholestyramine, the lower cationic nature as well as the non–dispersibility of the resin could be the most likely reasons for its slower physicochemical adsorption, both in terms of rate and extent of SC onto the surfaces. Figure–6.25 summarizes the chemical structures of the components involved in the AKTs.

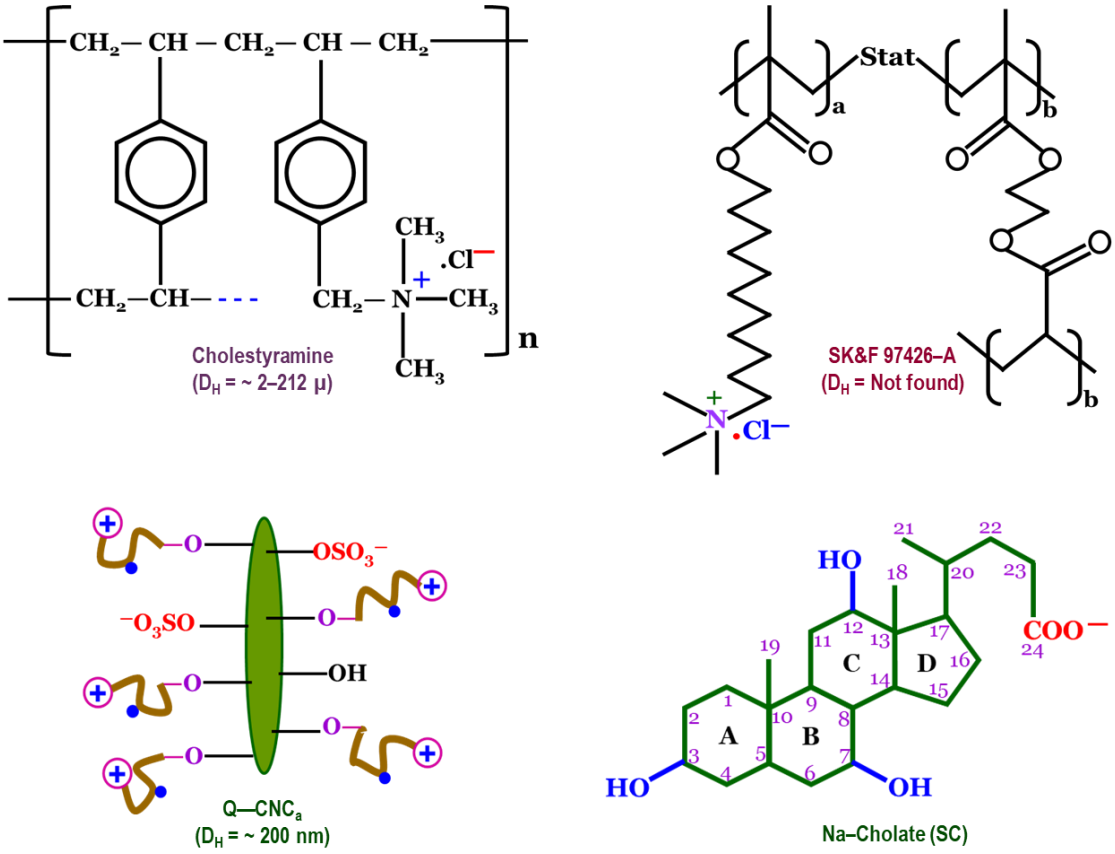


Figure 6.25: *Chemical structures of cholestyramine (top left), the novel compound SK&F 97426-A (top right), sodium cholate (bottom right), and the schematic representation of the Zwitterionic NPs Q–CNC_a (bottom left).*

6.8 Conclusions

This chapter discusses the successful development of the cholate selective membrane (CSM) followed by the fabrication of a prototype, an elementary model of a CSE (cholate sensor). The membranes were subjected to quality control experiments to establish the conditions for the operation of the CSE. The sensor was successfully demonstrated and was capable to quantify the SC for the binding and kinetic experiments. The fabricated CSE/sensor was used extensively in several BATs with SC for NMs selected from the library of the prepared NMs discussed in Chapter 3 to Chapter 5. The max adsorption (Q_{max}) obtained with the CSE from the BATs of NMs allowed us to conclude the successful development of NMs based BAS that exhibited better performance than the commercial BAS, cholestyramine. Additionally, the hydrophobic–CNCs, brush–CNCs, QCS & QCS–g–CNCs, Q–Cht.NWs, and the Cht.NF_P5 possessed superior Q_{max} for the binding of SC over the cholestyramine. All the Q_{max} of the NMs based BASs should be cross-checked with other established methods of detection (enzyme kits, HPLC etc.) before proceeding to animal studies for *in vivo* evaluations.

Figure–6.26 summarizes the Q_{max} values of several NPs on which all the three methods (namely the conductance, UV–Vis for the colored analogue of SC, and the cholate selective electrode, CSE) of SC detections were applied. Although notable variations were observed depending on the detection methods, the plot provided a summary of the approx. efficiencies of NMs that showed potential as BASs.

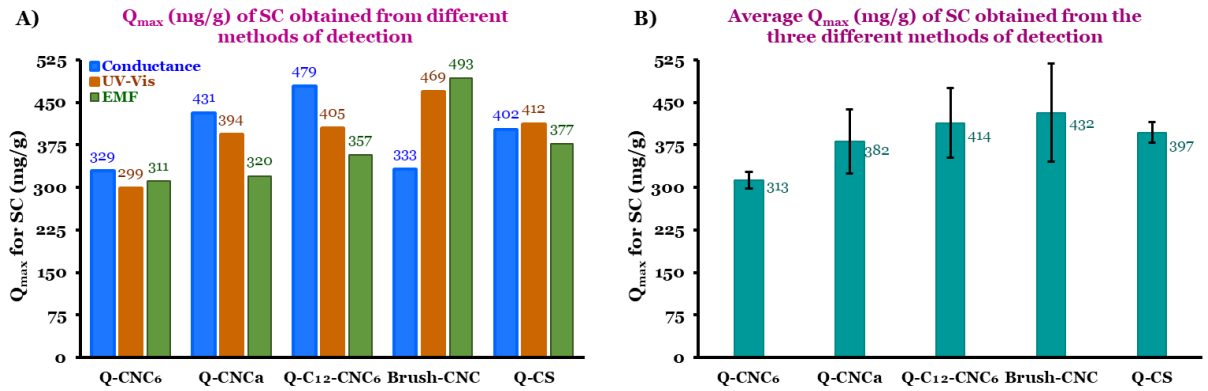


Figure 6.26: A) *The max. adsorption capacities (Q_{max}) of some of the NPs which lies in common over the three methods of detection for the free/unbound SC.* ***B)*** *The averaged plot based on the three detection methods.*

6.9 Future directions

The constructed CSE in suffered from moderate to significant EMF variations. Furthermore, the membrane became saturated or lost its sensitivity sooner than expected. One potential approach to eliminate the notable EMF drifting could be the use of partially cationic PVC. The initial process of synthesizing cationic–PVC was conducted, but due to lack of time, the modification of the CSM was not completed. Further attention should be devoted to combining the two half–cells (CSE & the RE) into a single electrode.

Chapter 7: Biosafety of the developed NMs

7.1 Introduction

It had been widely known that the quaternary ammonium groups, QAGs ($R_4N^+.X^-$) containing compounds possess some antimicrobial (antibacterial or antifungal) characteristics,[276–283] whose MICs (minimum inhibitory concentrations) depend on their chemical structures. The nanomaterials (NMs) developed in this study all contained the QAGs, while several possessed the PAG (primary amino groups, —NH_2) in their chemical structures that could be protonated in acidic conditions. As the NMs were to be used for human application in treating hypercholesterolemia, the biosafety of these NMs should be determined. Thus, in this chapter, the biosafety of the NMs is discussed. In the biosafety evaluation, yeasts' fermentation of glucose/sugar was used as the model experiment, which was conducted to evaluate if the NMs were toxic to living cells. The agar–disc diffusion or the culture broth[284] were NOT considered for bacteria (*E. coli, S. aureus*) or the yeast cells due to their time-consuming protocols. However, it is recommended that the NMs should be evaluated through standard bacterial culture and on human cell culture to obtain precise information for their safety profile.

The hypothesis of such biosafety experimentations by yeast fermentation was to determine the relative safety profile of the NMs compared to the well-known BAS, cholestyramine resin. Cholestyramine is available commercially for over 200 years and is known to have an excellent safety profile for human use, thus if the NMs developed in this

study displayed better responses from the fermentation of glucose by Baker's yeasts then we can conclude that these NMs are safe for human application.

7.2 Yeast cell: Anatomy and fermentation of glucose

Yeast belongs to the kingdom Fungi and is a eukaryote, grows as single cells, and produces daughter cells through asexual reproduction and self-cloning either by budding (the budding yeasts) or by binary fission (the fission yeasts). The most common and commercially available Baker's yeast, *Saccharomyces cerevisiae* is a budding yeast predominantly employed in the commercial production of fermented beverages. Although most of the fungi are multicellular and possesses spherical, cylindrical, or oval shape, it is generally ellipsoidal in shape with a diameter of 5–10 μm.[285,286] Yeasts have structural features similar to higher eukaryotic cells comprising of a cell wall, nucleus, mitochondria, endoplasmic reticulum (ER), Golgi apparatus, vacuoles, microbodies, and secretory vesicles together with a complex extracellular and intracellular membrane network.[285,287] Here the cell wall possesses a net negative surface charge due to the presence of phosphate groups. In terms of composition, the yeast's cell wall is made up of a variety of polysaccharides, such as α-mannan (soluble in water and alkali and linked to proteins (mannoprotein), alkali-soluble β-glucan, and alkali-insoluble β-glucan bonded with chitin. Its cell membrane is rather fluid and flexible due to the presence of lipids, sterols, and proteins.[285,287] Figure –7.1 A & B shows the main features of a yeast cell, and a commercially available yeast, respectively.

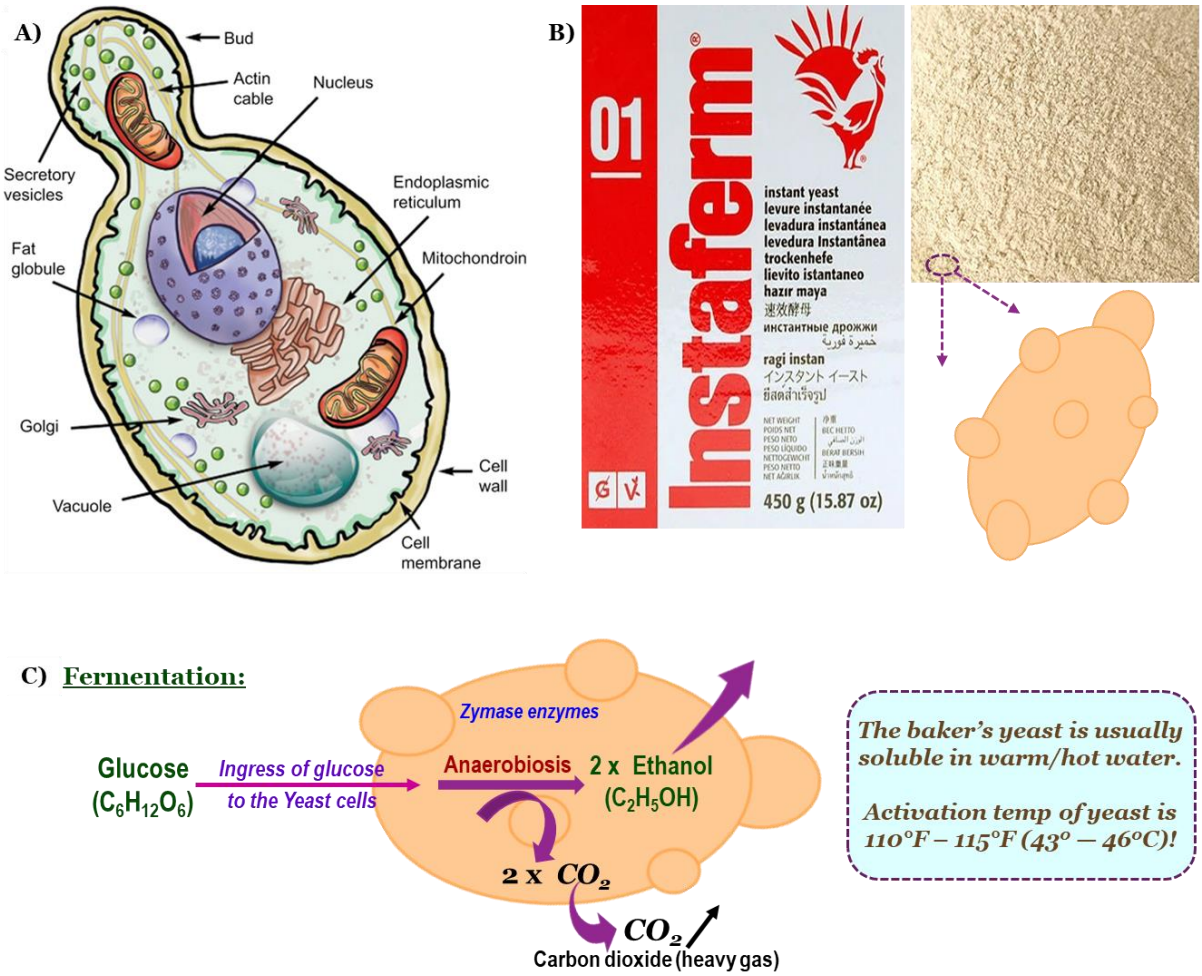


Figure 7.1: A) *The main features of the baker's yeast cell, Saccharomyces cerevisiae. The cellular division usually leaves bud scars on the mother cells which are composed mainly of chitin. Reproduced from.*[285] ***B)*** *An example of the commercially available bakers' yeast, Lallemand Instaferm® Instant dry yeast. The insert represents the schematic of the cellular structure of the yeast.* ***C)*** *The overall intracellular anaerobic fermentation process of a glucose molecule to its products: ethanol (C_2H_5OH) and carbon dioxide (CO_2). The groups of enzymes, zymase usually catalyze the fermentation reaction through the Embden–Meyerhof–Parnas (EMP) pathway. Under anaerobic conditions, the yeasts convert pyruvate to ethanol and CO_2.*

N.B.: Overall fermentation reaction for glucose:[286,288–290] $C_6H_{12}O_6 \rightarrow 2\ C_2H_5OH + 2\ CO_2$

For yeast-mediated fermentation, water is essential, and higher water activity is required for *S. cerevisiae* cells. Regarding temperature and pH requirements for such fermentations, yeasts thrive in warm and acidic environments with the *S. cerevisiae* strains growing well at between 20 – 30^0C and pH of 4.5 – 6.5.[286] Due to the fermentation of sugars, yeast cell produces ethanol, CO_2 and other compounds that add aroma & flavor to the target mixture.[286,288–290] Yeast possesses intracellular groups of enzymes called zymase that catalyzes the fermentation process. Ethanol fermentation occurs because of the enzymatic activity of the yeast at the Embden–Meyerhof–Parnas (EMP) pathway, which leads to glucose conversion to pyruvate. Under anaerobic conditions, the yeasts convert pyruvate to ethanol and CO_2. In aerobic conditions, yeasts consume sugars, mainly for biomass accumulation and CO_2 production.[286,288,289] Figure–7.1C shows the intracellular fermentation process by the yeast cell.

7.3 Reported effects of polymers on yeast cells & mechanism of inhibition

Literature suggests that the fermentation of glucose by Baker's yeast is usually inhibited by cations at the yeast cell surface that prevent the entry of glucose.[291] Under most conditions, such forms of inhibitions are practically irreversible as the fermentation's rate is dependent on the concentration of yeast but independent of the concentration or the amount of existing sugar in the bulk. Ralston *et. al.* (1964) reported[291] that the chitosan samples at a concentration of 2 x 10^{-5} M (based on glucosamine–N content) can completely inhibit the fermentation of glucose by 0.03% yeast suspension at a pH of 4.5. Such inhibition by the chitosan was approximately ten times (10x) as effective as an equivalent concentration of the detergent dodecyl–

trimethylammonium bromide (DDTAB), one of the most potent cationic inhibitors reported in the literature.[291]

In a study conducted by Ralston *et. al.* (1964), the yeast fermentation was conducted under nitrogen measured using the Warburg manometers at 37^0C. In the study, the reaction mixture consisted of 0.08 % (w/v) Baker's yeast with 0.03 M glucose in a 0.025 M sodium acetate-acetic acid buffer (pH 4.5) with a final volume of 3 mL. The study compared the inhibitory effects of the cationic diethylaminoethyl cellulose (DEAE–Cellulose) on yeast-mediated glucose fermentation, with that of chitosan fibers (CS). They concluded that, although the CS was found to be more efficacious, both cationic polymers inhibit the fermentation process and eventually, flocculate the yeast cells leading to precipitation.[291]

The results of further investigations on the aggregation of yeast suggested that both the DEAE–Cellulose and chitosan were electrostatically and irreversibly bound to yeast cell surfaces (negatively charged ≥ pH 2) neutralizing the charges, and reversal of the net negative charge on the yeast cell surface could occur at or above pH 2. Thus, the cationic-polymer–yeast particles, being neutral or, slightly cationic become aggregated leading to precipitation.[291] Figure –7.2 shows the schematic of the surface adsorption of quaternized–nanofibers (Q–NFs, the cationic polymers here) onto the yeast cells inhibiting the glucose fermentation.[291]

The authors also indicated that the Q–NFs (here the chitosan and DDEA–Cellulose) acted outside the yeast cell, but not inside the cells, by conducting an experiment using a pre–treated yeast preparation. The pre–treated yeast preparation indicated the dispersion with yeast cells which have an artificially induced high internal concentration of glucose.[291] The pre–

treatment was done by incubating 1 g of dried yeast for 17 h at 37^0C with 100 mL of 0.01 M acetate buffer (pH 4.5) containing 9 g of glucose. The treated yeast was centrifuged, washed five times with buffer and finally suspended in 50 mL of 0.05 M acetate buffer (pH 4.5).[291]

When incubated with buffer in the Warburg flasks, the yeast displayed appreciable fermentation, indicating that it did have a high internal concentration of fermentable substrate. Glucose, chitosan, or chitosan plus glucose was added from the side arm of the flask to the yeast plus buffer system to observe their effects on the rate of CO_2 production. Only the flask containing no chitosan showed an increased CO_2 output when glucose was added externally, while the addition of chitosan or chitosan plus glucose had no effect,[291] as shown in Figure–7.2 B. Such findings thus indicated the inhibitory actions of chitosan on yeast to be external, having no effect on fermentation of the internal substrate but preventing the ingress of glucose into the cell by forming a layer on the yeast cell surface.[291] The chitosan layer is held in position by the interaction between the chitosan's amino groups and anionic groups on the yeast cell surface. The inhibition is irreversible under most conditions and is proportional to the chitosan chain length, cationic nature, and concentration.[291]

From the literature,[291] the conclusion is that cationic NMs can irreversibly inhibit the yeast fermentation rate and their efficacy. Thus, before utilizing our NMs for human application it is necessary to determine their safety.

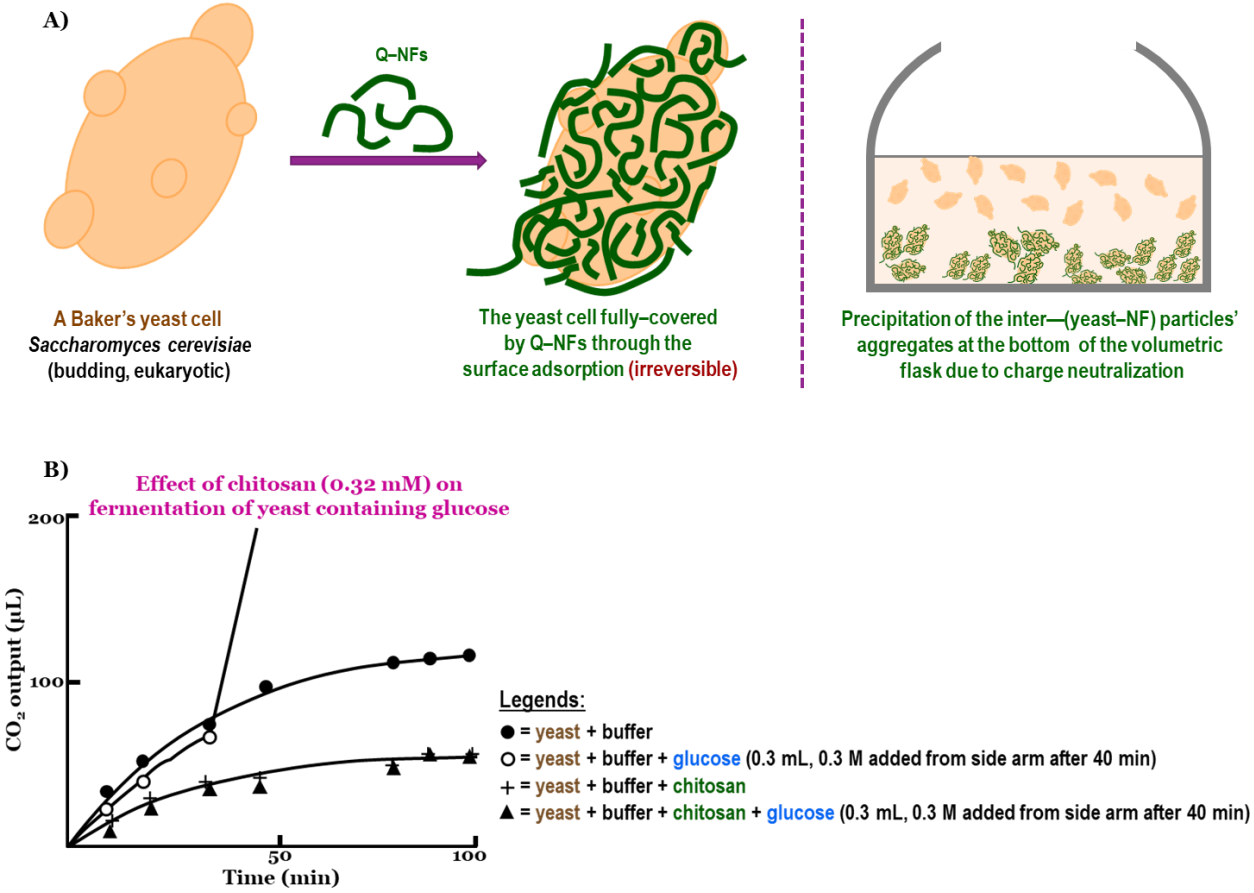


Figure 7.2: A) *The schematic representation of the mechanism of inhibition of the yeast cells by the physicochemical adsorption of the cationic nanofibers (Q–NFs) of carbohydrate polymers, like the chitosan or DDEA–Cellulose. The yeast cell wall is negatively charged, and thus the NFs are ionically attracted thus bound onto the surface causing the gradual cessation of glucose influx to complete blockage of the intake. Consequently, no further fermentation takes place as well because the NF–bound yeast cells got flocculated and precipitated out. The schematic of the adsorption of cationic NFs onto the yeast cells was drawn based on the discussion from.* ***B)*** *Effect of buffer and chitosan on the fermentation rate of glucose and CO_2 output. Both* ***A)*** *and* ***B):*** *Drawn from the discussions of reference.*[291]

7.4 Materials and methods

7.4.1 Materials

The Lallemand Instaferm® Instant dry yeast was purchased from a commercial vendor. D–glucose, hydrochloric acid, and acetic acid were purchased from MilliporeSigma and used as received without any further modifications. Purified water (Milli-Q water) from a Millipore system (>18 MΩcm) adjusted to pH 4.5 was used to prepare the samples' solutions.

7.4.2 Methods

Based on the discussion of literature findings, the yeast fermentation experiments for the selected NMs were conducted following the procedure described below. In a typical method, 50 mg of D–glucose and 50 mg of the yeast were weighed in a 10 mL sized volumetric flask and then 5 mL of M.Q. water (adjusted to pH 4.5) was added to the flask. The phosphate buffer was not considered here as the media of fermentation to eliminate any probable interactions of the NMs with the electrolytes. The content within the flask was then mixed well and placed in the hot water bath set @ $43^0 \pm 0.5^0$C while waiting for 5 min (incubation period) to equilibrate to the same temperature of the solution in the flask prior to the commencement of the fermentation process. One end of the transparent PTFE tubing was attached with the needle inserted through the cork at the volumetric flask and the other end of the tube was inserted inside a burette that was prefilled with a dye solution while the inverted burette (upside down) was placed in a beaker containing the dye solution.

The whole experimental set–up is schematically illustrated in Figure–7.3 mimicking the modified version of the Warburg flasks/manometer. Here, a MO solution of an arbitrary conc. was placed inside the burette (and the burette–bath as well) for better visibility of the lower meniscus while recording the measurement of the liquid's height inside the burette.

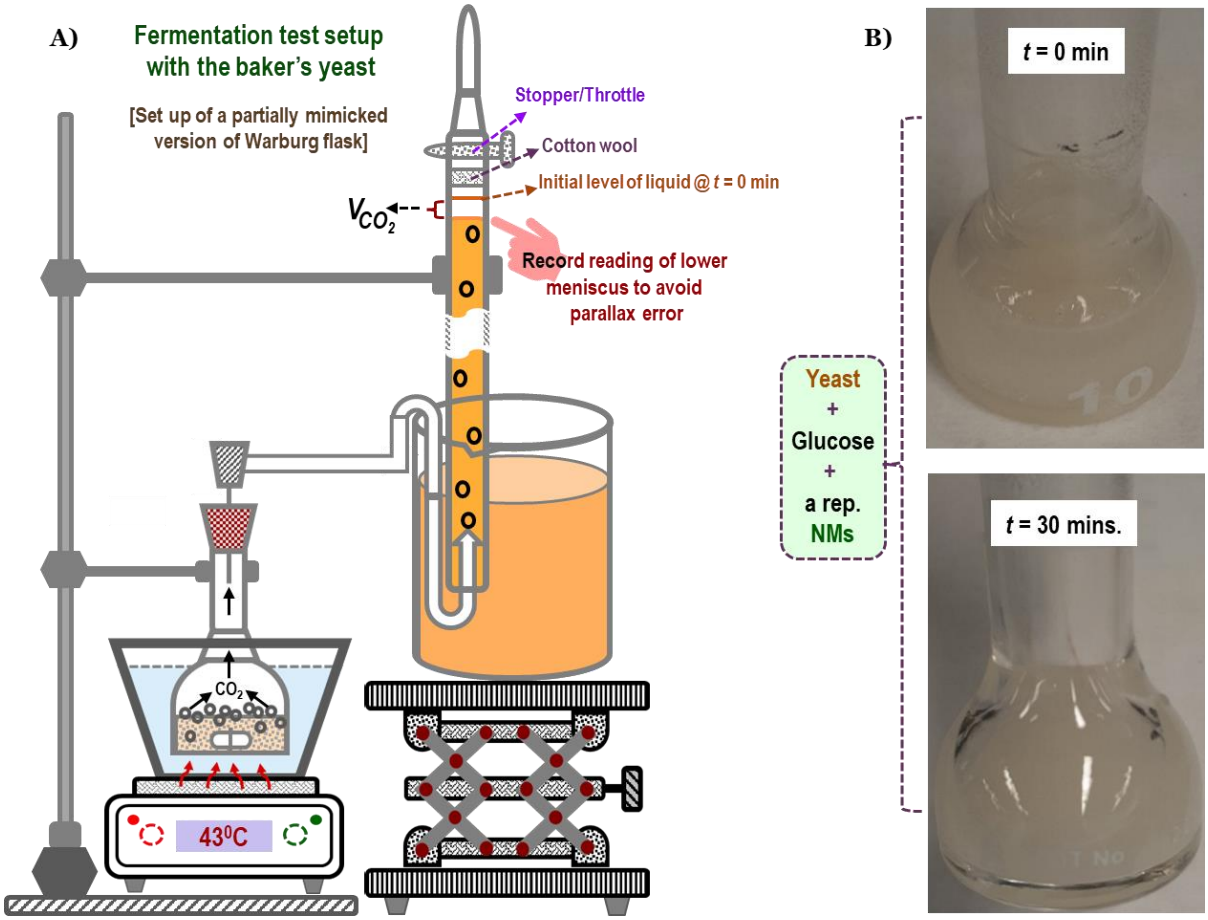


Figure 7.3: A) *Set–up for yeast fermentation experiments which apparently is similar to the mimicked & modified version of the Warburg flask. An arbitrary conc. of MO solution was used as the colored liquid for the ease of measuring the liquid level inside the burette.* ***B)*** *The 10 mL volumetric flasks in which the yeast's fermentation experiments were conducted. The two flasks are @ t= 0 mins (when the temperature was 43^{0}C, the yeast got dissolved) and t= 30 mins, where @ t= 30 mins, most of the yeasts were found precipitated at the bottom (not clearly visible from the image).*

Each of the fermentation experiments was conducted for 30 min and the volume of CO_2 (V_{CO2}) released was recorded at every 2 min time interval. The cumulative V_{CO2} were then plotted against the time duration and the slope of the individual plots were used to compare the fermentation rate as well as the volume fraction of the released CO_2 between the various NMs.

In this experimental study, the NCC™ was considered as the negative control and Questran™ (Cholestyramine) was used as the positive control for the cationic NMs (Q–NMs) tested for the yeast mediated fermentation. The control study was conducted only with glucose and yeast, whereas for the positive/negative controls or the experimental Q–NMs, a final concentration of 100 ppm (100 μg/mL) was used based on the antibacterial studies[276–283] of different compounds or nanocomposites or PS-based NPs or metal NPs.

7.5 Results and discussion

The plot of the volume of CO_2 released due to fermentation against the time duration was linear up to 30 min as the endpoint, one of the examples of such a plot is illustrated from the combined plots of all the NMs shown in Figure–7.4.

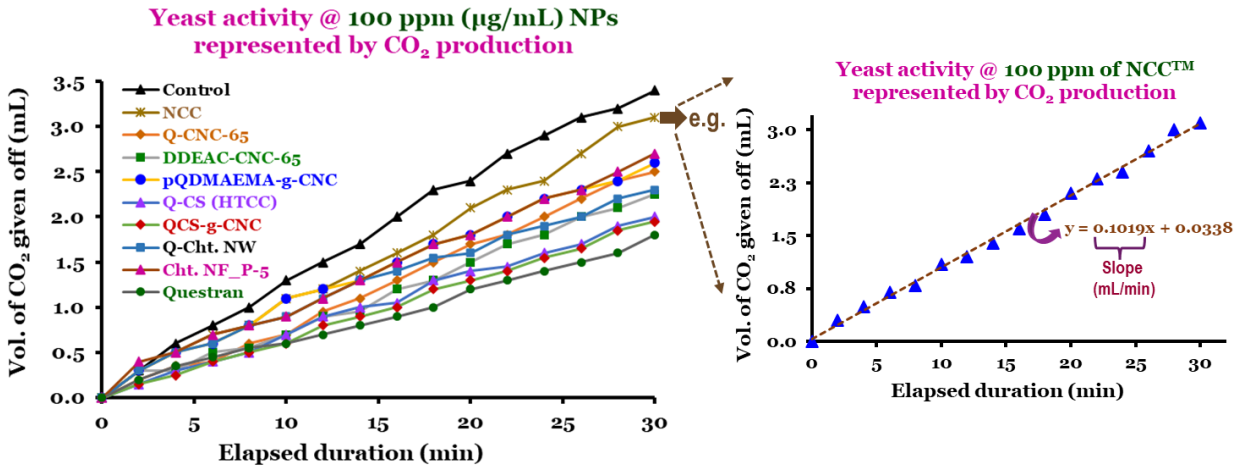


Figure 7.4: *The released CO_2* ***vs*** *time (mins) plots for the control, positive & negative controls, and the experimental NMs obtained from the yeast mediated fermentation of glucose. Except the control experiment, in all the other experiments (positive & negative control, and the non–control experiments with the NMs) the concentration of the NMs in the flasks was 100 ppm.*

From Figure–7.4, it is evident that the highest amount of CO_2 released (3.4 mL) at 30 min was observed for the control experiment where no cationic NPs were added, only glucose and yeast were present inside the flask. For the negatively charged NPs, i.e., NCC™, the V_{CO2} was recorded as approx. ~ 3.1 mL and this small decrease of CO_2 released compared to the control might be due to the partial inhibition of the glucose influx due to the adsorption of NCC™ on the yeast cells driven by non–ionic interaction. Thus, the diffusion of glucose from the bulk into the cells was inhibited leading to the proportional reduction in the rate of fermentation. Table 7.1 provides a summary of the impact of the NMs on the production of CO_2 by the yeast.

Table 7.1: The determined experimental parameters obtained from the recorded V_{CO2} till 30 mins intervals during the fermentation experiments. For the volume fraction and % inhibition calculations, the control was considered as 1 and 0 respectively, and the same parameters for the other NPs were calculated based on the corresponding data of the control.

NPs Name	V_{CO2} (mL) @ 30 min	Fraction of V_{CO2} (mL) @ 30 min	Slope from plot (mL/min)	Slope (mL/hr)	Relative % inhibition of yeast activity
Control	3.4	1.00	0.1141	6.85	0
NCC™	3.1	0.91	0.1019	6.11	8.8
Q-CNC$_6$	2.5	0.74	0.0854	5.12	26.5
Q-C$_{12}$-CNC$_6$	2.3	0.66	0.0743	4.46	33.8
Brush-CNC	2.6	0.76	0.0839	5.03	23.5
Q-CS	2.0	0.59	0.0664	3.98	41.2
QCS-g-CNC	2.0	0.57	0.0649	3.89	42.6
Q-Cht.NW$_a$	2.3	0.68	0.0731	4.39	32.4
Cht.NF-P$_5$	2.7	0.79	0.0853	5.12	20.6
Questran™	1.8	0.53	0.0556	3.34	47.1

Following a similar trend, however, sharp reductions were observed for the fermentation experiments when cationic NPs or polymers were used (Figure–7.4 and Table 7.1). As such, the lowest amount (1.8 mL) of CO_2 released was recorded for the positive control, the cholestyramine (Questran^{TM}) here. The results on the reduction of released CO_2 up to 30 min time interval were indicative of the probable partial (or complete) blockage of pores present on the cell wall of the yeast due to the strong physicochemical adsorption of the cationic NPs (Q–NPs).

Figure –7.5 illustrates the rate of fermentation, represented by the volume fraction of the released CO_2 and the relative % inhibition of the yeast cell's activity for the NPs used in the yeast fermentation tests.

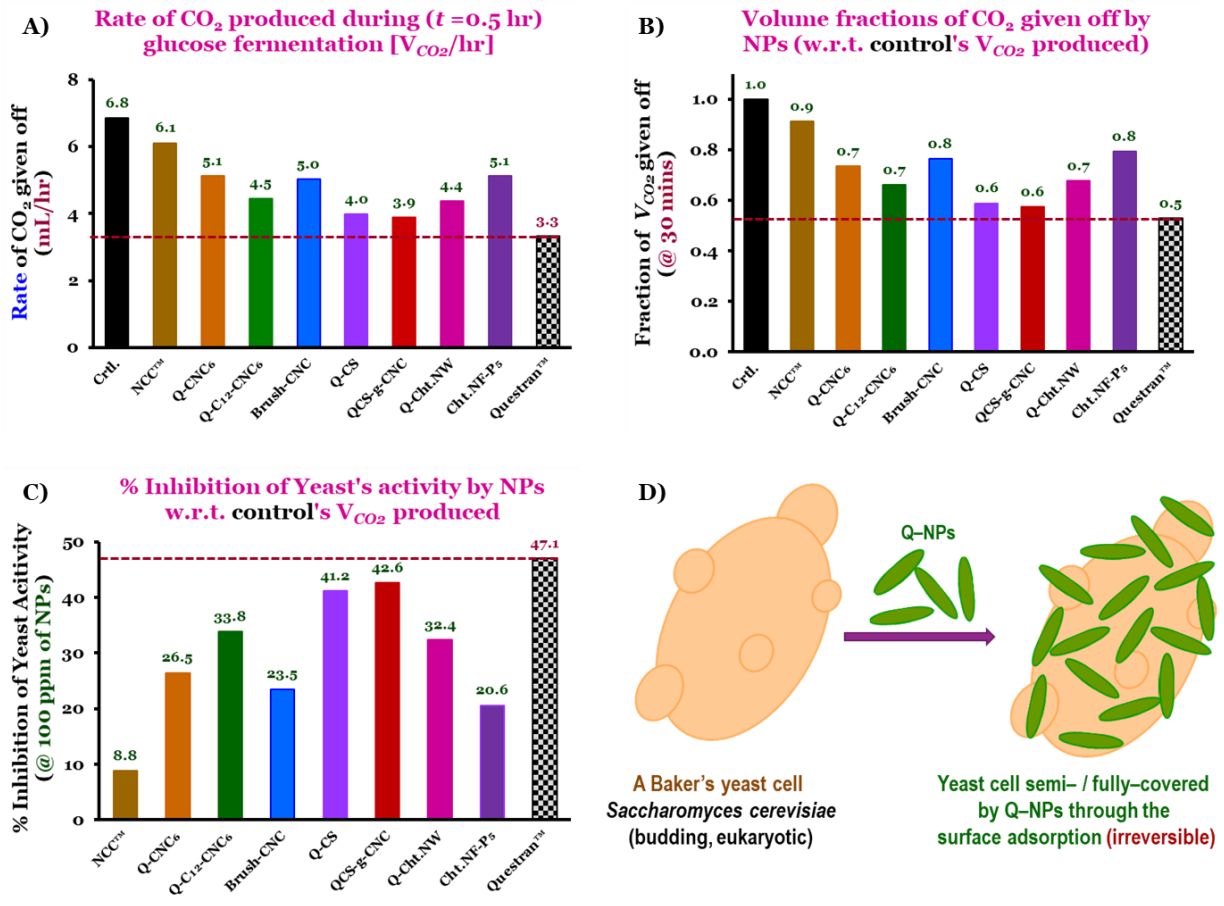


Figure 7.5: A) *Rate of release of CO_2 —, and* ***B)*** *Volume fractions of released CO_2 — due to the yeast mediated fermentation of glucose by the control, positive (Questran™) and negative controls (NCC™), and the Q–NPs.* ***C)*** *Relative % inhibition of yeast cells' activities leading to reduced fermentation rate, and* ***D)*** *Schematic of yeast cell's inhibition by the Q–NPs.*

From the rate of fermentation (CO_2 released) plot, it is evident that the commercially available BAS cholestyramine (Questran^{TM}, the positive control in this experimental design), with a well-known safety profile, displayed the highest reduction in the rate of fermentation among all the other Q–NPs. Similar trends were evident from the plot where the volume fractions of the CO_2 were compared. Due to the irreversible binding or surface adsorptions of the NMs with the yeast cells (as shown in Figure–7.5 D), several scenarios could be possible: (a) most of the glucose molecules were inhibited from the yeast cells and the influx of the glucose molecules into the yeast cells were reduced, (b) the viability of the yeasts were impacted by the adsorbed NMs, and (c) the NMs break the yeast walls and kill the yeast cells. Consequently, the rate of fermentation was reduced. The results of the experiments indicated that such inhibition of the yeast cells was highest for the established BAS, cholestyramine (Figure–7.5 C). The Q–CS and the QCS–g–CNC was within the same range for relative % of inhibition of the yeast cells activity, and they were found slightly below the % inhibition of cholestyramine. All the other Q–NPs displayed lower degrees of % inhibition than cholestyramine.

All these results led us to conclude that the natural and sustainable NMs developed in this study for use as BAS exhibited lesser inhibition of the yeast cells' activity than the commercial BAS, cholestyramine. Overall, it could be concluded that the developed NMs should not be harmful to human cells as well as overall health. However, further studies with the live cell culture (human cells) should be conducted to further confirm these findings.

Chapter 8

8.1 Conclusions and Future directions

8.1.1 Conclusions

Diet-induced obesity (DIO) and raised blood cholesterol (hypercholesterolemia) are interrelated and cause fetal health consequences if persist as chronic conditions and are left untreated. Among the pharmacological interventions for treating hypercholesterolemia, sequestration of the bile acids/salts (BAs/BSs) using bile acid sequestrants (BAS) is one of the treatment options. This Ph.D. study was designed to develop NMs from natural and sustainable resources for an application that utilized these NMs for reducing plasma cholesterol by directly sequestering the BAs/BSs from the GIT. Simultaneously, due to the removal of the BAs/BSs, such NMs should also have the capabilities to stop or reduce the progressive DIO.

Throughout this Ph.D. study, cellulose nanocrystals (CNC), the most abundant naturally derived sustainable biomaterial on earth, were modified with different chemical compounds possessing quaternary ammonium groups (QAGs) or with polymers. Hydrophilic, hydrophobic, or brush–like CNCs or chitosan–modified CNCs were prepared for evaluation. The second most naturally abundant polysaccharide, the chitin, was also modified to obtain a library of nanofibers (NFs) possessing various lengths. The nanowhiskers/nanocrystals (NWs/NCs) of chitin were also derived from the chitin and modified with QAG containing molecules. All these permanently cationic NM systems (except the chitin–NFs, which were not permanently cationic) were then evaluated for their efficiencies to bind anionic species like

the organic dye, methyl orange (MO) or the sodium cholate (SC), one of the primary (1^0) BAs in the human body.

The binding capacities were found to be moderate to significantly higher for the NMs, and most of the NMs showed greater adsorption capacities for the SC than for the MO. We observed that the following factors control the binding of the NMs to SCs:

(a) cationic charges on the NPs surfaces,

(b) shape/morphology of the NPs (e.g., the brush–CNC),

(c) hydrophobic moiety on the NPs,

(d) other functional groups capable of establishing H–bonds with the analyte/ligands,

(e) aqueous dispersibilities /solubilities of the NPs,

(f) apparent viscosities of the NP dispersions, and

(g) size of NPs

The above factors contributed to the physicochemical interaction and binding with the SC or MO. The results also indicate that the presence of the inherent primary amino–groups (PAGs, —NH_2) on the NPs, such as for the chitosan or chitin–based NPs was advantageous to impart pH–responsive properties to the NPs that enhanced their cationic characteristics at the optimum pH conditions.

Methyl orange (MO) was initially used to evaluate the efficiencies of the NMs as a model compound since its concentration could be readily determined from UV–Vis spectroscopy, and there is a lack of a robust tool for BA detection. The removal of MO from an aqueous sample from the physicochemical adsorption onto the NPs indicated that such NPs

could be utilized for effluent treatment in the wastewater system. The NMs could be utilized for effluent treatment in the pharmaceutical industry.

A polymeric membrane ion-selective electrode (ISE sensor) was fabricated for the detection of sodium cholate in the aqueous solutions. After extensive quality control studies on the sensor to optimize its sensing capabilities, it was found to be working for the detection of SCs. Thus, the sensor was utilized to quantify the unbound SC from the post–BATs (batch adsorption tests) samples conducted with selected NMs. The Q_{max} determined for the selected NMs using the ISE sensor was promising and the conclusions from these studies indicated that the NMs produced in this study could bind SC molecules with performance better than cholestyramine. The Q_{max} results suggested that the NMs have the potential to reduce the raised plasma cholesterol by removing the BAs/BSs from the GIT.

Lastly, the safety of the NMs was evaluated by conducting the yeast fermentation tests and compared with cholestyramine. The results indicated that the NMs displayed a lower rate of fermentation than cholestyramine due to the lower inhibition of the yeast cells. We concluded that all the NMs produced in this study are less toxic than cholestyramine and are safe for human application in hypercholesterolemia treatment.

Overall, the natural and sustainable NMs could be modified to produce cationic NPs, where these NPs offer tremendous potential for use as BAS. These NPs can be considered as the naturally derived alternative to cholestyramine. However, for the precise efficacy of the NPs, *in vivo* studies should be conducted with appropriate animal models followed by clinical trials.

8.1.2 Future directions

The NMs were evaluated for their adsorption efficiencies with only trihydroxy bile acid (designated as **sodium cholate, SC**). There are other primary (chenodeoxy cholic acid) and secondary (deoxycholic acid, lithocholic acid) bile acids, and their corresponding conjugated salts present in the human body where the NPs' efficacies were not determined. Such study should be conducted in the future. Furthermore, the specificities of adsorption by the NPs were not determined for the BA/BSs or from mixtures of BAs/BSs which should also be conducted to simulate the condition in the human body. The *in vivo* efficacy of the bile acid sequestrants (BASs) depends on how strongly they can bind free BA molecules to form BAS–BA/BS complexes, and then excreted through the feces. During this Ph.D. study, the strength of binding/adsorption of the BAs/BSs molecules on the NPs was not established by conducting desorption studies. Thus, the desorption studies for all the BAs/BSs should be conducted for these NMs.

The effects of C–12 alky chain were only evaluated for one NP and significant improvement in the adsorption of SC (as well as for MO) was observed. Thus, the presence of such hydrophobic moiety should be considered for several NPs, especially for the Q–CNC_{MCC}, Q–CS, QCS–g–CNCs, and the Cht.NWs, to evaluate if there is an expected improvement of efficacy on the physicochemical adsorption of the targeted analyte (SC). Furthermore, the Cht.NFs that possess surface primary amino groups, PAGs (—NH_2 groups) were not considered for quaternization in this study. Thus, the quaternization of Cht.NFs with molecules containing the quaternary ammonium groups, QAG (GTMAC) or the molecules possessing QAG + C–12 chains (DDEAC) should be investigated regarding their efficacy as BASs.

Along with the evaluations of the presence of hydrophobe on the NMs as the BAS, the different morphologies of the NMs could be considered. This doctoral study concluded that NMs having a 'bottle brush like' structure (the polymeric–CNCs: the pQDMAEMA–g–CNCs) or the 'block co–polymer type' structure, (for example, the quaternized–chitosan modified CNCs: the QCS–g–CNCs, also denoted as the QCS–g–QCS) possessed higher capabilities to bind/sequester the bile salts/acids (BAs/BSs). The effects of other morphological shapes[29], for example hyperbranched like the dendrimers, cross–linked NMs, or the star–shaped block copolymer[29] modified NMs could be considered for evaluation on their efficacies as bile acid sequestrants, BASs. Additionally, the polyethylene imine (PEI)[292–295] modified–CNC or PEI–coupled chitin NWs (PEI–g–Cht.NWs) could also be considered for evaluation as the BASs.

The effects of factors such as the presence of enzymes, food contents & nutrients, gut microflora etc. on the binding or adsorption of BA onto the NPs' surfaces were not evaluated. Such evaluations are only possible through the *in vivo* studies structured and designed on a suitable high-fat meal-induced obese animal model. Thus, the *in vivo* studies are necessary to determine the efficacy of the NPs for raised plasma cholesterol reduction in humans. Through such structured *in vivo* studies, the efficacy of the NPs for the reduction or cessation of DIO could be determined from the reduction of cholesterol. Lastly, the biosafety evaluation could be conducted from the *in vivo* studies for the NPs.

The obtained Q_{max} values for selected NMs from three different techniques, namely through the conductometric measurement, UV–Vis technique (colored analogue of SC), and the sensor, showed moderate to high variations. Thus, the Q_{max} values for the NMs with SC

should be determined and crossed checked via an established and widely used method such as the Total Bile Acid (TBA) Enzyme kit or through the HPLC.

The in-house sensor used in the quantification of SC was a prototype and improvement to the design and fabrication should be considered. Further research should be conducted to improve the membrane construction and reliability in order to eliminate the EMF drifting, loss of sensitivity, frequent changing of inner solutions, improvement in the specificity of the membrane from accessory ions and producing one membrane for all BAs/BSs. The sensor should be miniaturized so that it should be implemented to continuously monitor the concentration of bile salts using a microfluidic device.

References

1. Mohammadzadeh V, Barani M, Amiri MS, et al. Applications of plant-based nanoparticles in nanomedicine: A review. *Sustain Chem Pharm*. 2022;25(September 2021):100606. doi:10.1016/j.scp.2022.100606
2. García-Álvarez R, Vallet-Regí M. Bacteria and cells as alternative nano-carriers for biomedical applications. *Expert Opin Drug Deliv*. 2022;19(1):103-118. doi:10.1080/17425247.2022.2029844
3. Raja IS, Kang MS, Kim KS, Jung YJ. Two-Dimensional Theranostic Nanomaterials in. *Cancers (Basel)*. 2020;12:1657.
4. Perumal AB, Nambiar RB, Moses JA, Anandharamakrishnan C. Nanocellulose: Recent trends and applications in the food industry. *Food Hydrocoll*. 2022;127(March 2021):107484. doi:10.1016/j.foodhyd.2022.107484
5. Abdalkarim SYH, Chen LM, Yu HY, et al. Versatile nanocellulose-based nanohybrids: A promising-new class for active packaging applications. *Int J Biol Macromol*. 2021;182:1915-1930. doi:10.1016/j.ijbiomac.2021.05.169
6. Nasseri R, Deutschman CP, Han L, Pope MA, Tam KC. Cellulose nanocrystals in smart and stimuli-responsive materials: a review. *Mater Today Adv*. 2020;5:100055. doi:10.1016/j.mtadv.2020.100055
7. Tang J, Sisler J, Grishkewich N, Tam KC. Functionalization of cellulose nanocrystals for advanced applications. *J Colloid Interface Sci*. 2017;494:397-409. doi:10.1016/j.jcis.2017.01.077
8. Grishkewich N, Mohammed N, Tang J, Tam KC. Recent advances in the application of cellulose nanocrystals. *Curr Opin Colloid Interface Sci*. 2017;29:32-45. doi:10.1016/j.cocis.2017.01.005
9. Habibi Y. Key advances in the chemical modification of nanocelluloses. *Chem Soc Rev*. 2014;43(5):1519-1542.
10. Bakshi MS. Impact of nanomaterials on ecosystems: Mechanistic aspects in vivo. *Environ Res*. 2020;182(December 2019):109099. doi:10.1016/j.envres.2019.109099

11. Diallo MS, Fromer NA, Jhon MS. Nanotechnology for sustainable development: Retrospective and outlook. *J Nanoparticle Res*. 2013;15(11). doi:10.1007/s11051-013-2044-0
12. Chiang JYL. Bile acid metabolism and signaling. *Compr Physiol*. 2013;3(3):1191-1212. doi:10.1002/cphy.c120023
13. Out C, Groen AK, Brufau G. Bile acid sequestrants: More than simple resins. *Curr Opin Lipidol*. 2012;23(1):43-55. doi:10.1097/MOL.0b013e32834f0ef3
14. Šarenac TM, Mikov M. Bile acid synthesis: From nature to the chemical modification and synthesis and their applications as drugs and nutrients. *Front Pharmacol*. 2018;9(SEP):1-22. doi:10.3389/fphar.2018.00939
15. Bestehorn K, Smolka W, Pittrow D, Schulte H, Assmann G. Atherogenic dyslipidemia as evidenced by the lipid triad: prevalence and associated risk in statin-treated patients in ambulatory care. *Curr Med Res Opin*. 2010;26(12):2833-2839. doi:10.1185/03007995.2010.532088
16. Feng Y, Li Q, Ou G, Yang M, Du L. Bile acid sequestrants: A review of mechanism and design. *J Pharm Pharmacol*. 2021;73(7):855-861. doi:10.1093/jpp/rgab002
17. Padró T, Cubedo J, Camino S, et al. Detrimental Effect of Hypercholesterolemia on High-Density Lipoprotein Particle Remodeling in Pigs. *J Am Coll Cardiol*. 2017;70(2):165-178. doi:10.1016/j.jacc.2017.05.018
18. Mozaffarian D. Dietary and Policy Priorities for Cardiovascular Disease, Diabetes, and Obesity. *Circulation*. 2016;133(2):187-225. doi:10.1161/CIRCULATIONAHA.115.018585
19. Pouliou T, Elliott SJ. An exploratory spatial analysis of overweight and obesity in Canada. *Prev Med (Baltim)*. 2009;48(4):362-367. doi:10.1016/j.ypmed.2009.01.017
20. Ferrières J. Hypercholesterolaemia and coronary artery disease: A silent killer with several faces. *Arch Cardiovasc Dis*. 2019;112(2):75-78. doi:10.1016/j.acvd.2018.11.007
21. Raal FJ, Hovingh GK, Catapano AL. Familial hypercholesterolemia treatments: Guidelines and new therapies. *Atherosclerosis*. 2018;277:483-492.

doi:10.1016/j.atherosclerosis.2018.06.859

22. Hopkins PN. Familial hypercholesterolemia - Improving treatment and meeting guidelines. *Int J Cardiol*. 2003;89(1):13-23. doi:10.1016/S0167-5273(02)00420-5
23. Paquette M. Dyslipidemias. In: *Compendium of Therapeutic Choices*. ; 2021:1-23.
24. Zhang LH, Janout V, Renner JL, Uragami M, Regen SL. Enhancing the "stickiness" of bile acids to cross-linked polymers: A bioconjugate approach to the design of bile acid sequestrants. *Bioconjug Chem*. 2000;11(3):397-400. doi:10.1021/bc990151v
25. William Insull J. Clinical utility of bile acid sequestrants in the treatment of dyslipidemia: a scientific review. *South Med J*. 2006;99(3):257-274. https://go.galegroup.com/ps/anonymous?id=GALE%7CA144298829&sid=googleScholar&v=2.1&it=r&linkaccess=abs&issn=00384348&p=AONE&sw=w
26. Mazidi M, Rezaie P, Karimi E, Kengne AP. The effects of bile acid sequestrants on lipid profile and blood glucose concentrations: A systematic review and meta-analysis of randomized controlled trials. *Int J Cardiol*. 2017;227:850-857. doi:10.1016/j.ijcard.2016.10.011
27. Bays HE, Goldberg RB. The "forgotten" bile acid sequestrants: Is now a good time to remember? *Am J Ther*. 2007;14(6):567-580. doi:10.1097/MJT.0b013e31815a69fc
28. Schaap FG, Trauner M, Jansen PLM. Bile acid receptors as targets for drug development. *Nat Rev Gastroenterol Hepatol*. 2014;11(1):55-67. doi:10.1038/nrgastro.2013.151
29. Heřmánková E, Žák A, Poláková L, Hobzová R, Hromádka R, Širc J. Polymeric bile acid sequestrants: Review of design, in vitro binding activities, and hypocholesterolemic effects. *Eur J Med Chem*. 2018;144:300-317. doi:10.1016/j.ejmech.2017.12.015
30. Staels B, Fonseca VA. Bile acids and metabolic regulation: mechanisms and clinical responses to bile acid sequestration. *Diabetes Care*. 2009;32 Suppl 2. doi:10.2337/dc09-s355
31. Staels B, Handelsman Y, Fonseca V. Bile acid sequestrants for lipid and glucose control. *Curr Diab Rep*. 2010;10(1):70-77. doi:10.1007/s11892-009-0087-5
32. Varma K, Gopi S. Biopolymers and their role in medicinal and pharmaceutical

applications. In: *Biopolymers and Their Industrial Applications*. Elsevier; 2021:175-191. doi:10.1016/B978-0-12-819240-5.00007-9

33. Gopi S, Amalraj A, Sukumaran NP, Haponiuk JT, Thomas S. Biopolymers and Their Composites for Drug Delivery: A Brief Review. *Macromol Symp*. 2018;380(1):1-14. doi:10.1002/masy.201800114
34. Joye IJ, McClements DJ. Biopolymer-based nanoparticles and microparticles: Fabrication, characterization, and application. *Curr Opin Colloid Interface Sci*. 2014;19(5):417-427. doi:10.1016/j.cocis.2014.07.002
35. Wróblewska-Krepsztul J, Rydzkowski T, Michalska-Pożoga I, Thakur VK. Biopolymers for biomedical and pharmaceutical applications: Recent advances and overview of alginate electrospinning. *Nanomaterials*. 2019;9(3):7-9. doi:10.3390/nano9030404
36. Torres FG, Troncoso OP, Pisani A, Gatto F, Bardi G. Natural polysaccharide nanomaterials: An overview of their immunological properties. *Int J Mol Sci*. 2019;20(20). doi:10.3390/ijms20205092
37. Neffe AT, Wischke C, Racheva M, Lendlein A. Progress in biopolymer-based biomaterials and their application in controlled drug delivery. *Expert Rev Med Devices*. 2013;10(6):813-833. doi:10.1586/17434440.2013.839209
38. Jummaat F, Yahya EB, Abdul Khalil HPS, et al. The role of biopolymer-based materials in obstetrics and gynecology applications: A review. *Polymers (Basel)*. 2021;13(4):1-21. doi:10.3390/polym13040633
39. Islam MS, Chen L, Sisler J, Tam KC. Cellulose nanocrystal (CNC)-inorganic hybrid systems: Synthesis, properties and applications. *J Mater Chem B*. 2018;6(6):864-883. doi:10.1039/c7tb03016a
40. Habibi Y, Lucia LA, Rojas OJ. Cellulose Nanocrystals : Chemistry , Self-Assembly , and Applications. *Chem Rev*. 2010;110(6):3479-3500. doi:10.1007/s10570-006-9061-4
41. Peng BL, Dhar N, Liu HL, Tam KC. Chemistry and applications of nanocrystalline cellulose and its derivatives: A nanotechnology perspective. *Can J Chem Eng*. 2011;89(5):1191-1206. doi:10.1002/cjce.20554

42. Delepierre G, Vanderfleet OM, Niinivaara E, Zakani B, Cranston ED. Benchmarking Cellulose Nanocrystals Part II: New Industrially Produced Materials. *Langmuir*. 2021;37(28):8393-8409. doi:10.1021/acs.langmuir.1c00550
43. Reid MS, Villalobos M, Cranston ED. Benchmarking Cellulose Nanocrystals: From the Laboratory to Industrial Production. *Langmuir*. 2017;33(7):1583-1598. doi:10.1021/acs.langmuir.6b03765
44. Trache D, Hussin MH, Haafiz MKM, Thakur VK. Recent progress in cellulose nanocrystals: Sources and production. *Nanoscale*. 2017;9(5):1763-1786. doi:10.1039/c6nr09494e
45. Pakizeh M, Moradi A, Ghassemi T. Chemical extraction and modification of chitin and chitosan from shrimp shells. *Eur Polym J*. 2021;159(August):110709. doi:10.1016/j.eurpolymj.2021.110709
46. Sirajudheen P, Poovathumkuzhi NC, Vigneshwaran S, Chelaveettil BM, Meenakshi S. Applications of chitin and chitosan based biomaterials for the adsorptive removal of textile dyes from water — A comprehensive review. *Carbohydr Polym*. 2021;273(August):118604. doi:10.1016/j.carbpol.2021.118604
47. Anitha A, Sowmya S, Kumar PTS, et al. Chitin and chitosan in selected biomedical applications. *Prog Polym Sci*. 2014;39(9):1644-1667. doi:10.1016/j.progpolymsci.2014.02.008
48. Parhi R. Drug delivery applications of chitin and chitosan: a review. *Environ Chem Lett*. 2020;18(3):577-594. doi:10.1007/s10311-020-00963-5
49. Kostag M, El Seoud OA. Sustainable biomaterials based on cellulose, chitin and chitosan composites - A review. *Carbohydr Polym Technol Appl*. 2021;2(April):100079. doi:10.1016/j.carpta.2021.100079
50. Hua Y, Wei Z, Xue C. Chitosan and its composites-based delivery systems: advances and applications in food science and nutrition sector. *Crit Rev Food Sci Nutr*. 2021;0(0):1-20. doi:10.1080/10408398.2021.2004992
51. Sogias IA, Williams AC, Khutoryanskiy V V. Why is chitosan mucoadhesive? *Biomacromolecules*. 2008;9(7):1837-1842. doi:10.1021/bm800276d

52. Ways TMM, Lau WM, Khutoryanskiy V V. Chitosan and its derivatives for application in mucoadhesive drug delivery systems. *Polymers (Basel)*. 2018;10(3). doi:10.3390/polym10030267
53. DeLoid GM, Sohal IS, Lorente LR, et al. Reducing Intestinal Digestion and Absorption of Fat Using a Nature-Derived Biopolymer: Interference of Triglyceride Hydrolysis by Nanocellulose. *ACS Nano*. 2018;12(7):6469-6479. doi:10.1021/acsnano.8b03074
54. Dias OAT, Konar S, Leão AL, Yang W, Tjong J, Sain M. Current State of Applications of Nanocellulose in Flexible Energy and Electronic Devices. *Front Chem*. 2020;8(May). doi:10.3389/fchem.2020.00420
55. Shen J, Yang X, Sun X, et al. Amino-functionalized cellulose: a novel and high-efficiency scavenger for sodium cholate sorption. *Cellulose*. 2020;27(7):4019-4028. doi:10.1007/s10570-020-03066-0
56. J.G. Marin J, I.R. Macias R, Briz O, M. Banales J, J. Monte M. Bile Acids in Physiology, Pathology and Pharmacology. *Curr Drug Metab*. 2015;17(1):4-29. doi:10.2174/1389200216666151103115454
57. Chiang JYL. Bile acids: Regulation of synthesis. *J Lipid Res*. 2009;50(10):1955-1966. doi:10.1194/jlr.R900010-JLR200
58. Monte MJ, Marin JJ, Antelo A, Vazquez-Tato J. Bile acids: Chemistry, physiology, and pathophysiology. *World J Gastroenterol*. 2009;15(7):804. doi:10.3748/wjg.15.804
59. Hofmann AF, Hagey LR. Bile acids: Chemistry, pathochemistry, biology, pathobiology, and therapeutics. *Cell Mol Life Sci*. 2008;65(16):2461-2483. doi:10.1007/s00018-008-7568-6
60. Urdaneta V, Casadesús J. Interactions between bacteria and bile salts in the gastrointestinal and hepatobiliary tracts. *Front Med*. 2017;4(OCT):1-13. doi:10.3389/fmed.2017.00163
61. Ma H, Patti ME, Endocrinologist A. Bile acids, obesity, and the metabolic syndrome. *Best Pract Res Clin Gastroenterol*. 2014;28(4):573-583. doi:10.1016/j.bpg.2014.07.004
62. Wahlström A, Sayin SI, Marschall HU, Bäckhed F. Intestinal Crosstalk between Bile Acids and Microbiota and Its Impact on Host Metabolism. *Cell Metab*. 2016;24(1):41-

50. doi:10.1016/j.cmet.2016.05.005

63. Martinot E, Sèdes L, Baptissart M, et al. Bile acids and their receptors. *Mol Aspects Med*. 2017;56:2-9. doi:10.1016/j.mam.2017.01.006

64. Hofmann AF. The enterohepatic circulation of bile acids in mammals: Form and functions. *Front Biosci*. 2009;14(7):2584-2598. doi:10.2741/3399

65. Cai JS, Chen JH. The Mechanism of Enterohepatic Circulation in the Formation of Gallstone Disease. *J Membr Biol*. 2014;247(11):1067-1082. doi:10.1007/s00232-014-9715-3

66. Molinaro A, Wahlström A, Marschall HU. Role of Bile Acids in Metabolic Control. *Trends Endocrinol Metab*. 2018;29(1):31-41. doi:10.1016/j.tem.2017.11.002

67. Grant SM, Demorrow S. Bile acid signaling in neurodegenerative and neurological disorders. *Int J Mol Sci*. 2020;21(17):1-25. doi:10.3390/ijms21175982

68. Stubbs, D. W. (Donald William)., Brown AM. *Medical Physiology*. 3rd ed. Wiley; 1983.

69. Mancini GBJ, Hegele RA, Leiter LA. Dyslipidemia. *Can J Diabetes*. 2018;42:S178-S185. doi:10.1016/j.jcjd.2017.10.019

70. HONDA Y, NAKANO M. Studies on Adsorption Characteristics of Bile Acids and Methotrexate to a New Type of Anion-Exchange Resin, Colestimide. *Chem Pharm Bull*. 2000;48(7):978-981. doi:10.1248/cpb.48.978

71. Mendonça P V., Serra AC, Silva CL, Simões S, Coelho JFJ. Polymeric bile acid sequestrants - Synthesis using conventional methods and new approaches based on “controlled”/living radical polymerization. *Prog Polym Sci*. 2013;38(3-4):445-461. doi:10.1016/j.progpolymsci.2012.09.004

72. Polomoscanik SC, Holmes-Farley SR, Petersen JS, Sacchiero RJ, Dhal PK. Hydrophobically modified poly(allylamine) hydrogels containing internal quaternary ammonium groups as cholesterol lowering agents: Synthesis, characterization, and biological studies. *J Macromol Sci Part A Pure Appl Chem*. 2012;49(12):1011-1021. doi:10.1080/10601325.2012.728460

73. Debele TA, Mekuria SL, Tsai HC. Polysaccharide based nanogels in the drug delivery system: Application as the carrier of pharmaceutical agents. *Mater Sci Eng C*.

2016;68:964-981. doi:10.1016/j.msec.2016.05.121

74. Islam MS, Chen L, Sisler J, Tam KC. Cellulose nanocrystal (CNC)–inorganic hybrid systems: synthesis, properties and applications. *J Mater Chem B*. 2018;6(6):864-883. doi:10.1039/C7TB03016A

75. Zhu W, Liu L, Liao Q, et al. Functionalization of cellulose with hyperbranched polyethylenimine for selective dye adsorption and separation. *Cellulose*. 2016;23(6):3785-3797. doi:10.1007/s10570-016-1045-4

76. Zhu X, Wen Y, Cheng D, Li C, An X, Ni Y. Cationic amphiphilic microfibrillated cellulose (MFC) for potential use for bile acid sorption. *Carbohydr Polym*. 2015;132:598-605. doi:10.1016/j.carbpol.2015.06.063

77. Zhu X, Wen Y, Wang L, et al. Binding of sodium cholate in vitro by cationic microfibrillated cellulose. *Ind Eng Chem Res*. 2014;53(48):18508-18513. doi:10.1021/ie503909g

78. Hyun JK, White PJ. In vitro bile-acid binding and fermentation of high, medium, and low molecular weight β-glucan. *J Agric Food Chem*. 2010;58(1):628-634. doi:10.1021/jf902508t

79. Gao J, Lin L, Sun B, Zhao M. Comparison Study on Polysaccharide Fractions from Laminaria japonica: Structural Characterization and Bile Acid Binding Capacity. *J Agric Food Chem*. 2017;65(44):9790-9798. doi:10.1021/acs.jafc.7b04033

80. Huang K, Du B, Xu B. Alterations in physicochemical properties and bile acid binding capacities of dietary fibers upon ultrafine grinding. *Powder Technol*. 2018;326:146-150. doi:10.1016/j.powtec.2017.12.024

81. Kazlauske J, Ramanauskiene K, Liesiene J. BINDING OF BILE ACIDS BY CELLULOSE-BASED CATIONIC ADSORBENTS. *Cellul Chem Technol*. 2014;48(1-2):11-17.

82. Barsanti L, Passarelli V, Evangelista V, Frassanito AM, Gualtieri P. Chemistry, physico-chemistry and applications linked to biological activities of β-glucans. *Nat Prod Rep*. 2011;28(3):457-466. doi:10.1039/c0np00018c

83. Šantek B, Friehs K, Lotz M, Flaschel E. Production of paramylon, a β-1,3-glucan, by

heterotrophic growth of Euglena gracilis on potato liquor in fed-batch and repeated-batch mode of cultivation. *Eng Life Sci*. 2012;12(1):89-94. doi:10.1002/elsc.201100025

84. Shibakami M, Shibata K, Akashi A, et al. Creation of Straight-Chain Cationic Polysaccharide-Based Bile Salt Sequestrants Made from Euglenoid β-1,3-Glucan as Potential Antidiabetic Agents. *Pharm Res*. 2019;36(1):1-11. doi:10.1007/s11095-018-2553-8
85. Shibakami M, Nemoto T, Sohma M. Dependence of dissolution, dispersion, and aggregation characteristics of cationic polysaccharides made from euglenoid β-1,3-glucan on degree of substitution. *Cellulose*. 2018;25(4):2217-2234. doi:10.1007/s10570-018-1740-4
86. Donnelly D. The structure and function of the glucagon-like peptide-1 receptor and its ligands. *Br J Pharmacol*. 2012;166(1):27-41. doi:10.1111/j.1476-5381.2011.01687.x
87. Morimoto K, Watanabe M, Sugizaki T, Irie JI, Itoh H. Intestinal bile acid composition modulates prohormone convertase 1β (PC1/3) expression and consequent GLP-1 production in male mice. *Endocrinology*. 2016;157(3):1071-1081. doi:10.1210/en.2015-1551
88. Garg SK, Ritchie PJ, Moser EG, Snell-Bergeon JK, Freson BJ, Hazenfield RM. Effects of colesevelam on LDL-C, A1c and GLP-1 levels in patients with type 1 diabetes: a pilot randomized double-blind trial. *Diabetes, Obes Metab*. 2011;13(2):137-143. doi:10.1111/j.1463-1326.2010.01320.x
89. Chen L, McNulty J, Anderson D, et al. Cholestyramine reverses hyperglycemia and enhances glucose-stimulated glucagon-like peptide 1 release in Zucker diabetic fatty rats. *J Pharmacol Exp Ther*. 2010;334(1):164-170. doi:10.1124/jpet.110.166892
90. Tang T, Effiong K, Hu J, Li C, Xiao X. Chemical Prevention and Control of the Green Tide and Fouling Organism Ulva: Key Chemicals, Mechanisms, and Applications. *Front Mar Sci*. 2021;8(February). doi:10.3389/fmars.2021.618950
91. Kidgell JT, Magnusson M, de Nys R, Glasson CRK. Ulvan: A systematic review of extraction, composition and function. *Algal Res*. 2019;39(January):101422. doi:10.1016/j.algal.2019.101422

92. Wang L, Wang X, Wu H, Liu R. *Overview on Biological Activities and Molecular Characteristics of Sulfated Polysaccharides from Marine Green Algae in Recent Years*. Vol 12.; 2014. doi:10.3390/md12094984
93. Jiao G, Yu G, Zhang J, Ewart HS. Chemical structures and bioactivities of sulfated polysaccharides from marine algae. *Mar Drugs*. 2011;9(2):196-233. doi:10.3390/md9020196
94. Qi H, Sheng J. The antihyperlipidemic mechanism of high sulfate content ulvan in rats. *Mar Drugs*. 2015;13(6):3407-3421. doi:10.3390/md13063407
95. Mayakrishnan V, Kannappan P, Abdullah N, Ahmed ABA. Cardioprotective activity of polysaccharides derived from marine algae: An overview. *Trends Food Sci Technol*. 2013;30(2):98-104. doi:10.1016/j.tifs.2013.01.007
96. Tang T, Cao S, Zhu B, Li Q. Ulvan polysaccharide-degrading enzymes: An updated and comprehensive review of sources category, property, structure, and applications of ulvan lyases. *Algal Res*. 2021;60(May):102477. doi:10.1016/j.algal.2021.102477
97. Li B, Xu H, Wang X, et al. Antioxidant and antihyperlipidemic activities of high sulfate content purified polysaccharide from Ulva pertusa. *Int J Biol Macromol*. 2020;146:756-762. doi:10.1016/j.ijbiomac.2019.11.061
98. Qi H, Huang L, Liu X, Liu D, Zhang Q, Liu S. Antihyperlipidemic activity of high sulfate content derivative of polysaccharide extracted from Ulva pertusa (Chlorophyta). *Carbohydr Polym*. 2012;87(2):1637-1640. doi:10.1016/j.carbpol.2011.09.073
99. Qi H, Liu X, Zhang J, Duan Y, Wang X, Zhang Q. Synthesis and antihyperlipidemic activity of acetylated derivative of ulvan from Ulva pertusa. *Int J Biol Macromol*. 2012;50(1):270-272. doi:10.1016/j.ijbiomac.2011.11.006
100. Liu X, Sun Z, Zhang M, et al. Antioxidant and antihyperlipidemic activities of polysaccharides from sea cucumber Apostichopus japonicus. *Carbohydr Polym*. 2012;90(4):1664-1670. doi:10.1016/j.carbpol.2012.07.047
101. Vinodh R, Sasikumar Y, Kim HJ, Atchudan R, Yi M. Chitin and chitosan based biopolymer derived electrode materials for supercapacitor applications: A critical review. *J Ind Eng Chem*. 2021;104:155-171. doi:10.1016/j.jiec.2021.08.019

102. Seidi F, Khodadadi Yazdi M, Jouyandeh M, et al. Chitosan-based blends for biomedical applications. *Int J Biol Macromol*. 2021;183:1818-1850. doi:10.1016/j.ijbiomac.2021.05.003
103. Dash M, Chiellini F, Ottenbrite RM, Chiellini E. Chitosan - A versatile semi-synthetic polymer in biomedical applications. *Prog Polym Sci*. 2011;36(8):981-1014. doi:10.1016/j.progpolymsci.2011.02.001
104. Fakhri E, Eslami H, Maroufi P, et al. Chitosan biomaterials application in dentistry. *Int J Biol Macromol*. 2020;162:956-974. doi:10.1016/j.ijbiomac.2020.06.211
105. Crini G. Historical review on chitin and chitosan biopolymers. *Environ Chem Lett*. 2019;17(4):1623-1643. doi:10.1007/s10311-019-00901-0
106. Xu W, Mohan A, Pitts NL, Udenigwe C, Mason B. Bile acid-binding capacity of lobster shell-derived chitin, chitosan and chitooligosaccharides. *Food Biosci*. 2020;33(July 2018):100476. doi:10.1016/j.fbio.2019.100476
107. Rana AK, Frollini E, Thakur VK. Cellulose nanocrystals: Pretreatments, preparation strategies, and surface functionalization. *Int J Biol Macromol*. 2021;182:1554-1581. doi:10.1016/j.ijbiomac.2021.05.119
108. Mali P, Sherje AP. Cellulose nanocrystals: Fundamentals and biomedical applications. *Carbohydr Polym*. 2022;275(August 2021):118668. doi:10.1016/j.carbpol.2021.118668
109. Moon RJ, Martini A, Nairn J, Simonsen J, Youngblood J. *Cellulose Nanomaterials Review: Structure, Properties and Nanocomposites*. Vol 40.; 2011. doi:10.1039/c0cs00108b
110. Kaushik M, Moores A. Review: Nanocelluloses as versatile supports for metal nanoparticles and their applications in catalysis. *Green Chem*. 2016;18(3):622-637. doi:10.1039/c5gc02500a
111. Ivanova N, Gugleva V, Dobreva M, Pehlivanov I, Stefanov S, Andonova V. Current Trends in the Production of Cellulose Nanoparticles and Nanocomposites for Biomedical Applications. *Intech*. 2016;i(tourism):13.
112. Park NM, Choi S, Oh JE, Hwang DY. Facile extraction of cellulose nanocrystals.

Carbohydr Polym. 2019;223(July):115114. doi:10.1016/j.carbpol.2019.115114

113. Wang H, He J, Zhang M, Tam KC, Ni P. A new pathway towards polymer modified cellulose nanocrystals via a “grafting onto” process for drug delivery. *Polym Chem*. 2015;6(23):4206-4209. doi:10.1039/c5py00466g
114. Kalashnikova I, Bizot H, Cathala B, Capron I. Modulation of cellulose nanocrystals amphiphilic properties to stabilize oil/water interface. *Biomacromolecules*. 2012;13(1):267-275. doi:10.1021/bm201599j
115. Pandey A, Derakhshandeh M, Kedzior SA, et al. Role of interparticle interactions on microstructural and rheological properties of cellulose nanocrystal stabilized emulsions. *J Colloid Interface Sci*. 2018;532:808-818. doi:10.1016/j.jcis.2018.08.044
116. Wohlhauser S, Delepierre G, Labet M, et al. Grafting Polymers from Cellulose Nanocrystals: Synthesis, Properties, and Applications. *Macromolecules*. 2018;51(16):6157-6189. doi:10.1021/acs.macromol.8b00733
117. Yu HY, Qin ZY, Liu L, Yang XG, Zhou Y, Yao JM. Comparison of the reinforcing effects for cellulose nanocrystals obtained by sulfuric and hydrochloric acid hydrolysis on the mechanical and thermal properties of bacterial polyester. *Compos Sci Technol*. 2013;87:22-28. doi:10.1016/j.compscitech.2013.07.024
118. Yang X, Xie H, Du H, et al. Facile Extraction of Thermally Stable and Dispersible Cellulose Nanocrystals with High Yield via a Green and Recyclable FeCl3-Catalyzed Deep Eutectic Solvent System. *ACS Sustain Chem Eng*. 2019;7(7):7200-7208. doi:10.1021/acssuschemeng.9b00209
119. Akhlaghi SP, Zaman M, Mohammed N, et al. Synthesis of amine functionalized cellulose nanocrystals: Optimization and characterization. *Carbohydr Res*. 2015;409:48-55. doi:10.1016/j.carres.2015.03.009
120. Kargarzadeh H, Mariano M, Gopakumar D, et al. *Advances in Cellulose Nanomaterials*. Vol 25. Springer Netherlands; 2018. doi:10.1007/s10570-018-1723-5
121. Jiang F, Esker AR, Roman M. Acid-catalyzed and solvolytic desulfation of H2SO 4-hydrolyzed cellulose nanocrystals. *Langmuir*. 2010;26(23):17919-17925. doi:10.1021/la1028405

122. Lin N, Gèze A, Wouessidjewe D, Huang J, Dufresne A. Biocompatible Double-Membrane Hydrogels from Cationic Cellulose Nanocrystals and Anionic Alginate as Complexing Drugs Codelivery. *ACS Appl Mater Interfaces*. 2016;8(11):6880-6889. doi:10.1021/acsami.6b00555
123. Abitbol T, Palermo A, Moran-Mirabal JM, Cranston ED. Fluorescent labeling and characterization of cellulose nanocrystals with varying charge contents. *Biomacromolecules*. 2013;14(9):3278-3284. doi:10.1021/bm400879x
124. Hou L, Bian H, Wang Q, Zhang N, Liang Y, Dong D. Direct functionalization of cellulose nanocrystals with polymer brushes via UV-induced polymerization: access to novel heterogeneous visible-light photocatalysts. *RSC Adv*. 2016;6(58):53062-53068. doi:10.1039/C6RA11403B
125. Lokanathan AR, Uddin KMA, Rojas OJ, Laine J. Cellulose Nanocrystal-Mediated Synthesis of Silver Nanoparticles: Role of Sulfate Groups in Nucleation Phenomena. *Biomacromolecules*. 2014;15(1):373-379. doi:10.1021/bm401613h
126. Zoppe JO, Johansson L-S, Seppala J. Manipulation of cellulose nanocrystal surface sulfate groups toward biomimetic nanostructures in aqueous media. *Carbohydr Polym*. 2015;126:23-31. doi:10.1016/j.carbpol.2015.03.005
127. Reid MS, Villalobos M, Cranston ED. Cellulose nanocrystal interactions probed by thin film swelling to predict dispersibility. *Nanoscale*. 2016;8(24):12247-12257. doi:10.1039/C6NR01737A
128. Boluk Y, Lahiji R, Zhao L, McDermott MT. Suspension viscosities and shape parameter of cellulose nanocrystals (CNC). *Colloids Surfaces A Physicochem Eng Asp*. 2011;377(1-3):297-303. doi:10.1016/j.colsurfa.2011.01.003
129. Phan-Xuan T, Thuresson A, Skepö M, Labrador A, Bordes R, Matic A. Aggregation behavior of aqueous cellulose nanocrystals: the effect of inorganic salts. *Cellulose*. 2016;23(6):3653-3663. doi:10.1007/s10570-016-1080-1
130. Oguzlu H, Danumah C, Boluk Y. Colloidal behavior of aqueous cellulose nanocrystal suspensions. *Curr Opin Colloid Interface Sci*. 2017;29:46-56. doi:10.1016/j.cocis.2017.02.002

131. Boluk Y, Zhao L, Incani V. Dispersions of nanocrystalline cellulose in aqueous polymer solutions: Structure formation of colloidal rods. *Langmuir*. 2012;28(14):6114-6123. doi:10.1021/la2035449
132. Silva CEP, Tam KC, Bernardes JS, Loh W. Double stabilization mechanism of O/W Pickering emulsions using cationic nanofibrillated cellulose. *J Colloid Interface Sci*. 2020;574:207-216. doi:10.1016/j.jcis.2020.04.001
133. Hasani M, Cranston ED, Westman G, Gray DG. Cationic surface functionalization of cellulose nanocrystals. *Soft Matter*. 2008;4(11):2238-2244. doi:10.1039/B806789A
134. Zaman M, Xiao H, Chibante F, Ni Y. Synthesis and characterization of cationically modified nanocrystalline cellulose. *Carbohydr Polym*. 2012;89(1):163-170. doi:10.1016/j.carbpol.2012.02.066
135. Quinlan PJ, Tanvir A, Tam KC. Application of the central composite design to study the flocculation of an anionic azo dye using quaternized cellulose nanofibrils. *Carbohydr Polym*. 2015;133:80-89. doi:10.1016/j.carbpol.2015.06.095
136. Odabas N, Amer H, Bacher M, Henniges U, Potthast A, Rosenau T. Properties of Cellulosic Material after Cationization in Different Solvents. *ACS Sustain Chem Eng*. 2016;4(4):2295-2301. doi:10.1021/acssuschemeng.5b01752
137. Abitbol T, Kloser E, Gray DG. Estimation of the surface sulfur content of cellulose nanocrystals prepared by sulfuric acid hydrolysis. *Cellulose*. 2013;20(2):785-794. doi:10.1007/s10570-013-9871-0
138. Beck S, Methot M, Bouchard J. General procedure for determining cellulose nanocrystal sulfate half-ester content by conductometric titration. *CELLULOSE*. 2015;22(1):101-116. doi:10.1007/s10570-014-0513-y
139. Lavorante MJ, Franco JI. Conductometric titration as a technique to determine variation in conductivity in perfluorosulfonic acid materials for fuel cells and electrolyzers. *Int J Energy Environ Eng*. 2017;8(2):123-134. doi:10.1007/s40095-017-0230-z
140. Sze A, Erickson D, Ren L, Li D. Zeta-potential measurement using the Smoluchowski equation and the slope of the current-time relationship in electroosmotic flow. *J Colloid Interface Sci*. 2003;261(2):402-410. doi:10.1016/S0021-9797(03)00142-5

141. Dosedělová V, Itterheimová P, Kubáň P. Analysis of bile acids in human biological samples by microcolumn separation techniques: A review. *Electrophoresis*. 2021;42(1-2):68-85. doi:10.1002/elps.202000139
142. Dutta M, Cai J, Gui W, Patterson AD. A review of analytical platforms for accurate bile acid measurement. *Anal Bioanal Chem*. 2019;411(19):4541-4549. doi:10.1007/s00216-019-01890-3
143. Liu Y, Rong Z, Xiang D, Zhang C, Liu D. Detection technologies and metabolic profiling of bile acids: A comprehensive review. *Lipids Health Dis*. 2018;17(1):1-13. doi:10.1186/s12944-018-0774-9
144. Sharma K. Review on bile acid analysis. *Int J Pharm*. 2012;3(2):28-34. http://www.pharmainterscience.com/Docs/IJPBS-2012-03-35.pdf
145. Lyutakov I, Ursini F, Penchev P, et al. Methods for diagnosing bile acid malabsorption: a systematic review. *BMC Gastroenterol*. 2019;19(1):185. doi:10.1186/s12876-019-1102-1
146. Choucair I, Nemet I, Li L, et al. Quantification of bile acids: A mass spectrometry platform for studying gut microbe connection to metabolic diseases. *J Lipid Res*. 2020;61(2):159-177. doi:10.1194/jlr.RA119000311
147. Gómez C, Stücheli S, Kratschmar D V., Bouitbir J, Odermatt A. Development and validation of a highly sensitive LC-MS/MS method for the analysis of bile acids in serum, plasma, and liver tissue samples. *Metabolites*. 2020;10(7):1-17. doi:10.3390/metabo10070282
148. Manna LB, Ovadia C, Lövgren-Sandblom A, et al. Enzymatic quantification of total serum bile acids as a monitoring strategy for women with intrahepatic cholestasis of pregnancy receiving ursodeoxycholic acid treatment: a cohort study. *BJOG An Int J Obstet Gynaecol*. 2019;126(13):1633-1640. doi:10.1111/1471-0528.15926
149. Brandvold KR, Weaver JM, Whidbey C, Wright AT. A continuous fluorescence assay for simple quantification of bile salt hydrolase activity in the gut microbiome. *Sci Rep*. 2019;9(1):1-7. doi:10.1038/s41598-018-37656-7
150. Ghaffarzadegan T, Essén S, Verbrugghe P, et al. Determination of free and conjugated

bile acids in serum of Apoe(−/−) mice fed different lingonberry fractions by UHPLC-MS. *Sci Rep*. 2019;9(1):1-13. doi:10.1038/s41598-019-40272-8

151. Kakiyama G, Muto A, Takei H, et al. A simple and accurate HPLC method for fecal bile acid profile in healthy and cirrhotic subjects: Validation by GC-MS and LC-MS. *J Lipid Res*. 2014;55(5):978-990. doi:10.1194/jlr.D047506
152. Yadav R S. Liquid Chromatography/Tandem Mass Spectrometry Method for Estimation of Cholic Acid in Rat Plasma, Urine and its Application. *J Anal Bioanal Tech*. 2014;5(4). doi:10.4172/2155-9872.1000200
153. Marksteiner J, Blasko I, Kemmler G, Koal T, Humpel C. Bile acid quantification of 20 plasma metabolites identifies lithocholic acid as a putative biomarker in Alzheimer's disease. *Metabolomics*. 2018;14(1):1-10. doi:10.1007/s11306-017-1297-5
154. Gao XF, Li YS, Karube I. Flow injection spectrophotometric determination of sulfated bile acids in urine with immobilized enzyme reactors using water soluble tetrazolium blue-5. *Anal Chim Acta*. 2001;443(2):257-264. doi:10.1016/S0003-2670(01)01227-2
155. Žížalová K, Vecka M, Vítek L, Leníček M. Enzymatic methods may underestimate the total serum bile acid concentration. *PLoS One*. 2020;15(7 July):3-9. doi:10.1371/journal.pone.0236372
156. Danese E, Salvagno GL, Negrini D, Brocco G, Montagnana M, Lippi G. Analytical evaluation of three enzymatic assays for measuring total bile acids in plasma using a fully-automated clinical chemistry platform. *PLoS One*. 2017;12(6):1-13. doi:10.1371/journal.pone.0179200
157. Kurzawa M, Koter I, Szlyk E. Determination of cholic acid in bile and pharmaceutical preparation. *Chem Analityczna*. 2006;51(3):411-426.
158. Lai CW, Bee Abd Hamid S, Tan TL, Lee WH. Rapid Formation of 1D Titanate Nanotubes Using Alkaline Hydrothermal Treatment and Its Photocatalytic Performance. *J Nanomater*. 2015;2015:1-8. doi:10.1155/2015/145360
159. Azami M, Bahram M, Nouri S, Naseri A. A central composite design for the optimization of the removal of the azo dye, Methyl Orange, from waste water using the Fenton reaction. *J Serbian Chem Soc*. 2012;77(2):235-246.

doi:10.2298/JSC110315165A

160. Wang W, Yang S. Photocatalytic Degradation of Organic Dye Methyl Orange with Phosphotungstic Acid. *J Water Resour Prot*. 2010;02(11):979-983. doi:10.4236/jwarp.2010.211116

161. Kumar K, Patial BS, Chauhan S. Conductivity and fluorescence studies on the micellization properties of sodium cholate and sodium deoxycholate in aqueous medium at different temperatures: Effect of selected amino acids. *J Chem Thermodyn*. 2015;82:25-33. doi:10.1016/j.jct.2014.10.014

162. Mohammed N, Lian H, Islam MS, et al. Selective adsorption and separation of organic dyes using functionalized cellulose nanocrystals. *Chem Eng J*. 2021;417(February):129237. doi:10.1016/j.cej.2021.129237

163. Mohammed N, Grishkewich N, Berry RM, Tam KC. Cellulose nanocrystal-alginate hydrogel beads as novel adsorbents for organic dyes in aqueous solutions. *Cellulose*. 2015;22(6):3725-3738. doi:10.1007/s10570-015-0747-3

164. Aravindhan R, Fathima NN, Rao JR, Nair BU. Equilibrium and thermodynamic studies on the removal of basic black dye using calcium alginate beads. *Colloids Surfaces A Physicochem Eng Asp*. 2007;299(1-3):232-238. doi:10.1016/j.colsurfa.2006.11.045

165. Kloser E, Gray DG. Surface grafting of cellulose nanocrystals with poly(ethylene oxide) in aqueous media. *Langmuir*. 2010;26(16):13450-13456. doi:10.1021/la101795s

166. Jin E, Guo J, Yang F, et al. On the polymorphic and morphological changes of cellulose nanocrystals (CNC-I) upon mercerization and conversion to CNC-II. *Carbohydr Polym*. 2016;143:327-335. doi:10.1016/j.carbpol.2016.01.048

167. Halonen H, Larsson PT, Iversen T. Mercerized cellulose biocomposites: A study of influence of mercerization on cellulose supramolecular structure, water retention value and tensile properties. *Cellulose*. 2013;20(1):57-65. doi:10.1007/s10570-012-9801-6

168. Sahlin K, Forsgren L, Moberg T, Bernin D, Rigdahl M, Westman G. Surface treatment of cellulose nanocrystals (CNC): effects on dispersion rheology. *Cellulose*. 2018;25(1):331-345. doi:10.1007/s10570-017-1582-5

169. Lin N, Dufresne A. Surface chemistry, morphological analysis and properties of

cellulose nanocrystals with gradiented sulfation degrees. *Nanoscale*. 2014;6(10):5384-5393. doi:10.1039/c3nr06761k

170. George M, Montemagno C. Estimation of the sulfur ester content of cellulose nanocrystals prepared by sulfuric acid hydrolysis: a reproducible and fast infrared method. *Wood Sci Technol*. 2017;51(3):535-556. doi:10.1007/s00226-016-0885-2
171. Dhar P, Tarafder D, Kumar A, Katiyar V. Thermally recyclable polylactic acid/cellulose nanocrystal films through reactive extrusion process. *Polymer (Guildf)*. 2016;87:268-282. doi:10.1016/j.polymer.2016.02.004
172. Koziolek M, Grimm M, Becker D, et al. Investigation of pH and Temperature Profiles in the GI Tract of Fasted Human Subjects Using the Intellicap® System. *J Pharm Sci*. 2015;104(9):2855-2863. doi:10.1002/jps.24274
173. Qian J, Sullivan BP, Berkland C. pH-Responsive Micelle Sequestrant Polymers Inhibit Fat Absorption. *Biomacromolecules*. 2015;16(8):2340-2346. doi:10.1021/acs.biomac.5b00560
174. Prathapan R, Thapa R, Garnier G, Tabor RF. Modulating the zeta potential of cellulose nanocrystals using salts and surfactants. *Colloids Surfaces A Physicochem Eng Asp*. 2016;509:11-18. doi:10.1016/j.colsurfa.2016.08.075
175. Chung HK, Kim WH, Park J, Cho J, Jeong TY, Park PK. Application of Langmuir and Freundlich isotherms to predict adsorbate removal efficiency or required amount of adsorbent. *J Ind Eng Chem*. 2015;28:241-246. doi:10.1016/j.jiec.2015.02.021
176. Jin L, Sun Q, Xu Q, Xu Y. Adsorptive removal of anionic dyes from aqueous solutions using microgel based on nanocellulose and polyvinylamine. *Bioresour Technol*. 2015;197:348-355. doi:10.1016/j.biortech.2015.08.093
177. Foo KY, Hameed BH. Insights into the modeling of adsorption isotherm systems. *Chem Eng J*. 2010;156(1):2-10. doi:10.1016/j.cej.2009.09.013
178. Pan H, Zhao T, Xu L, Shen Y, Wang L, Ding Y. Preparation of novel chitosan derivatives and applications in functional finishing of textiles. *Int J Biol Macromol*. 2020;153:971-976. doi:10.1016/j.ijbiomac.2019.10.226
179. Freitas ED, Moura Jr. CF, Kerwald J, Beppu MM. An Overview of Current Knowledge

on the Properties, Synthesis and Applications of Quaternary Chitosan Derivatives. *Polymers (Basel)*. 2020;12(12):2878. doi:10.3390/polym12122878

180. Niculescu A, Grumezescu AM. Applications of Chitosan-Alginate-Based Nanoparticles—An Up-to-Date Review. *Nanomaterials*. 2022;12(2):186. doi:10.3390/nano12020186
181. Pal K, Bharti D, Sarkar P, et al. Selected applications of chitosan composites. *Int J Mol Sci*. 2021;22(20). doi:10.3390/ijms222010968
182. Shariatinia Z. Pharmaceutical applications of chitosan. *Adv Colloid Interface Sci*. 2019;263:131-194. doi:10.1016/j.cis.2018.11.008
183. Zhao D, Yu S, Sun B, Gao S, Guo S, Zhao K. Biomedical applications of chitosan and its derivative nanoparticles. *Polymers (Basel)*. 2018;10(4). doi:10.3390/polym10040462
184. Tao F, Cheng Y, Shi X, et al. Applications of chitin and chitosan nanofibers in bone regenerative engineering. *Carbohydr Polym*. 2020;230(October 2019):115658. doi:10.1016/j.carbpol.2019.115658
185. Liu Y, Yang X, Li Y, Chen Y, Zhou X, Li T. Synthesis and characterization of the epoxy-functionalized quaternary ammonium chloride. *Colloids Surfaces A Physicochem Eng Asp*. 2016;498:248-257. doi:10.1016/j.colsurfa.2016.03.066
186. Zou X, Zhao X, Ye L. Synthesis of cationic chitosan hydrogel with long chain alkyl and its controlled glucose-responsive drug delivery behavior. *RSC Adv*. 2015;5(116):96230-96241. doi:10.1039/C5RA16328E
187. Liu P, Meng W, Wang S, Sun Y, Aqeel Ashraf M. Quaternary ammonium salt of chitosan: Preparation and antimicrobial property for paper. *Open Med*. 2015;10(1):473-478. doi:10.1515/med-2015-0081
188. Akhlaghi SP, Berry RC, Tam KC. Surface modification of cellulose nanocrystal with chitosan oligosaccharide for drug delivery applications. *Cellulose*. 2013;20(4):1747-1764. doi:10.1007/s10570-013-9954-y
189. Xiao B, Wan Y, Wang X, et al. Synthesis and characterization of N-(2-hydroxy)propyl-3-trimethyl ammonium chitosan chloride for potential application in gene delivery.

Colloids Surfaces B Biointerfaces. 2012;91(1):168-174. doi:10.1016/j.colsurfb.2011.10.053

190. Abo-Elseoud WS, Hassan ML, Sabaa MW, Basha M, Hassan EA, Fadel SM. Chitosan nanoparticles/cellulose nanocrystals nanocomposites as a carrier system for the controlled release of repaglinide. *Int J Biol Macromol*. 2018;111:604-613. doi:10.1016/j.ijbiomac.2018.01.044
191. Zhao F, Repo E, Song Y, et al. Polyethylenimine-cross-linked cellulose nanocrystals for highly efficient recovery of rare earth elements from water and a mechanism study. *Green Chem*. 2017;19(20):4816-4828. doi:10.1039/c7gc01770g
192. Tang J, Lee MFX, Zhang W, Zhao B, Berry RM, Tam KC. Dual responsive pickering emulsion stabilized by poly[2-(dimethylamino) ethyl methacrylate] grafted cellulose nanocrystals. *Biomacromolecules*. 2014;15(8):3052-3060. doi:10.1021/bm500663w
193. Rosilo H, McKee JR, Kontturi E, et al. Cationic polymer brush-modified cellulose nanocrystals for high-affinity virus binding. *Nanoscale*. 2014;6(20):11871-11881. doi:10.1039/c4nr03584d
194. El Knidri H, Belaabed R, Addaou A, Laajeb A, Lahsini A. Extraction, chemical modification and characterization of chitin and chitosan. *Int J Biol Macromol*. 2018;120:1181-1189. doi:10.1016/j.ijbiomac.2018.08.139
195. Cui J, Yu Z, Lau D. Effect of acetyl group on mechanical properties of chitin/chitosan nanocrystal: A molecular dynamics study. *Int J Mol Sci*. 2016;17(1):1-13. doi:10.3390/ijms17010061
196. Berezina N. Production and application of chitin. *Phys Sci Rev*. 2016;1(9):1-8. doi:10.1515/psr-2016-0048
197. El Knidri H, Belaabed R, Addaou A, Laajeb A, Lahsini A. Extraction, chemical modification and characterization of chitin and chitosan. *Int J Biol Macromol*. 2018;120:1181-1189. doi:10.1016/j.ijbiomac.2018.08.139
198. Oh DX, Cha YJ, Nguyen HL, et al. Chiral nematic self-assembly of minimally surface damaged chitin nanofibrils and its load bearing functions. *Sci Rep*. 2016;6(March):1-6. doi:10.1038/srep23245

199. Fernando LD, Dickwella Widanage MC, Penfield J, et al. Structural Polymorphism of Chitin and Chitosan in Fungal Cell Walls From Solid-State NMR and Principal Component Analysis. *Front Mol Biosci*. 2021;8(August):1-12. doi:10.3389/fmolb.2021.727053

200. Facchine EG, Bai L, Rojas OJ, Khan SA. Associative structures formed from cellulose nanofibrils and nanochitins are pH-responsive and exhibit tunable rheology. *J Colloid Interface Sci*. 2021;588:232-241. doi:10.1016/j.jcis.2020.12.041

201. Shchipunov Y, Sarin S, Kim I, Ha CS. Hydrogels formed through regulated self-organization of gradually charging chitosan in solution of xanthan. *Green Chem*. 2010;12(7):1187-1195. doi:10.1039/b925138c

202. Jin SA, Khan SA, Spontak RJ, Rojas OJ. Anion-Specific Water Interactions with Nanochitin: Donnan and Osmotic Pressure Effects as Revealed by Quartz Microgravimetry. *Langmuir*. 2021;37(38):11242-11250. doi:10.1021/acs.langmuir.1c01585

203. Pasquier E, Beaumont M, Mattos BD, et al. Upcycling Byproducts from Insect (Fly Larvae and Mealworm) Farming into Chitin Nanofibers and Films. *ACS Sustain Chem Eng*. 2021;9(40):13618-13629. doi:10.1021/acssuschemeng.1c05035

204. Zhou H, Dai T, Liu J, et al. Chitin nanocrystals reduce lipid digestion and β-carotene bioaccessibility: An in-vitro INFOGEST gastrointestinal study. *Food Hydrocoll*. 2021;113(September 2020). doi:10.1016/j.foodhyd.2020.106494

205. Zhou H, Tan Y, Lv S, et al. Nanochitin-stabilized pickering emulsions: Influence of nanochitin on lipid digestibility and vitamin bioaccessibility. *Food Hydrocoll*. 2020;106(January):105878. doi:10.1016/j.foodhyd.2020.105878

206. Bai L, Kämäräinen T, Xiang W, et al. Chirality from Cryo-Electron Tomograms of Nanocrystals Obtained by Lateral Disassembly and Surface Etching of Never-Dried Chitin. *ACS Nano*. 2020;14(6):6921-6930. doi:10.1021/acsnano.0c01327

207. Bi S, Li F, Qin D, et al. Construction of chitin functional materials based on a “green” alkali/urea solvent and their applications in biomedicine: Recent advance. *Appl Mater Today*. 2021;23:101030. doi:10.1016/j.apmt.2021.101030

208. Liu L, Seta FT, An X, et al. Facile isolation of colloidal stable chitin nano-crystals from Metapenaeus ensis shell via solid maleic acid hydrolysis and their application for synthesis of silver nanoparticles. *Cellulose*. 2020;27(17):9853-9875. doi:10.1007/s10570-020-03499-7
209. Mincea M, Negrulescu A, Ostafe V. Preparation, modification, and applications of chitin nanowhiskers: A review. *Rev Adv Mater Sci*. 2012;30(3):225-242.
210. Zeng JB, He YS, Li SL, Wang YZ. Chitin whiskers: An overview. *Biomacromolecules*. 2012;13(1):1-11. doi:10.1021/bm201564a
211. Gopalan Nair K, Dufresne A. Crab shell chitin whisker reinforced natural rubber nanocomposites. 1. Processing and swelling behavior. *Biomacromolecules*. 2003;4(3):657-665. doi:10.1021/bm020127b
212. Salaberria AM, Diaz RH, Labidi J, Fernandes SCM. Role of chitin nanocrystals and nanofibers on physical, mechanical and functional properties in thermoplastic starch films. *Food Hydrocoll*. 2015;46:93-102. doi:10.1016/j.foodhyd.2014.12.016
213. Chan CH, Joy J, Maria HJ, Thomas S. CHAPTER 1. Natural Rubber-Based Composites and Nanocomposites: State of the Art, New Challenges and Opportunities. 2013;2(8):1-33. doi:10.1039/9781849737654-00001
214. João CFC, Echeverria C, Velhinho A, Silva JC, Godinho MH, Borges JP. Bio-inspired production of chitosan/chitin films from liquid crystalline suspensions. *Carbohydr Polym*. 2017;155:372-381. doi:10.1016/j.carbpol.2016.08.039
215. Bai L, Huan S, Xiang W, et al. Self-Assembled Networks of Short and Long Chitin Nanoparticles for Oil/Water Interfacial Superstabilization. *ACS Sustain Chem Eng*. 2019;7(7):6497-6511. doi:10.1021/acssuschemeng.8b04023
216. Wang J, Kasuya K, Koga H, Nogi M, Uetani K. Thermal conductivity analysis of chitin and deacetylated-chitin nanofiber films under dry conditions. *Nanomaterials*. 2021;11(3):1-11. doi:10.3390/nano11030658
217. Zhou H, Lv S, Liu J, et al. Modulation of Physicochemical Characteristics of Pickering Emulsions: Utilization of Nanocellulose- A nd Nanochitin-Coated Lipid Droplet Blends. *J Agric Food Chem*. 2020;68(2):603-611. doi:10.1021/acs.jafc.9b06846

218. Liu L, Bai L, Tripathi A, et al. High Axial Ratio Nanochitins for Ultrastrong and Shape-Recoverable Hydrogels and Cryogels via Ice Templating. *ACS Nano*. 2019;13(3):2927-2935. doi:10.1021/acsnano.8b07235
219. Liu L, Borghei M, Wang Z, Xu J, Fan Y, Rojas OJ. Salt-Induced Colloidal Destabilization, Separation, Drying, and Redispersion in Aqueous Phase of Cationic and Anionic Nanochitins. *J Agric Food Chem*. 2018;66(35):9189-9198. doi:10.1021/acs.jafc.8b02062
220. Pang K, Ding B, Liu X, Wu H, Duan Y, Zhang J. High-yield preparation of a zwitterionically charged chitin nanofiber and its application in a doubly pH-responsive Pickering emulsion. *Green Chem*. 2017;19(15):3665-3670. doi:10.1039/c7gc01592e
221. Min BM, Lee SW, Lim JN, et al. Chitin and chitosan nanofibers: Electrospinning of chitin and deacetylation of chitin nanofibers. *Polymer (Guildf)*. 2004;45(21):7137-7142. doi:10.1016/j.polymer.2004.08.048
222. Younes I, Rinaudo M. Chitin and chitosan preparation from marine sources. Structure, properties and applications. *Mar Drugs*. 2015;13(3):1133-1174. doi:10.3390/md13031133
223. Fan Y, Saito T, Isogai A. Individual chitin nano-whiskers prepared from partially deacetylated α-chitin by fibril surface cationization. *Carbohydr Polym*. 2010;79(4):1046-1051. doi:10.1016/j.carbpol.2009.10.044
224. Campos EVR, Oliveira JL, Fraceto LF. Poly(ethylene glycol) and cyclodextrin-grafted chitosan: From methodologies to preparation and potential biotechnological applications. *Front Chem*. 2017;5(NOV):1-15. doi:10.3389/fchem.2017.00093
225. Zhu Y, Huan S, Bai L, et al. High Internal Phase Oil-in-Water Pickering Emulsions Stabilized by Chitin Nanofibrils: 3D Structuring and Solid Foam. *ACS Appl Mater Interfaces*. 2020;12(9):11240-11251. doi:10.1021/acsami.9b23430
226. Grande R, Bai L, Wang L, et al. Nanochitins of Varying Aspect Ratio and Properties of Microfibers Produced by Interfacial Complexation with Seaweed Alginate. *ACS Sustain Chem Eng*. 2020;8(2):1137-1145. doi:10.1021/acssuschemeng.9b06099
227. Pereira AGB, Muniz EC, Hsieh Y Lo. Chitosan-sheath and chitin-core nanowhiskers.

Carbohydr Polym. 2014;107(1):158-166. doi:10.1016/j.carbpol.2014.02.046

228. Lavall RL, Assis OBG, Campana-Filho SP. β-Chitin from the pens of Loligo sp.: Extraction and characterization. *Bioresour Technol*. 2007;98(13):2465-2472. doi:10.1016/j.biortech.2006.09.002
229. Rinaudo M. Chitin and chitosan: Properties and applications. *Prog Polym Sci*. 2006;31(7):603-632. doi:10.1016/j.progpolymsci.2006.06.001
230. Sultana H, Barai M, Mandal MK, et al. Effect of ionic liquid on the micellization behavior of bile salts in aqueous medium. *J Dispers Sci Technol*. 2021;0(0):1-11. doi:10.1080/01932691.2021.1915155
231. Ćirin DM, Poša MM, Krstonošić VS. Interactions between selected bile salts and Triton X-100 or sodium lauryl ether sulfate. *Chem Cent J*. 2011;5(1):1-8. doi:10.1186/1752-153X-5-89
232. Loh W, Brinatti C, Tam KC. Use of isothermal titration calorimetry to study surfactant aggregation in colloidal systems. *Biochim Biophys Acta - Gen Subj*. 2016;1860(5):999-1016. doi:10.1016/j.bbagen.2015.10.003
233. Olesen NE, Westh P, Holm R. Determination of thermodynamic potentials and the aggregation number for micelles with the mass-action model by isothermal titration calorimetry: A case study on bile salts. *J Colloid Interface Sci*. 2015;453:79-89. doi:10.1016/j.jcis.2015.03.069
234. Coreta-Gomes FM, Martins PAT, Velazquez-Campoy A, Vaz WLC, Geraldes CFG, Moreno MJ. Interaction of Bile Salts with Model Membranes Mimicking the Gastrointestinal Epithelium: A Study by Isothermal Titration Calorimetry. *Langmuir*. 2015;31(33):9097-9104. doi:10.1021/acs.langmuir.5b01810
235. Thongngam M, McClements DJ. Isothermal titration calorimetry study of the interactions between chitosan and a bile salt (sodium taurocholate). *Food Hydrocoll*. 2005;19(5):813-819. doi:10.1016/j.foodhyd.2004.11.001
236. Ollila F, Pentikäinen OT, Forss S, Johnson MS, Peter Slotte J. Characterization of bile salt/cyclodextrin interactions using isothermal titration calorimetry. *Langmuir*. 2001;17(22):7107-7111. doi:10.1021/la0109258

237. Garidel P, Hildebrand A, Neubert R, Blume A. Thermodynamic characterization of bile salt aggregation as a function of temperature and ionic strength using isothermal titration calorimetry. *Langmuir*. 2000;16(12):5267-5275. doi:10.1021/la9912390

238. Fares MY, Abdelwahab NS, Hegazy MA, Abdelrahman MM, Mahmoud AM, EL-Sayed GM. Nanoparticle-enhanced in-line potentiometric ion sensor for point-of-care diagnostics for tropicamide abuse in biological fluid. *Anal Chim Acta*. 2022;1192:339350. doi:10.1016/j.aca.2021.339350

239. Bakker E, Meyerhoff ME. Ionophore-based membrane electrodes: New analytical concepts and non-classical response mechanisms. *Anal Chim Acta*. 2000;416(2):121-137. doi:10.1016/S0003-2670(00)00883-7

240. Tan JPK, Zeng AQF, Chang CC, Tam KC. Release kinetics of procaine hydrochloride (PrHy) from pH-responsive nanogels: theory and experiments. *Int J Pharm*. 2008;357(1-2):305-313. doi:10.1016/j.ijpharm.2008.01.058

241. Tan JPK, Tam KC. Application of drug selective electrode in the drug release study of pH-responsive microgels. *J Control Release*. 2007;118(1):87-94. doi:10.1016/j.jconrel.2006.11.017

242. Tan JPK, Goh CH, Tam KC. Comparative drug release studies of two cationic drugs from pH-responsive nanogels. *Eur J Pharm Sci*. 2007;32(4-5):340-348. doi:10.1016/j.ejps.2007.08.010

243. Vadnere M, Lindenbaum S. Surfactant-selective electrode study of bile salt-protein binding. *Int J Pharm*. 1982;11(1):57-69. doi:10.1016/0378-5173(82)90178-8

244. Campanella L, Tomassetti M, Mazzei F, Sbrilli R. Polymeric membrane electrodes for drug analysis. *J Pharm Biomed Anal*. 1988;6(6-8):717-723. doi:10.1016/0731-7085(88)80083-9

245. Seguí MJ, Lizondo-Sabater J, Benito A, et al. A new ion-selective electrode for anionic surfactants. *Talanta*. 2007;71(1):333-338. doi:10.1016/j.talanta.2006.04.005

246. Campanella L, Mazzei F, Tomassetti M, Sbrilli R. Polymeric Membrane Cholate-selective Electrode. *Analyst*. 1988;113(February):325-328.

247. Campanella L, Sorrentino L, Tomassetti M. Cholate liquid membrane ion-selective

electrode for drug analysis. *Analyst*. 1983;108(1293):1490-1494. doi:10.1039/an9830801490

248. Campanella L, Tomassetti M, Cordatore M. Application of a new cholate liquid membrane electrode to the determination of the cholic acids pool in human bile. *J Pharm Biomed Anal*. 1986;4(2):155-162. doi:10.1016/0731-7085(86)80037-1
249. De Marco R, Clarke G, Pejcic B. Ion-selective electrode potentiometry in environmental analysis. *Electroanalysis*. 2007;19(19-20):1987-2001. doi:10.1002/elan.200703916
250. Alizadeh N, Mehdipour R. Drug-selective electrode for ketamine determination in pharmaceutical preparations and electrochemical study of drug with BSA. *J Pharm Biomed Anal*. 2002;30(3):725-731. doi:10.1016/S0731-7085(02)00350-3
251. Harsányi G. Polymer films in sensor applications: a review of present uses and future possibilities. *Sens Rev*. 2000;20(2):98-105. doi:10.1108/02602280010319169
252. Wang J, Liang R, Qin W. Thin polymeric membrane ion-selective electrodes for trace-level potentiometric detection. *Anal Chim Acta*. 2020;1139:1-7. doi:10.1016/j.aca.2020.09.024
253. Höfler L, Bedlechowicz I, Vigassy T, Gyurcsányi RE, Bakker E, Pretsch E. Limitations of current polarization for lowering the detection limit of potentiometric polymeric membrane sensors. *Anal Chem*. 2009;81(9):3592-3599. doi:10.1021/ac802588j
254. Qin Y, Peper S, Bakker E. Plasticizer-free polymer membrane ion-selective electrodes containing a methacrylic copolymer matrix. *Electroanalysis*. 2002;14(19-20):1375-1381. doi:10.1002/1521-4109(200211)14:19/20<1375::AID-ELAN1375>3.0.CO;2-8
255. Bakker E, Bühlmann P, Pretsch E. Polymer membrane ion-selective electrodes-what are the limits? *Electroanalysis*. 1999;11(13):915-933. doi:10.1002/(SICI)1521-4109(199909)11:13<915::AID-ELAN915>3.0.CO;2-J
256. Rich M, Mendecki L, Mensah ST, et al. Circumventing Traditional Conditioning Protocols in Polymer Membrane-Based Ion-Selective Electrodes. *Anal Chem*. 2016;88(17):8404-8408. doi:10.1021/acs.analchem.6b01542
257. Hu J, Stein A, Bühlmann P. Rational design of all-solid-state ion-selective electrodes and reference electrodes. *TrAC - Trends Anal Chem*. 2016;76:102-114.

doi:10.1016/j.trac.2015.11.004

258. Chen LD, Lai CZ, Granda LP, et al. Fluorous membrane ion-selective electrodes for perfluorinated surfactants: Trace-level detection and in situ monitoring of adsorption. *Anal Chem*. 2013;85(15):7471-7477. doi:10.1021/ac401424j

259. Fraga ARL, Quintana JC, Destri GL, Giamblanco N, Toro RG, Punzo F. Polymeric membranes conditioning for sensors applications: Mechanism and influence on analytes detection. *J Solid State Electrochem*. 2012;16(3):901-909. doi:10.1007/s10008-011-1456-y

260. Rubinova N, Chumbimuni-Torres K, Bakker E. Solid-contact potentiometric polymer membrane microelectrodes for the detection of silver ions at the femtomole level. *Sensors Actuators, B Chem*. 2007;121(1):135-141. doi:10.1016/j.snb.2006.09.007

261. Hassan AK, Ameen ST, Saad B. Tetracaine – selective electrodes with polymer membranes and their application in pharmaceutical formulation control. *Arab J Chem*. 2017;10:S1484-S1491. doi:10.1016/j.arabjc.2013.04.029

262. Pavlović N, Goločorbin-Kon S, Danić M, et al. Bile acids and their derivatives as potential modifiers of drug release and pharmacokinetic profiles. *Front Pharmacol*. 2018;9(NOV):1-23. doi:10.3389/fphar.2018.01283

263. Simonović BR, Momirović M. Determination of Critical Micelle Concentration of Bile Acid Salts by Micro-calorimetric Titration. *Mikrochim Acta*. 1997;127(1):101-104. doi:10.1007/bf01243172

264. Weber C, Halisch M, Stanjek H. Low-frequency electrical conductivity of aqueous kaolinite suspensions II: Counterion effects and estimating stern layer mobilities of counterions. *Clays Clay Miner*. 2018;66(1):86-95. doi:10.1346/CCMN.2018.064087

265. Bordi F, Colby RH, Cametti C, de Lorenzo L, Gili T. Electrical conductivity of polyelectrolyte solutions in the semidilute and concentrated regime: The role of counterion condensation. *J Phys Chem B*. 2002;106(27):6887-6893. doi:10.1021/jp020262i

266. Smith GN, Brown P, James C, et al. The effects of counterion exchange on charge stabilization for anionic surfactants in nonpolar solvents. *J Colloid Interface Sci*.

2016;465:316-322. doi:10.1016/j.jcis.2015.11.062

267. Adio SA, Sharifpur M, Meyer JP. Factors affecting the pH and electrical conductivity of MgO-ethylene glycol nanofluids. *Bull Mater Sci*. 2015;38(5):1345-1357. doi:10.1007/s12034-015-1020-y

268. Bhat N V., Upadhyay DJ. Plasma-induced surface modification and adhesion enhancement of polypropylene surface. *J Appl Polym Sci*. 2002;86(4):925-936. doi:10.1002/app.11024

269. Moghimipour E, Ameri A, Handali S. Absorption-Enhancing Effects of Bile Salts. *Molecules*. 2015;20(8):14451-14473. doi:10.3390/molecules200814451

270. Santhanalakshmi J, Shantha Lakshmi G, Aswal VK, Goyal PS. Small-angle neutron scattering study of sodium cholate and sodium deoxycholate interacting micelles in aqueous medium. *Proc Indian Acad Sci Chem Sci*. 2001;113(1):55-62. doi:10.1007/BF02708552

271. Maslova VA, Kiselev MA. Structure of Sodium Cholate Micelles. *Crystallogr Reports*. 2018;63(3):472-475. doi:10.1134/S1063774518030173

272. Meier AR, Yehl JB, Eckenroad KW, Manley GA, Strein TG, Rovnyak D. Stepwise Aggregation of Cholate and Deoxycholate Dictates the Formation and Loss of Surface-Available Chirally Selective Binding Sites. *Langmuir*. 2018;34(22):6489-6501. doi:10.1021/acs.langmuir.8b00467

273. Yu RB, Quirino JP. Chiral selectors in capillary electrophoresis: Trends during 2017–2018. *Molecules*. 2019;24(6). doi:10.3390/molecules24061135

274. Eckenroad KW, Manley GA, Yehl JB, Pirnie RT, Strein TG, Rovnyak D. An Edge Selection Mechanism for Chirally Selective Solubilization of Binaphthyl Atropisomeric Guests by Cholate and Deoxycholate Micelles. *Chirality*. 2016;28(7):525-533. doi:10.1002/chir.22609

275. Benson GM, Alston DR, Hickey DMB, et al. SK&F 97426-A: A Novel Bile Acid Sequestrant with Higher Affinities and Slower Dissociation Rates for Bile Acids in vitro Than Cholestyramine. *J Pharm Sci*. 1997;86(1):76-81. doi:10.1021/js960207j

276. Bespalova Y, Kwon D, Vasanthan N. Surface modification and antimicrobial properties

of cellulose nanocrystals. *J Appl Polym Sci*. 2017;134(18):1-7. doi:10.1002/app.44789

277. Grigoras AG. Natural and synthetic polymeric antimicrobials with quaternary ammonium moieties: a review. *Environ Chem Lett*. 2021;19(4):3009-3022. doi:10.1007/s10311-021-01215-w
278. Bureš F. Quaternary Ammonium Compounds: Simple in Structure, Complex in Application. *Top Curr Chem*. 2019;377(3):1-21. doi:10.1007/s41061-019-0239-2
279. Makvandi P, Jamaledin R, Jabbari M, Nikfarjam N, Borzacchiello A. Antibacterial quaternary ammonium compounds in dental materials: A systematic review. *Dent Mater*. 2018;34(6):851-867. doi:10.1016/j.dental.2018.03.014
280. Elena P, Miri K. Formation of contact active antimicrobial surfaces by covalent grafting of quaternary ammonium compounds. *Colloids Surfaces B Biointerfaces*. 2018;169(December 2017):195-205. doi:10.1016/j.colsurfb.2018.04.065
281. Jiao Y, Niu L na, Ma S, Li J, Tay FR, Chen J hua. Quaternary ammonium-based biomedical materials: State-of-the-art, toxicological aspects and antimicrobial resistance. *Prog Polym Sci*. 2017;71:53-90. doi:10.1016/j.progpolymsci.2017.03.001
282. Jennings MC, Minbiole KPC, Wuest WM. Quaternary Ammonium Compounds: An Antimicrobial Mainstay and Platform for Innovation to Address Bacterial Resistance. *ACS Infect Dis*. 2016;1(7):288-303. doi:10.1021/acsinfecdis.5b00047
283. Buffet-Bataillon S, Tattevin P, Bonnaure-Mallet M, Jolivet-Gougeon A. Emergence of resistance to antibacterial agents: The role of quaternary ammonium compounds - A critical review. *Int J Antimicrob Agents*. 2012;39(5):381-389. doi:10.1016/j.ijantimicag.2012.01.011
284. Balouiri M, Sadiki M, Ibnsouda SK. Methods for in vitro evaluating antimicrobial activity: A review. *J Pharm Anal*. 2016;6(2):71-79. doi:10.1016/j.jpha.2015.11.005
285. Speers A, Forbes J. Yeast. In: *Brewing Microbiology*. Elsevier; 2015:3-9. doi:10.1016/B978-1-78242-331-7.00001-0
286. Walker GM, Stewart GG. Saccharomyces cerevisiae in the production of fermented beverages. *Beverages*. 2016;2(4):1-12. doi:10.3390/beverages2040030
287. Bzducha-Wróbel A, Kieliszek M, Błażejak S. Chemical composition of the cell wall of

probiotic and brewer's yeast in response to cultivation medium with glycerol as a carbon source. *Eur Food Res Technol*. 2013;237(4):489-499. doi:10.1007/s00217-013-2016-8

288. Maicas S. The role of yeasts in fermentation processes. *Microorganisms*. 2020;8(8):1-8. doi:10.3390/microorganisms8081142
289. Chang YH, Chang KS, Chen CY, Hsu CL, Chang TC, Jang H Der. Enhancement of the efficiency of bioethanol production by Saccharomyces cerevisiae via gradually batch-wise and fed-batch increasing the glucose concentration. *Fermentation*. 2018;4(2). doi:10.3390/fermentation4020045
290. Iorizzo M, Coppola F, Letizia F, Testa B, Sorrentino E. Role of yeasts in the brewing process: Tradition and innovation. *Processes*. 2021;9(5):1-16. doi:10.3390/pr9050839
291. Ralston GB, Tracey MV, Wrench PM. The inhibition of fermentation in baker's yeast by chitosan. *Biochim Biophys Acta - Gen Subj*. 1964;93(3):652-655. doi:10.1016/0304-4165(64)90350-2
292. Swasy MI, Brummel BR, Narangoda C, et al. Degradation of pesticides using amine-functionalized cellulose nanocrystals. *RSC Adv*. 2020;10(72):44312-44322. doi:10.1039/d0ra08308a
293. Riva L, Fiorati A, Punta C. Synthesis and application of cellulose-polyethyleneimine composites and nanocomposites: A concise review. *Materials (Basel)*. 2021;14(3):1-22. doi:10.3390/ma14030473
294. Li W, Ju B, Zhang S. Novel amphiphilic cellulose nanocrystals for pH-responsive Pickering emulsions. *Carbohydr Polym*. 2020;229(September 2019):115401. doi:10.1016/j.carbpol.2019.115401
295. Ndong Ntoutoume GMA, Grassot V, Brégier F, et al. PEI-cellulose nanocrystal hybrids as efficient siRNA delivery agents—Synthesis, physicochemical characterization and in vitro evaluation. *Carbohydr Polym*. 2017;164:258-267. doi:10.1016/j.carbpol.2017.02.004

Appendix A

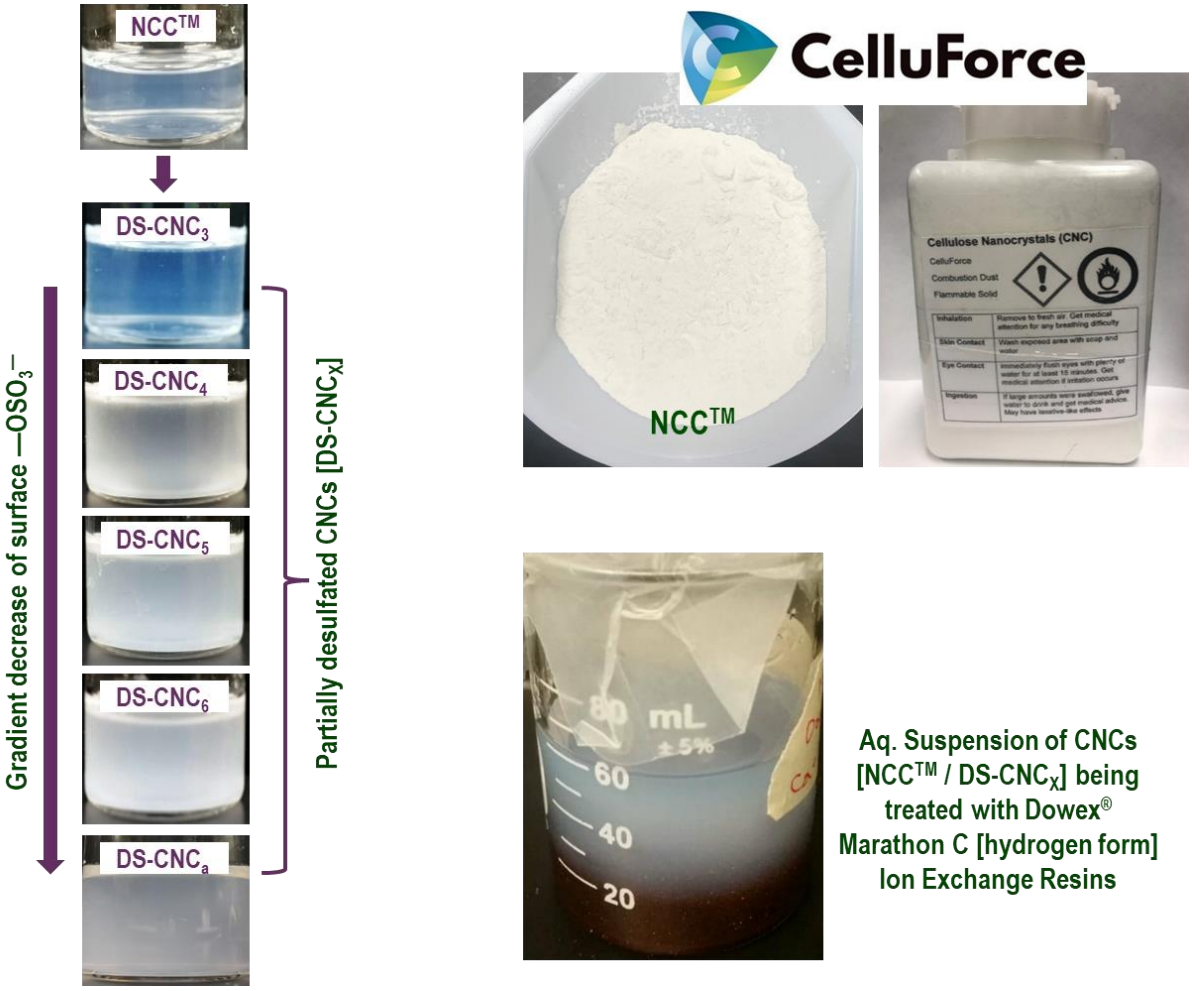


Figure 8.1: *Gradient desulfation of NCC™, the nanocellulose (NCC™) used as the base materials for the work done in chapter 3, and the ion exchange procedure for to convert the* ***Na****–form of the surface sulphate half ester groups, SHE (—OSO_3^-****Na*$^+$*) to* ***acid (protonated, H)*** *forms of the SHE groups(—OSO_3^-****H*$^+$*).*

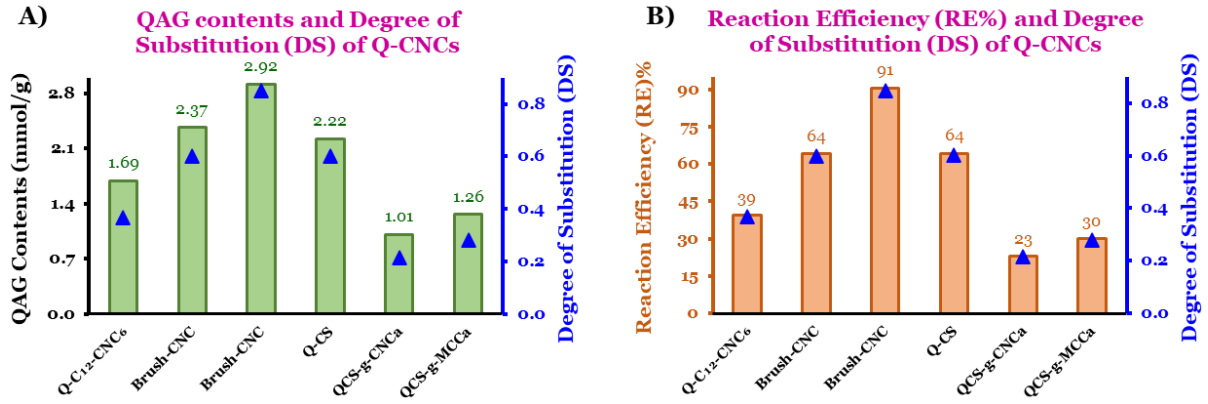


Figure 8.2: *Degree of substitutions (DS) and cationization reaction efficiencies (CRE%) of selected Q–NPs that are modified with hydrophilic/hydrophobic moieties or polymerized.*

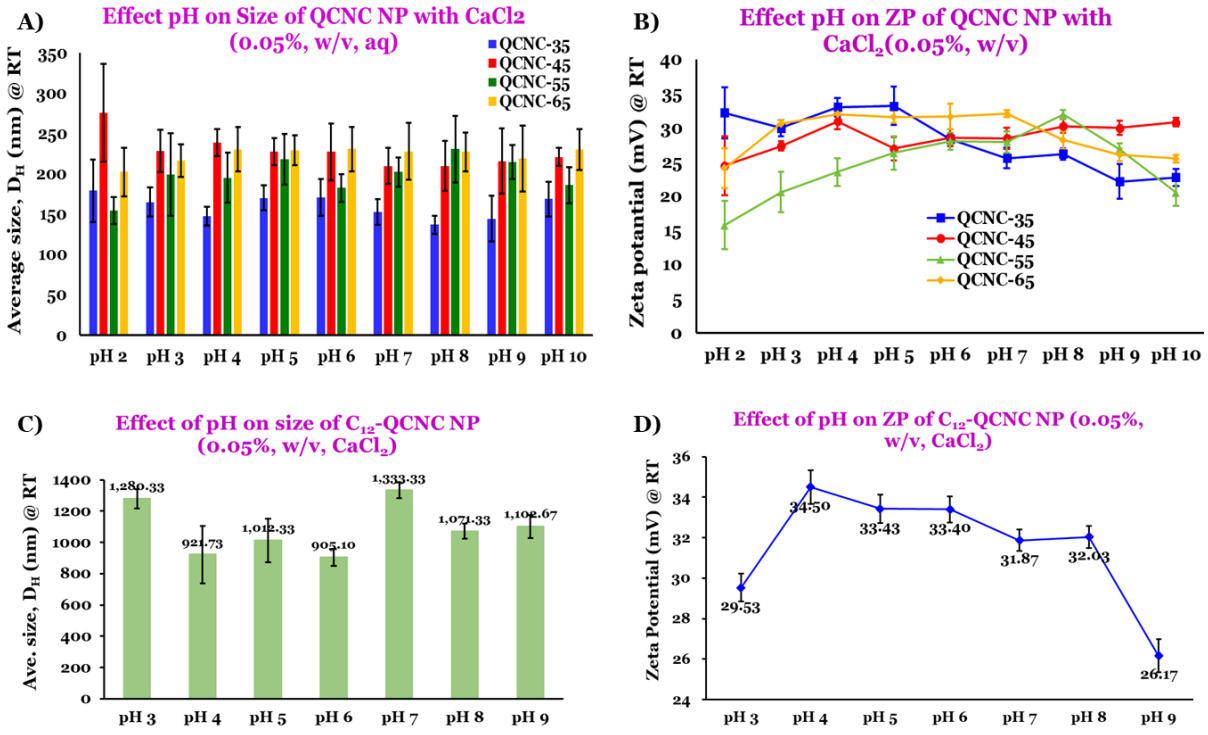


Figure 8.3: *Effect of $CaCl_2$ on the sizes (**A, C**) and ZP (**B, D**) of Q–NPs based on CNCs.*

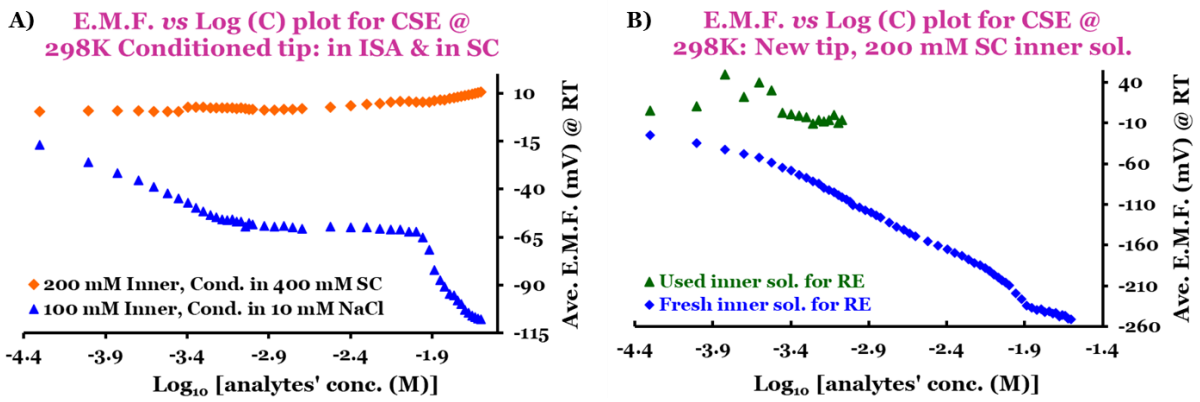


Figure 8.4: A) *Effect of conditioning the desensitized cholate selective membrane, CSM/tip on sensing/detecting the target analyte (sodium cholate, SC). The conditioning of the used CSM/tip (that lost sensitivity) was carried out into highly concentrated (400 mM) sodium cholate (SC) solution in ISA (10 mM NaCl) and ISA only. The results proved that the conditioning of used CSM does not revert the CSMs to their pristine condition.* ***B)*** *Effect of used and fresh inner solutions in reference electrode (RE) for the detection of SC from aqueous samples.*

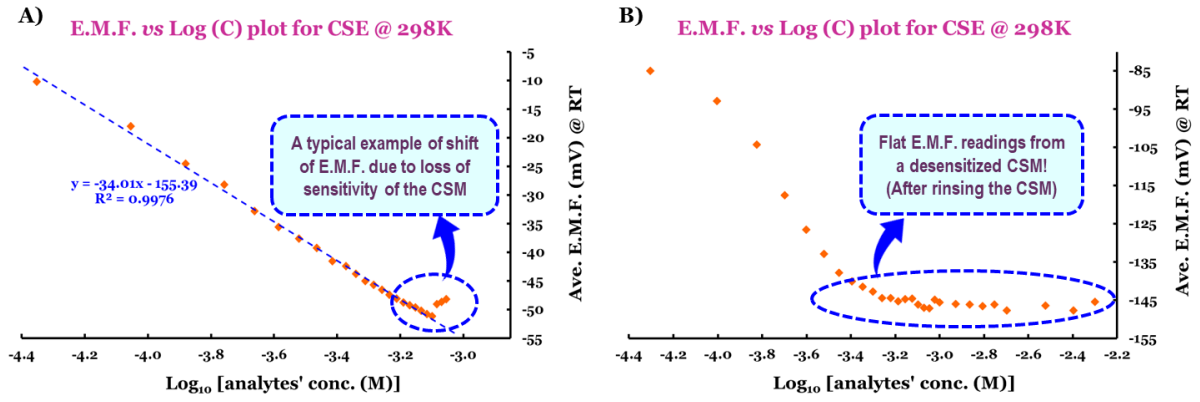


Figure 8.5: A) *Example showing the occurrence of loss of sensitivity of the CSM after more than 150 readings.* ***B)*** *Rinsing the desensitized CSM/tip with MQ water does not help to establish the sensitivity for continuous usage of the same tip.*

A)

Actual Conc. (mM)	*Measured Conc. (mM)	Error (%)	Regression Model Used
3	5.4	80.0	Logarithmic (n)
5	6.7	33.8	Logarithmic (n)
17	17.7	4.3	Averaged
35	34.8	0.4	Logarithmic (n)
51	50.2	1.6	Polynomial
85	84.7	0.4	Logarithmic (n)

B)

Samples' name	*Measured Conc. (mM)	Regression Model Used	Error (%) (disclosed by investigator)
SBT—1	49.8	Logarithmic (n)	0.4
SBT—2	9.3	Logarithmic (n)	7.0

Figure 8.6: *The results of the **A)** unblind test (UBT) and **B)** single-blind test (SBT) conducted for the CSE developed in the lab.*